Angle-resolved femtosecond photoelectron spectroscopy of fullerenes

Olof Johansson

Degree of Doctor of Philosophy

University of Edinburgh

2010

Abstract

An experimental apparatus has been constructed to investigate ionisation mechanisms of complex molecules and nanoparticles after femtosecond and/or picosecond laser excitation. The photoproducts are detected by time-of-flight mass spectrometry and velocity-map imaging (VMI) photoelectron spectroscopy. Test measurements on C_{60} and Xe have successfully reproduced previously published work indicating that the setup is working in a satisfactory manner. New detailed investigations of mass spectra and angle resolved photoelectron spectra (PES) have been carried out as a function of laser intensity, wavelength and pulse duration for C_{60} and C_{70}, providing new insights into the electronic structure and ionisation mechanisms of these molecules.

For 400 nm, 130 fs laser excitation, an isotropic contribution from thermally emitted electrons is found. A series of peaks are seen superimposed on the thermal background with binding energies in agreement with the recently discovered superatom molecular orbitals (SAMOs) of C_{60} [Feng et.al. Science 320 (2008) p. 359]. Furthermore, the angular dependence of the peak in the PES corresponding to the s-SAMO is in agreement with this assignment. To confirm the assignment of the other observed peaks it is concluded that the measured photoelectron angular distributions (PADs) need to be compared to calculated angular distributions. Measurements have also been made with the same wavelength but with a pulse duration of about 5 ps. Mass spectra, PES and PADs for these measurements show that the main ionisation mechanism for these laser conditions is delayed (thermionic) ionisation.

For 800 nm, 130 and 180 fs laser excitation, thermally emitted electrons are observed. In contrast to the 400 nm measurements, the PADs show an asymmetry with higher apparent temperatures along the laser polarisation direction. Measurements were also made for longer pulse durations (1.0 – 3.8 ps). For pulse durations above 1 ps the asymmetry is gradually reduced while the delayed ionisation component in the mass spectrum increases with increasing pulse duration. The asymmetry is compared to calculations made assuming a field-assisted thermal electron emission. Similarly to the 400 nm experiments, a series of peaks are seen superimposed on the thermal background. PADs are presented for these peaks. PADs for peaks with the same binding energy as peaks seen in the 400 nm experiments follow the same trend.

Isotropic PADs after ns laser excitation are also presented confirming delayed ionisation for these pulse durations.

Declaration

I declare that the work presented in this thesis is my own unless otherwise stated by reference.

Olof

Olof Johansson, 2010

To Alexander and Jeanette

Acknowledgements

First of all I would like to thank my supervisor, Prof. Eleanor Campbell for giving me the great opportunity to go on an adventure and do my PhD in Scotland. I am very grateful for everything you have taught me and all your advice and support have truly meant a lot to me. Thank you very much!

I am also very thankful for all the help and advice that I have received when planning and building the experimental apparatus, especially from Drs. Oleg Nerushev, Mikael Kjellberg and Andrei Gromov. I would also like to thank Prof. Alexander Bulgakov for sharing his knowledge during the initial stages of the project. I had a lot of fun putting everything together thanks to all of you.

I am very thankful to Dr. Mikael Kjellberg for teaching me how to work in a lab and plan an experiment. I would also like to thank Gordon Henderson for doing some of the experiments together with me and for taking the late-night shift.

When we were waiting for the labs to be refurbished, Drs. Pat Langridge Smith, Logan Mackay and Stefan Weidt very kindly provided lab space, equipment and a lot of help and advice. I am very happy for this – thank you.

I have really enjoyed the many discussions with Dr. Trevor Ridley about molecular Rydberg states from which I have learnt a lot. Thank you for also teaching me about working with lasers and optics and for also lending us equipment.

Dr. Juraj Fedor, Jakob Stenfalk and Dr. Klavs Hansen, who did the modelling of the asymmetric thermal electron distributions, have answered many of my questions on this subject. Thank you for this.

I would like to thank the two undergraduate students whom I have had the pleasure to work with in the lab: Darren Smith helped with experiments and to test the various acquisition programs; Andreas Molberg help with experiments and wrote the code for smoothing raw VMI images.

I would like to thank Prof. Hanna Reisler and Dr. Boris Karpichev for kindly supplying me a copy of BASEX and Dr. Gustavo Garcia for a copy of pBASEX.

I would like to thank the whole Campbell group for contributing to a nice working environment, for listening to many of my research-related problems and eating

Swedish/Thai/Korean octopus (Wow, thanks for the help in the kitchen and thanks to Eleanor for the cookbook).

I would like to thank my family and friends in Sweden for your patience with me during the many periods when I have been completely absorbed in work and you haven’t heard back from me.

David, muchas gracias por to ayuda fenomenal con todo, especialmente durante el fin de este epoca pesado. Me encanta que Alex tenga tan bueno contacto con su abuelo.

Finally, I would like to thank my family – Jeanette and Alexander. I could not have done this without you. On so many occasions when I have come home disappointed and troubled about something in the lab, you two have cheered me up so that I have forgotten all about lasers that will not work or a pressure in the vacuum chamber that just will not go down! Jeanette, you have been absolutely amazing these last two month when I have been writing up the thesis and I cannot thank you enough. Alex, I fully agree with you when you say that life is “gottigottigott”. This thesis is dedicated to the two of you. I love you.

Table of Contents

Chapter 1 – Introduction

The aim of this thesis is to study the energy redistribution and ionisation mechanisms of fullerenes C_{60} and C_{70} after femtosecond and picosecond laser excitation through means of mass spectrometry and angle-resolved photoelectron spectroscopy. In chapter 1, ionisation mechanisms after ultrafast laser excitation of atoms, molecules and clusters are briefly reviewed. An introduction to the experimental technique used to measure angle-resolved photoelectron spectra is also given. A detailed description of the newly constructed experimental setup including various tests of the apparatus is presented in chapter 2. The new apparatus is based on a similar setup in Prof. Campbell's previous lab in Gothenburg University, Sweden. An initial period of the research project was spent in this lab working on the apparatus and also participating in some of the experiments together with Mikael Kjellberg, Alexander Bulgakov and Klavs Hansen. The results from these experiments are presented in chapter 3 where the importance of excitation energy redistribution among the valence electrons in determining the ionisation mechanism of C_{60} and C_{70} is discussed. Chapter 4 deals with the population and subsequent ionisation of what is thought to be Rydberg states in fullerenes. A conclusion is presented in chapter 5 together with an outlook of future experiments.

1.1 Why do we study fullerenes?

The use of femtosecond lasers has enabled the study of chemical reactions in real-time. The duration of femtosecond laser pulses is of the same order of magnitude as atomic motion in molecules. Therefore it is thought that it can be possible to control photochemical reactions using pulsed lasers. Coherent control is a particular method that is believed to achieve this and involves exciting a molecule or cluster through a specific quantum mechanical pathway using phase-shaped ultrashort laser pulses [1, 2]. However, in large molecules, ultrafast internal energy dissipation quickly destroys the coherence and therefore makes coherent control impossible. It is therefore of interest to study time scales and processes involved in the dissipation process in complex molecules. Fullerenes C_{60} and C_{70} can be seen as model systems for clusters and complex molecules and because they are homonuclear molecules and possess high symmetry, theoretical modelling is facilitated.

Many experiments using coherent control have successfully been carried out on atoms and relatively simple molecules [1]. In contrast, an extensive experimental study by Lozovoy *et. al.* of several organic molecules showed that the fragmentation pattern observed in mass spectra depended only on parameters such as pulse energy and duration [3]. This is indicative that energy redistribution and loss of coherence is important for large organic molecules. Some results concerning the application of a model developed for C_{60} to three different polycyclic aromatic hydrocarbons (PAHs) are given in chapter 3.

By using laser pulses with varying duration, intensity and wavelength, much work over the last 20 years has been done on the fullerene C_{60} in the gas phase [4-7]. Many interesting aspects have emerged out of this research and one is related to the fact that in order to gain knowledge about a quantum system, the observer has to perturb the system in some way [8]. If the pulse duration is short enough (femtoseconds, i.e. 10^{-15} s), the observer can to some extent draw the conclusion that the behaviour of C_{60} is similar to that of a single atom. On the other hand, if the laser pulse is longer (typically nanoseconds, i.e. 10^{-9} s), the observer will detect a response usually seen in bulk metals. Thus, the conclusions drawn about the system depend on how the system is perturbed. Studies of different perturbations of the C_{60} molecule will provide insight into the mechanisms controlling light-matter interaction with systems of comparable size which in turn will increase the understanding of how nano-scale material behaves.

An interesting discovery about C_{60} was published by Boyle *et. al*. in 2001 [7] concerning the observation of Rydberg states in C_{60}. These had previously not been seen with conventional spectroscopic methods but with ultrafast lasers these states became accessible. A Rydberg state is a highly excited state in an atom or molecule. The radius of the excited orbital is large compared to the spatial extension of the inner core electrons. The remaining inner electrons screen the charge of the nucleus so the excited electron effectively sees a single charge. This results in what appears to be a highly excited hydrogen-like atom. A Rydberg series can be defined for each orbital angular momentum quantum number ℓ. A quantum defect δ_ℓ is normally introduced since the system lowers its energy if the Rydberg electron penetrates through the inner core electrons and thus feels a greater attractive potential. The energy level $E_{n,\ell}$ for each principal quantum number n in a Rydberg atom or molecule can for a given ℓ be described as

$$E_{n,\ell} = -\frac{R}{(n-\delta_{\ell})^2}, \tag{1.1}$$

where R is the Rydberg constant (13.6 eV).

Recently Feng *et.al*. published theoretical and experimental results in *Science* showing orbitals in C_{60} that appeared as if the molecule was one large H-like atom [9]. Adsorbed molecules on a copper surface were investigated using low-temperature scanning tunneling microscopy (STM) and individual molecules could be distinguished (see Figure 1.1). The finding that the orbitals of C_{60} showed resemblance to atomic orbitals led the authors to label them superatom molecular orbitals (SAMOs). It is interesting to investigate whether the SAMOs can also be seen in gas-phase experiments where the fullerenes are heated to high temperatures (ca 500 °C). Especially, it would be interesting to see if there could be a link between the SAMOs and the Rydberg states seen by Boyle *et. al.*. Such investigations are presented in chapter 4.

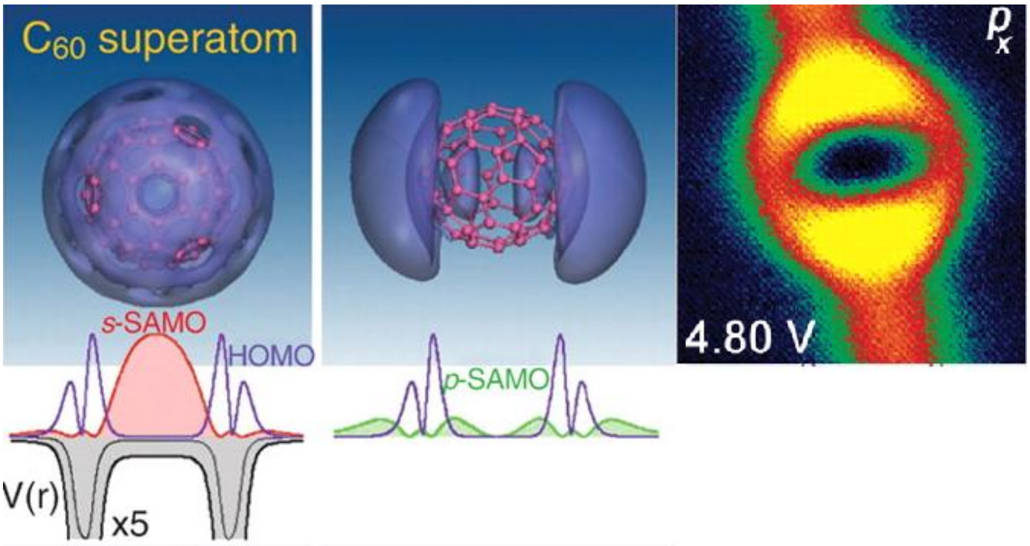

Figure 1.1: The two images on the left show superatom molecular orbitals (SAMOs) of C_{60}. These were obtained by plane-wave DFT calculations where s, p and d-like orbitals were found akin to atomic orbitals. In the image s and p states are shown. The radial distribution functions are shown below the images. An STM image is shown to the right showing a p_x orbital in an isolated C_{60} on a copper surface. The states were found about 3–4 eV above the lowest unoccupied molecular orbital. Modified figure from ref. [9].

1.2 The interaction of atoms with ultrashort pulses of non-resonant laser light

During the last two decades much attention has been focused on the interaction of atoms and molecules with intense and ultrashort laser pulses. In these experiments one typically studies photoionisation and uses mass spectrometry and photoelectron spectroscopy in order to detect the ions and free electrons created in the ionisation process. One advantage of photoelectron spectroscopy is that selection rules are not as strict as when using e.g. UV/VIS absorption spectroscopy [10]. In order to ionise gas-phase atoms or molecules with wavelengths in the optical or near-infrared region the combined energy of several photons is needed and typically relatively high laser intensities are therefore needed (on the order of 10^{10} – 10^{13} W/cm^2). These high intensities can give rise to effects which will influence the ionisation mechanism. In atoms and simple diatomic molecules, three ionisation mechanisms are traditionally used to describe the influence of a non-resonant laser field on the atom or molecule when the photon energy is much lower than the ionisation potential [11]. These are (i) multiphoton ionisation, (ii) tunneling and (iii) over-the-barrier ionisation. Because the coupling of the laser photons with the atom is so strong one has to consider the system "atom + field + $V_{a,f}$" where $V_{a,f}$ is the coupling of the atom with the laser field [12]. This results in shifting of atomic energy levels and is called the A.C. Stark shift or light shift. For the laser intensities typically used in these kinds of experiments (10^{10}–10^{16} W/cm^2) the light shift can be approximated by the ponderomotive energy U_p [13]. This is the average energy that a free electron acquires in a time varying electric field and can be expressed as

$$U_p = \frac{e_0^2 I}{2m_e \varepsilon_0 c \omega^2} = 9.34\times10^{-20}[\{\lambda(\text{nm})\}^2 \times I(\text{W/cm}^2)] \quad \text{eV} \tag{1.2}$$

where e_0 is the elementary charge, I is the laser peak intensity, m_e is the mass of the electron, c is the speed of light in vacuum, ε_0 is the vacuum permittivity, λ is the wavelength of the light in vacuum and ω is the angular frequency of the laser field. The right hand side in the above equation gives U_p in eV. The equation above is valid in the long-wavelength limit [13]. If the light shift is to be calculated for loosely bound systems or for ultraviolet light the equation is no longer valid [13] and a more formal approach has to be taken (see e.g. [12]). Since the light shift can be approximated by the ponderomotive energy it is also often called the ponderomotive shift and it can be seen from the above equation that it scales linearly with laser intensity.

The Keldysh parameter γ is traditionally used to distinguish between the three different ionisation mechanisms mentioned above [11, 14]:

$$\gamma = \sqrt{\frac{IP}{2U_p}} = 2.31\times10^{9}\sqrt{\frac{IP(\text{eV})}{I(\text{W/cm}^2)[\lambda(\text{nm})]^2}} \tag{1.3}$$

where IP is the ionisation potential of the atom. The Keldysh parameter will be discussed in more detail below where the three ionisation mechanisms are explained.

1.2.1 Multiphoton ionisation

For relatively low intensities (typically 10^{10}–10^{13} W/cm^2) direct multiphoton ionisation occurs. This means that the atom coherently absorbs the number of photons needed to overcome the ionisation potential. Due to the ponderomotive shift the ionisation potential (IP) is also shifted by an extra amount U_p while the ground state is not affected [13]. Thus the measured kinetic energy of the ejected electron is $E_{kin}=mh\nu-IP-U_p$ where m is the number of photons needed to fulfil $mh\nu-IP-U_p \geq 0$. Usually the atom can absorb more energy than necessary to promote an electron into the continuum. If the excess energy is carried away with the photoelectron this will result in equidistant peaks in the photoelectron spectrum (PES) separated by the photon energy. The process is called above threshold ionisation (ATI) and a typical PES can be seen in Figure 1.2a. When no resonances are involved the ionisation probability scales with light intensity as I^n where n is the number of photons needed to ionise the atom and I is the laser intensity [15]. If any intermediate electronic states can be reached by a certain number of photons the ionisation probability is greatly enhanced. The process is then called resonance enhanced multiphoton ionisation (REMPI). In the multiphoton regime the Keldysh parameter is larger than one. The electric field of the laser acts as a perturbation and is considerably weaker than the field holding the atom together.

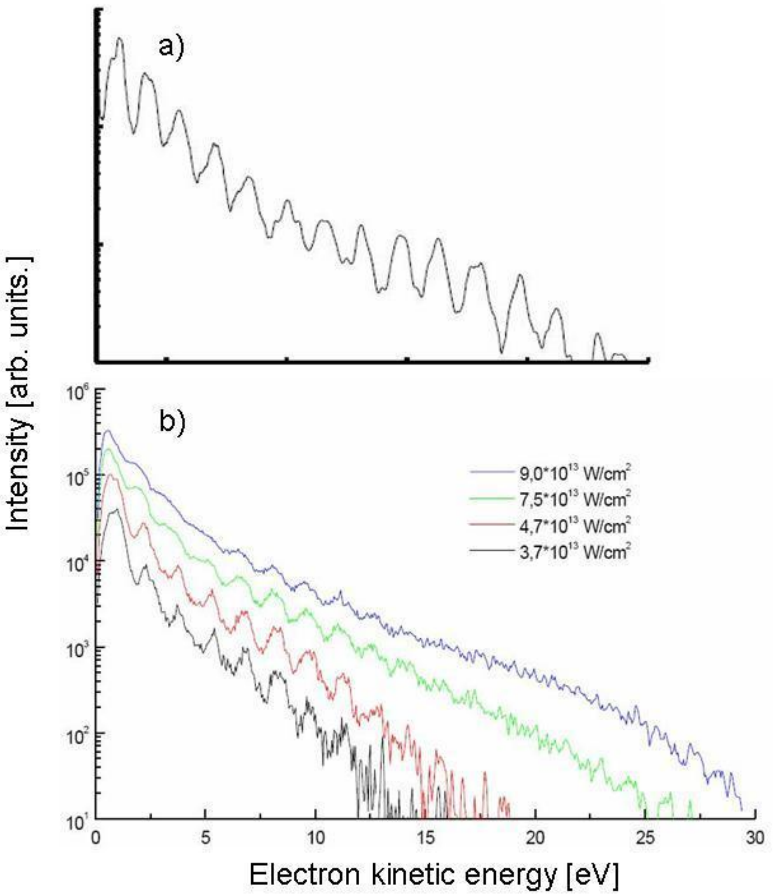

Figure 1.2: PES of a) argon using 800 nm photons and intensity 3x10^{13} W/cm^2 (adapted from ref.[16]) and b) C_{60} with 800 nm wavelength and 25 fs pulse duration. Plot adapted from ref.[17]. The figures illustrate the similarities between atoms and C_{60} when the laser intensity is in the multiphoton regime (<5x10^{13} W/cm^2 in figure b) and below ca. 70 fs. The plots have the same energy-scale.

1.2.2 Tunneling ionisation

When the magnitude of the electric field of the laser is increased it becomes comparable with the binding potential of the atom. This results in suppression of the barrier that confines the electrons in the atom. The electrons can then tunnel through the barrier resulting in the formation of an ion which is shown in Figure 1.3. Since the Keldysh parameter depends on the ratio of the ionisation potential and the ponderomotive potential (which is proportional to the square of the field strength of the laser) this process occurs when $\gamma \approx 1$. When the electric field of the laser changes sign, the electron is driven back towards the ion. The electron can subsequently either scatter off the ion [18] or recombine with the ion (resulting in high harmonic emission [19]). However, if the tunneling period is long compared to the frequency of the light the electron does not have time to tunnel through the barrier before the field changes sign. It is possible to show that γ can be related to the period of the laser and the tunneling time. This mechanism is called tunneling ionisation.

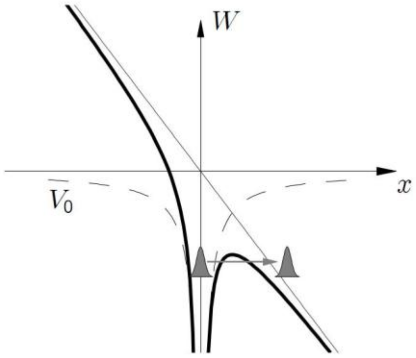

Figure 1.3: Potential energy (W) experienced by an electron bound to an atom as a function of distance from the nucleus. The solid black line shows the potential energy in the presence of a strong laser field (straight line with negative gradient). Due to the resulting suppression of the confining barrier the electron can tunnel through and the atom becomes ionised. The dashed line shows the unperturbed potential energy. Figure from [16].

1.2.3 Over-the-barrier ionisation

When the laser field is strong enough the electrons can simply escape over the barrier without tunneling and the confining potential is weaker than the energy of the escaping electron. Therefore, the mechanism is called over-the-barrier ionisation. The latter two cases (tunneling and over-the-barrier) are usually referred to as field ionisation.

In summary, when $\gamma<1$ the intensity is in the field ionisation regime and $\gamma>1$ corresponds to the multiphoton regime. The model above is usually referred to as the quasistatic model and it assumes one single active electron (SAE) that is involved in the excitation and ionisation dynamics. A characteristic feature for multiphoton ionisation is, as mentioned before, ATI peaks in the photoelectron spectrum. In Figure 1.2 b) photoelectron spectra of C_{60} ionised with an 800 nm femtosecond laser can be seen. For laser intensities above 7×10^{13} W/cm^2 the spectra show the gradual disappearance of ATI peaks and a more structureless spectrum becomes visible, indicating field ionisation. For the lowest intensity in Figure 1.2 b) $\gamma = 1.3$ and for the highest $\gamma = 0.8$.

1.3 Photoionisation of C_{60}

If gas phase fullerenes in vacuum are excited to sufficiently high internal energies they decay by C_2 evaporation, electron emission and photon emission. It has been found that the mechanisms describing ionisation of C_{60} depend on the pulse duration. ATI peaks have been observed in photoelectron spectra when using sub-50 femtosecond pulses [6] (Figure 1.2 b and Figure 1.5 e,f), as have signs of field ionisation [17, 20]. In the following brief review of photoionisation of C_{60}, the experimental results were all acquired using photon energies below the ionisation potential of C_{60} (7.58 eV [21, 22]).

When C_{60} is excited with a laser pulse of a few picoseconds up to nanosecond duration, the main ionisation mechanism is thermionic emission [23]. In these types of experiments, several photons are absorbed by the molecule and the absorbed energy is quickly dissipated into the various degrees of freedom of the molecule. Eventually the molecule will be heated to the extent that the vibrational energy is enough to ionise it. This process can be seen as the evaporation of an electron. The event does not have to be direct with respect to the laser pulse. In fact, it has been found that the electron emission can take place up to several µs after the laser pulse [23]. This phenomenon is seen in the time-of-flight (TOF) mass spectrum as a tail on the C_{60}^{+} peak due to the delayed electron emission. In this time domain the mass spectrum is dominated by singly charged species and hardly any multiply charged species are seen. The fullerenes fragment with C_2 evaporation and for these experimental conditions the smallest fullerene detected in mass spectra is C_{32}^{+} [24]. This is seen in Figure 1.4 (a) where the delayed ionisation of the singly charged parent ion can also be seen. At high laser fluences the fullerenes break down and emit larger fragments which form small carbon rings and chains. These are seen in the lower mass section of the spectrum. In Figure 1.4 (a) there is a small peak on the low-mass side of each fullerene peak. These minor peaks are due to the fragmentation of fullerenes in the drift region of the time-of-flight reflectron mass spectrometer and since the fragments are created after the ionisation region they are called metastable fragments. The fragmentation of fullerenes can be described with a statistical model which assumes that all energy is distributed among all internal degrees of freedom [25].

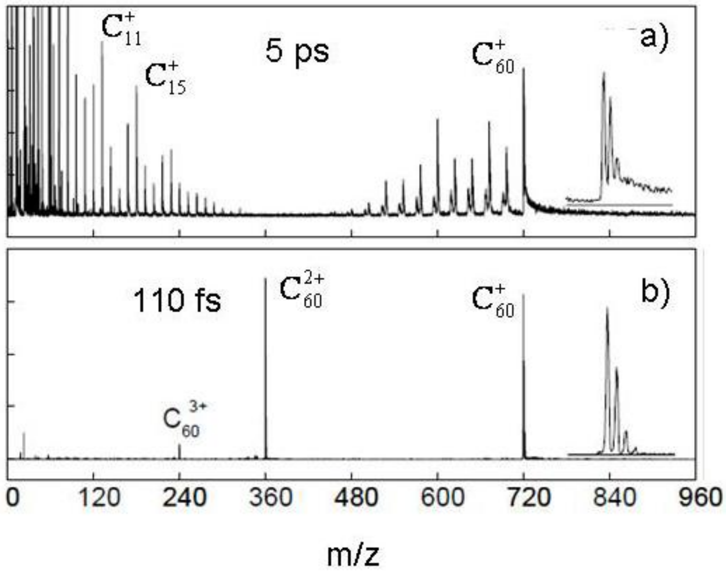

Figure 1.4: Typical mass spectra illustrating the difference between ionising C_{60} using ps–ns laser pulses (thermionic emission) compared to using pulses of 110 fs duration (transient thermal electron emission). Both spectra were obtained using the same wavelength (790 nm) but with different pulse durations: (a) 5 ps (with intensity 3.0 × 10^{12} W/cm^2) and (b) 110 fs (with intensity 3.7 × 10^{13} W/cm^2). The insets show the isotope distribution of C_{60} and in (a) a tail on the parent ion peak can also be seen due to delayed ionisation. Figure from ref.[17].

The PES, *S(ε)*, resulting from thermionic electron emission is structureless and can be described by a Boltzmann function [26-28] with an associated apparent temperature T_a according to

$$S(\varepsilon)d\varepsilon \propto \exp(-\varepsilon / \mathrm{k_B} T_a)d\varepsilon \tag{1.4}$$

where ε is the photoelectron kinetic energy and k_B is the Boltzmann constant. T_a can be related to the amount of energy absorbed by the molecules on average and typical apparent temperatures on the order of 3000–4000 K are observed [4, 29]. It is possible to set Boltzmann's constant equal to unity so that T_a is given in units of eV [30] (which is done in this thesis). A typical PES after ps laser excitation can be seen in both a lin-lin and log-lin scale in Figure 1.5 (a) and (b) respectively.

When the pulse duration is decreased to 150 – 200 fs a similar Boltzmann-like PES is seen as for the picosecond and nanosecond case (Figure 1.5 c,d). However, there are two main differences. One is that the apparent temperature is much higher although the mass spectrum shows much less fragmentation for similar pulse energies. This has been interpreted as a thermalisation of the excitation energy among the valence electrons and subsequent evaporation of electrons prior to coupling of the excitation energy with vibrational degrees of freedom [6, 29]. The heat capacity is lower for the electronic sub-system alone compared to when the vibrational degrees of freedom are also included. That is why higher apparent temperatures are detected and since most of the excitation energy is carried away with the emitted electron, the residual ion is left cool and that is why little fragmentation is seen in the mass spectra (see Figure 1.4 b). The other difference compared to pico- and nanosecond PES is that there is some structure seen below kinetic energies corresponding to the photon energy (about 1.5 eV in Figure 1.5). The structure is thought to be due to single-photon ionisation of the aforementioned Rydberg states [7].

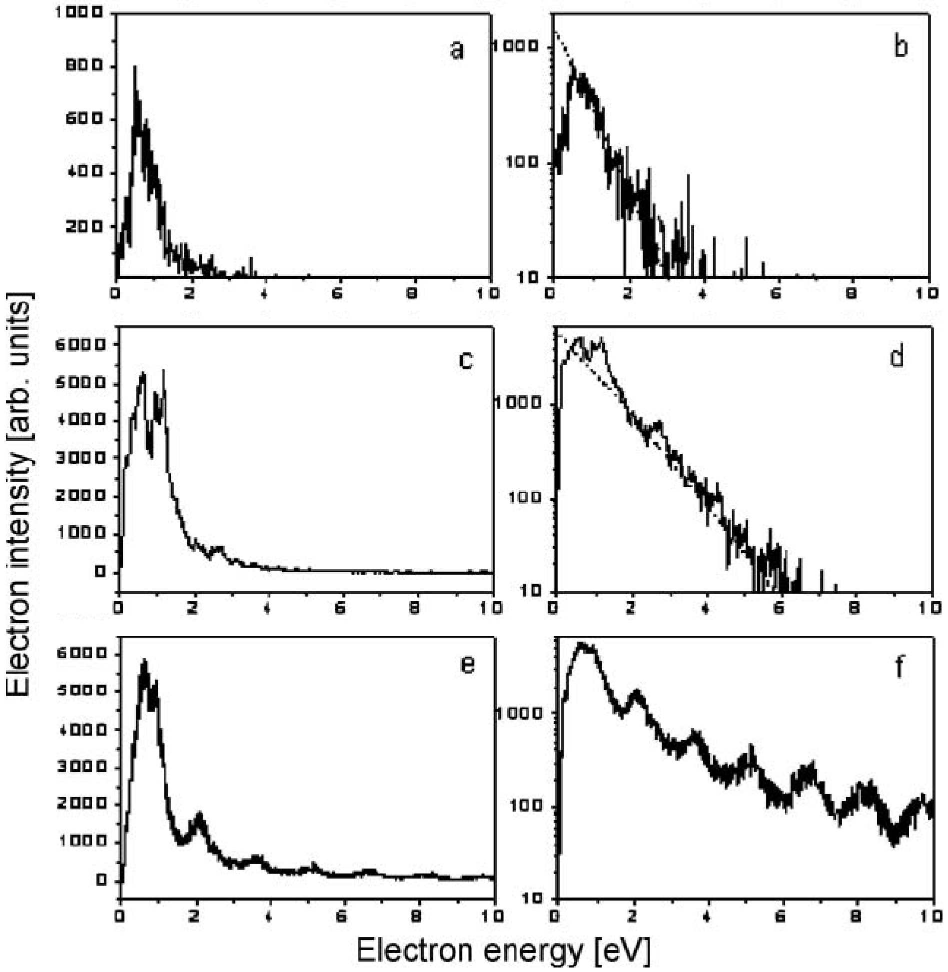

Figure 1.5: PES of C_{60} for pulse durations (fluence) a,b) 5 ps (3 J/cm^2); c,d) 250 fs (3 J/cm^2) and e,f) 25 fs (1 J/cm^2). The laser wavelength was 800 nm. The detector sensitivity is low for electrons with kinetic energies below 0.5 eV. Modified figure from ref. [4].

The experimental work presented in this thesis covers pulse durations from 120 fs up to nanoseconds. Nevertheless, it is interesting and useful to review experimental findings of ionisation mechanisms of C_{60} for even shorter pulse durations. It seems that more direct processes are involved in the ionisation process with decreasing pulse duration [6]. Both mass spectrometry and photoelectron spectroscopy obtained using sub-50 fs laser pulses show that the transition between the various intensity regimes can be defined by the Keldysh parameter [31]. Ion yields as a function of laser intensity show a direct multiphoton process with no signs of REMPI when using 400 and 800 nm pulses [31]. The ATI peaks seen in PES also suggest a direct ionisation mechanism (Figure 1.5 e,f). For longer wavelengths (1500–1800 nm), high charge states up to C_{60}^{12+} are seen in the mass spectrum [32] and barely any fragmentation [33]. The Keldysh parameter characterising the laser intensity used in refs. [32, 33] was less than unity which indicates a tunneling mechanism. In ref. [33] the authors investigated the influence of the recolliding electron produced in the tunneling ionisation process on the fragmentation pattern and concluded that in the long-wavelength limit, recollision processes dominate the occurrence of fragmentation. The experiments indicate that in this intensity and wavelength limit, field ionisation is indeed the main ionisation mechanism.

The observations presented above are consistent with a SAE picture and support the quasistatic model. However, there are some aspects that contradict this conclusion and indicate that several electrons are excited during the laser pulse. In a theoretical paper by Bauer *et. al*. [34, 35] it is shown that ATI can occur through multielectron dynamics demonstrating that ATI does not necessarily imply ionisation by a SAE. Furthermore, the quasistatic model does not take into account any intermediate resonances which for C_{60} may be important because there is a small peak at about 2 eV in the optical absorption spectrum [36, 37] and the first optically allowed transition occurs around 3.75 eV [38] (much stronger than the peak at 2 eV). Furthermore, the intensity dependence of the aforementioned ion yield results can, instead of a direct multiphoton mechanism, also be described by the transient thermal emission model which does indeed take into account multiple excited electrons [29]. In experiments using 400 and 800 nm, sub-50 fs pulses the fragmentation pattern can be described with statistical models [39]. This indicates that the ion is left with excitation energy equilibrated over the vibrational degrees of freedom after an electron has been emitted. Apparent temperatures of around 3000 K are found which is equivalent to an internal excitation energy of about 40 eV. Even with 9 fs and 800 nm pulses, fragmentation has been observed [40]. It seems unlikely that energies up to 40 eV could be deposited into one excitation channel without causing prompt ionisation. Therefore it is likely that several electrons are excited during the ultrashort laser pulse. A comparison between mass spectra obtained using 800 and 1500 nm excitation (with approximately the same intensity) is shown in Figure 1.6. For the longer wavelength, where field ionisation is thought to be dominant, the mass spectrum is consistent with the adiabatic removal of electrons without any residual vibrational excitation. In the case of 800 nm, the amount of fragmentation suggests that vibronic transitions are important in redistributing the excitation energy into vibrational degrees of freedom.

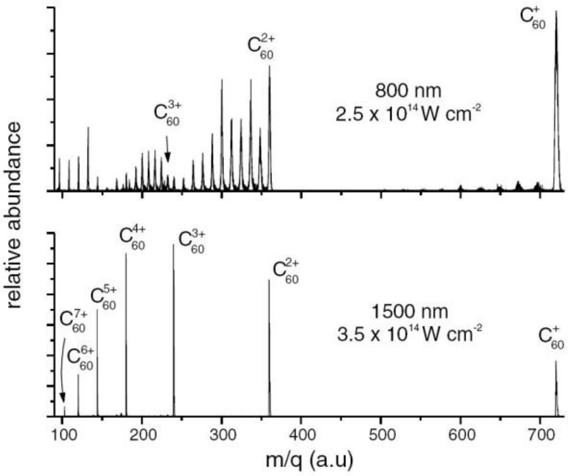

Figure 1.6: Mass spectra obtained with different wavelengths when ionising C_{60} with 800 nm (40 fs) and 1500 nm (70 fs) laser light. Figure from ref. [33].

1.3.1 Summary of ionisation models

A brief summary is given in Table 1 to clarify what signatures in experimental data (angle-resolved PES and time-of-flight mass spectra) one would expect from the different ionisation models discussed in Sections 1.2 and 1.3.

Table 1: Summary of different ionisation models discussed in the thesis.

Model	**Electron emission time scale**	**Signature in PES**	**Signature in mass spectrum**
Multiphoton ionisation	Promt	ATI peaks	Multiply charged parent ions with little or no fragmentation
Field ionisation	Promt	Structureless PES, highly directed along laser polarisation direction	Multiply charged parent ions with little or no fragmentation
Transient thermal electron emission	Fs – ps	Isotropic, structureless PES. T_a on the order of eV.	Multiply charged parent ions with little or no fragmentation
Thermionic emission	Fs – µs	Isotropic structureless PES. T_a on the order of hundreds of meV.	Singly charged species with a bimodal mass distribution. Asymmetric tail on C_{60}^{+} peak in TOF spectrum due to delayed ionisation.

1.4 Photoionisation of clusters and organic molecules

For atomic clusters with relatively high internal temperatures, the jellium model is often applicable [41]. The high temperature smears out detailed arrangements of the ionic core and it is only the overall shape of the cluster that determines its stability [42]. For closed-shell clusters, the delocalised valence electrons are confined in a potential that is spherically symmetric. The jellium model has successfully described the results of many experiments on sodium clusters [42] which justifies the use of the model. From the spherical symmetry and the nature of the delocalised valence electrons of these clusters, it is reasonable to compare experimental results on metallic clusters with fullerenes. However, one difference lies in the optical absorption spectra. It has been found that the delocalised electrons in a metallic cluster can easily adjust to an external field [43]. This results in excitation of a surface plasmon and typical energies lie in the optical region. The energy needed to excite the plasmon in C_{60} is about 20 eV [44] which means that coherent excitation of the plasmon is unlikely for the intensity range used for the experimental results presented in this thesis. The transient thermal electron emission model used to interpret experimental results on C_{60} [6, 29] has also been used on sodium clusters. Measured structure-less PES obtained after femtosecond excitation of Na_{93}^{+} were interpreted in ref. [45] as a rapid thermalisation of the excitation energy among the valence electrons with subsequent evaporation of electrons. This illustrates the similarities between the two systems.

The ionisation mechanisms of many organic molecules with an extended delocalised electronic system have also been studied. Of particular interest in the comparison with fullerenes, are PES obtained after femtosecond excitation of benzene, naphthalene and anthracene by DeWitt and Levis [46]. They observed, for the same laser intensity, that benzene showed ATI structure in the PES whereas a smooth, structure-less PES was obtained for anthracene. The authors concluded that it was easier to field-ionise larger molecules. However, due to the similarities with the structure-less PES obtained from fullerenes under similar laser conditions, it is possible to interpret the anthracene results in view of the transient thermal emission model. The electron-electron interactions involved in the thermalisation process in clusters and fullerenes could be related to the so-called quasicontinuum (QC) of excited electronic states invoked by Markevitch *et. al.* [47] for large organic molecules. They present evidence that the QC, which arises due to large mixing between electronically excited states caused by the high laser intensity, can lead to dissociative ionisation. The non-adiabatic multielectron dynamics (NMED) involved in forming the QC could also lead to a thermalisation of the excitation energy which could result in thermal electron emission.

1.5 Angle-resolved photoelectron spectroscopy

The various experimental results reviewed above were typically taken with either a linear time-of-flight or magnetic bottle photoelectron spectrometer. In this thesis, some of the old experiments on C_{60} will be revisited using a relatively new technique called velocity-map imaging (VMI) photoelectron spectroscopy. This method simultaneously records photoelectron kinetic energy distributions and angular distributions of the emitted electrons with respect to the polarisation direction of the ionising laser. In the remaining part of this chapter, an introduction to photoelectron spectroscopy and VMI is given.

1.5.1 Introduction to photoelectron spectroscopy and photoelectron angular distributions (PADs)

Photoelectron spectroscopy is a technique widely used in many areas of physics and chemistry to obtain information about e.g. energy levels in atoms, molecules and solids. The technique involves the removal of one or several electrons from the sample under investigation using a light source and measures the kinetic energy distribution of the emitted electrons. Since free electrons are created using light, these electrons are usually referred to as photoelectrons. To understand why information about energy levels can be obtained it is useful to consider a neutral atom A, ionised with a photon of energy $h\upsilon$. After the ionisation process an ion A^+ and a free electron e^- are created. This can be written as $A + h\upsilon \rightarrow A + e^-$. Conservation of energy yields $E(\mathrm{A}) + h\nu = E(\mathrm{A}^+) + E(\mathrm{e}^-)$ which shows that if the photon energy and electron kinetic energy $E(\mathrm{e}^-)$ are known, the energy difference between the initial and finial state can be found. If the neutral atom is in its ground state before ionisation and the finial state of the ion is the ground state, then the energy difference is the first ionisation potential. Depending on the photon energy, different states in both the initial and final species can be probed.

Photoelectron angular distributions (PADs) can provide further information about the ionisation dynamics compared to the angle-integrated photoelectron spectra. The angular part of the outgoing electron's wavefunction can be described as a series expansion in spherical harmonics Y_{LM} which are also known as partial waves [48]. The expansion coefficients are related to the radial dipole matrix elements which gives information about how strong the coupling between the initial bound state and the continuum is for each partial wave. The outgoing partial waves will interfere in a way that is determined by their relative phase difference. The phase difference is related to how each partial wave interacts with the ion core as it leaves the ion. Therefore, the phase shifts are related to the quantum defect. Although the outgoing electron waves can carry many units of angular momentum, the PAD $I(\theta)$ for a specific kinetic energy resulting from single-photon ionisation of a randomly oriented sample is [48, 49]

$$I(\theta) = \frac{\sigma}{4\pi}\left(1 + \beta_2 \, \mathrm{P}_2(\cos\theta)\right) \tag{1.5}$$

where β_2 is the so-called anisotropy parameter, P_2 is the second order Legendre polynomial and σ is the angle-integrated cross section for emitting a photoelectron of the specific kinetic energy. The distribution above cannot be negative which gives the restriction on the value of the anisotropy parameter to be between –1 and 2. The anisotropy parameter contains information about the radial dipole matrix elements and the phase difference between the different partial waves.

In the case of a central potential, where ℓ is a good quantum number, optical selection rules dictate that the outgoing electron waves are only comprised of two partial waves with angular momentum corresponding to $\ell_i \pm 1$ (ℓ_i refers to the angular momentum quantum number of the initial state). In this case the β_2 parameter can be calculated with the Cooper-Zare formula [50]

$$\beta_2 = \frac{\ell(\ell-1)R_{\ell-1}^2 + (\ell+1)(\ell+2)R_{\ell+1}^2 - 6\ell(\ell+1)R_{\ell+1}R_{\ell-1}\cos\left(\delta_{\ell+1}-\delta_{\ell-1}\right)}{(2\ell+1)(\ell R_{\ell-1}^2 + (\ell+1)R_{\ell+1}^2)} \tag{1.6}$$

where

$$R_{\ell\pm1} = \int \psi_f^{\ell\pm1}(r)\psi_i^{\ell\pm1}(r)r^3 dr$$

are the radial dipole matrix elements for the final (f) and initial (i) states. The orbital angular momentum quantum number ℓ in the above equation is that of the initial state. As can be seen from the above equation the experimental determination of β_2 will not be enough to find the radial dipole matrix elements and the phase shifts since there are more unknown than known variables. Therefore, a complete description of the ionisation dynamics cannot be gained from experiments involving one-photon ionisation of a randomly oriented target. On the other hand, one implication of equation (1.6) is that if the initial state is an s-state (given that ℓ is a good quantum number) the outgoing wave will only consist of one partial wave. This would be a pure p-wave due to optical selection rules and from equation (1.6) $\beta_2 = 2$. This might not provide much information about the ionisation dynamics but if the initial state is not known, a measured anisotropy parameter equal to two could provide insight into the initial state. However, even in the simple case of an s-state, a β_2 value different from two can arise due to electron exchange and correlations and relativistic effects (see e.g. [51] and references therein). Therefore, a measured β_2 value different from two does not necessarily mean that the initial state is not an s-state.

In REMPI, the initial state is optically prepared by the pump photons which introduces an anisotropy in the system. Therefore, higher order partial waves will be seen in the PADs. For a single pulse of linearly polarised light, an *N*-photon process will give a PAD according to

$$I(\theta) = \frac{\sigma}{4\pi}\left(1 + \sum_{k=1}^{N} \beta_{2k}\ \mathrm{P}_{2k}(\cos\theta)\right). \tag{1.7}$$

If the intermediate state in the REMPI process is spherically symmetric, equation (1.7) will reduce to equation (1.6). If the *N*-photon process is not coherent and the intermediate state has time to depolarise equation (1.7) will also reduce to equation (1.6). [52]

Although a PAD following equation (1.6) cannot be used alone to extract all the information contained in the β_2 parameter, it can still provide some information about the initial state should that state not be known. For example, the Rydberg states of C_{60} are thought to be one-photon ionised [7]. If the ionisation mechanism is a coherent multiphoton ionisation mechanism then the PAD should be described by equation (1.7). This would imply that there is a memory in the excited Rydberg states of how it was populated which is reflected in the PAD. On the other hand, if simple PADs as described by equation (1.6) above are found, then it is possible that the Rydberg states do not have any memory of how they were populated. This could imply that they are related to the thermalisation process previously mentioned. On the other hand, another reason for a simple PAD can also be that the initial state is spherically symmetric. Nevertheless, even though a complete description of the ionisation dynamics through PADs seems to be difficult to obtain for complex molecules, some information can still be extracted.

The method of using PADs as a way to investigate the angular momentum character of electronic shells in Na clusters was presented in ref. [53]. The anisotropy parameter after single-photon ionisation was measured for a range of different photoelectron kinetic energies. In the study the authors concluded that the clusters were well-described by the orbital angular momentum quantum numbers arising from the use of a simple jellium-like potential. Calculations of the kinetic energy dependence of the anisotropy parameter were made which were in reasonable agreement with experiments. However, the 2s state did not result in $\beta_2 = 2$ for any of the measured photoelectron kinetic energies which was on the order of electronvolts. The time the electrons spend in the vicinity of the cluster is on the same order as the inverse of the plasmon frequency for these clusters. Therefore the authors attribute the discrepancy between theory and experiments due to multielectron effects. These effects have been treated in calculations by Solov'yov *et. al.* which give a better agreement with experimental findings [54] although it was not discussed why an anisotropy value different from 2 could arise from ionisation of the 2s state.

1.5.2 Velocity-map imaging

With a velocity-map imaging detector, the simultaneous detection of both kinetic energy distributions and angular distributions is possible. In a general photoionisation experiment electrons are created and, if no external fields are present, these electrons can expand freely in space. The direction of emission will depend on the initial momentum of the ejected photoelectron. One can define a Cartesian coordinate system where the electrons are created at the origin and the laser propagates along the x-axis (see Figure 1.7). The polarisation direction of the laser is parallel with the z-axis. Electrons with the same kinetic energy will span the surface of a sphere after some time t. The radius R of the sphere is the product of the initial velocity v_0 of the electron and the time t elapsed. The angular distribution $F(\theta,\varphi)$ of the emitted electrons can be described with two variables on the surface of the sphere, where θ,φ are the polar and azimuthal angles used in the spherical coordinate system.

In order to measure the 3D distribution of photoelectrons an electric field is applied antiparallel to the y-direction. The electrons are then accelerated in the opposite direction towards a position sensitive detector. This is illustrated in Figure 1.7. The extraction field is achieved with the three electrodes HV_2, HV_1 and the grounded electrode G_1 (see chapter 2 for a description of the electrodes). The electrons propagate in the field-free region between G_1 and the detector. Normally the detector consists of a pair of microchannel plates (MCPs) and a phosphor screen. The electrode configuration used enables one to relate the impact position on the screen with the initial momentum of the electron (i.e. both direction and magnitude) [55, 56]. There are no metallic meshes over HV_1 and G_1 which results in curved equipotential surfaces. The advantage of this is that spatial focusing is achieved. This implies that photoelectrons with the same initial momentum created at different sites along the laser propagation axis will be focused at the same point in the focal plane. The detector is typically placed 10–20 cm away from G_1 and by varying HV_2 and HV_1 one can focus the image onto the detector. In the apparatus in Edinburgh the electrons travel 160 mm.

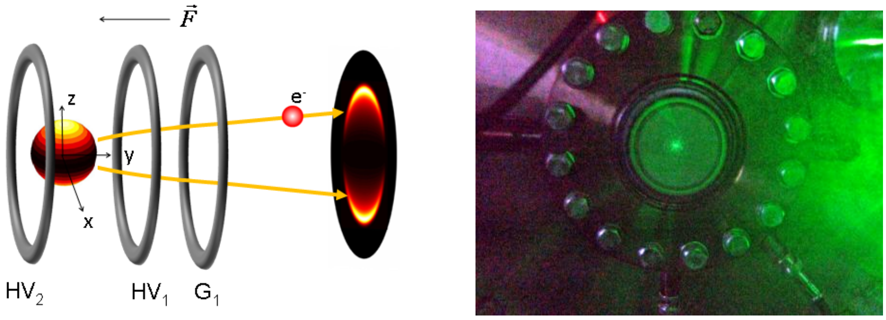

Figure 1.7: *Left)* Principle behind VMI. Photoelectrons are created at the origin and extracted towards the position sensitive detector (in the xz-plane) with a static electric field (**F**). The field is achieved with three electrodes HV_2, HV_1 and G_1. The laser propagates along the x-axis and the polarisation direction is parallel with the z-axis. The sphere between HV_2 and HV_1 illustrates a spatial distribution of emerging photoelectrons with the same kinetic energy after ionisation under field-free conditions. The distribution shows that the species favours ejection of electrons along the laser polarisation direction. The calculated projection is shown on the detector to the right in the image. *Right)* Photo of the VMI detector used in Edinburgh showing an experiment where C_{60} was ionised with the second harmonic of a Nd:YAG laser. The photo was taken during the detection of the first signal ever produced on the newly constructed apparatus.

For rotationally symmetric photoelectron distributions, the angular dependence for a specific velocity can be simplified to $F(v,\theta,\varphi) = F(v,\theta)$. This is achieved when using linearly polarised light to ionise a randomly oriented target. The reduction from three variables to two makes it possible to retrieve the original 3D distribution of photoelectrons from the measured 2D distribution on the detector. This is done with the inverse Abel transform and can be understood from Figure 1.8 where a distribution $s_z(x,y)$ is defined for a specific z value along a ring on a sphere spanned by electrons with the same velocity. The distribution gives the number of photoelectrons found in the volume element $dxdydz$. When applying static electric fields the distribution is projected onto a line on the detector (given that the energy gained from the extraction field is much greater than the initial kinetic energy of the photoelectron [57]). The line is parallel with the *x*-axis. Mathematically, the extraction of photoelectrons onto the detector means integrating over all *y*-values:

$$\int_{-\infty}^{\infty} s_z(x,y)dy = 2\int_{0}^{\infty} s_z(x,y)dy\,.$$

The last step is valid since the distribution is rotationally symmetric. One can make the substitution $r = \sqrt{x^2 + y^2}$ so that

$$dy = \tfrac{dy}{dr}\,dr = \tfrac{r}{\sqrt{r^2 - x^2}}\,dr\,.$$

The substitution of variables leads to

$$2\int_{0}^{\infty} s_z(x,y)dy = 2\int_{x}^{\infty} \frac{rs_z(r)}{\sqrt{r^2 - x^2}}dr$$

which is the Abel transform of $s_z(r)$ [58]. Therefore to recover the original 3D distribution one has to apply the inverse Abel transform to the measured image.

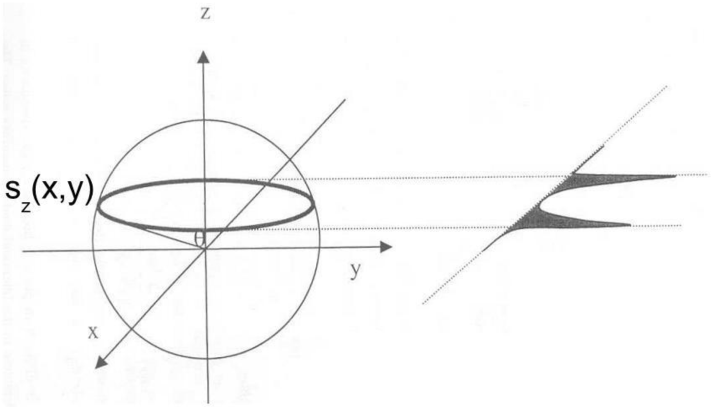

Figure 1.8: Illustration of how photoelectrons emitted with the same velocity will span the surface of a sphere. The projection of the distribution $s_z(x,y)$ onto a line on the detector is the Abel transform of the distribution. Figure adapted from ref. [59].

Once the original 3D velocity distribution is retrieved *via* the inverse Abel transform the result is usually plotted in a slice along the v_x-v_z plane for $v_y = 0$. An example of an inverted image of xenon ionised with the femtosecond laser in the Edinburgh lab is shown in Figure 1.9. The angle θ shown in the figure is the ejection angle of the photoelectron with respect to the laser polarisation direction. All the VMI images presented in this thesis have the same geometry as the given example. Each point $F(v_x,0,v_z)$ in the image is related to the number of electrons emitted in the volume $dv_x dv_y dv_z$ centred at (v_x,v_y,v_z). The actual number of emitted electrons N is proportional to

$$N \propto \iiint F(v_x, v_y, v_z) dv_x dv_y dv_z = \\ \iiint F(v,\theta,\varphi) v^2 \sin(\theta) dv d\theta d\varphi.$$

By expressing the 3D distribution in spherical coordinates and integrating over the angles the angle-independent velocity distribution is obtained according to

$$F(v)dv \propto \int_0^{2\pi}\int_0^{\pi} F(v,\theta,\varphi) v^2 \sin(\theta) d\theta d\varphi dv \propto \int_0^{\pi} F(v,\theta) v^2 \sin(\theta) d\theta dv,$$

where the last step is allowed due to the rotational symmetry of the distribution. Once the velocity distribution is obtained, a conventional photoelectron spectrum (PES) as a function of kinetic energy E can be obtained by changing variables into

$$F(v)dv = F(E)\frac{dv}{dE}dE \propto F(E)\frac{dE}{\sqrt{E}}.$$

A PES obtained from the inverted VMI image in Figure 1.9 is shown in Figure 1.10.

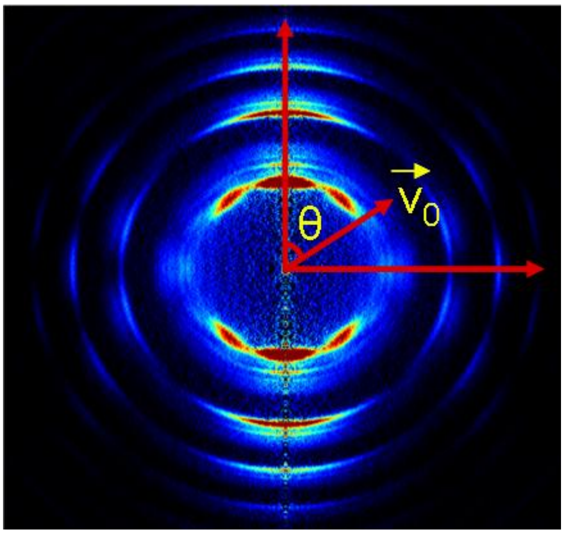

Figure 1.9: Slice through the v_x-v_z plane for $v_y = 0$ of the momentum distribution of emitted photoelectrons from xenon ionised with a femtosecond laser (800 nm, 130 fs). The radial distance from the origin is proportional to the initial velocity of the electron. If the angle θ is 0 or 180 degrees the electron was ejected along the laser polarisation direction.

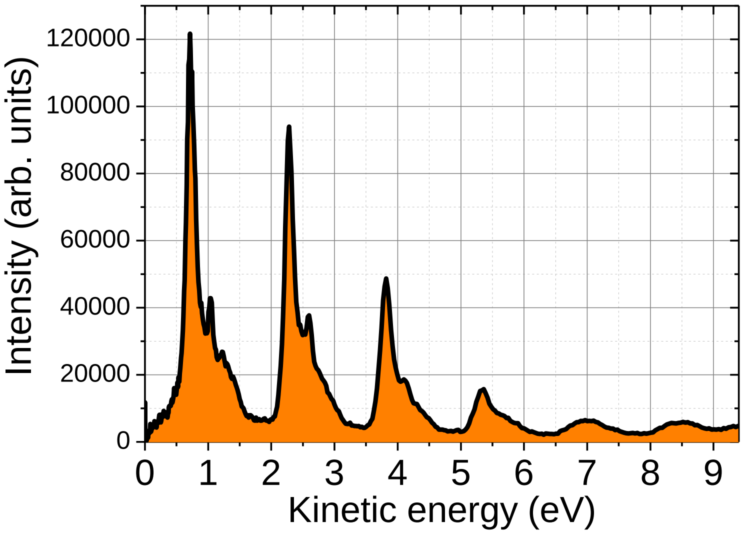

Figure 1.10: Integrating over all the angles in an inverted VMI image produces a velocity distribution which can be converted into a PES. The spectrum presented in this figure was obtained from the inverted image in Figure 1.9. Obtained after 130 fs, 800 nm laser excitation.

Chapter 2 – Experimental Setup

2.1 Introduction and overview of the experimental apparatus

A major part of the research work has involved planning, designing and building the experimental apparatus. This chapter describes how the equipment is constructed and how it functions. In the chapter, test results and characterisations of the various components are presented. The interaction of the molecules with the laser light takes place in a vacuum chamber (called the interaction chamber). The molecular beam source consists of an effusive oven which is resistively heated and is placed in a separate vacuum chamber (called the oven chamber). The oven chamber is situated so that the effusive molecular beam propagates vertically into the interaction chamber (as seen in Figure 2.1). A 4 mm orifice separates the interaction and oven chambers. The laser intersects the molecular beam perpendicularly and neutral molecules are ionised resulting in the production of ions and photoelectrons. Electrodes are used to extract the photoproducts towards the ion and electron detectors (also seen in Figure 2.1).

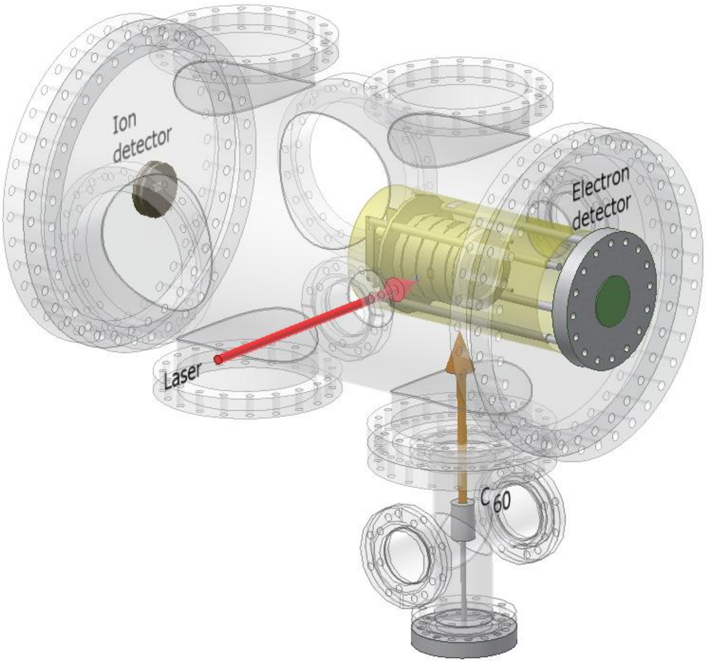

Figure 2.1: Sketch showing the experimental setup. Molecules are produced in the effusive oven situated in the lower vacuum chamber. Sublimed molecules rise into the interaction chamber where they are intersected by the laser. The molecules are ionised by the laser and ions are extracted with the electrodes towards the ion detector and the electrons towards the position-sensitive detector (this is done separately because the present configuration does not allow for simultaneous detection of electrons and ions).

2.2 Vacuum system

The interaction chamber was custom built by CVT Ltd. and is of cylindrical shape (as seen in Figure 2.1) and made from stainless steel. The chamber has two DN300CF flanges on which the ion and electron detectors are mounted. The overall length of the chamber is 615 mm and given that the inner diameter is 300 mm the volume can be estimated as $(length)\times(area) = 615\times\pi\times\frac{300^2}{4}mm^3 \approx 45$ l. A drawing of the chamber is presented in the appendix. The interaction chamber is pumped by a 300 l/s turbomolecular pump (Edwards, STP-301C, DN100CF inlet flange) which is backed by an oil-free scroll pump (Edwards, part no. XDS10). The oven chamber is pumped by a 60 l/s turbo pump (Edwards, EXT 75DX, DN63CF inlet flange) and is backed by the same type of backing pump as the interaction chamber. The system can be vented to atmospheric pressure by introducing N_2 gas into the chambers. This is done automatically by the 60 l/s turbo pump controller which is connected to an electrically controlled valve. There is also a possibility to vent the interaction chamber directly through an on/off valve (Swagelok, part no. SS-1GS6MM). Active Inverted Magnetron vacuum gauges are installed on both chambers (Edwards, AIM-S-DN40CF) and the lowest pressure that can be measured with these gauges is 10^{-8} mbar. The pressure measured in both the interaction and oven chambers reaches the 10^{-8} mbar lower limit even when the effusive oven is turned on. Pirani gauges (Edwards, APG100-XM) are used to measure the pressure between the turbo pumps and backing pumps and typically a pressure of about 10^{-2} mbar is measured.

It is possible to introduce gas through a needle valve (Swagelok part no. SS-SS6MM-VH). Xenon gas, used for calibration purposes, is contained in a pressure can (Air Liquide UK Ltd., part no. 7950 3065, 99.99 % purity) that is connected to the vacuum chamber through Swagelok stainless steel tubing with an outer diameter of 6 mm. Typically a pressure of about 10^{-7}–10^{-6} mbar is in the interaction chamber during a xenon experiment.

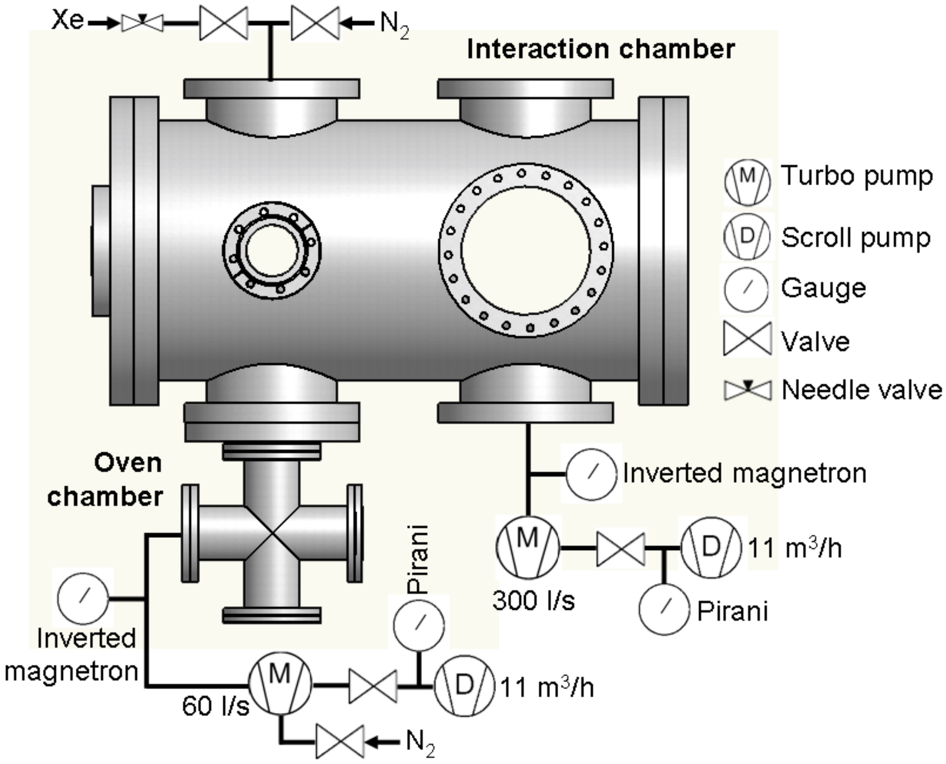

Figure 2.2: Schematic drawing showing the vacuum system configuration.

2.3 Fullerene effusive beam source

This section describes the formation and characterisation of the fullerene effusive beam source. At room temperature fullerenes are in the solid state and the vapour pressure is very low. It is possible to heat a sample of fullerenes to sublime the molecules into the gas phase. Typical temperatures needed to get a sufficient signal for photoionisation experiments are 450 – 500 ºC (corresponding to a partial pressure of 10^{-4} – 10^{-2} mbar [60]). Therefore an effusive oven has been constructed and the sample used is a commercial powder of C_{60} with 99.95 % purity, bought from SES Research. Experiments have also been carried out with C_{70} purified in-house using HPLC by Andrei Gromov. The oven is mounted on a DN63CF vacuum flange which in turn is mounted on a DN63CF cross piece vacuum chamber (called the oven chamber, bought from Kurt Lesker, part no. C-0450). The flange of the interaction chamber is a DN160CF so a zero-length reducing flange from DN160 to DN63 is used. A solid copper gasket with a 4 mm hole in the centre is used between the two chambers to define the molecular beam. The oven chamber is mounted on to the bottom flange of the interaction chamber as seen in Figure 2.1. The oven consists of a relatively large piece of metal (compared to the fullerene sample) so that the large mass provides an even source of heat for the sample to be heated. Furthermore, it is important to choose a metal that conducts heat efficiently to the sample, which is placed inside the oven. Since a Molybdenum rod of 25 mm diameter was already in the lab this was chosen to be the container. The rod was cut to a length of 50 mm. However, from experience [61], it has been found that it is not good to have the hot fullerene powder in direct contact with the metallic surface. Therefore a quartz ampoule of length 25 mm with inner and outer diameter 2 mm and 4 mm respectively is placed inside the metallic cylinder. This also has the advantage that it is easier to change sample if a different type of molecule is to be studied. A hole of 4.2 mm diameter and 25 mm deep was drilled along the central axis of the rod to encompass the ampoule. A hole of 2 mm diameter was drilled through out the rod so that it would be possible to push the ampoule out of the cylinder from the other end, in case the ampoule would get stuck. A thermocouple (TC) was used to measure the temperature of the oven. It is important to place the TC as close as possible to the sample. Therefore another hole was drilled in the rod so that the TC could be placed inside the cylinder. The TC was an unsheathed K-type (Omega Engineering, part no. CHAL-015) and was insulated using ceramics beads. To ensure that the TC was in mechanical contact with the metallic rod, a threaded hole was made perpendicular to the TC hole. This enabled an M3 screw to be inserted into the rod ensuring that the TC had good contact with the metallic surface. A TC was also initially welded onto the nozzle to be able to gauge the temperature. The welding was very brittle and during a sample change, the wires broke. It is important to know the nozzle temperature because if it is significantly lower than that of the oven, condensation can occur and passage through the nozzle may be constricted. The first measurements before the TC connection broke, showed that the temperature of the nozzle was about 15 ºC lower than the temperature in the Mo cylinder. The only slightly lower temperature in combination with the wide nozzle diameter, prevented any possible obstruction in the nozzle. A sketch of the molecular beam source is presented in Figure 2.3.

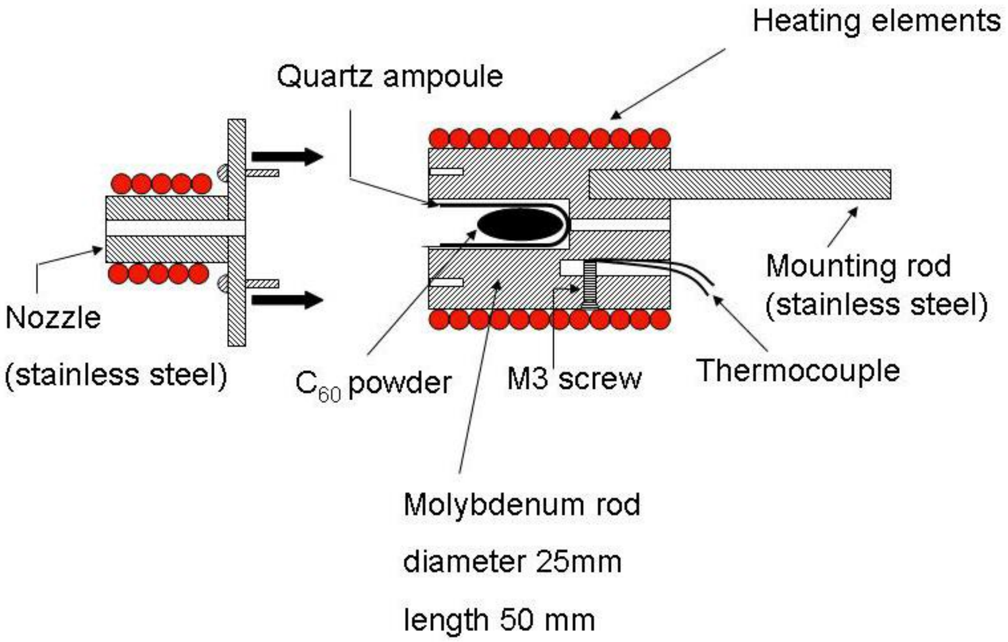

Figure 2.3: Sketch showing a cross section of the main part of the effusive oven. The C_{60} or C_{70} powder is placed in a quartz ampoule which in turn is placed inside a Molybdenum cylinder. A thermocouple is inserted into the metal cylinder to measure the temperature in the vicinity of the sample and an M3 screw secures the tip of the thermocouple to the surface of metal cylinder. A heating wire is coiled around the cylinder and the nozzle. The nozzle is fixed onto the cylinder with two M3 screws.

A nozzle made of stainless steel and with a relatively large orifice of 3 mm and 25 mm length is attached to the oven. The outer diameter of the nozzle is 12 mm. The base of the nozzle is 32 mm wide, which is larger than the outer diameter of the Molybdenum cylinder. On the base plate there are two holes wide enough to fit M3 screws. Matching threaded holes in the Molybdenum cylinder allows the nozzle to be fixed with screws onto the cylinder.

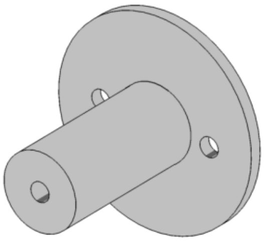

Figure 2.4: Drawing of the nozzle used to collimate the molecular beam.

The oven is heated with a heating wire (Thermocoax, part no. IHc20252). The conducting wire is made from NiCr (80/20) and is surrounded with MgO insulating material which in turn is covered with a stainless steel sheath. The outer diameter is 2 mm and the total length is 252 cm. The advantage with this type of heater is that it is not necessary to insulate the heating wire with ceramic beads. Furthermore, the bending radius of the heating wire is three times larger than the outer diameter of the wire. The length and the small bending radius allowed for the wire to be coiled around the nozzle as well as the Mo cylinder. The slightly larger diameter of the nozzle base plate (see Figure 2.4) allows the heating wire to be fixed in position around the Molybdenum cylinder while a washer at the opposite end of the cylinder serves a similar purpose. Some characteristics of the heating wire are presented in Table 2 and it is important not to exceed these values as this might damage the heating wire. To minimise heat loss from black-body radiation, aluminium foil is wrapped around the oven which should reflect part of the emitted infrared radiation back to the oven. When using a power of 1.35 A × 25.2 V = 34 W it has been found that a temperature of 500 °C was reached. It is not recommended to exceed this value because the melting point of aluminium is close to 600 °C and if the oven is heated to this temperature the aluminium foil surrounding the oven might then melt. Experiments have also been performed with the Al foil removed. For an oven heater power of 1.70 A × 31.7 V = 54 W a temperature of 420 °C was reached.

Table 2: Characteristics of the heating wire used to heat the sample in the effusive oven (Thermocoax, part no. IHc20252).

Maximum voltage	Maximum power	Maximum current	Resistance
41 V	100 W	2.43 A	16.98 Ohm

2.3.1 Characterisation of the molecular beam

The molecular beam profile from the hot source has been characterised at the place in the chamber where the laser intersects the molecular beam. In order to characterise the molecular beam, a thin film of fullerenes from the source was deposited on a microscope glass slide. The oven was heated to about 480° C and the film was deposited during 8 hours. A special holder was made in the mechanical workshop to accommodate the glass slide. The holder was installed where the extraction electrodes normally are mounted (see Figure 2.5). A drawing of the holder is presented in the appendix and a picture showing the holder installed on the mounting flange is shown in Figure 2.6.

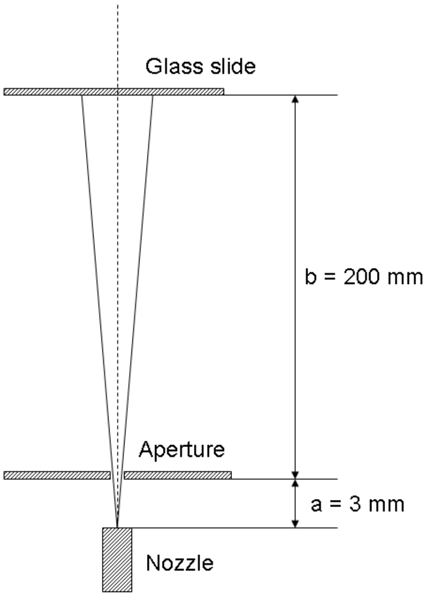

Figure 2.5: Sketch showing the hot source geometry during the measurement of the molecular beam profile. During normal operation of the apparatus the laser intersects the molecular beam at the position of the glass slide.

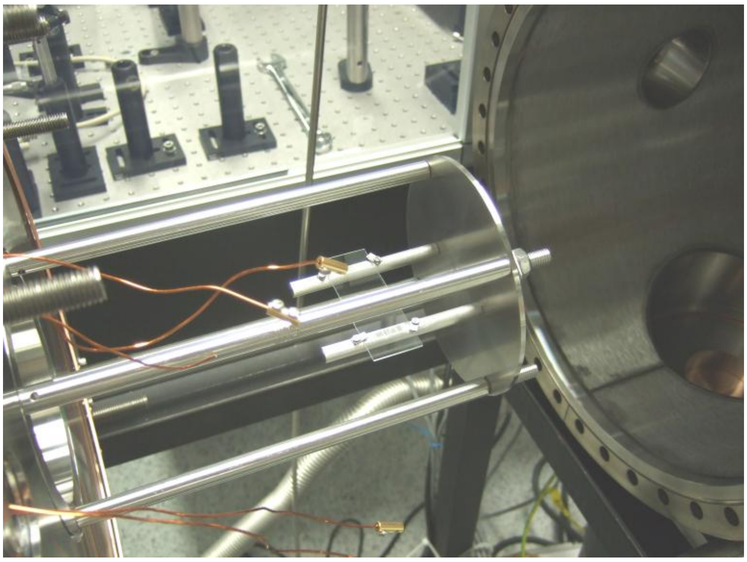

Figure 2.6: Picture showing the sample holder mounted on the four rods normally holding the ion optics. On the right hand side of the image, the solid gasket acting as an aperture is seen.

The fullerene film deposited on the glass slide was investigated with a Raman microscope (*InVia, Renishaw*). An optical microscope in the machine enabled the user to position the Raman laser beam (diameter 2 μm) on the desired spot on the sample. Spectra were taken at 1 mm intervals along two perpendicular lines on the deposited fullerene film (see Figure 2.7). A typical sample spectrum is shown in Figure 2.8. The peak corresponding to the pentagonal pinch mode of C_{60} $A_g(2)$ was fitted to a Gaussian function after background subtraction in the commercial software *Wire 2.0*. The fitted peak areas as a function of relative distance on the glass slide were found for the two perpendicular scan lines and the result is plotted in Figure 2.9. By assuming that the Raman signal is proportional to the film density, the full width at half maximum (FWHM) of the molecular beam is found to be 11–12 mm.

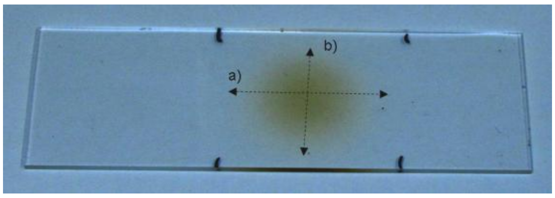

Figure 2.7: Photo of glass slide with deposited C_{60} film. Raman spectra were taken at 1 mm intervals along the lines a) and b).

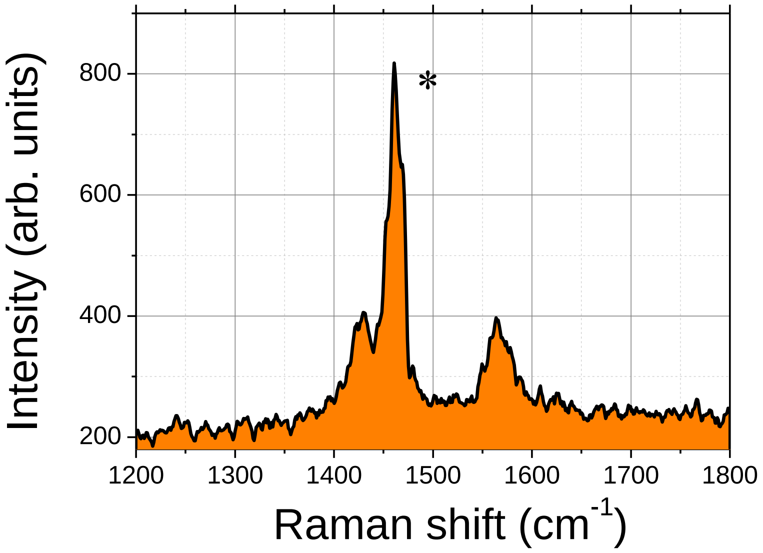

Figure 2.8: Typical Raman spectrum taken with laser wavelength of 514 nm. All spectra were accumulated for about 3 minutes. The asterisk shows the peak corresponding to excitation of the pentagonal pinch mode $A_g(2)$. This peak was fitted to a Gaussian function in commercial software *Wire 2.0* which also supplied the peak area. The spectra were smoothed in the software and the background around the peak of interest was subtracted.

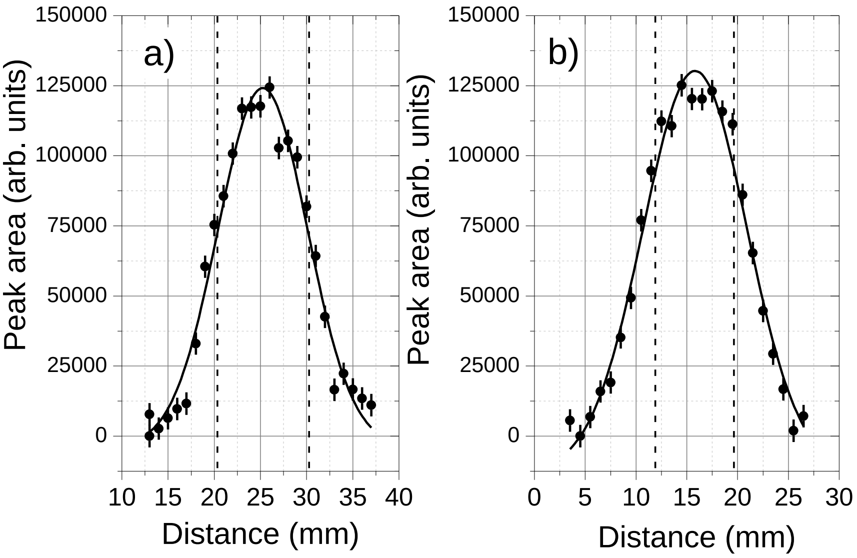

Figure 2.9: Integrated peak areas of the pentagonal pinch vibrational mode of C_{60} as a function of distance on the glass slide for the two lines a) and b) seen in Figure 2.7. The error in peak area was estimated during the fitting procedure and was taken as half the value of the smallest peak area found. The origin on the abscissa is arbitrary but the relative scale is absolute. A Gaussian function was fitted in *Origin* to the data in a) and b) and the FWHMs extracted from the fits were 11 ± 1 mm and 12 ± 1 mm respectively (standard error from the fit in *Origin*). The vertical dashed lines indicate the widths of the entrances holes of the ion optics.

2.4 Lasers

In this section the lasers used to ionise the gas phase molecules are described. A brief description of the components of a typical femtosecond laser is given below together with a presentation of the characteristics of the laser system in the lab. First a definition of the laser pulse intensity and fluence is given. The laser beam propagates along the z-axis and the radial distance r from the propagation axis is $r = \sqrt{x^2 + y^2}$. The intensity distribution $I(x,y,t)$ of the laser beam as a function of distance from the propagation axis and time is

$$I(x,y,t)dxdydt = I_0 \exp\left(-\frac{2(x^2+y^2)}{w_0^2}\right)\exp\left(-\frac{4\ln(2)t^2}{\Delta t^2}\right)dxdydt =$$
$$= I_0 \exp\left(-\frac{2r^2}{w_0^2}\right)\exp\left(-\frac{4\ln(2)t^2}{\Delta t^2}\right)2\pi r dr dt$$

where I_0 is the peak intensity typically given in units of W/cm^2, w_0 is the beam waist (the radius when the intensity has dropped to 1/e^2 of the peak intensity) and Δt is the FWHM of the laser pulse duration. In the laboratory the total pulse energy E_p is measured but it is more relevant to discuss results in terms of peak intensity I_0. The pulse energy is obtained by integrating over the spatial coordinates and time as is shown below

$$E_p = \int_{-\infty}^{\infty}\left(\int_{-\infty}^{\infty} I(x,y,t)\,dxdy\right)dt = I_0\int_0^{\infty}\exp\left(-\frac{2r^2}{w_0^2}\right)2\pi r dr\int_{-\infty}^{\infty}\exp\left(-\frac{4\ln(2)t^2}{\Delta t^2}\right)dt =$$
$$= \sqrt{\frac{\pi^3}{16\ln(2)}}\times I_0\times\Delta t\times w_0^2.$$

Solving for I_0 gives

$$I_0 = \sqrt{\frac{16\ln(2)}{\pi}}\times\frac{E_p}{\Delta t\times\pi w_0^2}.$$

The beam waist w_0 and the pulse duration can both be measured in the lab and therefore the peak intensity can be found. It is also useful to find the spatial dependent fluence $F(r)$ which is the time-integrated intensity and is typically given in units of J/cm^2. Usually the value of $F(r)$ at $r = 0$ is given and is simply called the fluence. By integrating out the time dependence of the intensity one obtains

$$F = \sqrt{\frac{\pi}{4\ln(2)}}\Delta t\times I_0 = 0.94\times\Delta t\times I_0.$$

2.4.1 Femtosecond Ti:Sapph oscillator

To localise an electromagnetic wave in time, a broad frequency spectrum is needed. This follows directly from the uncertainty principle stating that for a Gaussian pulse the product of the uncertainty in time Δt with the uncertainty in frequency $\Delta\upsilon$ equals $\Delta t \times \Delta\upsilon = 0.441$ [62]. In order to achieve a short laser pulse the laser medium has to have a broad bandwidth. It has been found that sapphire doped with titanium (commonly referred to as a Ti:Sapph crystal) has the required bandwidth to form femtosecond laser pulses. These Ti:Sapph lasers are available commercially and have been used in this work. By using a Ti:Sapph crystal as the lasing medium one can generate the needed broad frequency spectrum. However, the relative phase of the different waves is completely random. Since there are so many modes present, all these cancel out due to destructive interference. In order to generate a short laser pulse it is necessary to make the waves oscillate in phase with each other which is usually referred to as mode-locking. There are two approaches and one is called active mode-locking which involves forcing the modes to oscillate together in phase by external means. The other method is passive mode-locking and is based on constructing the oscillator in such a way that any accidental mode-locking experiences positive feedback resulting in the build-up of mode-locked laser pulses. The oscillator used in this work is a Coherent Mantis producing sub-35 fs laser pulses at a repetition rate of 80 MHz. The central wavelength is around 800 nm with a bandwidth of 80 nm (spectrum is shown in Figure 2.10). The laser is pumped by a quantum well laser (OPS, Coherent) which is focussed on to a Ti:Sapph crystal. The Mantis can be operated in either CW or mode-locked mode. The pump beam profile in the crystal is such that the CW laser light experiences a poor overlap with the pump beam due to the larger diameter of the CW beam. In contrast, the high power produced in accidental mode-locking results in self-focussing of the laser beam due to the optical Kerr effect [62]. This greatly enhances the overlap with the pump beam and mode-locked lasing experiences a positive feedback in the oscillator and is therefore greatly amplified. The pulses will be stretched in time due to dispersion when propagating in air causing a positive chirp on the pulse (red wavelengths travel faster than bluer ones in a medium with a refractive index larger than one). This is compensated for in the oscillator by using a series of mirrors with a special coating which introduces a negative chirp which will exactly compensate the positive chirp at the output of the laser. The mode-locked power at the output of the Mantis is typically 500 mW but is too weak to pump any of the non-collinear optical parametric amplifiers that are used in the lab. For that reason the laser light emerging from the oscillator is passed into a regenerative amplifier.

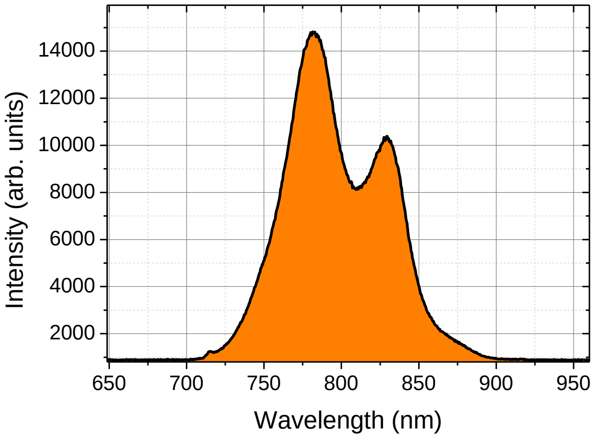

Figure 2.10: Spectrum after the Mantis output taken with an Ocean Optics HR2000 spectrometer with grating HC1 and a 25 µm slit. Central wavelength is 800 nm and FWHM is about 80 nm.

2.4.2 Femtosecond Ti:Sapph regenerative amplifier

The pulses emerging from the Mantis are amplified in a so called regenerative amplifier [62]. This type of amplifier uses a second Ti:Sapph crystal that is pumped by another laser. The amplifier used in this work is a Legend Elite from Coherent. In order to amplify the pulses it is first necessary to reduce the intensity of the pulse because the short pulse duration can lead to very high peak intensities even for moderate pulse energies. After the amplification stage the pulses are recompressed again. The technique of stretching, amplifying and finally recompressing the pulse again is called chirped pulse amplification (CPA). The pulses are stretched by reflecting them twice off a grating. The optical path is made so that longer wavelengths will travel a shorter distance than short wavelengths which creates a positive chirp, stretching the pulses in time. Typically the pulses are stretched to several hundred picoseconds [62]. A frequency doubled Nd:YLF ns laser (Evolution, Coherent) pumps the crystal which is enclosed in a temperature controlled environment maintained at –10° C. The polarisation of the incoming laser pulse is such that it cannot enter the amplifier after the stretcher. However, the polarisation can be changed by a Pockels cell and the timing with respect to the pump laser is controlled by a delay generator (SDG, Coherent). The pulse is then trapped in the amplifier and typically makes about 20–30 roundtrips in the cavity (this is why the technique is called regenerative amplification). Once the pulse has experienced maximum amplification it is let out of the cavity by using a second Pockels cell which is controlled by the same delay generator as the first Pockels cell. The user adjusts the delay of the Pockels cells with respect to the arrival time of the pump laser to the crystal by optimising the power whilst looking at the signal from a photodiode on an oscilloscope to ensure that production of post- and pre-pulses is kept at a minimum. After the amplification stage the pulses are recompressed by reflecting them off a grating but this time a negative dispersion is created so that the shortest pulse duration is achieved at the laser output. Two mirrors situated on a motorised translation stage are used to optimise the distance travelled by the pulse in the compressor. By monitoring the pulse duration the chirp can be reduced to a minimum by adjusting the translation stage. However, by deliberately detuning the compressor a longer pulse duration can be obtained. The longest possible travel distance of the translation stage limits the maximum length of the stretched pulse to 3.8 ps.

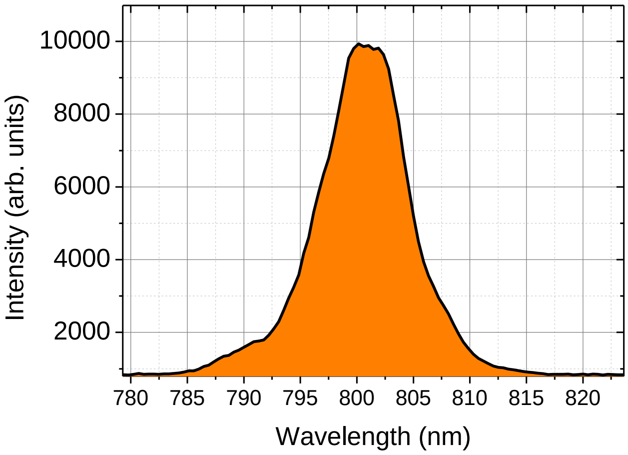

Figure 2.11: Spectrum after Legend output (120 fs pulse duration) taken with an Ocean Optics HR2000 spectrometer with grating HC1 and a 25 μm slit. Central wavelength is 800 nm (1.55 eV) and FWHM is 9 nm (17 meV).

2.4.3 Second harmonic generation

The fundamental output from the Legend can be passed through a BBO crystal (β-barium borate) to produce the second harmonic (400 nm). The crystal is aligned in such a way that the input polarisation should be vertical for maximum yield. The resulting output power is usually too high for a typical fullerene experiment and therefore the input polarisation is rotated by a λ/2 plate to reduce the power. The 400 nm output is reflected off a highly reflecting mirror which transmits the majority of the residual 800 nm light producing a laser pulse with a spectrum shown in Figure 2.12.

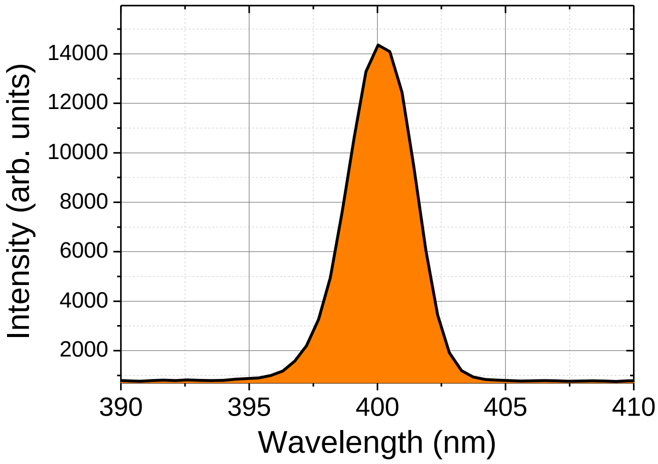

Figure 2.12: Spectrum of the second harmonic produced from the Legend fundamental output. Spectrum obtained using an Ocean Optics HR2000 spectrometer with grating HC1 and a 25 µm slit. Central wavelength is 400 nm (3.10 eV) and FWHM is 3 nm (23 meV).

The second harmonic can also be created in a second harmonic bandwidth compressor (SHBC, Light Conversion) which produces bandwidth limited ps pulses. The output from the Legend is directed into the SHBC and is split up into two parts. The two resulting beams are stretched in time with a negative chirp ($-\Delta\nu$) on one of them and a positive chirp ($+\Delta\nu$) on the other. When the two beams are recombined in a BBO crystal to produce the second harmonic the chirp will cancel for the second harmonic according to $\nu_{400nm} = (\nu_{800\mathrm{nm}} - \Delta\nu) + (\nu_{800nm} + \Delta\nu) = 2\nu_{800nm}$. The bandwidth of the second harmonic is 5 cm^{-1} and the pulse duration is about 4–5 ps. A typical spectrum is presented in Figure 2.13.

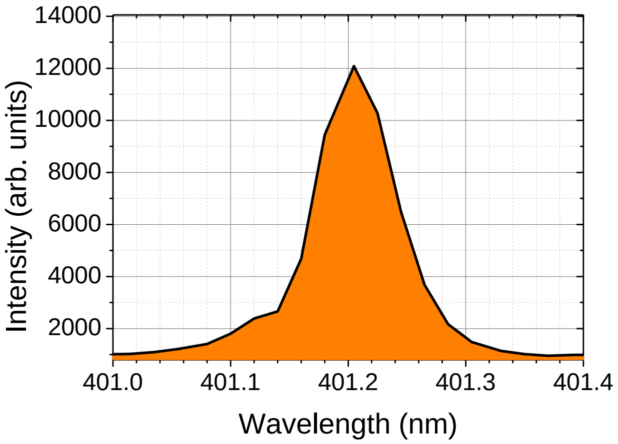

Figure 2.13: Spectrum from the SHBC (4–5 ps pulse duration). Central wavelength is 401.21 nm (3.090 eV) and the FWHM is 5 cm^{-1} (0.6 meV). Spectrum obtained using an Ocean Optics HR2000 spectrometer with grating H11 and a 5 μm slit.

2.4.4 Measuring the laser pulse duration

It is not possible to measure the pulse duration of a femtosecond laser pulse using electronic devices since a typical measurable timescale using electronics is just below a nanosecond. Therefore it is necessary to use optical methods. One way is to divide the pulse in two parts and then recombine them to form the second harmonic [62]. Since the production of the second harmonic is sensitive to the intensity of the fundamental beam, the second harmonic yield will be greatest when the two pulses overlap in time. By introducing a delay for one of the beams and recording the second harmonic signal as a function of delay it is possible to obtain a second order autocorrelation. If the input pulse has a Gaussian temporal profile the measured FWHM can be deconvoluted yielding a 1.414 times shorter FWHM of the input pulse. Typical second order autocorrelations measured using a commercial autocorrelator (APE Pulsecheck) for the Legend for different pulse durations are shown in Figure 2.14. Before the beam was directed into the autocorrelator it was passed through a set of neutral density filters, a λ/2 plate, a Glan-Laser polarizer and a vacuum viewport identical to the one mounted on the interaction chamber.

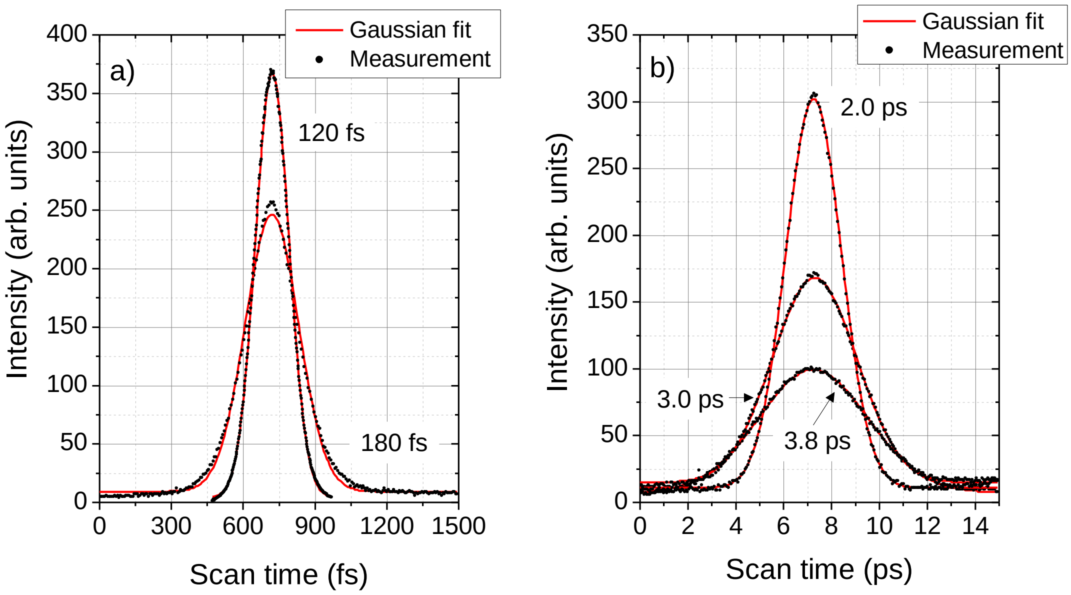

Figure 2.14: Second order intensity autocorrelation measured for the Legend fundamental output (800 nm) for different pulse durations. The pulse duration is changed by detuning the compressor. a) The shortest possible pulse duration obtainable from the Legend and a slightly stretched pulse are shown. Fitted deconvoluted FWHMs assuming a Gaussian temporal profile yield 120 and 182 fs. b) Pulses stretched above a picosecond where deconvoluted FWHMs are given in the figure.

2.4.5 Measuring the laser beam waist

In order to compare experimental data taken in different laboratories it is important to compare the laser intensity in the focus which is typically given in units of W/cm^2. The area compared is usually the area inside the beam waist which is the radial distance from the propagation axis which corresponds to a 1/e^2 drop of the peak intensity [63]. Since the beam waist is usually on the order of tens of microns it can be quite difficult to measure explicitly. There are various ways of measuring the beam waist and in this section two methods are given for the fundamental output of the 800 nm femtosecond laser. The first method relies on measuring the unfocussed beam waist and then calculating the focussed beam waist assuming a Gaussian spatial profile. An aperture with an opening of about 1 mm was placed on a translation stage (see insert in Figure 2.15) that was scanned in the horizontal direction. After the aperture, a power meter was placed that recorded the power as a function of horizontal distance travelled by the aperture. A Gaussian fit to the measurement gave a beam waist of 2.85 ± 0.04 mm where the error is the standard error. The beam waist in the focus was then calculated assuming a Gaussian beam profile which is justified by the small fit error in Figure 2.15. The focal beam waist w_0 was found to be

$$w_0 = \frac{2\lambda}{\pi}\left(\frac{F}{D}\right) = 26.8 \pm 0.4\mu m$$

where λ is the wavelength, F is the focal length of the lens and $D/2$ is the unfocussed beam waist [63]. The error is the same fractional error as for the unfocussed beam waist. The 1/e^2 area A is (using standard error propagation)

$$A = \pi w_0^2 = (2.26 \pm 0.06) \times 10^{-5} cm^2 .$$

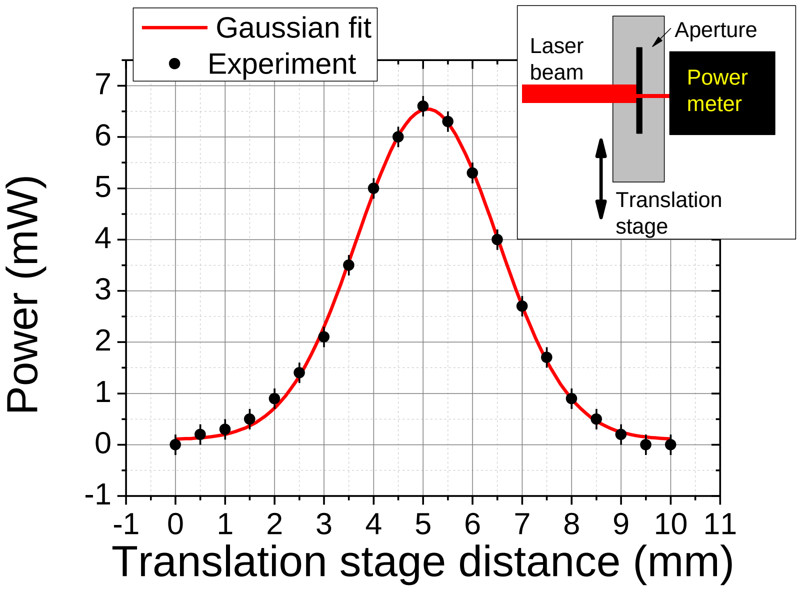

Figure 2.15: Average power measured after the Legend output was passed through an aperture with a 1 mm opening that was scanned in the horizontal direction. The beam had first passed through the optical components typically used in the experiments (λ/2 plate and a Glan-Laser polarizer). Error bars show the uncertainty in the power meter readout which was constant at ± 0.2 mW.

The focussed beam waist can also be measured by laser ablation. The method used is presented in ref. [64]. Ablation of dielectric materials often occurs above a certain threshold energy E_a. The energy as a function of radial distance r from the beam axis is given by $E(r) = E_0 \exp(2r^2 / w_0^2)$. The radial distance r_a for which damage occurs is related to the threshold energy by

$$E(r_a) = E_0 \exp(2r_a^2 / w_0^2) = E_a \,.$$

Rearranging the above equation gives the damaged radius squared as a function of the natural logarithm of the pulse energy E_0

$$r_a^2 = \frac{w_0^2}{2}\left(\ln(E_0) - \ln(E_a)\right).$$

By measuring the damaged diameter $d_a = r_a / 2$ for different pulse energies the focussed beam waist can be obtained from the slope $2w_0^2$ when d_a^2 is plotted versus $\ln(E_0)$ according to

$$d_a^2 = 2w_0^2\left(\ln(E_0) - \ln(E_a)\right).$$

This was done for several laser powers and different distances between the lens and the target (although the absolute distance is arbitrary). The laser was focussed using an f = 30 cm lens onto a 4 mm thick Perspex plate for about 2 seconds. The Perspex plate was mounted onto a translation stage. The damaged beam diameter was analysed using the built-in optical microscope in a Raman microscope (*InVia, Renishaw*) which allows for distances to be measured on the micrometer scale. An example taken with a pulse energy of 20 μJ is shown in Figure 2.16. The spots were slightly elliptical and as shown in the figure both the vertical and horizontal diameters were measured. All the spots on the Perspex plate were analysed and d_a^2 was plotted against the natural logarithm of the laser energy. An example is given in Figure 2.17 a) of a linear fit made in *Origin* to a series measured for different laser powers. The diameter presented in the figure is the mean of the two diameters measured for each spot. The error is half the difference between the two diameters (from standard error propagation of a power function). The trend in Figure 2.17 b) indicates that the focus was at a relative distance on the translation stage equal to 6 mm. For this relative distance the damaged spots were the most circular which further indicates that the focus was at this distance. Therefore the slope of the damaged area squared plotted versus the natural logarithm of the laser power was taken to be the focussed beam waist. From the fit the beam waist was w_0 = 33 ± 2 μm where the error is propagated from the standard error given in *Origin*. The corresponding 1/e^2 area is then

$$A = \pi w_0^2 = (3.4 \pm 0.4) \times 10^{-5}\, cm^2$$

which is slightly larger than the area found from the measurements of the unfocussed laser beam diameter but is almost within experimental error.

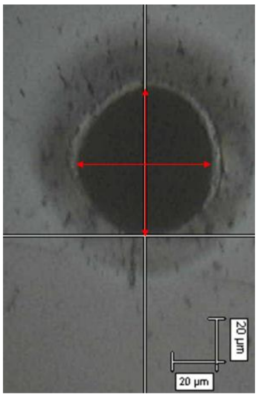

Figure 2.16: Image of a damaged area on a Perspex plate made by focussing a 20 μJ pulse using *f* = 30 cm lens onto the plate. The measured diameters were 63 and 68 μm. The relative distance on the translation stage (which controlled the distance between the lens and the target) was 6 mm.

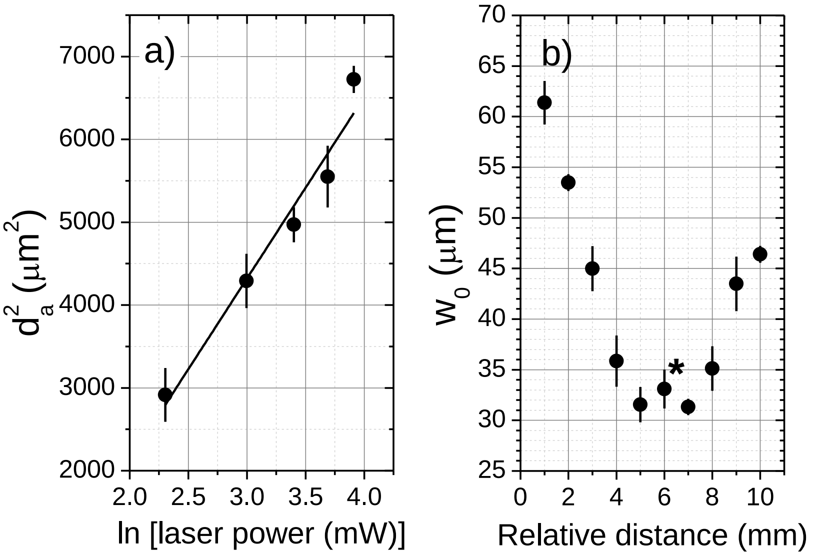

Figure 2.17: a) Mean of the measured damaged radius for different laser powers for a relative distance of 6 mm on the translation stage. Errors were estimated as half the difference between the minimum and maximum measured damage diameter (see Figure 2.16). This analysis was made for different relative distances on the translation stage. From a linear fit the focussed beam waist can be estimated. The diameter squared measured with natural logarithm of the laser power equal to 3 is taken from the image shown in Figure 2.16. b) Extracted focussed beam waists as a function of relative distance on the translation stage. The datum point marked with an asterisk is obtained from the slope of the linear fit made in a). Uncertainties from least square fits.

2.4.6 Optical setup

The optical setup for the various experiments presented in the results section is shown below in Figure 2.18. For the experiments using 800 nm the laser power is adjusted using a λ/2 plate (AHWP05M-980, Thorlabs) in combination with an uncoated Glan-Laser calcite polarizer (GL15, Thorlabs). The polarizer is adjusted to transmit vertically polarised light. These optical components are sensitive to high laser powers and therefore the power is reduced by a beamsplitter and a series of neutral density filters (ND filters). The laser beam is focussed outside the vacuum chamber using either an f = 50 or 30 cm lens. In all the figures presented in the experimental chapter the f = 30 cm lens is used unless otherwise stated. In experimental setups presented in Figure 2.18 a-c) the beam height is adjusted to match the height of the vacuum chamber by using a periscope. For b-c) this also serves to rotate the laser polarisation so that it is vertical (which is essential for VMI). The average laser power was measured using a thermopile sensor connected to a Coherent FieldMaxII-TO which is connected to a computer and controlled via software delivered with the power meter. Typically 1 measurement of the laser power is taken every 2 or 4 seconds during a measurement. An average is then recorded every 30 minutes together with the standard deviation.

A ns Nd:YAG laser has also been used for a number of experiments (Minilite II, Continuum). The laser outputs the second harmonic (532 nm) and has a pulse duration of about 3–5 ns. A variable repetition rate between 10 – 15 Hz is possible. The maximum pulse energy is 25 mJ. The optical setup using this laser is presented in Figure 2.18 d). The laser was mounted on a laboratory jack to match the beam height with the vacuum chamber.

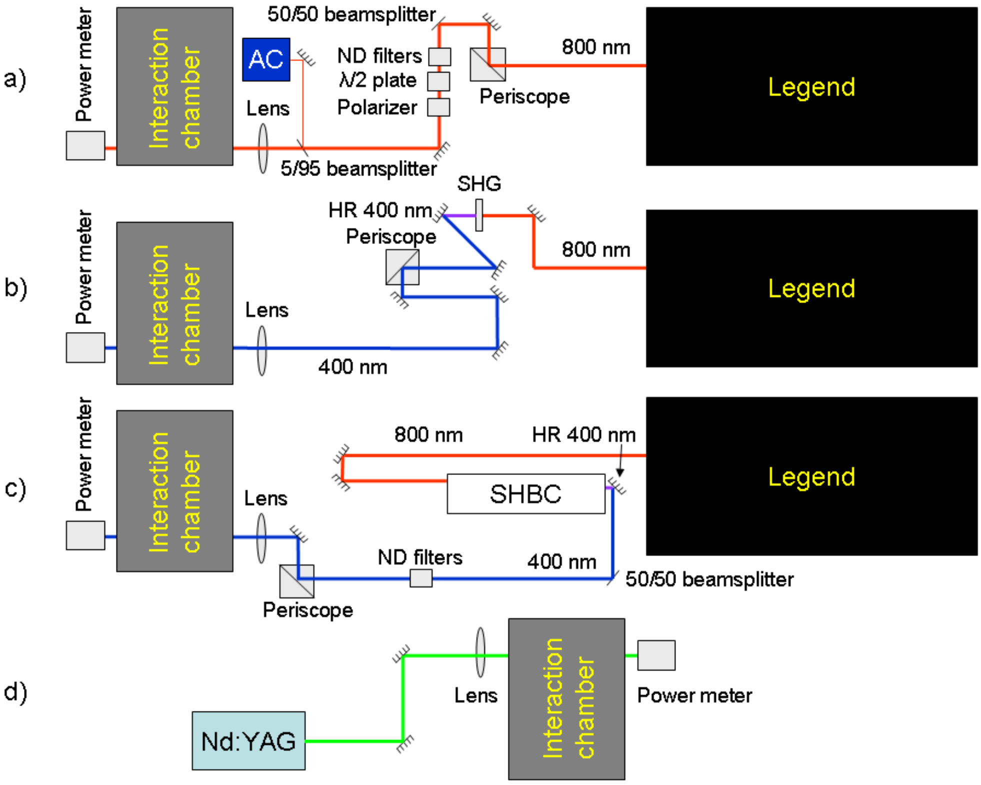

Figure 2.18: Optical setup for experiments with different lasers and wavelengths. a) The fundamental output from the Legend. The pulse energy is first reduced by a beamsplitter and a set of ND filters. The energy is then more finely controlled by a λ/2 plate in combination with a polarizer. A periscope is used to align the beam to the same height as the vacuum chamber. A 5/95 percent beamsplitter is placed in a flippable mount just before the lens that is used to focus the beam into the chamber. The beam reflected off the beamsplitter is directed into an autocorrelator (AC) which allows for pulse duration measurements with an almost identical beampath to the beampath leading into the chamber. An identical vacuum viewport to the one mounted on the vacuum chamber is placed before the AC (although not shown in the figure). b) The beam path after second harmonic generation (SHG) of the Legend output. A highly reflective mirror for 400 nm (HR 400 nm) is used to filter out the residual 800 nm after the SHG. c) Beam path of the laser after the SHBC output producing bandwidth limited ps pulses (4–5 ps, 5 cm^{-1}). A beamsplitter and a set of ND filters are used to reduce the intensity. d) Optical setup for the use of a ns Nd:YAG laser. The second harmonic (532 nm) is produced inside the laser. The laser power is controlled by a throttle on the laser case.

2.5 Ion optics

After the sample is ionised, photoproducts are subsequently detected. In order to extract the products to the detectors a set of ion optics is used. The ion optics were made in the School of Chemistry's mechanical workshop and the drawings of the electrodes were based on the ones used for the experimental setup presented in ref. [28] and can be found in the appendix. The assembly consists of five cylindrical electrodes made from stainless steel mounted in a coaxial configuration. The inner diameter of the electrodes is 24 mm. The laser is focussed between the electrodes labelled HV_1 and HV_2 in Figure 2.19. The electrode between HV_2 and G_2 is introduced in order to achieve a more even potential drop to ground. Also, to avoid focussing effects on the ion trajectories, a 90 % transmitting metallic mesh was installed on the electrodes on the mass spectrometer side (HV_2, $HV_2/2$ and G_2). The wire thickness is 43.4 µm and the space between wires is 803 µm and it was bought from Precision Eforming (part no. MN8). The mesh was cut to appropriately sized pieces and was then glued on to the electrodes with graphite spray (Cramolin, part no. 1281412).

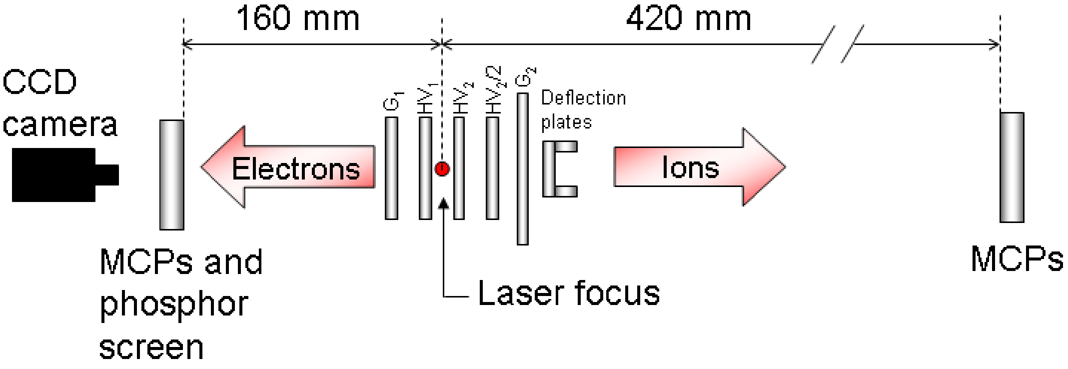

Figure 2.19: Schematic sketch (not to scale) of the electrode configuration. Electrodes G_1 and G_2 are electrically grounded.

During the design of the ion optics it was thought that a reflectron time-of-flight mass spectrometer would be installed. To obtain a good signal with these spectrometers one needs to steer the ions into the reflectron and therefore two pairs of deflection plates were installed. One of the plates in each pair is grounded and the other plate can be held at a potential (both positive and negative) in order to steer the ions. However, initial tests with the linear time-of-flight mass spectrometer used in this work, showed that the deflection plates were not needed and they are therefore kept at zero potential at all times.

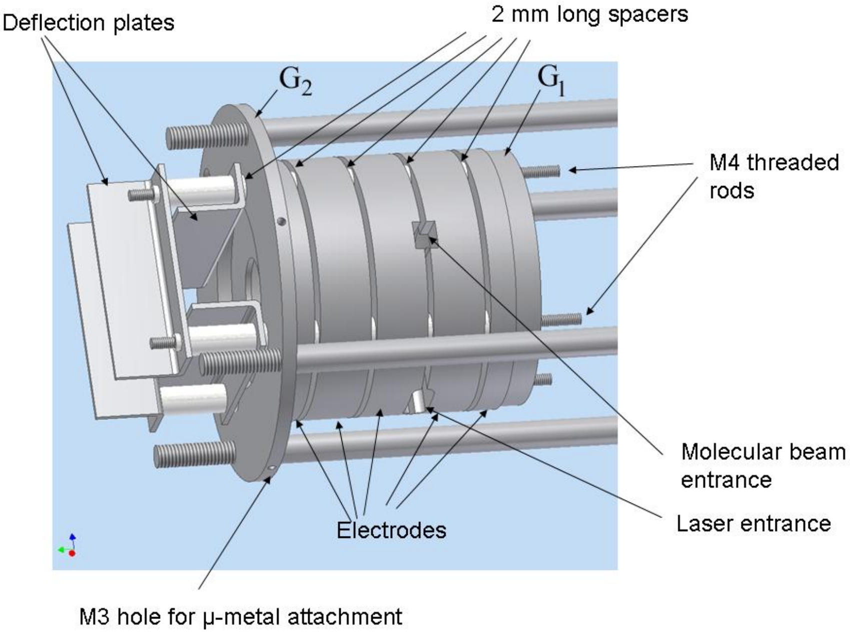

Figure 2.20: Autodesk Inventor drawing of the electrode assembly. The molecular entrance hole is 10 × 8 mm and the entrance hole for the laser is 22 × 8 mm. The outer diameter of the largest electrode (G_2) is 130 mm.

The electrodes are held together on a concentric axis by four threaded M4 rods made from stainless steel running through the electrodes (seen in Figure 2.20). G_1 is the only electrode in direct contact with the rods to ensure that this electrode is grounded. For all other electrodes the rods are surrounded by alumina tubes (inner diameter 4.1 mm and outer 6 mm, custom order from Caburn MDC), electrically insulating these electrodes from the rods. In order to also separate the electrodes from each other, alumina spacers were installed (outer diameter 10 mm, inner diameter 7 mm and height 2 ± 0.2 mm, also a custom order from Caburn MDC). The alumina spacers can be seen interlaying the electrodes in Figure 2.20. In order to achieve a potential drop from HV_2 to ground (G_2) over $HV_2/2$, two 10 MΩ resistors are used (Ohmite, MOX91021005FVE with maximum voltage rating 15 kV). These resistors are coated with silicone which make them ultrahigh-vacuum compatible.

The electrode assembly is mounted with four stainless steel rods screwed on to a DN300CF flange which is on one of the end sides of the interaction chamber (shown in Figure 2.21). The position-sensitive electron detector is also mounted on this flange. The end parts of the rods have an M8 thread applied to them. One end is screwed onto the supporting flange of the interaction chamber and the other end is for attaching the electrode assembly. Electrical feedthroughs with MHV connectors (CVT Ltd., part no. 794515-001) are used to connect electrodes HV_1 and HV_2 to power supplies (Stanford, part no. PS350, maximum voltage 5 kV). The wires inside the chamber connecting the electrodes with the electrical feedthroughs are coated with Kapton which is suitable for ultrahigh vacuum and the wires can be used with voltages up to 10 kV in vacuum.

A mu-metal cylinder surrounds the electrodes and extends all the way to the mounting flange. Mu-metal is a material which has a high magnetic permeability and is therefore used to screen against static or low frequency magnetic fields. The mu-metal cylinder was custom built by CVT Ltd. with an inner diameter of 133.4 mm and outer 135 mm. There are four holes into which an M3 screw can fit. These holes are used to attach the cylinder to G_2 with M3 screws. There is also a 6 mm deep groove in the mounting flange into which the mu-metal cylinder fits which serves as additional support of the cylinder. There are four additional holes in the cylinder for the entrance and exit of both the laser (22 x 12 mm) and molecular beams (8 x 12 mm). The drawings of the mu-metal cylinder can be found in the appendix.

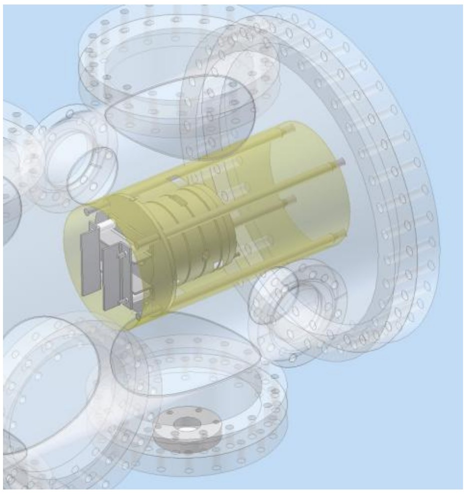

Figure 2.21: Autodesk Inventor drawing showing the electrode assembly mounted inside the interaction chamber. The transparent brown cylinder surrounding the assembly is the mu-metal cylinder.

2.6 Velocity-map imaging

2.6.1 Detector, CCD camera, accumulation software

A commercial detector is used to image the photoelectrons (Photonis USA Inc., part no. 31376). It consists of a pair of Chevron-style MCPs and a phosphor screen. The phosphor type is P20 and the characteristic decay time to 10 % of the initial intensity is about

200 μs (data supplied by the company). The MCPs and phosphor screen are mounted on the vacuum side of a DN100CF vacuum flange. The light emitted from the phosphor screen is coupled to the atmospheric side of the flange with fibre optics. Typical voltages over the electrodes in the VMI detector used are V_{MCP} = 1850 V and $V_{Phosphor}$ = 4850 V (see Figure 2.22). In order to ensure that the field-free region in front of the detector was properly grounded an additional electrode was made in the School of Chemistry's mechanical workshop. The electrode was made from stainless steel and had a larger diameter than the other electrodes.

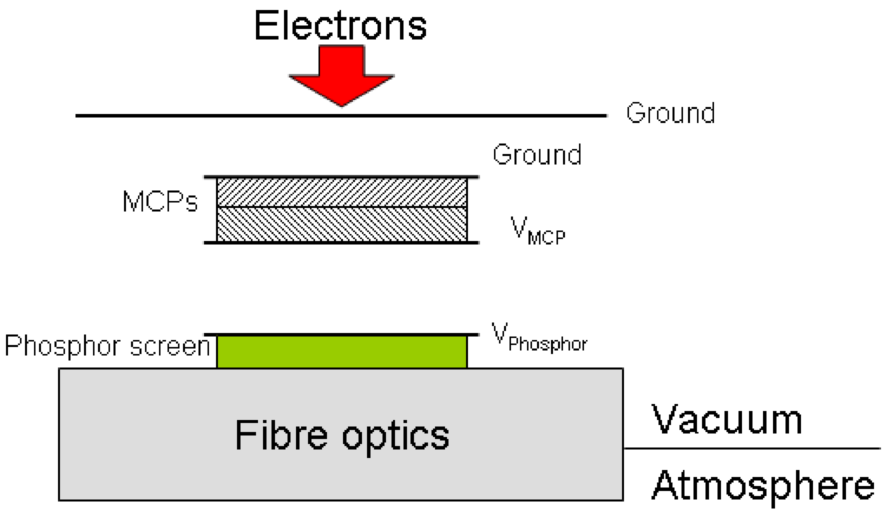

Figure 2.22: Schematic figure showing the electric configuration of the VMI detector.

The signal output from the phosphor screen is recorded with a CCD camera (Allied Vision Technology, Stingray) which is connected to a computer *via* a FireWire cable. The resolution of the camera is 1388 x 1038 pixels and the maximum transfer rate is 15 frames per second. The maximum shutter speed is 82 ms and this value has been used for all the results presented in this thesis. The camera can be controlled with two different accumulation programs written in LabView (presented in the appendix as *continuous_acquisition.vi* and *single_count_acquisition.vi*). *Continuous_acquisition.vi* simply adds several images together over many laser shots. Since the camera shutter speed is 82 ms and the femtosecond laser repetition rate is 1 kHz, about 80 laser shots are accumulated in one image. Typically 120,000 images are accumulated during one experiment and an equivalent number of background measurements with the laser blocked are taken (in total this takes about six hours). The images are then added offline in either the program *load_cont_images.m* or *load_cent_images.m* (appendix). Typically 50–200 ionisation events are recorded per image which gives about 1–3 ionisation events per laser shot. In total during the six hours accumulation period, on the order of 10^7 events are detected. However, during an experiment with low laser power the number of counts per image is typically quite low (about 0 – 30 counts per image). This gives the possibility to analyse each image before they are added together. The *single_count_acquisition.vi* program uses a built-in routine in LabView that applies a threshold to the image, which is determined by the user, so that only true counts are recorded while all other pixels are set equal to zero. Another built-in routine finds the centre-of-mass of each spot and adds one count to the corresponding coordinates in a new image. Therefore a higher resolution can be achieved [65, 66] because one electron spot with typically five to ten pixels in diameter is reduced to just one pixel. Furthermore, since the actual number of events is counted, any inhomogeneity in the detector does not influence the final image. This technique is usually referred to as centroiding. Normally it is necessary to smooth the raw data prior to inversion. This is done by transforming the image into polar coordinates. It is then possible to smooth only along the polar angle and not smooth over different radii and so the radial resolution is maintained. Once the raw image has been smoothed it is then converted back to Cartesian coordinates and subsequently inverted. Two programs to convert the image into polar coordinates and then transfer it back again to Cartesian coordinates were written by Andreas Molberg as part of an Erasmus exchange programme. The programs are presented in the appendix (*Carthage.m* and *Cato.m*). A MATLAB program written by Linda Winkler was used to smooth the data [67]. In Figure 2.23 a comparison of raw data obtained under identical conditions using the different accumulation programs is presented. The images were taken after ionising C_{60} with the fundamental output from the Legend. Another comparison is found in section 2.6.5.

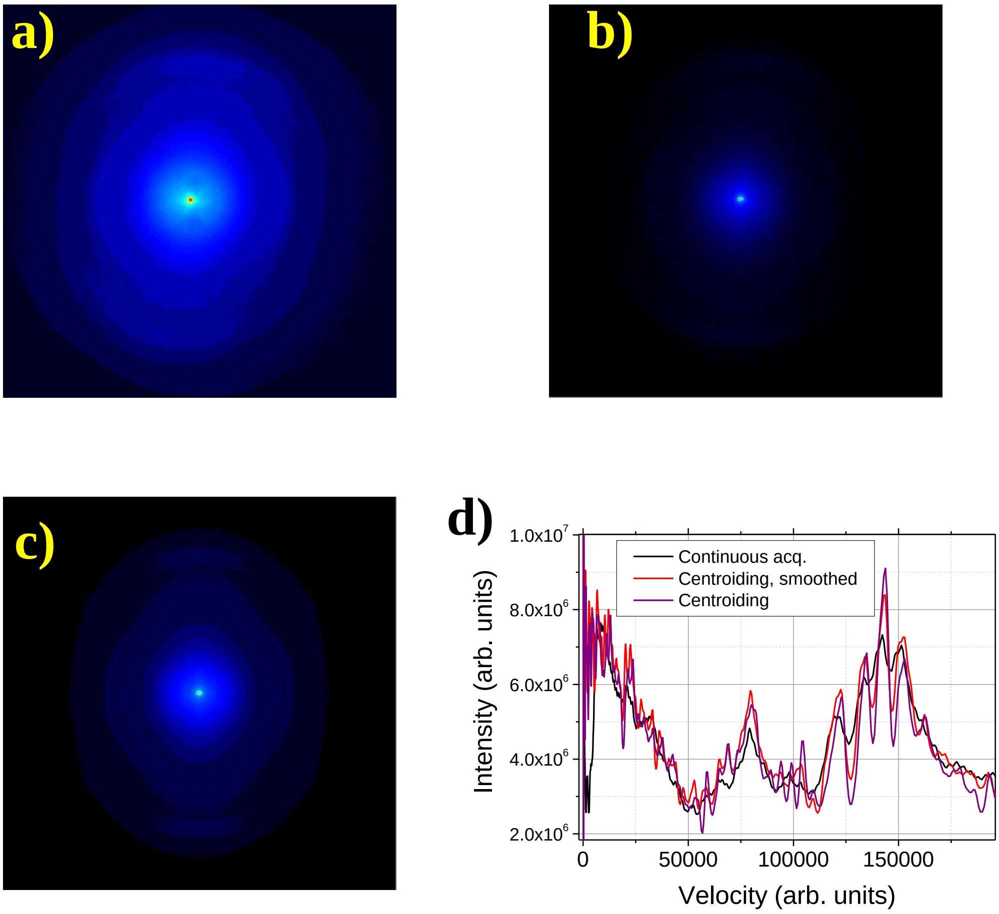

Figure 2.23: a) Raw VMI image of C_{60} taken with the continuous acquisition method using the fundamental output from the Legend. b) Raw VMI image taken under identical conditions as a) but using the centroiding method. c) Same as b) but after smoothing of raw data. d) Uncalibrated angle resolved velocity distributions for 0 – 10° obtained after the raw data were inverted using *pBASEX*. The resolution is better for the data taken using centroiding. Due to the inherent smoothing involved when using a continuous acquisition method a smoother spectrum is obtained during a shorter time period although at the expense of resolution.

2.6.2 Optimising VMI extraction voltages

As mentioned in the introduction to VMI, it is important to focus the image on the detector by optimising the ratio between electrodes HV_1 and HV_2. This is done by ionising xenon which produces a detailed structure in the VMI image (as seen in Figure 1.9). The extraction voltages are adjusted to obtain the narrowest rings possible. Usually a set of images are recorded as a function of voltage applied to HV_1 and are then subsequently inverted and analysed in order to find the optimum conditions. An example is shown in Figure 2.24 where velocity distributions (as a function of camera pixels) for different extraction voltages are shown (while keeping HV_2 constant at –720 V). The spectra were produced by ionising xenon using the SHBC (400 nm, 5 cm^{-1} bandwidth and 4 ps duration). This is a 3-photon non-resonant ionisation mechanism producing xenon ions in the $P_{3/2}$ state. To reach the excited spin-orbit state an additional photon is needed but at the laser intensity used this is not a likely process and therefore only one peak is seen in the VMI image. On the right-hand side of Figure 2.24 the velocity distribution for the best VMI setting has been calibrated and converted to a photoelectron spectrum (see below for calibration method). A Gaussian peak fit was made in *Origin* that was centred at x_c = 218.7 ± 0.2 meV with a *FWHM* of 23.4 ± 0.5 meV where the error is the standard error of the fit. A Lorentzian peak fit was also carried out resulting in a poorer fit compared to the Gaussian peak fit. The resolution in this energy interval can then be estimated to be $\frac{\Delta E_{kin}}{E_{kin}} = \frac{FWHM}{x_c} \approx 10\%$.

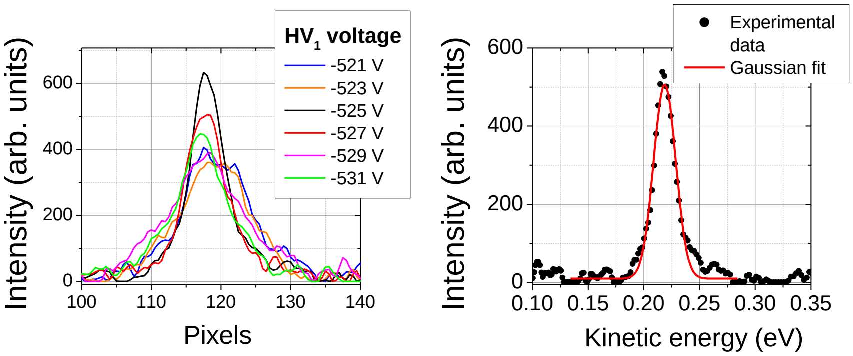

Figure 2.24: *Left)* Uncalibrated velocity distributions for different extraction voltages (see text for details). For clarity only a few voltage settings are shown. Normally VMI images are taken with 1 or 2 Volt increments of the extraction voltage. HV_2 voltage was kept constant at –720 V. *Right)* Calibrated photoelectron spectrum taken with HV_1 = –525 V (black dots). A Gaussian peak was fitted in *Origin* (red line) to identify the FWHM of the peak which was found to be about 20 meV.

2.6.3 Inversion methods and analysis

Once the experimental 2D raw image is obtained it needs to be inverted. This can be done using several different methods [68-73] and a summary can be found in ref. [56]. In this thesis both BASEX [71] and pBASEX [73] have been used although the Onion Peeling [57] and POP [72] algorithms have been used as well as a test for consistency of the inversion procedure. The BASEX method is based on projecting a set of well-behaved basis functions[1] onto a detector using the Abel transform. The measured raw image is then expanded in the set of the projected basis functions. The expansion coefficients found can then be used to expand the measured 3D distribution in the unprojected basis functions set which is then the inverted image. The inverted image (both in Cartesian and polar coordinates) and the velocity distribution are produced by the inversion program. The velocity distribution is then converted to a photoelectron spectrum and the kinetic energy scale of the distribution is calibrated according to the procedure presented below. The pBASEX method is very similar to BASEX with the main difference being that the raw image is first converted into polar coordinates. Gaussian functions are fitted to the radial part and Legendre polynomials of order up to ten are fitted to the angular part of the raw image. By transforming the image into polar coordinates the central-line noise which is seen along the laser polarisation when using BASEX is eliminated. The noise produced in the pBASEX algorithm is mainly seen in the centre of the inverted image (small radii) which is an advantage compared to the BASEX algorithm. Two disadvantages of pBASEX are that the number of radial basis functions compared to BASEX is smaller which reduces the resolution at higher kinetic energies and the final inverted image only shows the fit of the experimental data. The last point is crucial because a fit can look good despite a poor quality of the experimental data but by using several inversion methods one can judge the quality of the data.

There are several ways to analyse the angular dependence of the PES. The various inversion programs usually provide beta parameters for each velocity. However, from previous measurements of PES of C_{60} after femto- and picosecond laser excitation it is known that the spectra contain peak structure superimposed on a thermal electron background [6, 7]. It is therefore necessary to first separate the two components from each other before any further analysis can be carried out. This is achieved by dividing the VMI image into angular segments typically of 10° intervals and calculating the PES for each angular segment. From images inverted using BASEX this is done using a program called *BASEX_pizza.m* written in MATLAB (the code is presented in the appendix). The program analyses the inverted image $F(v,\theta)$ in polar coordinates which is produced by BASEX. For

---

[1] For the inverse Abel transform there is a possibility of singularities in the denominator. Well-behaved functions refers to functions that have an inverse Abel transform that avoids these singularities.

each velocity the angular contribution is integrated over the chosen interval (10°). The total number of emitted electrons in each interval $(dv, d\theta)$ centred at (v, θ) is calculated by $v^2 \sin(\theta) F(v, \theta) dv d\theta$. However, it is usually more intuitive to analyse the angular dependence of $F(v, \theta)$ without including $\sin(\theta)$ because it reflects the number of emitted electrons per steradian. Therefore, one can also choose to find the angular dependent PES calculated as $v^2 F(v, \theta) dv d\theta$. For images inverted using pBASEX no polar plot is provided. Therefore a program (*VMI_pizza_slices.m*, code presented in the appendix) was made to calculate the angular dependent PES from the inverted VMI image.

2.6.4 Calibration of photoelectron kinetic energy and laser intensity: non-resonant and resonant multiphoton ionisation of Xe

Ionisation of xenon serves as a test of the experimental apparatus. Once it has been shown that the setup can reproduce previously published studies of xenon, the same experiments can be used to calibrate the PES energy scale and the laser intensity in the focus. The kinetic energy scale has to be calibrated because the velocity distribution obtained by the inversion methods is given in units of CCD camera pixels. An inverted VMI image with corresponding PES of xenon ionised with 800 nm laser light is presented in Chapter 1 Figures 2 and 1. The result is similar to the results presented in refs. [28, 74] (obtained using VMI photoelectron spectroscopy and similar laser characteristics) which indicates that photoionisation of xenon can be used to characterise the system. The results presented in this thesis are taken with three different VMI extraction voltages (HV_2 = –2000, –720 and –400 V) and so three different energy scale calibrations are needed. Usually such a calibration is performed every time the laser has been realigned through the chamber or the VMI extraction voltages have been re-optimised. The results presented in this section are meant to illustrate a typical calibration procedure.

The case of non-resonant multiphoton ionisation of xenon is illustrated in Figure 2.25. At the laser intensity typically used in the experiments one has to consider that the electronically excited states in the neutral atom and the ground state of the ion shift in energy as a function of the laser intensity due to the A.C. Stark shift. Four 400 nm photons are needed to reach the $P_{3/2}$ ground state in the xenon ion. The combined energy of four photons is 12.40 eV which should produce photoelectrons with a kinetic energy of 270 meV (labelled $E_{kin,1}$ in Figure 2.25) because the ionisation potential of xenon is 12.13 eV [75]. However, the AC Stark shift alters the ionisation potential by an amount depending on laser wavelength and intensity, which will reduce the kinetic energy of the photoelectron. The first excited spin-orbit state $P_{1/2}$ in the xenon ion lies 1.306 eV above the ground state [76] so with four photons it is not possible to access this state. On the other hand, with five photons the excited state is accessible resulting in two additional peaks in the PES. The difference in energy between the two peaks ($E_{kin,2}$ and $E_{kin,3}$ in Figure 2.25) is the energy difference between the two spin-orbit states. Therefore the kinetic energy scale of the PES can be calibrated by using these two peaks.

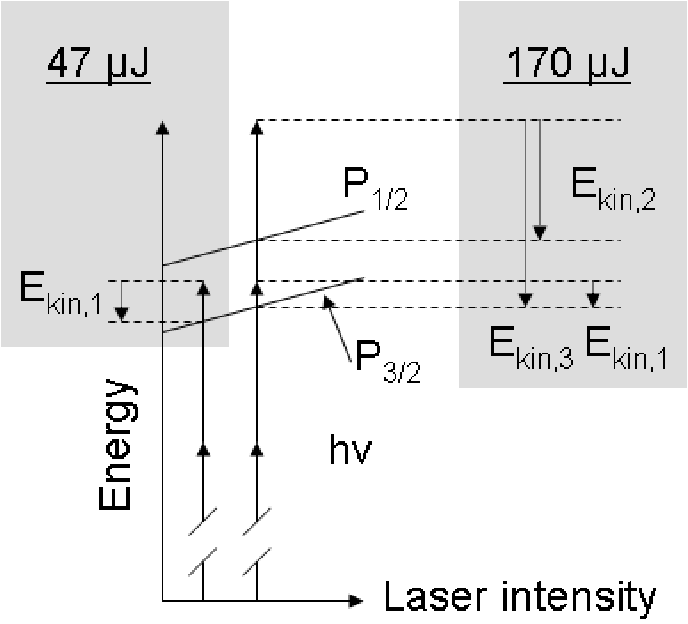

Figure 2.25: Schematic drawing illustrating the non-resonant ionisation of xenon. Solid arrows symbolise photons and dotted arrows photoelectron kinetic energies. For low pulse energies (comparable to measurements made with 47 µJ pulse energy) the intensity is just enough to reach the ground state in the ion (left-hand side) and photoelectrons with kinetic energy $E_{kin,1}$ are emitted. At higher pulse energies (right-hand side, comparable to 170 µJ) the intensity is enough to observe both four and five photon absorption resulting in photoelectrons emitted with three kinetic energies ($E_{kin,1}$, $E_{kin,2}$ and $E_{kin,3}$).

The SHBC output (4 ps, 400 nm and 5 cm^{-1} bandwidth) was used to ionise xenon through a non-resonant multiphoton process. The VMI settings used were $HV_2 = –720$ V and $HV_1 = –525$ V. For the highest pulse energy (170 µJ) three peaks are seen in the PES (inverted using *BASEX*) which can be related to the corresponding photoelectron energies shown in Figure 2.25. The angle resolved PES was obtained from the inverted VMI image using *BASEX_pizza.m*. A magnification of the 10–20° PES shows the peaks labelled $E_{kin,2}$

and $E_{kin,3}$ in Figure 2.26 plotted on an uncalibrated kinetic energy scale (the full spectrum is shown in Figure 2.28). The peaks have been fitted to Gaussian peaks in *Origin* which gave $E_{kin,2}$ = 127572 ± 31 pixels^2 (fractional error $\sigma_2/E_{kin,2} = 2.4\times10^{-4}$) and $E_{kin,3}$ = 209663 ± 38 pixels^2 (fractional error $\sigma_3/E_{kin,3} = 1.8\times10^{-4}$). The error is the standard error produced by the fit in *Origin*. By assuming that $\Delta = E_{kin,3} - E_{kin,2} = 1.306\ eV$ the abscissa can be given in units of eV. The fractional error in the energy difference is given by (omitting the error in the spin-orbit splitting)

$$\sigma_{3,2} / \Delta = \sqrt{\left(\frac{\sigma_2}{E_{kin,2}}\right)^2 + \left(\frac{\sigma_3}{E_{kin,3}}\right)^2} = 3\times10^{-4}.$$

The calibration factor k_{-720V} then becomes

$$k_{-720V} = (1.5958 \pm 0.0005)\times10^{-5}\ \text{eV/pixels}^2$$

where the same fractional error was used as for Δ.

The raw VMI image together with the inverted image is shown in Figure 2.27 and the angle resolved PES is shown in Figure 2.28. Since the PES is angle resolved it is also possible to characterise any ellipticity in the VMI image. The difference in peak positions for the 10–20° segment compared to the 80–90° segment shows a 1.7 % drift in position for the $E_{kin,2}$ peak. The same drift (1.7 %) is observed for a measurement taken with a lower pulse energy (47 μJ, Figure 2.29 and Figure 2.30).

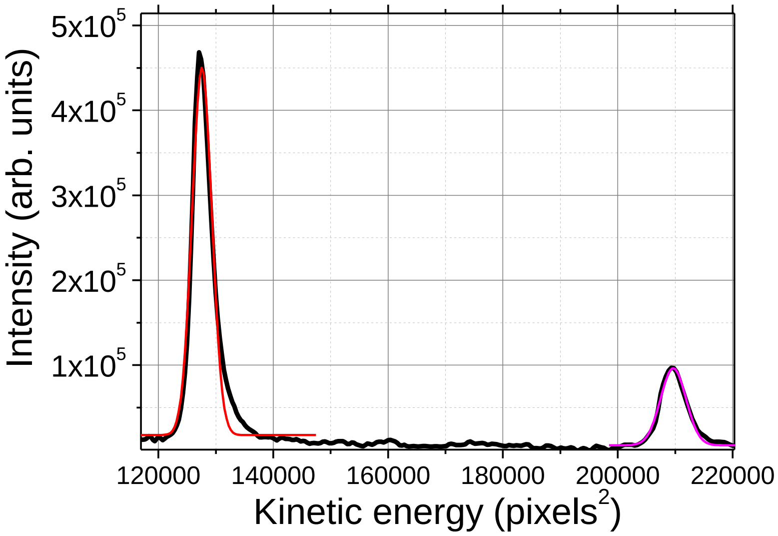

Figure 2.26: Magnification of the two outer peaks $E_{kin,2}$ and $E_{kin,3}$ seen in Figure 2.28 in units given by the inversion program (pixels^2). Xenon ionised using 4 ps, 400 nm (5 cm^{-1} bandwidth) laser excitation of pulse energy 170 μJ.

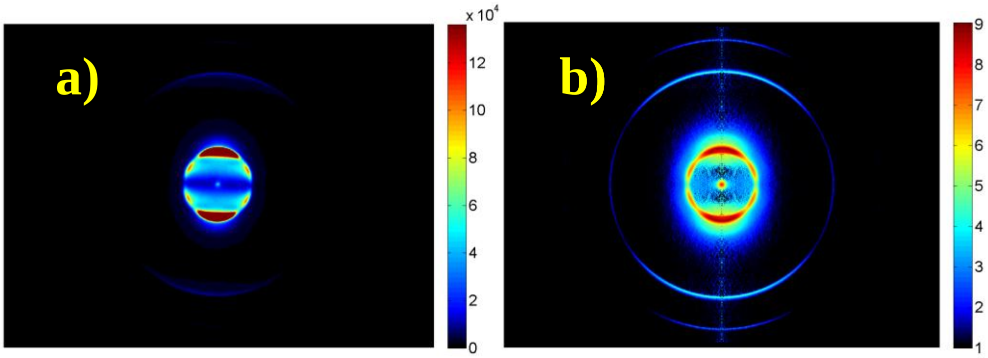

Figure 2.27: a) Raw VMI image of xenon ionised with the SHBC (4 ps, 400 nm and 5 cm^{-1} bandwidth, pulse energy 170 μJ). The extraction settings were HV_2 = –720 V and HV_1 = –525 V and *continuous_acquisition.vi* used. b) Inverted image (*BASEX*) in a logarithmic intensity scale.

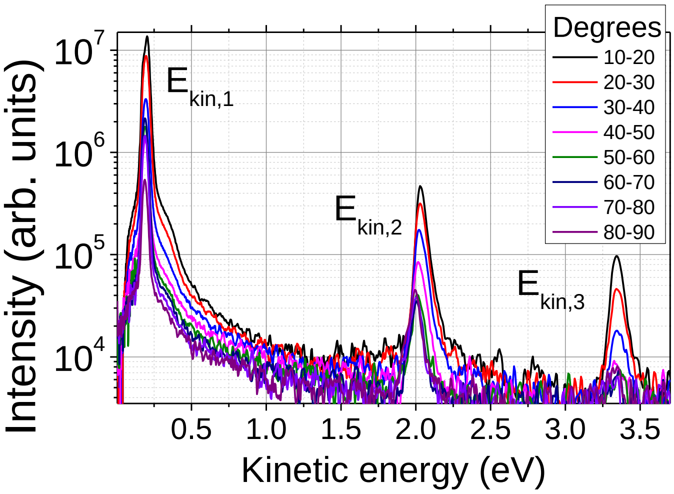

Figure 2.28: Angle resolved PES in logarithmic scale obtained from the inverted image in Figure 2.27. The peak labels are the same as in Figure 2.25. Xenon ionised using 4 ps, 400 nm (5 cm^{-1} bandwidth) laser excitation of pulse energy 170 μJ.

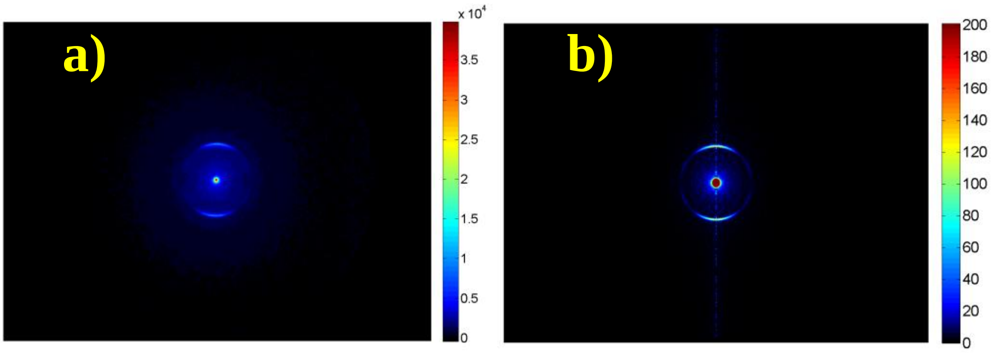

Figure 2.29: a) Raw VMI image of xenon ionised with the SHBC (4 ps, 400 nm and 5 cm^{-1} bandwidth, pulse energy 47 μJ) and collected using *continuous_acquisition.vi*. The extraction settings were HV_2 = –720 V and HV_1 = –525 V. b) Inverted image (*BASEX*) in a saturated linear intensity scale.

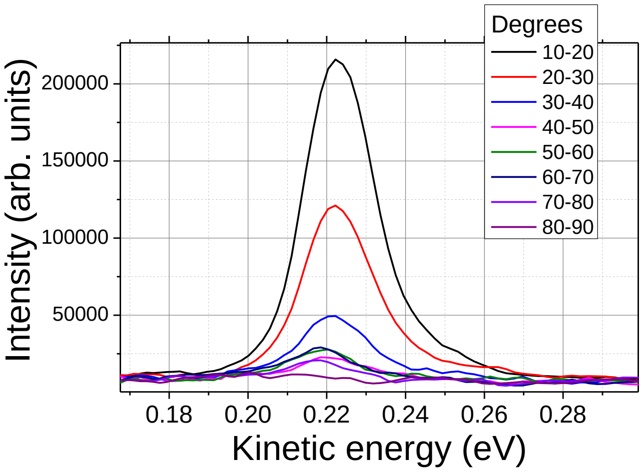

Figure 2.30: Angle resolved PES obtained from the inverted image in Figure 2.29. Xenon ionised using 4 ps, 400 nm (5 cm^{-1} bandwidth) laser excitation of pulse energy 47 μJ.

Raw and inverted VMI images taken with the second harmonic of the Legend output are given in Figure 2.31. Due to the shorter pulse duration compared to the SHBC, a higher intensity is achieved. In addition to the three peaks previously discussed several ATI peaks are now visible. During the measurement the fullerene oven was turned on resulting in a weak background signal from ionisation of fullerenes. This does not affect the peak positions resulting from ionisation of xenon. The kinetic energy scale of the PES was calibrated as previously shown and the calibration factor found was $k = (4.051 \pm 0.002) \times 10^{-5}$ eV/pixles^2. An approximation of the AC Stark shift together with the measured peak positions can be used to calibrate the laser intensity. The peak positions are found to be shifted from the value expected if no AC Stark shift was present. The measured peak positions compared to field-free conditions are presented in Table 3. The difference in peak position is almost constant and an average value of 0.154 ± 0.08 eV is found (error estimated as the standard deviation of the four differences). The AC Stark shift can be approximated by the ponderomotive shift (see introduction) which is

$$U_p[eV] = 9.34 \times 10^{-20} (\lambda[nm])^2 \times (I[Wcm^{-2}]) \, .$$

If the measured drift in peak position is estimated to equal the ponderomotive shift, the laser intensity can be calculated. Solving the above equation for the intensity I yields

$$I = (1.0 \pm 0.5) \times 10^{13} Wcm^{-2} \, .$$

The measured laser pulse energy after the chamber was 25 μJ giving a calibration factor *s* for the laser intensity (using a lens with 30 cm focal length)

$$s = \frac{1.0 \times 10^{13}[Wcm^{-2}]}{25[\mu J]}.$$

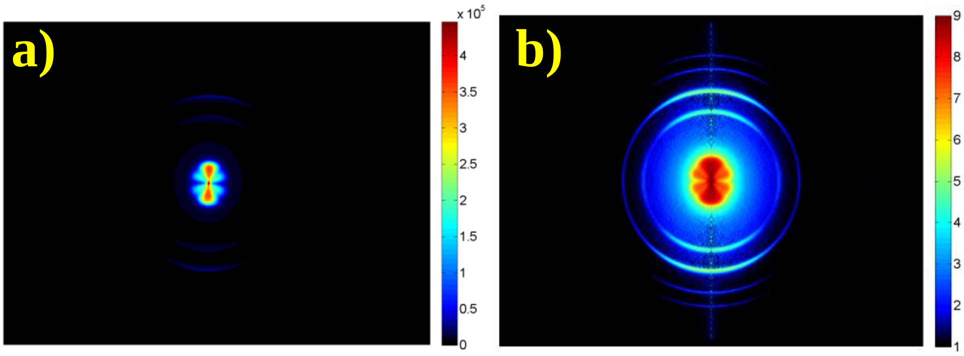

Figure 2.31: a) Raw VMI image of xenon ionised with 400 nm, 130 fs and 26 μJ pulse energy (second harmonic of the Legend fundamental output). Collected using the continuous acquisition method. The extraction settings were $HV_2 = -2000$ V and $HV_1 = -1440$ V. b) Inverted image (*BASEX*) in a saturated logarithmic intensity scale.

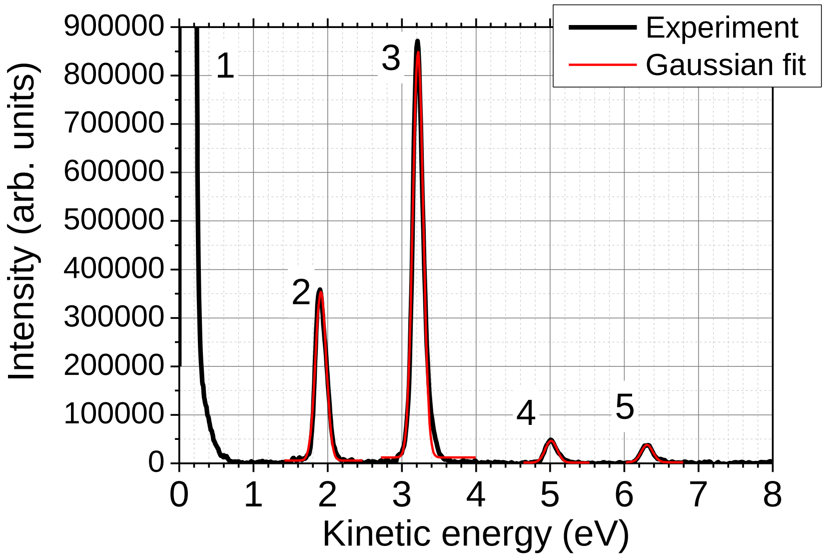

Figure 2.32: PES obtained from inverted raw data shown in Figure 2.31 after ionising xenon using 130 fs, 400 nm laser excitation of pulse energy 26 μJ. Gaussian peaks have been fitted to four of the peaks seen in the spectrum (peaks 2–5). The data were taken with a high oven temperature implying that a signal from C_{60} should also be present. Indeed, an exponential background was found and was subtracted from the spectrum presented in the figure. The maximum of peak 1 at 0.11 eV is not shown in order to highlight the peaks with lower intensity.

Table 3: Fitted peak positions from the spectrum presented in Figure 2.32 are compared to theoretical kinetic energies assuming no AC Stark shift. Peaks 4 and 5 are ATI peaks because (4) – (2) = (5) – (3) = 3.10 eV which is the photon energy.

Peak	**E_{kin} experiment (eV)**	**Field-free E_{kin} (eV)**	**Difference (eV)**
2	1.908 ± 0.001	2.06	0.152
3	3.218 ± 0.001	3.37	0.152
4	5.013 ± 0.001	5.16	0.147
5	6.305 ± 0.002	6.47	0.165

When using 800 nm light eight photons are needed to ionise xenon. With the combined energy of seven photons it is possible to reach the Rydberg manifold of xenon. If the combined photon energy coincides with an intermediate resonance the ionisation probability is greatly enhanced [15]. Since the excited states of the atom shift in energy with laser intensity there is always a possibility to ionise the atom for sufficiently high powers due to the large intensity range accessible because of the temporal and spatial intensity distribution of the laser beam [77]. Figure 2.33 illustrates the situation. For the laser intensities typically used in the experiments, several ATI peaks can be seen (seen in Figure 1.9). The kinetic energy scale of the PES can be calibrated since the difference between two ATI peaks is just the photon energy. However, for the lowest extraction voltage used (–400 V) it is not possible to see the first ATI peak. Therefore, a spectrum was measured for a slightly higher extraction voltage (–720 V). The result is presented in Figure 2.34 together with the uncalibrated angle resolved PES for 10–20° in Figure 2.35. Two Gaussian functions were fitted in *Origin* to the two peaks yielding peak positions of 87911 ± 92 pixels^2 and 187261 ± 119 pixels^2. The photon energy (1.548 eV) divided by the peak difference gives a calibration factor of $k_{-720V} = (1.560 \pm 0.002)\times 10^{-5}$ eV/pixels^2 where the error was propagated as in the 400 nm case. The calibration factor can now be used to find the peak position of the first peak which is also seen when using a lower extraction voltage. The peak energy in eV is $k \times 87911 = 1.371 \pm 0.002$ eV. Results using similar conditions but with a lower extraction voltage ($HV_2 = -400$ V) are shown in Figure 2.36. The angle resolved 10–20° PES is shown in Figure 2.37 where a Gaussian fit made in *Origin* is also shown. From the fitted peak position the calibration factor can be found since the peak position should correspond to a kinetic energy of 1.371 eV. Therefore $k_{-400V} = (8.311 \pm 0.017) \times 10^{-6}$ eV/pixels^2. The angle resolved PES for several angular segments is shown in Figure 2.38 to identify the ellipticity in the VMI image. In the case for –400 V extraction voltage the drift in peak position is about 8 %. This could be due to the lower kinetic energy the electrons gain in the extraction region which make them more susceptible to stray magnetic fields.

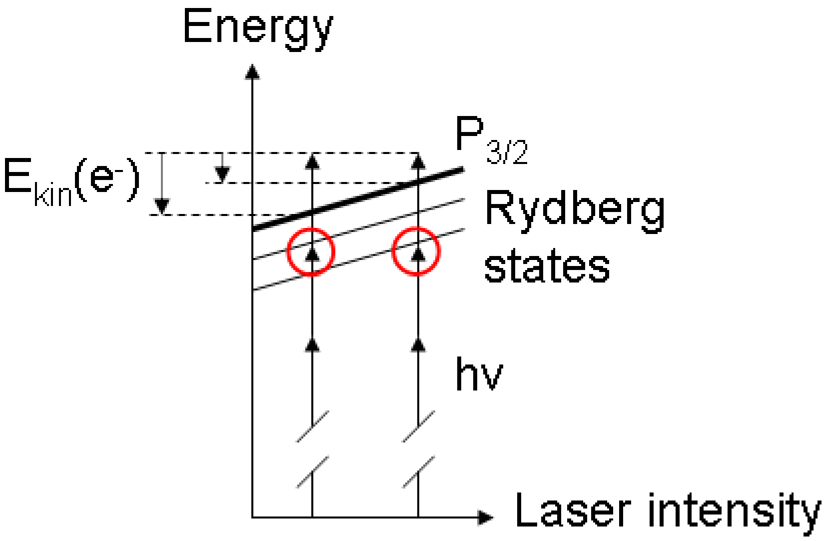

Figure 2.33: Schematic figure showing the resonance enhanced multiphoton ionisation of xenon. The temporal and spatial profiles of the laser beam ensure that there will be an intensity where a certain Rydberg state is tuned into resonance due to the AC Stark shift. Since the ionisation potential shifts by the same amount as the highly excited state of the neutral atom the measured photoelectron kinetic energies can be directly related to the binding energy of the Rydberg state.

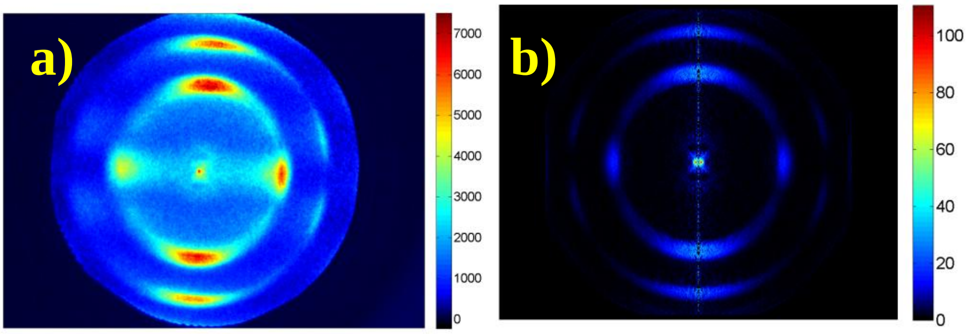

Figure 2.34: a) Raw VMI image of xenon ionised with the fundamental output from the Legend (800 nm, 120 fs, 71 µJ, f = 50 cm lens) collected using the continuous acquisition method. The extraction settings were HV_2 = –720 V and HV_1 = –522 V. b) Inverted image (*BASEX*) in a linear intensity scale.

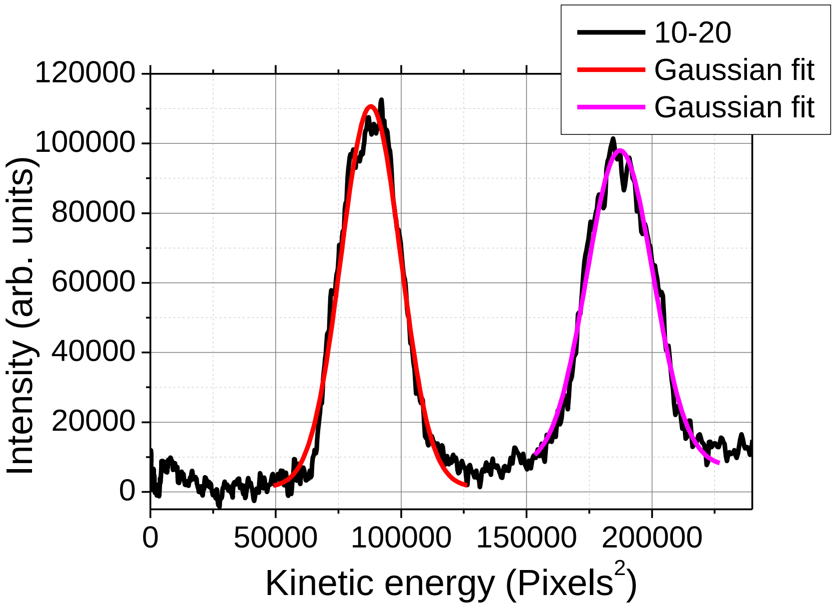

Figure 2.35: Angle resolved uncalibrated PES shown for 10–20° obtained from the inverted image in Figure 2.34. Two Gaussian functions were fitted to the data using *Origin*.

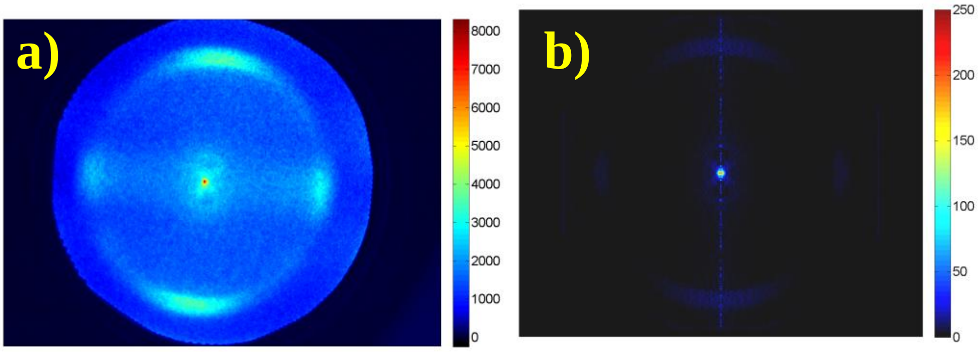

Figure 2.36: a) Raw VMI image of xenon ionised with the fundamental output from the Legend (800 nm, 123 fs, 66 μJ, *f* = 50 cm lens) collected using the continuous acquisition method. The extraction settings were HV_2 = –400 V and HV_1 = –287 V. b) Inverted image (*BASEX*) in a linear intensity scale.

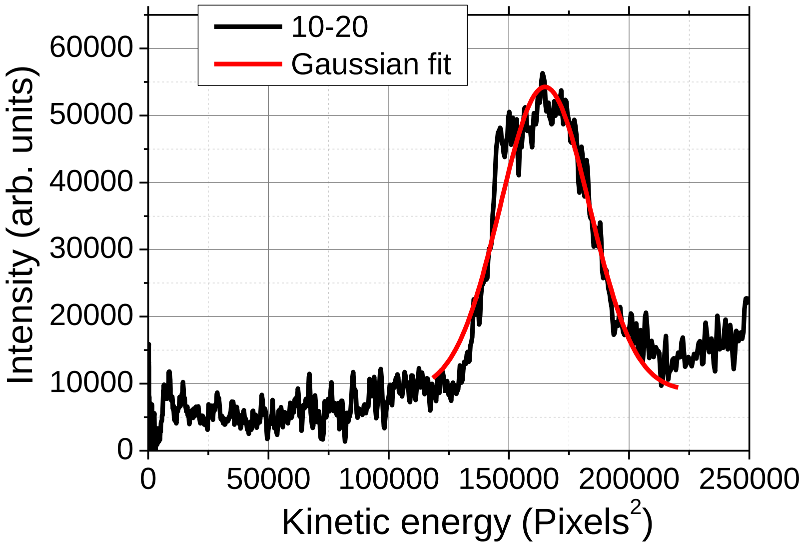

Figure 2.37: Angle resolved uncalibrated PES shown for 10–20° obtained from the inverted image in Figure 2.36. A Gaussian function was fitted to the data using *Origin*.

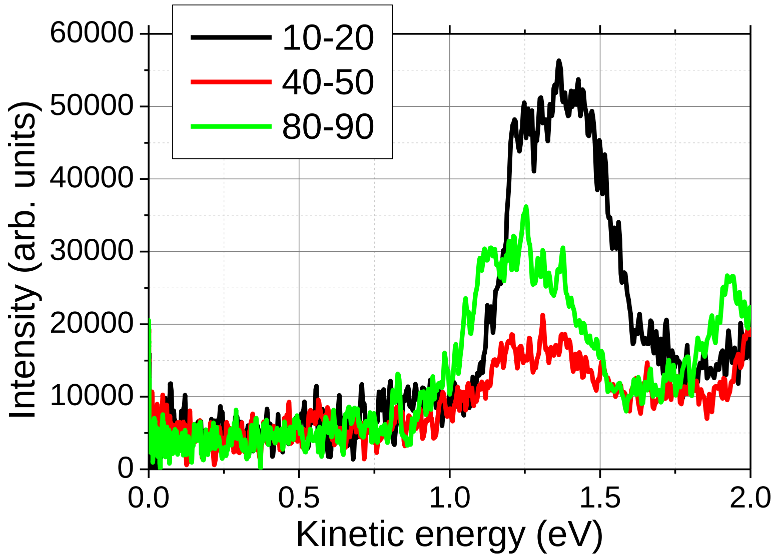

Figure 2.38: Angle resolved calibrated PES shown for 10–20°, 40–50° and 80–90° obtained from the inverted image in Figure 2.36. A drift in peak position is found to be 8 % between the 10–20° and 80–90° angular segments.

A measurement made using a high extraction voltage (–2 kV) is presented in Figure 2.39. The PES is similar to the one presented in Figure 1.9 and a part of the uncalibrated PES for 10–20° is shown in Figure 2.40. In a similar procedure to what has been shown above the calibration factor was found to be k_{-2000V} = (4.293 ± 0.003) × 10^{-5} eV/pixels^2. The angle resolved PES shows a 1.7 % drift of the first ATI peak position which was also found in the 400 nm case (–720 V extraction voltage).

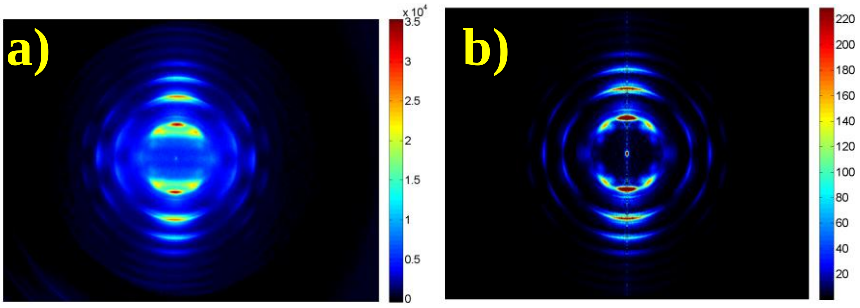

Figure 2.39: Raw VMI image of xenon ionised with the fundamental output from the Legend (800 nm, 117 fs, 41 μJ, f = 30 cm lens) collected using *continuous_acquisition.vi*. The extraction settings were HV_2 = –2000 V and HV_1 = –1445 V. b) Inverted image (*BASEX*) in a saturated linear intensity scale.

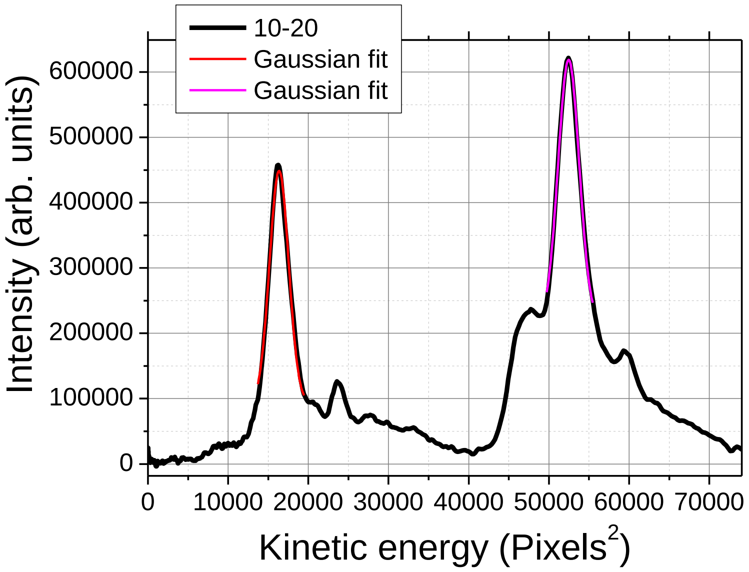

Figure 2.40: Angle resolved uncalibrated PES shown for 10–20° obtained from the inverted image in Figure 2.39. Two Gaussian functions were fitted to the data using *Origin*.

By recording a series of VMI images for 800 nm ionisation of xenon as a function of laser power it is possible to calibrate the laser intensity in the focus [74]. The result of such a series is shown in Figure 2.41. Assuming that the AC Stark shift can be approximated as the ponderomotive shift, the 4f Rydberg state of xenon should be tuned into resonance at a laser intensity of 1.8×10^{13} W/cm^2 [74]. The typical pattern seen in Figure 2.41 c)-d) but not in a) and b) is a signature of the 4f Rydberg state [74] and so one can estimate that the laser intensity taken with a pulse energy of about 33 μJ corresponds to an intensity of at least $I = 1.8 \times 10^{13}$ W/cm^2. This can be converted into a fluence as shown in section 2.4 assuming that the pulse has a Gaussian temporal distribution so that $F = I_0 \times \Delta t / 0.94 = 2.3$ J/cm^2 where Δt is the pulse duration (taken as the FWHM). This can be compared to the measured values of the laser beam waist in the focus made in section 2.4.5. The two measurements of the laser beam waist in the focus gave areas $(2.26 \pm 0.06) \times 10^{-5}$ cm^2 and $(3.4 \pm 0.4) \times 10^{-5}$ cm^2 which can be used to calculate the fluence and intensity. For a pulse energy of 33 μJ the corresponding intensities are $(2.29 \pm 0.06) \times 10^{13}$ W/cm^2 and $(1.5 \pm 0.2) \times 10^{13}$ W/cm^2. The fluences are 2.92 ± 0.08 J/cm^2 and 1.9 ± 0.2 J/cm^2. The value calculated assuming a Gaussian laser beam profile should give an upper limit of the intensity since the calculation was done assuming a perfect lens. This is usually not the case and typically a slightly larger beam waist is found in the focus compared to the theoretical value. Therefore an average of the two values of 15 and 18 TW/cm^2 is chosen and is equal to 16.5 ± 1.5 TW/cm^2. The error is estimated as half the maximum difference between the two values. For a measured pulse energy E_p after the chamber (0.96 × 33 μJ assuming that 4 % of the light reaching the exit vacuum viewport is reflected back) the peak intensity can be found by a conversion factor s_I which is

$$s_I = \frac{1.65 \times 10^{13}}{0.96 \times 33} = (5.2 \pm 0.5) \times 10^{11} \left(\frac{W / cm^2}{\mu J} \right).$$

This value corresponds to a pulse duration of 120 fs and an $f = 30$ cm lens. This corresponds to a conversion factor for the fluence of s_F

$$s_F = 66 \pm 6 \left(\frac{mJ / cm^2}{\mu J} \right).$$

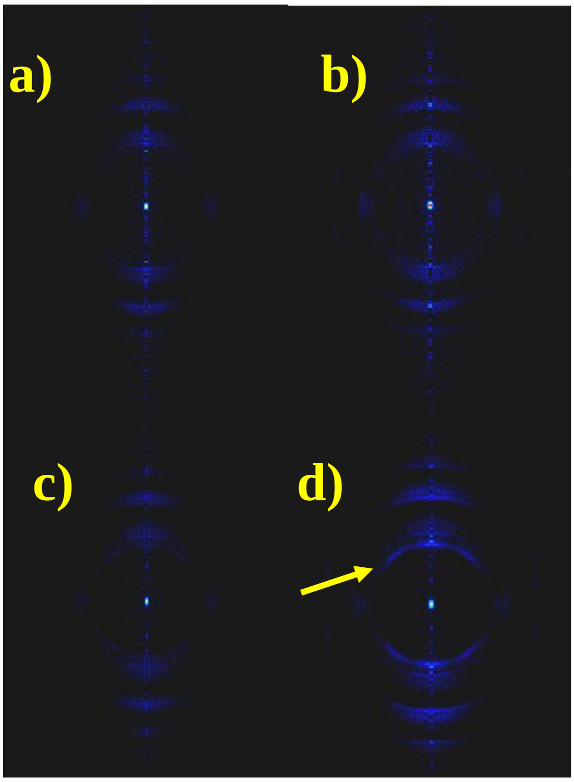

Figure 2.41: A series of inverted VMI images (BASEX) for different laser pulse energies inside the vacuum chamber (800 nm, pulse duration 120 fs and an *f* = 30 cm lens). a) 30.8 μJ, b) 32.0 μJ, c) 33.5 μJ and d) 35.7 μJ. The 4f Rydberg state can clearly be seen in d) (indicated with an arrow) as the inner-most ring but is only faintly seen in c).

2.6.5 Testing the VMI detector homogeneity: ionisation of C_{60} using ns laser pulses

In order to verify that the experimental setup generates reliable data, photoionisation experiments of C_{60} using ns lasers have been performed. The ionisation mechanism of C_{60} after ns excitation has been well studied and therefore serves as a test of the equipment [23, 26]. In the lab in Gothenburg, photoelectron spectra have been acquired using a nitrogen laser with pulse duration 4 ns and wavelength 337 nm together with Mikael Kjellberg, Alexander Bulgakov and Klavs Hansen. The experimental setup in the Gothenburg lab is similar to the one in Edinburgh and a description can be found in ref. [28]. The experiment was done to verify the statistical nature of fullerene decay after ns excitation using VMI photoelectron spectroscopy. If the polarisation of the laser is directed into the position sensitive detector, the photoelectron angular distribution is expected to be isotropic. This can be seen in Figure 1.7 where a 90 degree rotation of the polarisation into the detector would also rotate the sphere 90 degrees and a homogenous distribution would thus be detected. The experimental test was to compare VMI images obtained with vertical (parallel with detector) and horizontal polarisation. If no difference was found it would signify that the emitted distribution of photoelectrons is isotropic. The raw VMI images are shown in Figure 2.42. A bright spot is found slightly off centre and is attributed to background electrons that are not produced in the critical region between the electrodes producing velocity mapping. These electrons might originate from the fullerene oven which is situated below the electrodes. Another source of electrons might originate from the laser hitting a metallic surface or the ionisation of residual oil from the vacuum pumps. Due to this effect a small circle was cut out from the centre of the image. The angular dependences of the raw images for the two polarisations are shown in Figure 2.43 where different radii of the cut-out circles are shown. The number of counts in 9 degrees angular segments was found and the analysis was made using the program *Symmetry_check.m* as described in section 2.6.3. The influence of the radius of the circle that was cut out from the raw data was investigated and it was found that it did not have a large influence. The angular dependence for each polarisation is not a completely flat function as would be expected from an isotropic distribution. The reason for this might be that the extraction electrodes are not perfectly manufactured, there might be external electric or magnetic fields influencing the electron trajectories or inhomogeneous detection efficiency in the detector. However, the ratio of the data for the two polarisations reduces the influence of systematic errors as is seen in Figure 2.44. Based on the presented data one can conclude that the electron emission from C_{60} after nanosecond ionisation is isotropic. This result was used to check the performance of the detector in Edinburgh.

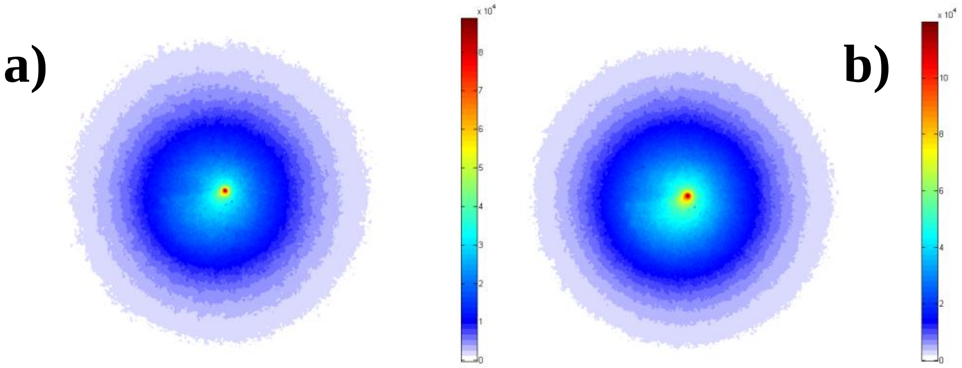

Figure 2.42: Raw photoelectron images from ionization of C_{60} using a 337 nm nitrogen laser with pulse duration 4 ns. Laser polarisation was either horizontal (a) or vertical (b) with respect to the detector screen. Data acquired in Gothenburg.

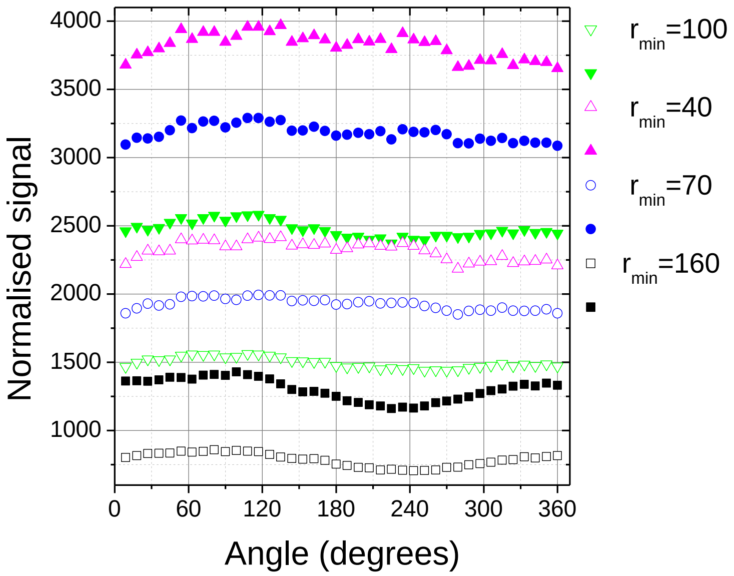

Figure 2.43: Angular dependence of the raw images shown in Figure 2.42. Different radii r_{min} have been used to eliminate the strong background signal in the centre. The unit of the radii are pixels. Open symbols show horizontal polarisation and filled symbols vertical polarisation.

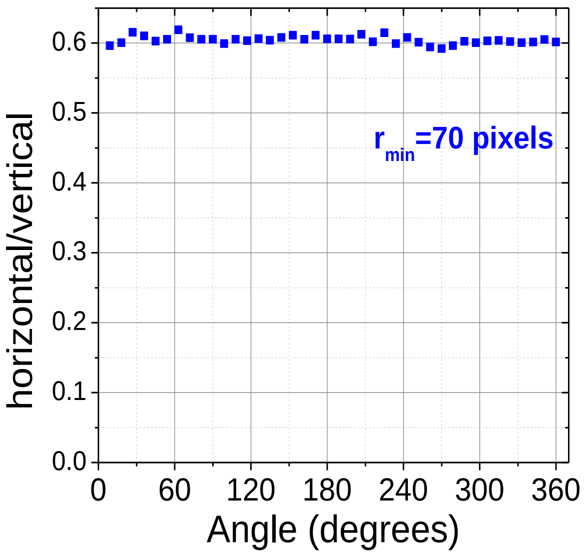

Figure 2.44: The ratio of the angular dependence for horizontal and vertical polarisation for r_{min} = 70 pixels. The ratio was found to be the same for the various radii shown in Figure 2.43 and a radius of 70 pixels was chosen.

In Edinburgh, the second harmonic (532 nm) from the YAG laser was used to ionise C_{60} in order to test the detector. Both the continuous and centroiding acquisition methods were used. This also served as a test to investigate the difference between the two acquisition methods. Recorded raw images and the corresponding inverted images (using BASEX) for laser pulse energies of 4 and 7 mJ are shown in Figure 2.45**.** The PES obtained from the inversion are presented in Figure 2.46 (mass spectra were also taken and are presented in section 2.7). The PES exhibit a structureless Boltzmann distribution, as expected from ns laser excitation, and apparent temperatures (see Equation (1.4) in Chapter 1) were fitted in Origin. For 7 mJ pulse energy the centroiding data gave an apparent temperature of about 0.31–0.35 eV while the continuous method produced a temperature of about 0.33–0.36 eV. The rather large uncertainty is due to the large amount of energy absorbed by the molecules resulting in non-exponential photoelectron distributions.

The centroiding images were taken for a high laser fluence, resulting in saturation in the detector centre. This is seen as the large discrepancy between the centroiding and continuous acquisition data at low kinetic energies (below 0.25 eV). The saturation occurs because two electrons hitting the same spot on the detector will only be counted as one electron in the centroiding method. In the data taken with lower pulse energy (4 mJ) and using the centroiding method, the photoelectron distribution exhibits a linear behaviour all the way to zero kinetic energy, as is expected. The data were also taken with a lower oven temperature which further reduces the signal. The fitted slope for the 4 mJ distribution is 0.292 ± 0.005eV. The data presented in Figure 2.45 and Figure 2.46 taken with the centroiding technique are not smoothed. A comparison of spectra obtained after smoothing the raw data is presented in Figure 2.47. It is concluded that the smoothing procedure does not influence the overall behaviour of the photoelectron distribution.

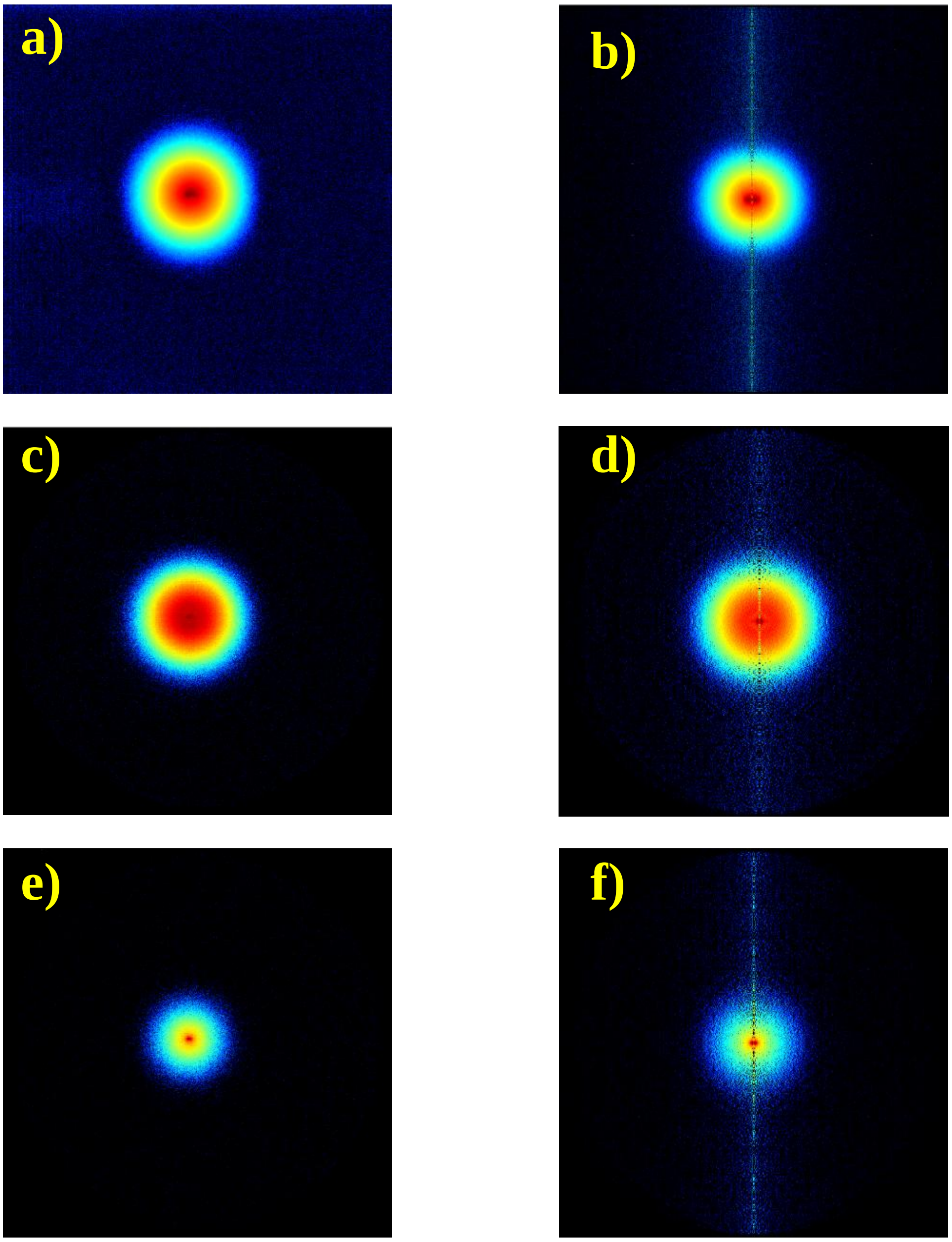

Figure 2.45: Raw (left) and inverted VMI images (right) using BASEX after 532 nm, ns laser excitation of C_{60}. a–b) Continuous acquisition for a laser pulse energy of 7 mJ. c–d) Centroiding acquisition and 7 mJ pulse energy. e–f) Centroiding and pulse energy 4 mJ.

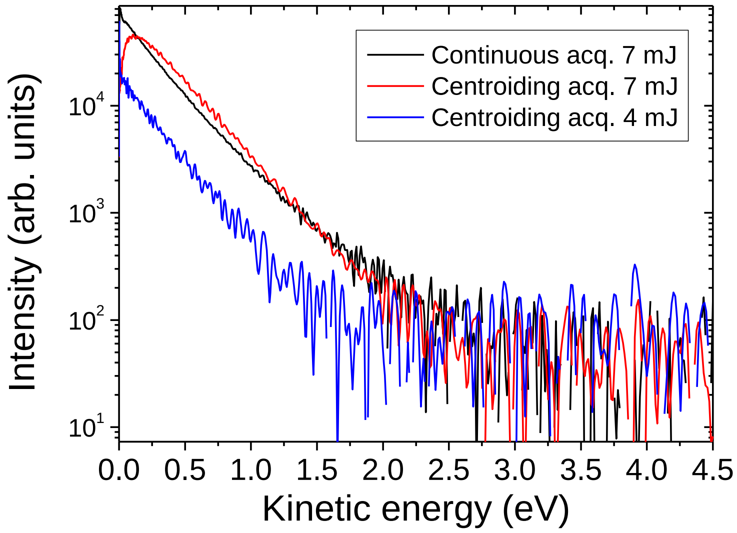

Figure 2.46: PES from the VMI images shown in Figure 2.45 obtained after ionising C_{60} using 532 nm, ns laser excitation.

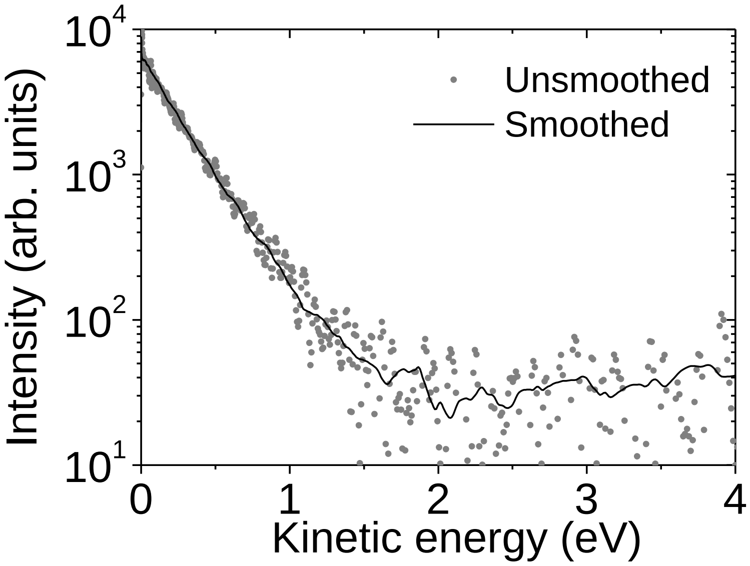

Figure 2.47: PES obtained from different amount of smoothing applied to the raw data inverted using BASEX. Data obtained after ionising C_{60} using ns, 532 nm laser excitation with a pulse energy of 4 mJ.

The angular dependences of the raw data were also investigated in the same way as the data taken in Gothenburg were. The result is presented in Figure 2.48 a) for both the continuous and centroiding methods taken with 7 mJ pulse energy. As expected, the centroiding method is less sensitive to any inhomogeneity in the detector. However, averaging over the four quadrants in the raw image shows that also the continuous acquisition method produces homogeneous detection efficiency. The PES from the inverted VMI images are presented in Figure 2.48 b) for 10 degrees angular segments. The distributions are identical for all angles which indicates that the detector and acquisition methods are working in a satisfactory manner.

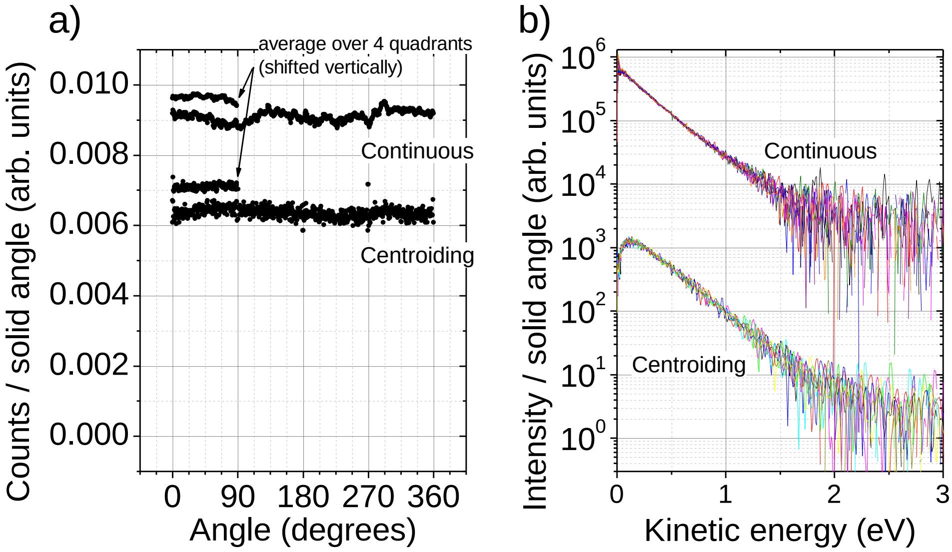

Figure 2.48: a) Number of counts per steradian plotted as a function of polar angle. Only pixels outside a radius of 70 pixels (corresponding to 0.2 eV) were included since the centroiding spectrum is saturated for lower radii and would therefore introduce an artefact in the comparison. In Figure 2.46 it can be seen that the signal is no longer discernable from background noise and therefore an outer cut-off radius was chosen at 300 pixels (corresponding to 4 eV). Averages over the four quadrants are also shown (shifted vertically for display purposes). b) Angle resolved PES per solid angle for polar angles intervals of 10 degrees from 10–90 degrees. The PES for the two measurement techniques have been shifted vertically with respect to each other.

2.7 Mass spectrometry

To investigate the species of ions created in a photoionisation experiment a mass spectrometer can be utilised. There are various types of mass spectrometers, and in this work a linear time-of-flight (TOF) mass spectrometer is used with a Wiley-McLaren extraction zone [78]. The principle behind the detector is based on extracting ions from the ionisation spot with an applied electric field and then allowing them to propagate a known distance under field-free conditions. The distance is field free so that the ions can propagate without being accelerated. By measuring the time of flight, the charge to mass ratio can be determined using the fact that the gained electrostatic energy is the charge of the ion times the accelerating potential. The ions are accelerated with two electrodes (one repeller (HV_1) and one grounded (G_2)). However, the region of ionisation is not a point source and there is some geometrical spread in where the ions are created between the two electrodes. By introducing a third electrode (labelled HV_2 between HV_1 and G_2 and at a lower potential than HV_1, the Wiley-McLaren assembly compensates for this spread. The ions created near the field free region will gain a lower energy (sum of potential and kinetic energy) than the ones created with the same initial momentum far away. This means that the latter will have a higher velocity when entering the field free region. After some time the ions created far from the drift region will approach the slower ones. The extraction voltages can be adjusted so that this occurs exactly when the ions collide with the detector. Thus the difference in flight time for ions created in different areas in the interaction zone with the same charge to mass ratio and with the same initial momentum will be compensated for. In other words, spatial focusing is achieved by adjusting the extraction voltages. This is illustrated in Figure 2.49. To achieve a smoother potential drop between HV_2 and ground a fourth electrode is introduced $HV_2/2$. A schematic figure of the electrode assembly is shown in Figure 2.22. Typical voltages applied in the experiments are HV_1 = 2000 kV and HV_2 = 714 V. The best HV_2 voltage is found by optimising the resolution for either a xenon or C_{60} mass spectrum. The measured time-of-flight spectrum is converted into a mass spectrum using the program *mass_spec.m* (appendix). The Jacobian ($1/\sqrt{m/q}$) needed to transform a time-of-flight distribution into a mass-to-charge distribution is not included in the mass spectra presented in this thesis for aesthetic reasons (since it magnifies noise at low mass-to-charge ratios).

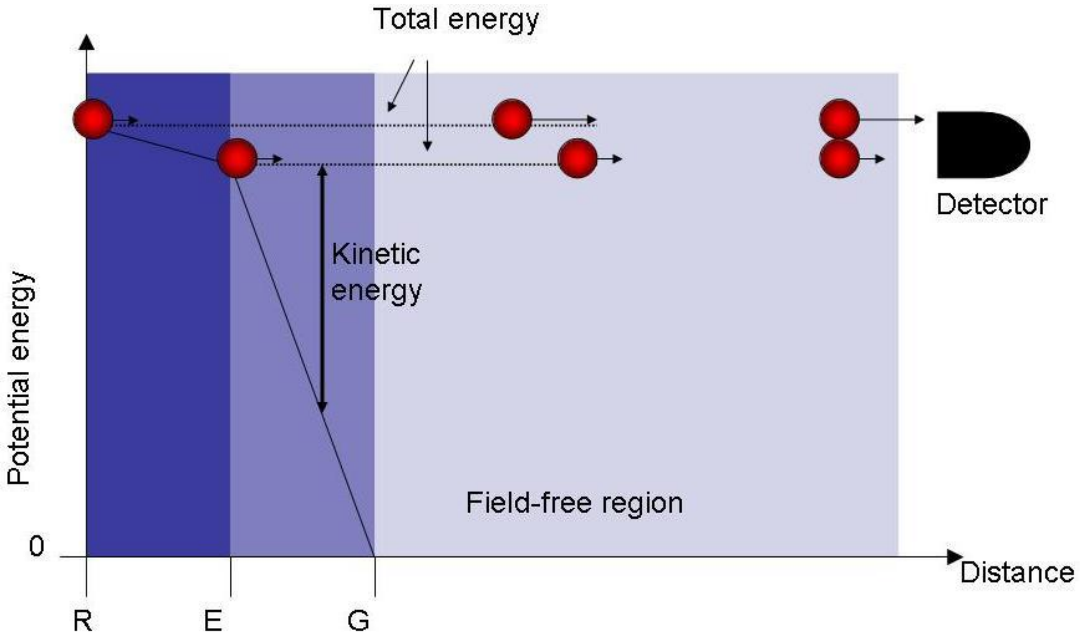

Figure 2.49: Schematic illustration of spatial focusing achieved by the Wiley-McLaren extraction assembly. The repeller electrode (R) is at a slightly higher potential than the extractor (E). Ions created with the same initial momentum (here equal to zero) but in different regions in the extraction zone will not gain the same total energy. This leads to a higher velocity for ions created far away from the detector compared to the ones created at a closer distance. By adjusting the potential difference between R and E, all ions will arrive at the detector simultaneously.

A commercial MCP detector (Jordan TOF Products Inc., part no. C-0701) was used to record the ion signal and was kindly lent by the Scottish Instrumentation and Resource Centre for Advanced Mass Spectrometry (SIRCAMS). The detector consists of a pair of Chevron-style MCPs that were replaced during the installation with a pair of fresh new plates (Photonis USA, part no. MCP 18/12/5 D 40:1 (PS30220)). The maximum voltage that can be applied over each plate is 1 kV. The voltage over the MCPs is controlled by a voltage divider supplied with the detector. A schematic drawing of the detector assembly is shown in Figure 2.50. The electron current produced by each ion impinging on the detector is directed on to an anode by static electric fields.

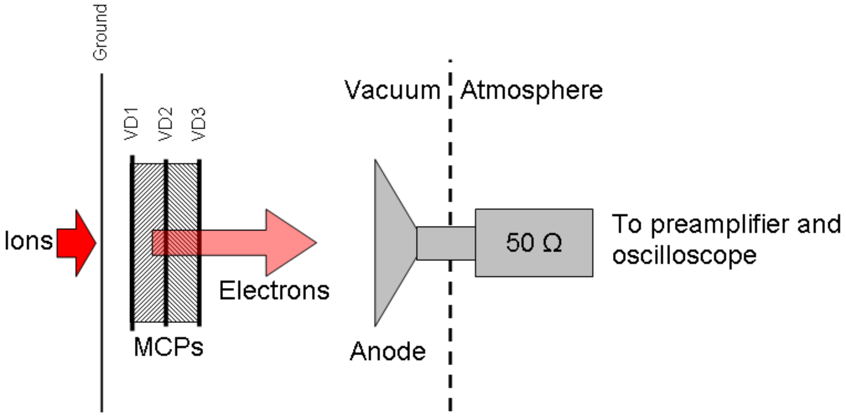

Figure 2.50: Schematic drawing of the ion detector. Typically a voltage of –4.3 kV is applied to the voltage divider resulting in voltages applied over the electrodes VD1,2 and 3 to be –1946, –1061 and –176 V. Cations are accelerated towards the first MCP because of the negative potential of VD1. When the ions collide with the walls of the MCP pores they produce an avalanche of electrons which are directed towards the other MCP due to the less negative potential of VD2. A similar process occurs in the other MCP. The electron pulse is then accelerated towards the anode where they are subsequently amplified in a preamplifier and then directed into an oscilloscope.

The anode is connected to an electrical feedthrough that is terminated in a 50 Ω N-plug on the atmosphere side of the vacuum chamber. An N-plug to BNC adaptor is used to connect a 1.8 GHz preamplifier (TA1800, FAST ComTec) to the detector output. The output signal is amplified ten times in the preamplifier and then passed on to a digital 500 MHz oscilloscope (MS06054A, Agilent Technologies capable of measuring 4×10^9 samples per second) via a BNC cable. The oscilloscope is triggered by the signal from the photodiode inside the Legend (see section 2.4.2) when using femtosecond pulses or from a trigger output on the YAG laser. The oscilloscope is connected to a computer via a USB cable and controlled by a LabView program (*Mass_spec.vi*, see appendix). Usually 200 spectra are accumulated in the oscilloscope before the data is sent to the computer. Typically 100–1000 accumulations are added together in the computer. A mass spectrum taken after ionisation of xenon with the fundamental output of the Legend is presented in Figure 2.51. Corresponding mass spectra for the VMI images presented in Figure 2.45 are shown in Figure 2.52.

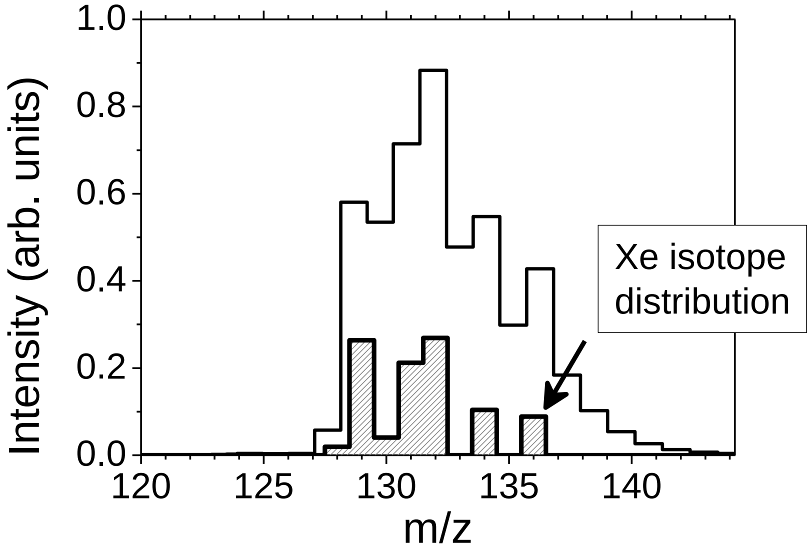

Figure 2.51: Mass spectrum obtained after ionisation of xenon using 800 nm, 120 fs laser light with an intensity of (1.9 ± 0.2) × 10^{13} W/cm^2. Only a small part of the spectrum is shown where singly charged xenon ions are seen. The isotopic distribution can almost be resolved at this mass range. The isotope distribution of xenon is shown below the measured mass spectrum.

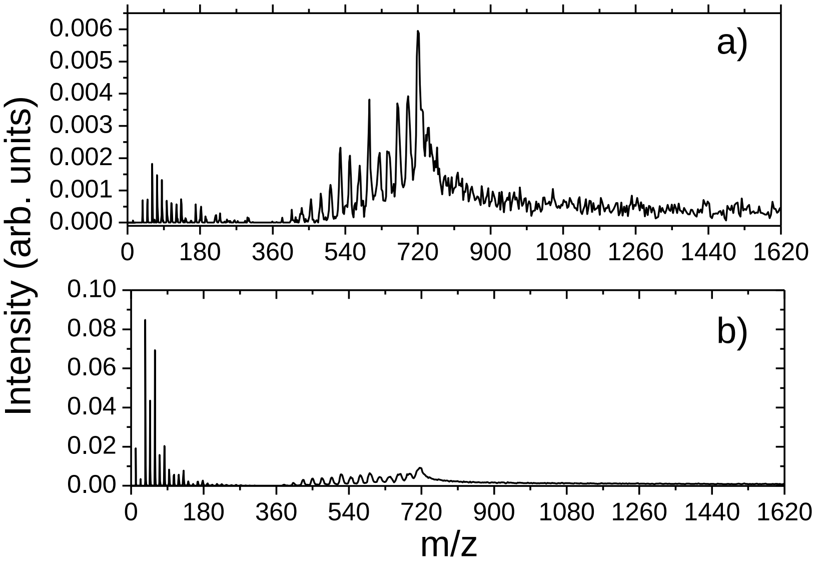

Figure 2.52: Mass spectra of C_{60} corresponding to the VMI images shown in Figure 2.45 after 532 nm, ns laser excitation and pulse energy a) 4 mJ and b) 7 mJ. For the highest pulse energy very few intact parent ions are seen due to the large energy absorbed by the molecules.

2.8 Possible improvements of experimental apparatus

From the analysis of the various tests performed on the apparatus it is concluded that it is working in a satisfactory manner. There are however some changes to the setup that could improve the performance of the apparatus. An additional mu-metal cylinder could be installed inside the mounting rods of the ion optics (see Figure 2.21). At the moment, the mounting rods are inside the mu-metal cylinder. Since they are made from stainless steel which can contain magnetic domains they can disturb the path of the electrons. The slight ellipticity seen in the VMI images could be the result of this effect. Another improvement would be to install a shutter for the molecular beam source. At the moment the only way to stop the molecular beam is to turn down the oven temperature. On the other hand, both VMI images and mass spectra are taken on a regular basis when the oven is turned off and no signal is detected. However, it would be more convenient not having to wait for the oven to cool in order to do background measurements.

Chapter 3 – Thermal electron emission from fullerenes

3.1 Introduction

In this section, energy redistribution in fullerenes after ultrafast laser excitation is discussed. As mentioned in the introduction, the large number of delocalised valence electrons of C_{60} should imply a quick redistribution of excitation energy due to intramolecular vibrational-energy redistribution (IVR) and intersystem crossings in photoionisation experiments. Energy redistribution in fullerenes has been studied previously with photoelectron spectroscopy (see e.g. [6, 29, 79]). In this thesis, complementary studies are presented using angle-resolved photoelectron spectroscopy. Ultrafast energy relaxation can be investigated using angle-resolved photoelectron spectroscopy which for example was recently studied in a polyatomic anion by Lecointre *et. al.* using velocity-map imaging [80]. By using a simple model the authors could extract the lifetime of the first excited state from the measured PADs. Angle-resolved photoelectron spectroscopy was successfully used in ref. [81] to separate direct from statistically emitted photoelectrons. However, the large number of degrees of freedom of C_{60} makes it difficult to monitor the redistribution process through state-specific spectroscopy. It is therefore reasonable to use statistical models just like the ones used to describe phenomena in the solid state. This is further justified because of the high temperature of the molecules in the effusive beam which reduces the energy level spacing because more vibrational levels are populated which in turn reduces finite-size effects (which was shown for sodium clusters in ref. [41]). For electronically excited molecules it may be justified to treat the 240 valence electrons of C_{60} as a Fermi gas confined in a potential well on the surface of a sphere. This treatment, also called the jellium model, is justified because it can be used to reproduce several measurable physical quantities (see e.g. [5] and references therein). In this chapter a brief introduction to the transient thermal electron emission model, based on such a treatment as mentioned in the introduction, is presented, followed by experimental results obtained both in Gothenburg and Edinburgh.

3.2 Transient thermal electron emission

The emission of electrons after ns excitation results in a structure-less photoelectron spectrum. This can be described with the principle of detailed balance which was first introduced to describe neutron emission from excited nuclei [82]. It is based on microreversibility which means that the probability of going from quantum state a to b is the same as going from b to a. The model is also based on statistical equilibrium with the conservation of energy and angular momentum [30]. The first assumption implies that one can relate the process of electron emission to the process of electron capture. If the level density of the parent ρ_{parent} is much smaller than the level density of the products $\rho_{product}$ (e.g. a daughter ion and a free electron) the decay rate k_{decay} is larger than the formation rate $k_{formation}$. This is simply because there are more available states for the products and since one assumes statistical equilibrium all states have equal probability. Detailed balance gives the following relation

$$\frac{\rho_{products}}{\rho_{parent}} = \frac{k_{decay}}{k_{formation}}. \tag{3.8}$$

The key idea of applying this equation to thermionic emission from fullerenes is that the rate for the reverse process (electron capture) can be estimated [30] and gives the following equation for the decay rate

$$k(E,\varepsilon)d\varepsilon = \frac{2m}{\pi^2\hbar^2}\sigma_c(\varepsilon)\frac{\rho_d(E-IP-\varepsilon)}{\rho_p(E)}d\varepsilon \tag{3.9}$$

where $k(E,\varepsilon)$ is the rate of electron emission in energy interval $d\varepsilon$ with electron kinetic energy ε when the parent is excited with energy E, m is the electron mass, $\sigma_c(\varepsilon)$ is the electron capture cross section, IP is the binding energy of the parent and ρ_p and ρ_d are the parent and daughter level densities. By expanding the daughter level density one can show that

$$k(E,\varepsilon)d\varepsilon = \frac{2m}{\pi^2\hbar^2}\sigma_c(\varepsilon)\frac{\rho_d(E-IP)\exp(-\varepsilon/\mathrm{k_b}T_d)}{\rho_p(E)}d\varepsilon \tag{3.10}$$

where T_d is the microcanonical temperature of the daughter at energy E–IP and $\mathrm{k_b}$ is the Boltzmann constant. A microcanonical temperature is used since gas phase fullerenes can be considered as isolated systems in the high vacuum typically used in experiments. Of course, in an experiment, contributions from isolated fullerenes with different excitation energies will be present but still Boltzmann-like spectra are seen. Therefore, one usually uses the apparent temperature T_a defined in Equation (1.4) in chapter 1 to characterise the measurement. The model used for thermionic emission is that the fullerenes absorb a large number of photons incoherently. The time between each absorption event is larger than the time it takes for the absorbed energy to be distributed to vibrational degrees of freedom. Thus the fullerenes become heated during the laser pulse and apparent temperatures up to 3000–4000 K are observed [4].

For shorter pulse durations the typical bimodal distribution seen in a ns mass spectrum is replaced by multiple charged species and their fragments (while keeping the fluence constant). This behaviour has also been observed in high-energy electron impact studies where the energy is transferred during a short period of time [83]. It is believed that for shorter interaction times the energy does not have time to couple to vibrations and the excess energy absorbed by the fullerenes is mainly quenched by electron emission. Photoelectron spectra acquired with a 180 fs laser with wavelength of 800 nm still yield a thermal distribution but with direct ionisation components. However, the apparent temperature compared to ns experiments is significantly higher (tens of thousands of Kelvin). This has been explained as a non-equilibrium situation where energy is deposited into the electronic system of the fullerene [6, 29]. This occurs while the vibrational degrees of freedoms are not excited. The absorbed energy is equilibrated among the electronic degrees of freedom by electron-electron coupling resulting in a thermal electron emission. Detailed balance was successfully applied in ref. [29] to describe total ion yields and photoelectron spectra as a function of laser fluence. Energy was assumed to be dissipated from the hot electronic system to the vibrational degrees of freedom by an exponential decay with a time-constant of 240 fs. Calculated rates for the case when only electrons are excited (called transient thermal electron emission) are compared to the thermionic case in Figure 3.1. The rate for the transient electron emission suggests that electrons are emitted on a ps to fs time scale which means that molecules cool before energy has coupled to vibrations.

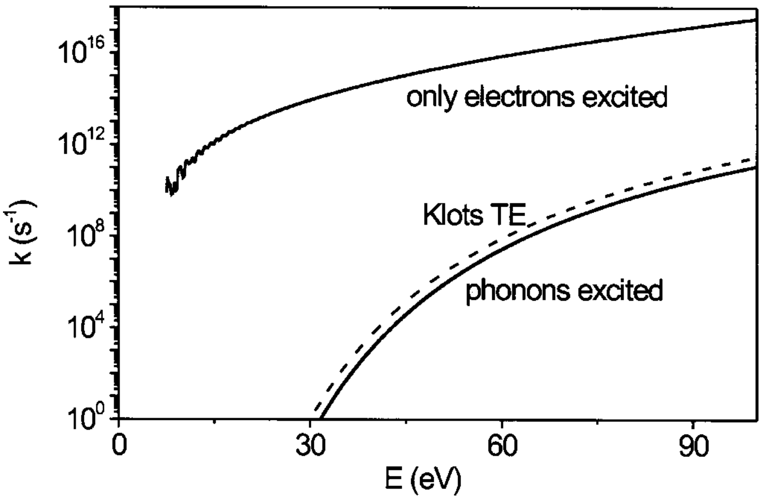

Figure 3.1: Electron emission rates for transient thermal electron emission and thermionic emission. A comparison of calculated rates from a frequently used rate equation by Klots is also presented [84]. Figure from ref. [29].

Detailed balance has also been applied successfully to femtosecond ionisation of sodium clusters [45] where a structureless thermal photoelectron spectrum was measured. Similarly, a thermalisation of the electronic system of transition metal clusters (Ni_n^- Pd_n^- Pt_n^- n=3–7) has been proposed (see review in ref. [85]). In these studies a thermalisation time constant[2] between 40–90 fs depending on the cluster size was observed. In bulk metals, the typical timescale for thermalisation of the electronic system is 10 fs [85]. When going from bulk metals to clusters containing a few atoms, the density of states is reduced. Since there are fewer states available for the electrons it is expected that the coupling time is increased which is indeed observed with the smaller transition metal clusters. However, detailed balance was never discussed in ref. [85]. Laarmann and colleagues used a similar interpretation of experiments where Ar clusters containing 70–900 atoms were irradiated with femtosecond pulses at 95 nm wavelength from a free-electron laser [86]. Photoelectron spectra measured after 780 nm, 170 fs pulse exposure of anthracene [46] showed a structure-less spectrum similar to what is seen for C_{60} [6, 29]. However, the authors concluded that the observed spectra were the result of field ionisation. Since the transient thermalisation model has successfully been applied to C_{60} with similar pulse

---

[2] This is not the electron-phonon coupling time but the time it takes to reach thermal equilibrium within the electronic system.

duration and wavelength it might also be used for smaller organic molecules. In the studies of transition metal clusters mentioned above it was found that the density of states was a critical factor for thermalisation. Ongoing research in Gothenburg is trying to answer the question of how small an organic molecule can be while still showing behaviour that can be interpreted in the context of the transient emission model. Some results from experiments obtained in collaboration with Mikael Kjellberg, Motoshi Goto, Alexander Bulgakov and Klavs Hansen in the Gothenburg lab are presented in this chapter.

3.3 Results and discussion

Results for mass spectra and angle-resolved PES for 400 and 800 nm with pulse durations ranging from 130 fs to 5 ps are presented below for C_{60} and C_{70}. The data were inverted using either BASEX or the onion-peeling algorithm because no assumption about the angular distribution is needed for the inversion procedure.

3.3.1 400 nm laser excitation

Results obtained for different laser intensities for 400 nm, 130 fs ionisation of C_{60} are presented in Figure 3.2 and Figure 3.3. In the figures, VMI images inverted using BASEX are presented together with corresponding mass spectra and angle-resolved PES for 10 degrees angular segments for 10–90 degrees. As previously reported by Boyle *et. al.* [7] a series of peaks are seen superimposed on an structureless background that can be well described by an exponential distribution. The 80–90 degrees angular segments have the least amount of structure of all the segments and therefore an exponential distribution was fitted to this data set. The fits were made by eye because the residual peak structure seen would interfere in a least-square fitting procedure. The apparent temperatures extracted from the fits were 1.15 ± 0.06 eV and 1.08 ± 0.05 eV and are shown as dashed lines in Figure 3.2 (middle). Exponential distributions with the same temperature could be fitted to all the other angle-resolved spectra. As expected from a statistical ionisation mechanism, electrons are emitted isotropically.

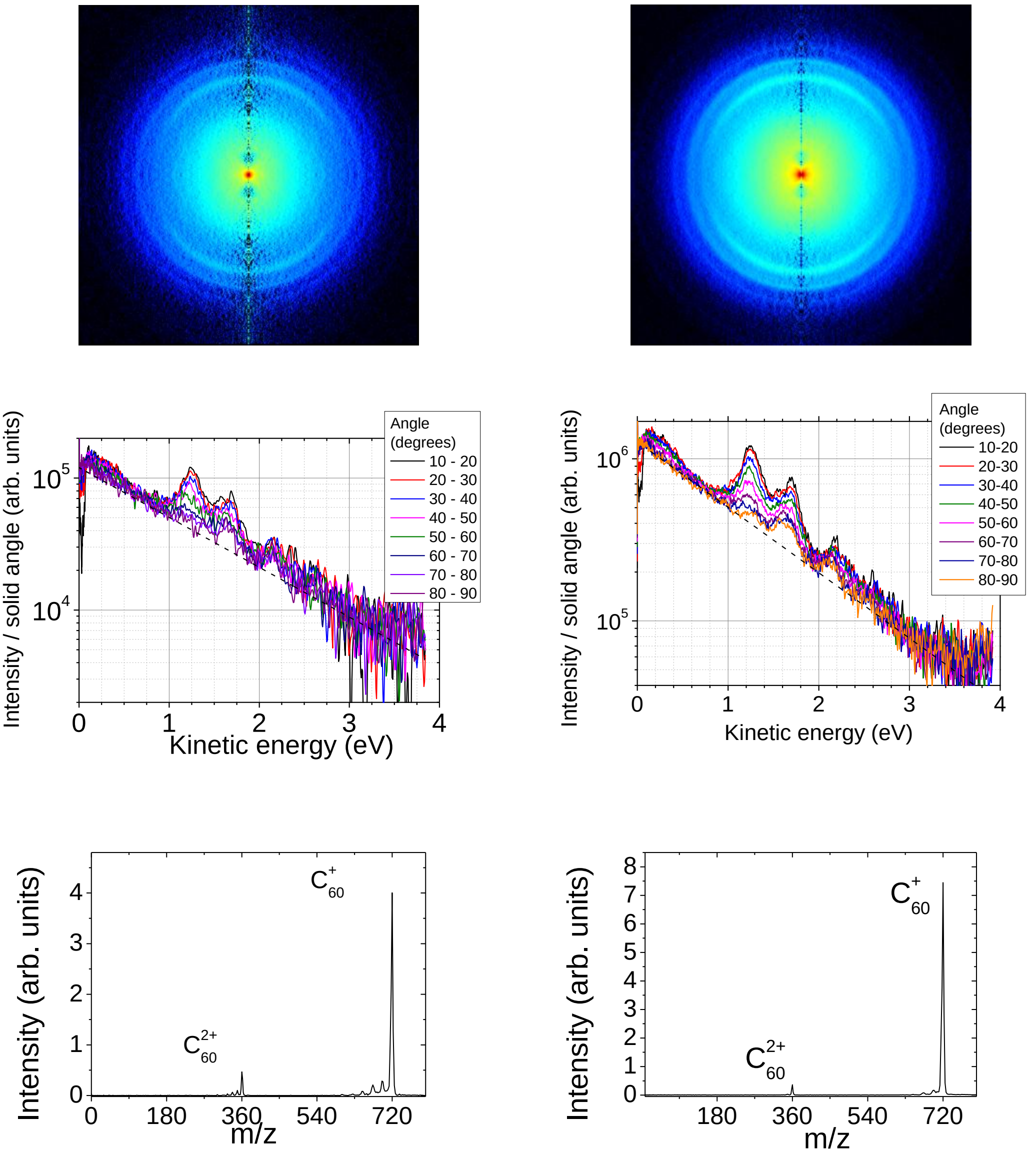

Figure 3.2: Inverted VMI images in logarithmic intensity scale for C_{60} ionised with 400 nm, 130 fs and intensities $(6 \pm 3) \times 10^{11}$ W/cm^2 using a lens with focal length 30 cm (left column, top) and $(3 \pm 1) \times 10^{11}$ W/cm^2 using a lens with 50 cm focal length (right column, top). Both images were accumulated using the continuous acquisition method and inverted using BASEX. The pattern seen in the very centre of both images is due to a damaged area in the detector. The damage is not important for the present discussion but does influence some of the results presented in the next chapter where the detector damage is further characterised. (Middle) Angle-resolved PES with an exponential distribution fitted to the 80–90 degrees angular segment (dashed line). Fitted apparent temperatures were 1.15 ± 0.06 eV (left) and 1.08 ± 0.05 eV (right). (Bottom) Corresponding mass spectra for the two different laser intensities.

For lower laser intensities the photoelectron signal becomes too weak and disappears in the noise level when using the continuous acquisition method. Therefore, experiments were done using the centroiding acquisition method for a low laser intensity of (1.4 ± 0.7) × 10^{11} W/cm^2. Both C_{60} and C_{70} were studied. The results for C_{60} are presented in Figure 3.3 and Figure 3.4. The result for C_{70} using a laser intensity of (1.3 ± 0.6) × 10^{11} W/cm^2 was very similar and is presented in the appendix (Figure F-1). Due to the low signal, the raw data had to be smoothed before it was inverted (as described in chapter 2). Fitted apparent temperatures were 0.98 ± 0.08 eV for C_{60} and 0.97 ± 0.05 eV for C_{70}. Little structure for C_{60} and no structure for C_{70} were seen for the 80–90 degrees angular segments and therefore the exponential fits were done for this segment.

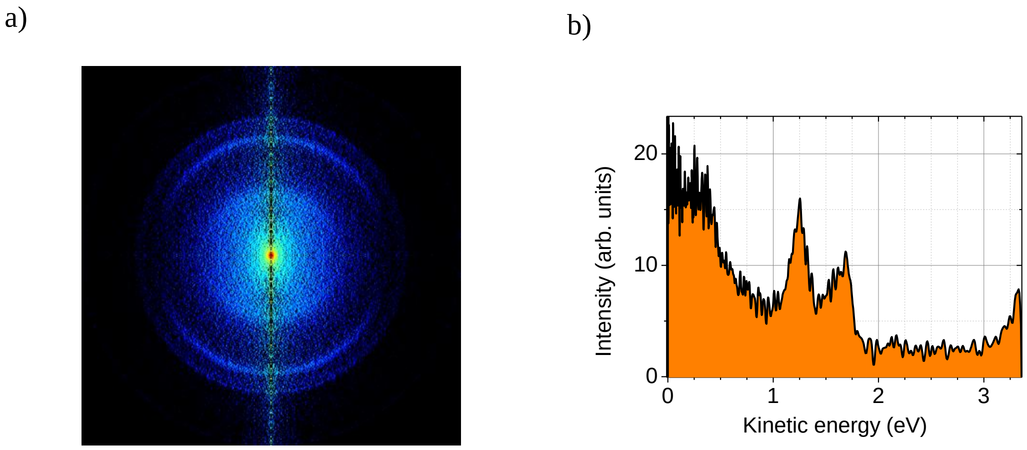

Figure 3.3: a) Inverted VMI image using BASEX of C_{60} ionised with 400 nm, 130 fs laser pulses of intensity (1.4 ± 0.7) × 10^{11} W/cm^2. The centroiding accumulation method was used. b) Angle-integrated PES from the inverted image in a).

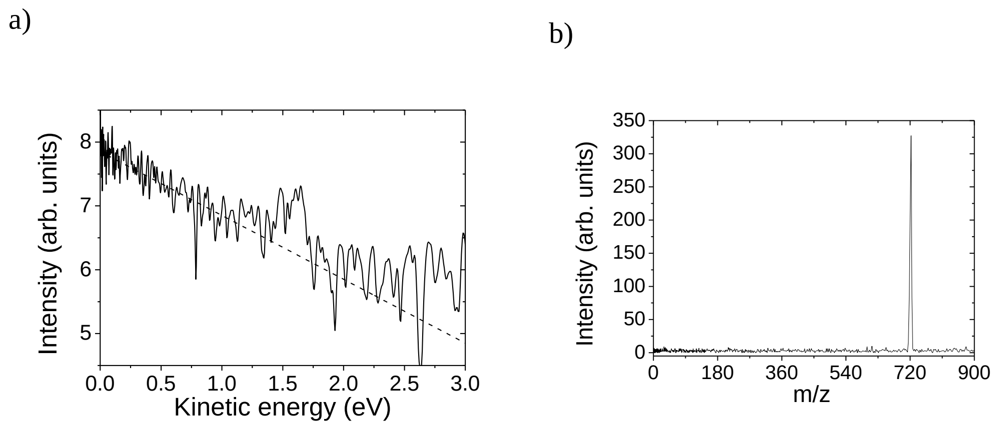

Figure 3.4: a) Angle-resolved PES for 80–90 degrees angular segment for the inverted VMI image presented in Figure 3.3 obtained after 400 nm, 130 fs laser excitation of intensity (1.4 ± 0.7) × 10^{11} W/cm^2. An exponential fit was made in *Origin* to the 80–90 degrees angular segment (dashed line) resulting in an apparent temperature of 0.98 ± 0.08 eV. b) Corresponding mass spectrum showing that for the low laser intensity used, only singly charged C_{60} was produced.

Angle-resolved PES from experiments using bandwidth limited ps pulses from the SHBC are presented in Figure 3.5 for three different pulse energies. The mass spectra for these pulse durations are identical to the ns experiments presented in Chapter 2. The three different pulse energies resulted in very similar VMI images and therefore only a typical inverted VMI is shown in Figure 3.5. At the highest power some structure is seen above 1 eV which was also seen for the short-pulse experiments and will be discussed in more detail in Chapter 4. It can be concluded from the mass spectra, PES and PADs that for the laser conditions used in this experiment, the main ionisation mechanism is thermionic emission.

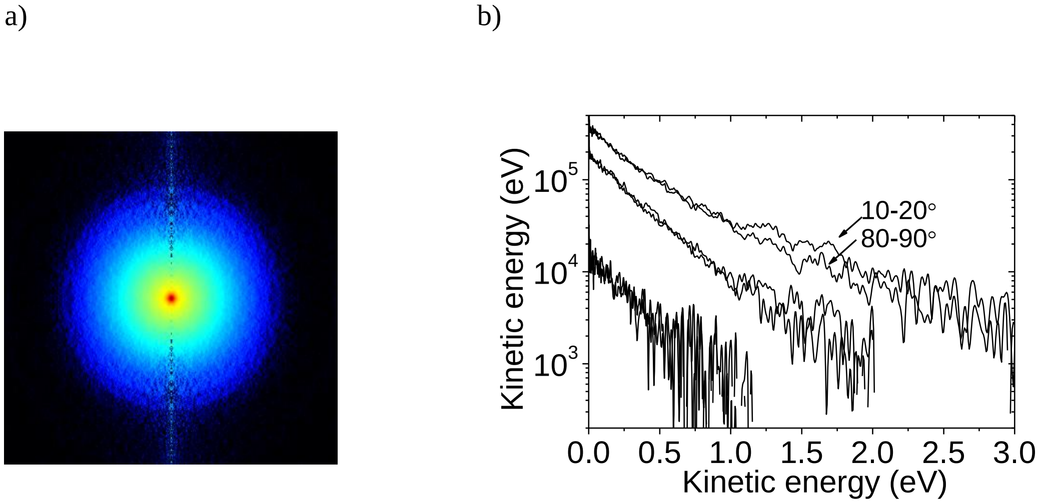

Figure 3.5: a) Inverted VMI images taken with the SHBC (401 nm, 5 cm^{-1}, 4–5 ps pulse duration) and a pulse energy of 6 μJ. b) Angle-resolved PES for 10–20° and 80–90° angular segments for pulse energies (from bottom to top) 1.6, 4.1 and 5.9 μJ.

3.3.2 800 nm laser excitation

In contrast to using 400 nm laser light, it is more difficult to pump energy into the molecule when using 800 nm because there is no allowed transition for 800 nm from the electronic ground state. Therefore a two-photon absorption is needed which is much less probable than the one-photon process in the 400 nm case. Therefore the intensities used in these experiments are typically one order of magnitude higher than in the 400 nm experiments. A longer wavelength also implies a smaller Keldysh parameter which is indicative that the intensity is approaching the field ionisation regime. As discussed in the introduction, a structure-less PES is not sufficient evidence for thermal electron emission and could instead be the result of field ionisation. In order to attempt to distinguish between the two ionisation mechanisms, a VMI detector was installed in Prof. Campbell's lab in Gothenburg. I was involved in some of the initial experiments although my main contribution to the work (presented in ref. [28]) was writing a VMI inversion program implementing the onion-peeling algorithm [87]. The program was written as a part of my Masters project in Sweden and was improved during my first year as a PhD student in Edinburgh. Results from the Gothenburg lab obtained in collaboration with Mikael Kjellberg (who did the data analysis), Alexander Bulgakov and Klavs Hansen are presented in the first section. At a first glance, the VMI data obtained using femtosecond laser pulses (Figures 4 and 4) are clearly different from VMI images taken with nanosecond lasers, e.g., Figure 2.45

in chapter 2. The PADs are not isotropic. More electrons are ejected along the laser polarisation direction for the femtosecond case. The data presented in the last part of the results section for 800 nm were all acquired in Edinburgh and concern the newly observed asymmetry. The asymmetry results are also compared to calculations made by Juraj Fedor and Jakob Stenfalk.

3.3.2.1 Angle-integrated PES

Raw and inverted VMI images obtained in the Gothenburg lab are presented in Figure 3.6 and Figure 3.7 after 780 nm, 150 fs laser excitation for both C_{60} and C_{70}. Experiments were performed for different laser powers and the PES obtained after inversion are presented in Figure 3.8 for C_{60} together with a typical mass spectrum. Similar spectra are presented for C_{70} in Figure 3.9. The ring structure seen in the VMI images corresponds to the structure seen in the PES below photoelectron kinetic energies equal to the photon energy (1.6 eV). The structure is the same set of peaks, although unresolved, discussed in Chapter 1 and is thought to originate from one-photon ionised Rydberg states (discussed further in chapter 4).

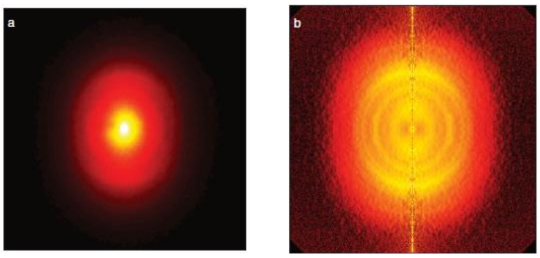

Figure 3.6: Raw (a) and inverted (b) data of C_{60} taken in Gothenburg using a Ti:Sapph laser (780 nm, 150 fs and fluence 1.84 J/cm^2). Figure from ref. [28].

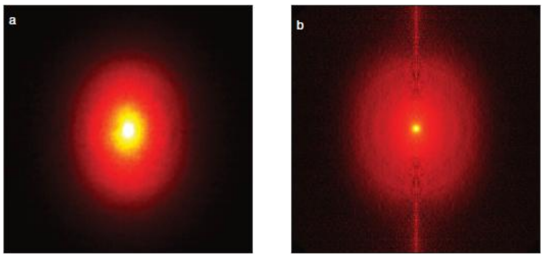

Figure 3.7: Raw (a) and inverted (b) data of C_{70} taken in Gothenburg using a Ti:Sapph laser (780 nm, 150 fs and fluence 1.84 J/cm^2). Figure from ref. [28].

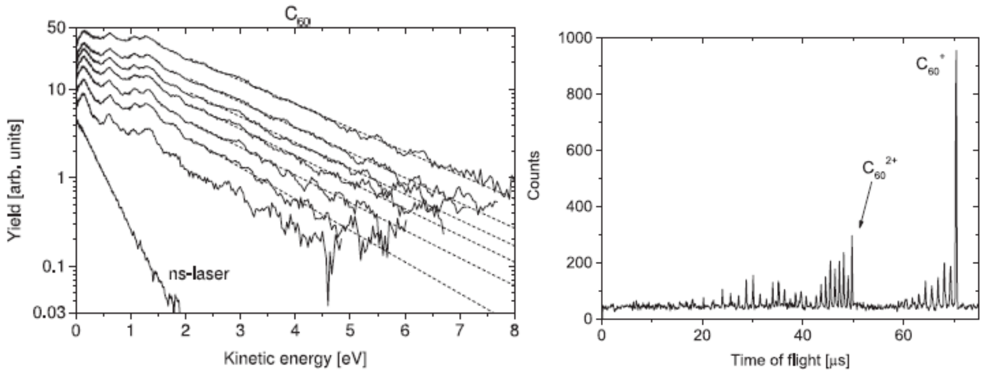

Figure 3.8: Left) Angle-integrated PES spectra obtained for different laser fluences (top to bottom: 2.2, 1.8, 1.7, 1.6, 1.4, 1.3 and 1.1 J/cm^2) with 780 nm, 150 fs laser excitation. A spectrum obtained after ns laser excitation from a N_2 laser is also shown for comparison. Right) Mass spectrum taken with a fluence of 1.1 J/cm^2. Figure from ref. [28].

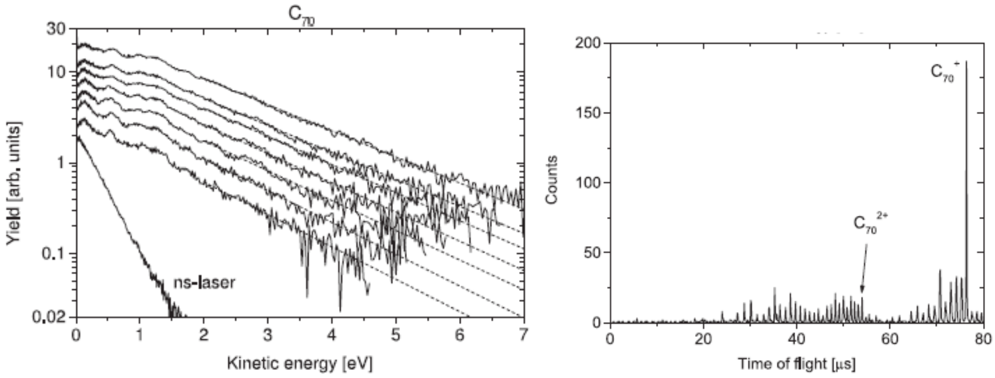

Figure 3.9: Same as in Figure 3.8 but for C_{70}. (Left) Angle-integrated PES spectra obtained for different laser fluences (top to bottom: 2.2, 1.8, 1.7, 1.6, 1.4, 1.3 and 1.1 J/cm^2) with 780 nm, 150 fs laser excitation. A spectrum obtained after ns laser excitation from a N_2 laser is also shown for comparison. (Right) Mass spectrum taken with a fluence of 1.1 J/cm^2. Figure from ref. [28].

The results for C_{60} are similar to the ones previously published using a linear time-of-flight photoelectron spectrometer [29]. When comparing the new data set with the previously published one it has to be kept in mind that a linear time-of-flight detects photoelectrons emitted within a small angular interval (about 5 degrees [88]). The results presented in ref. [29] were taken with the laser polarisation direction pointing towards the detector and hence the measurements recorded electrons emitted along the laser polarisation direction. The fitted apparent temperatures for both C_{60} and C_{70} are presented in Figure 3.10 (a) together with a comparison with the results in ref. [29] (dotted line). There is a linear dependence of apparent temperature on the laser fluence, which was also found in the previous study. The present study indicates that the transient thermal electron emission model can also be applied to C_{70}. The slightly lower temperatures measured for C_{70} are consistent with a larger heat capacity of the electron gas compared to C_{60} because there are more electrons to share the absorbed energy.

A series of experiments was also performed on C_{70} where the pulse duration was changed from 150 to 1528 fs. A direct ionisation mechanism depends on the laser intensity. This is for example the case for xenon (see experimental section) where a similar photoelectron spectrum is seen for different pulse durations and the only parameter that is important is the intensity of the laser (for pulses below a few ps). For a statistical ionisation mechanism the only parameter that should determine the photoelectron spectrum is the amount of energy absorbed. Therefore if it is a delayed (thermal) ionisation mechanism the shape of the spectra should depend predominantly on the laser fluence. In the latter case however, one has to consider that the electronic system of the molecule can reach temperatures high enough to ionise before the laser pulse has reached its peak value. But if the ionisation mechanism is a direct one, the same slope of the exponential photoelectron distribution should be measured for the same intensity (regardless of pulse duration). Results are presented in Figure 3.10 b) where it can be seen that several laser pulse durations for the same fluence give the same temperature. Also, data points taken with the same intensity but different pulse durations and therefore different fluences, give different temperatures. This suggests that it is the fluence rather than the intensity that is the important parameter in determining the shape of the PES. Therefore the data supports the proposed thermal model and it can be concluded that it is not a direct multiphoton or field ionisation mechanism that is responsible for the detected spectra. However, one can envision a combination of the various processes. For example, the electronic system of the molecule could be heated during the first part of the laser pulse. The system would then have a lower binding energy which would make it easier to field ionise at the peak intensity of the pulse.

A key feature of the transient thermal ionisation model is that the ionisation event can take place after the laser pulse has passed the sample. This is similar to thermionic emission although the electron emission in the latter case takes place on a much longer time scale (μs) which makes it possible to measure with a time-of-flight mass spectrometer. If the ionisation mechanism is delayed and has no memory of the laser pulse and the only parameter that decides the outcome of the experiment is the amount of energy absorbed, then this can be very important for coherent control experiments on complex molecules because under these conditions there can be no coherent control. If, on the other hand, there is a thermalisation of the absorbed energy but the ionisation mechanism is direct, it might still be possible to control the outcome of the experiments by adjusting the laser characteristics. It could therefore be more important to determine whether the ionisation is actually delayed or not than whether the energy is thermalised. The present experimental results do not answer the question whether the ionisation mechanism is delayed or not but indicate that the molecules interact with the laser pulse in a way that depends on the laser pulse duration. Possible experiments to measure if molecules are ionised after the laser pulse has passed the sample are discussed in section 3.5.

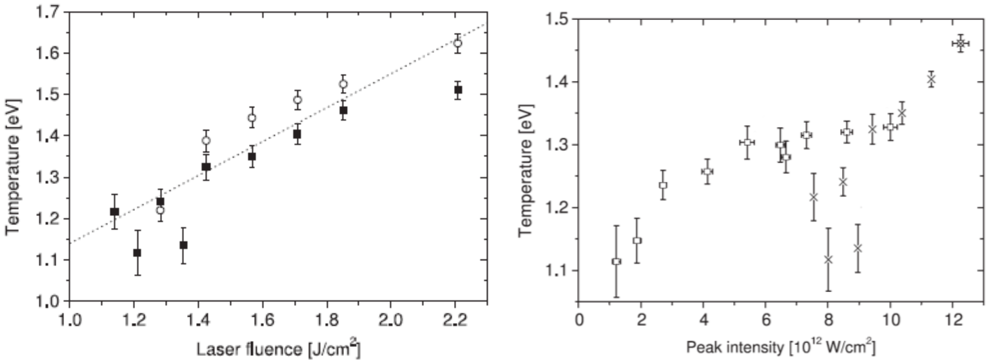

Figure 3.10: (Left) Fitted temperature as a function of laser fluence. Open symbols, C_{60}; filled, C_{70}. A fit made to experimental data from ref. [29] is also shown (dotted line). (Right) Temperature as a function of laser intensity for different pulse durations but with constant fluence (squares). The lowest intensity corresponds to 1528 fs and highest to 150 fs. Data points for different intensities but laser pulse duration fixed to 150 fs are also shown (crosses). Error bars are from least-square fits made in Origin. Figures from [28].

From the Gothenburg experiments there is an argument that speaks against the thermal ionisation mechanism which is the anisotropy seen in the VMI images in Figure 3.6 and Figure 3.7. Field ionisation of small molecules and atoms typically results in PADs strongly polarised along the laser polarisation (see e.g. ref. [74]). However, the results presented above do not indicate a field ionisation mechanism. It is therefore possible that another mechanism is responsible for the detected asymmetry which will now be discussed.

If the ionisation is statistical there should be no memory of the polarisation direction of the laser pulse and the PADs should be isotropic. This was seen for the 400 nm experiments and in the ns experiments presented in Chapter 2 where a thermionic ionisation mechanism is dominant. There is a difference between the emission time scales for transient thermal electron emission and thermionic emission. This can be seen in Figure 3.1 where the bulk part of the thermal electrons will be emitted during the laser pulse. It is therefore possible that the laser pulse might influence the PADs although the ionisation mechanism can still be regarded as statistical. To do a careful study of the asymmetry it is desirable to perform the experiments for laser powers where only singly charged intact parent fullerenes are seen in the mass spectra. This would ensure that only electrons from neutral fullerenes contribute to the measured PES. The vacuum conditions in the Gothenburg lab are such that the signal for low laser powers disappears in the noise level. Therefore, the study was carried out in the Edinburgh lab where the apparatus can achieve much better vacuum conditions and the laser is more stable. The next section presents data for various pulse durations, wavelengths and pulse energies, collected together with Gordon Henderson. The data are compared to a modified version of the transient thermal electron model where the presence of the electric field of the laser is taken into account. This results in what can be called a field-assisted thermal electron emission.

3.3.2.2 Angle-resolved PES

To investigate the anisotropic PADs further a series of experiments was carried out on C_{60} for pulse durations of 130 fs to 3.8 ps. Angle-resolved PES for polar angle intervals of 10–20 and 80–90 degrees are presented in Figure 3.11 for C_{60} obtained using different laser powers and for three different pulse durations. The wavelength was 800 nm. For the highest intensities heavy fragmentation is seen in the mass spectra along with triply charged species. It is worth mentioning the flattening of the spectra for 10–20 degrees seen at low kinetic energies for the highest intensities. Another observation concerns the two peaks at about 1 eV and 1.2 eV (which is actually a series of unresolved peaks bunching up into one peak). The two peaks are marked with two arrows in Figure 3.11. For almost all intensities and pulse durations the peak corresponding to the higher kinetic energy is larger than the peak at 1.0 eV. However, for the three highest intensities for the 130 fs data, the inner peak starts to become comparable in height with the outer peak. The laser intensity corresponds to the onset of the flattening of the spectra. The flattening is further characterised in section 3.3.2.3.

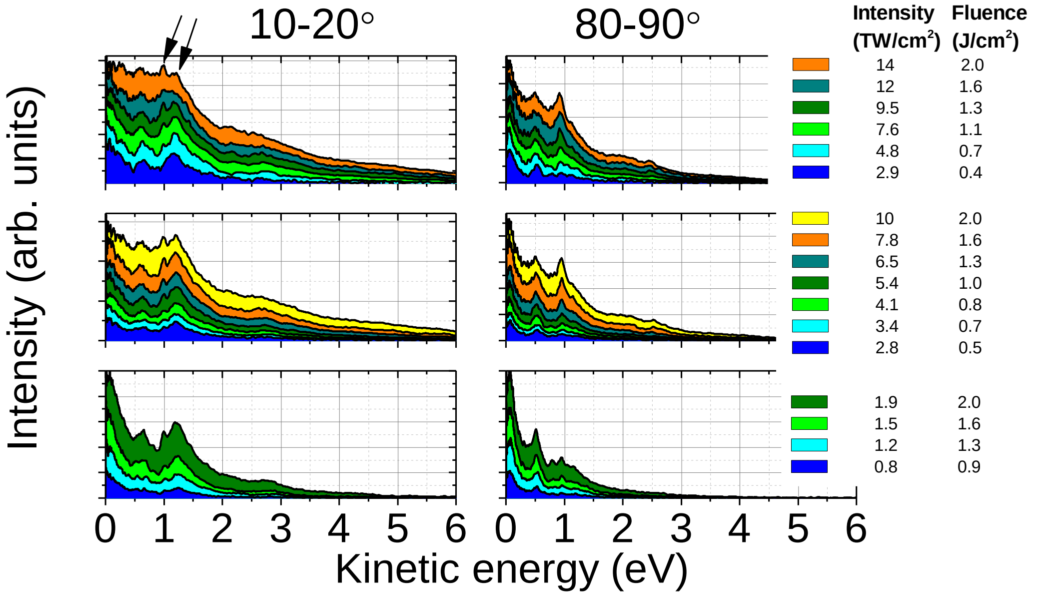

Figure 3.11: Angle-resolved PES for 10–20 and 80–90 degrees inverted using BASEX. C_{60} ionised using 800 nm and the pulse durations were (top to bottom) 130, 180 and 1000 fs. The distributions are shifted vertically for display purposes. The two arrows highlight two peaks that are discussed in the text.

In Figure 3.12, VMI images are presented for 180 fs pulse duration and fluences from 0.7 to 1.3 J/cm^2. Corresponding mass spectra are presented in Figure 3.13 for the same laser fluences. Angle-resolved PES for 10–20° and 80–90° angular segments are presented in Figure 3.14 in a log-lin scale. Only these two extremes of angular section are plotted for clarity. The intermediate segments follow a smooth transition between the two extremes. In the VMI images, Rydberg states can be seen as rings. For a slightly shorter pulse duration of 130 fs the VMI images and mass spectra are very similar to the 180 fs case (Figure G-1, appendix). A slightly larger contribution from ATI peaks are seen for the shortest pulse duration and the doubly to singly charged ion ratio is also higher. Inverted VMI images taken with 1 ps pulse duration are shown in the appendix with corresponding angle-resolved PES. The PES are very similar to the 180 fs case. The mass spectra are different however, as seen in Figure 3.15, since the longer pulse duration allows for more energy to be coupled into the vibrational degrees of freedom.

The angle-resolved PES presented in Figure 3.14 follow a distribution proportional to $\exp(-E_{kin}/s_T)$ where E_{kin} is the photoelectron kinetic energy. The slopes, s_T, of the distributions are related to the apparent temperature T_a defined in Equation (1.4). However, since T_a gives a measure of the amount of energy absorbed by the molecules on average, it should not change with electron emission angle. Therefore, due to the angular dependence of the slopes of the exponential distributions presented in this section, s_T is used to characterise the data instead of the apparent temperature.

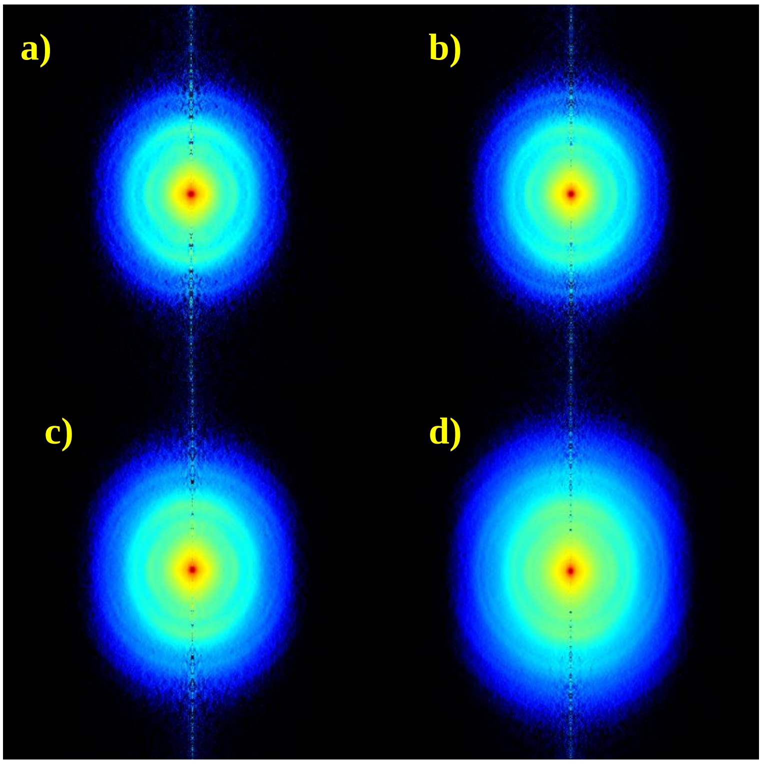

Figure 3.12: Inverted C_{60} VMI images (using BASEX) for 800 nm, 180 fs laser pulse excitation. The laser fluences (intensity) were a) 0.66 ± 0.06 J/cm^2 (3.4 ± 0.36 TW/cm^2), b) 0.79 ± 0.07 J/cm^2 (4.1 ± 0.46 TW/cm^2), c) 1.0 ± 0.1 J/cm^2 (5.4 ± 0.56 TW/cm^2) and d) 1.3 ± 0.1 J/cm^2 (6.5 ± 0.6 TW/cm^2).

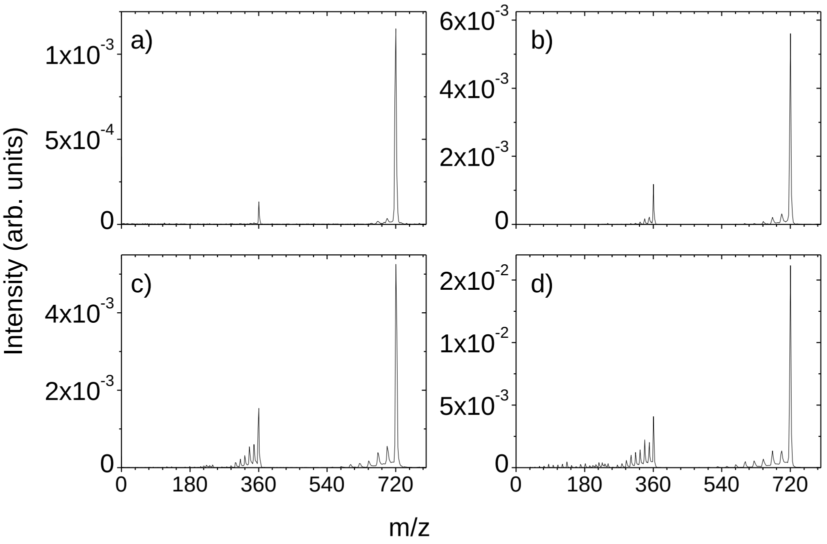

Figure 3.13: C_{60} mass spectra taken with 800 nm, 180 fs laser excitation. The laser fluences (intensity) were a) 0.66 ± 0.06 J/cm^2 (3.4 ± 0.36 TW/cm^2), b) 0.79 ± 0.07 J/cm^2 (4.1 ± 0.46 TW/cm^2), c) 1.0 ± 0.1 J/cm^2 (5.4 ± 0.56 TW/cm^2) and d) 1.3 ± 0.1 J/cm^2 (6.5 ± 0.6 TW/cm^2).

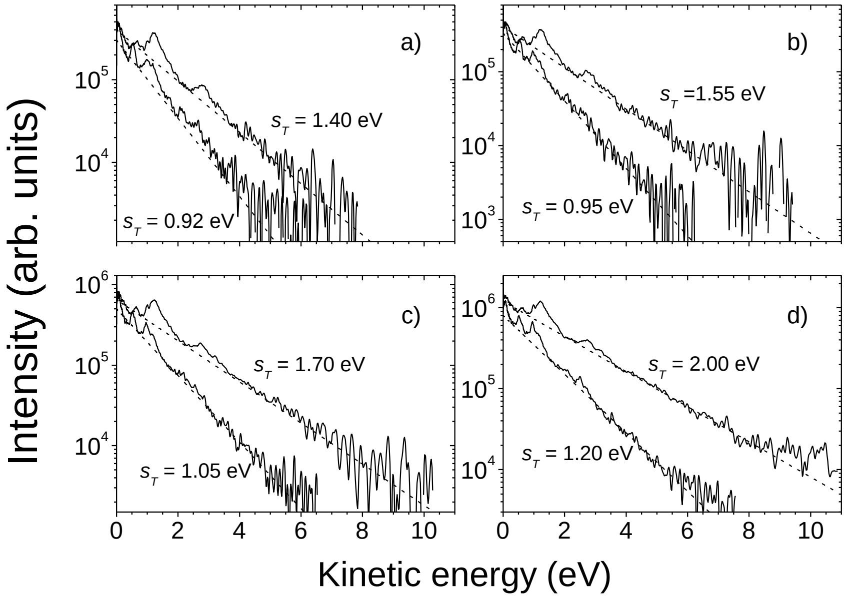

Figure 3.14: C_{60} angle-resolved PES obtained using 180 fs, 800 nm laser excitation for 10–20° and 80–90° angular segments (obtained from the VMI images shown in Figure 3.12). The laser fluences (intensity) were a) 0.66 ± 0.06 J/cm^2 (3.4 ± 0.36 TW/cm^2), b) 0.79 ± 0.07 J/cm^2 (4.1 ± 0.46 TW/cm^2), c) 1.0 ± 0.1 J/cm^2 (5.4 ± 0.56 TW/cm^2) and d) 1.3 ± 0.1 J/cm^2 (6.5 ± 0.6 TW/cm^2). The top curve corresponds to the 10–20° angular segment. Results from fitting an exponential distribution $\exp(-E_{kin}/s_T)$ to the data are shown as dashed lines. The values of the fitted slopes s_T are also given (see text for details). The spectra have been cut off at the noise level.

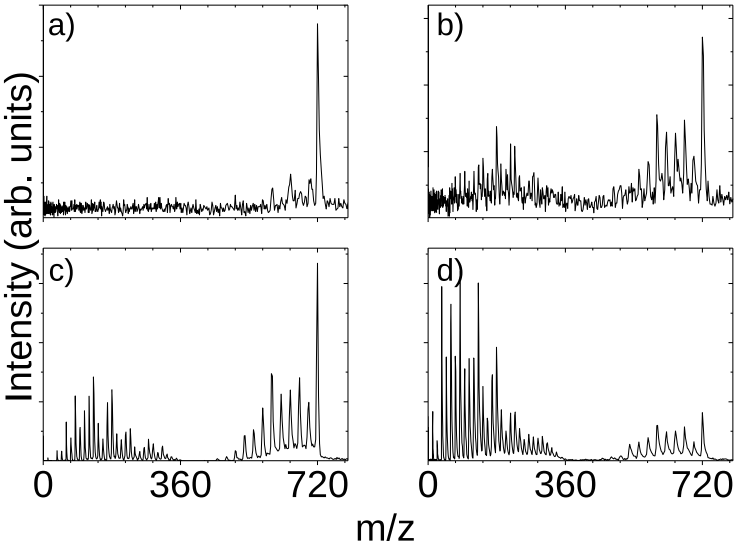

Figure 3.15: Mass spectra for C_{60} after 800 nm, 1 ps laser pulse excitation. The laser fluences (intensity) were a) 0.88 ± 0.08 J/cm^2 (0.82 ± 0.086 TW/cm^2), b) 1.3 ± 0.1 J/cm^2 (1.2 ± 0.16 TW/cm^2), c) 1.6 ± 0.2 J/cm^2 (1.5 ± 0.16 TW/cm^2) and d) 2.0 ± 0.2 J/cm^2 (1.9 ± 0.2 TW/cm^2).

It is known that thermionic ionisation starts to become important for pulse durations above a few picoseconds [89]. Therefore a set of experiments was performed for pulse durations of 2, 3 and 3.8 ps and the results are presented in Figure 3.16. The mass spectra are also plotted as a function of the time-of-flight on a logarithmic scale. It is known that the fullerene decay for thermionic emission follows a power law in time [89] which results in the straight line seen in the time-of-flight spectrum (inset in mass spectra in Figure 3.16). As the contribution from the delayed ionisation channel increases, the delayed component in the time-of-flight spectrum increases relatively to the prompt mass peak. It is also interesting to notice that the difference between the slopes of the 10–20° and 80–90° PES is reduced with an increased thermionic contribution. For the longest pulse duration the PES for the two different angular segments are almost identical except for some residual peak structure at about 0.5 and 1.2 eV for the 10–20° segment.

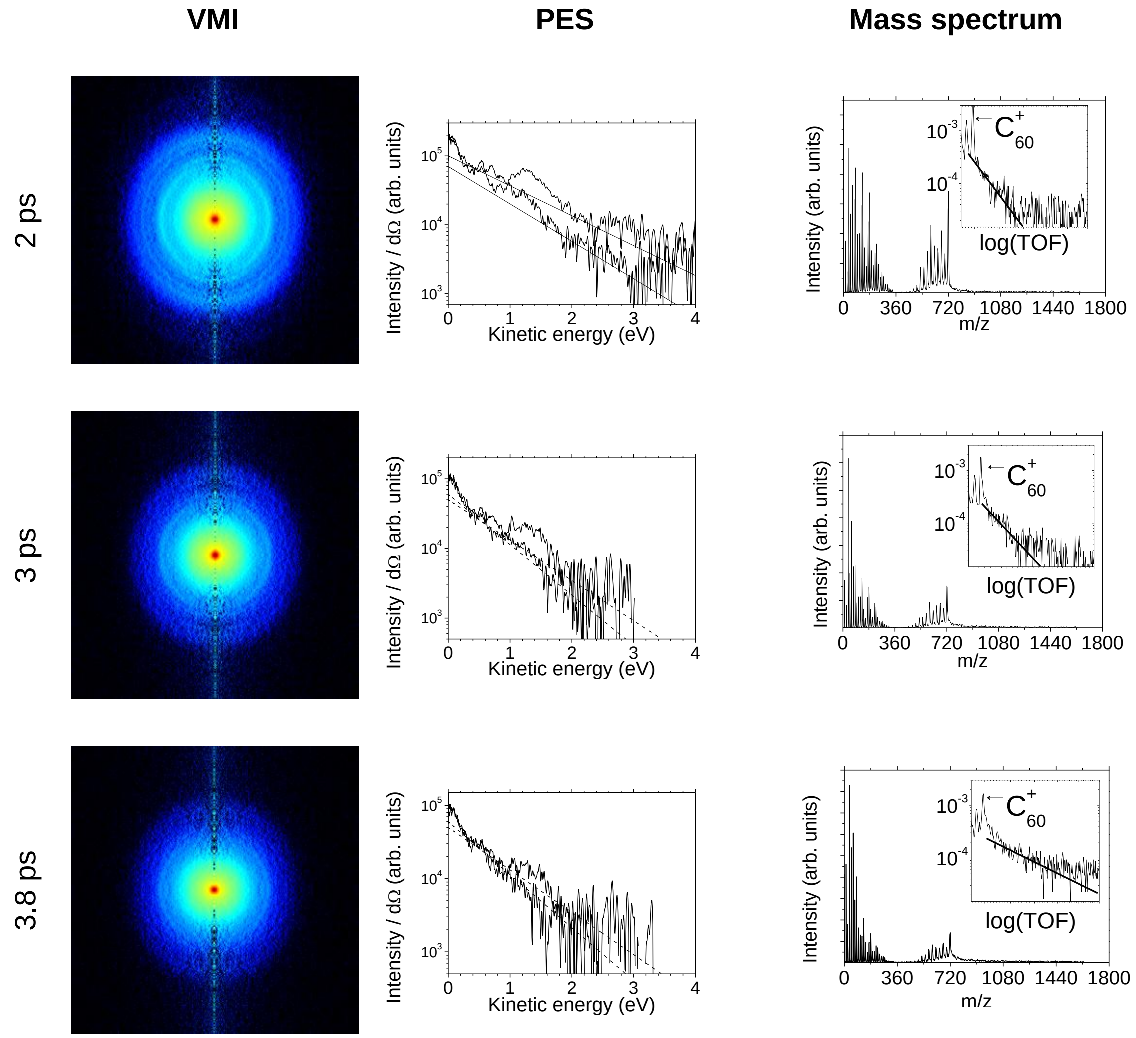

Figure 3.16: Inverted VMI images for 800 nm laser excitation using different pulse durations with fluence of 2.0 ± 0.2 J/cm^2. The intensities were 1.0 ± 0.1 TW/cm^2 (top), 0.64 ± 0.06 TW/cm^2 (middle) and 0.51 ± 0.05 TW/cm^2 (bottom).

A plot of s_T as a function of angular segment for the various pulse durations and intensities summaries the experimental findings in Figure 3.17. The errors are obtained from fitting a linear function to the natural logarithm of some of the spectra in *Origin* above 3.5 eV (to not include the first ATI peak). Typical errors from the procedure, result in errors around 1–3 %. The values of the fitted slopes obtained in this way depend on the start and ending points chosen in the spectrum. By using different start and end positions it was noted that the value of s_T would change around 5 % (which is the error shown in Figure 3.17). A systematic error was estimated from fitted slopes obtained by completely disregarding any ATI structure (procedure used by M. Kjellberg in ref. [28]) compared to taking into account the ATI peaks whilst making sure that the fitted exponential distribution does not overshoot the structure seen for kinetic energies below the photon energy. The systematic error can be estimated as the difference between these two extremes divided by two. Typical values lie between 10–20 %.

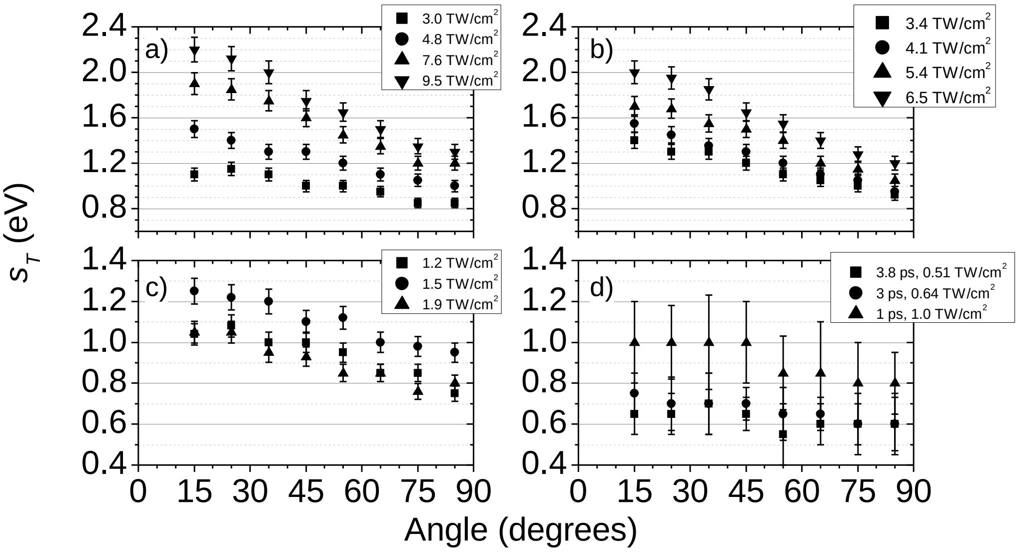

Figure 3.17: Summary for C_{60} of the fitted slopes s_T as a function of angular segment for different intensities. The pulse durations were a) 130 fs; b) 180 fs; c) 1 ps and d) 2 – 3.8 ps.

Similar experiments to those presented above for 800 nm, 117 and 180 fs were obtained on C_{70}. The results, presented in the appendix, were very similar to those for C_{60}. The fitted slopes s_T as a function of angle are presented in Figure 3.18.

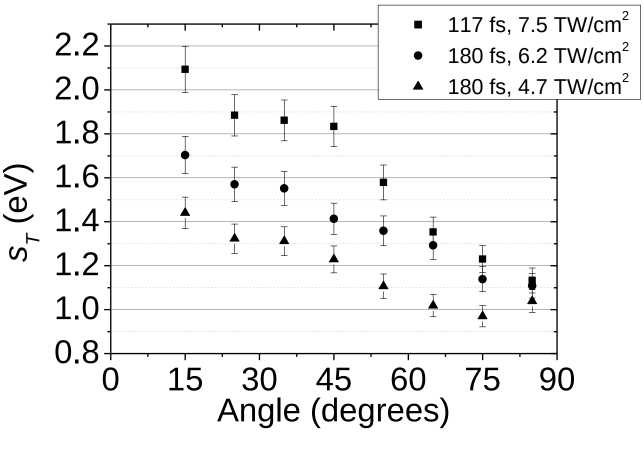

Figure 3.18: Fitted slopes s_T as a function of angle for C_{70} ionised with 800 nm laser light. The fluences were (top to bottom) 0.96, 1.2 and 0.89 J/cm^2.

The slopes as a function of laser fluence for the angular interval 50–60 degrees are presented in Figure 3.19. This angular interval was chosen since it includes the magic angle (54.7 degrees) at which any interaction that depends on the second order Legendre polynomial vanishes.

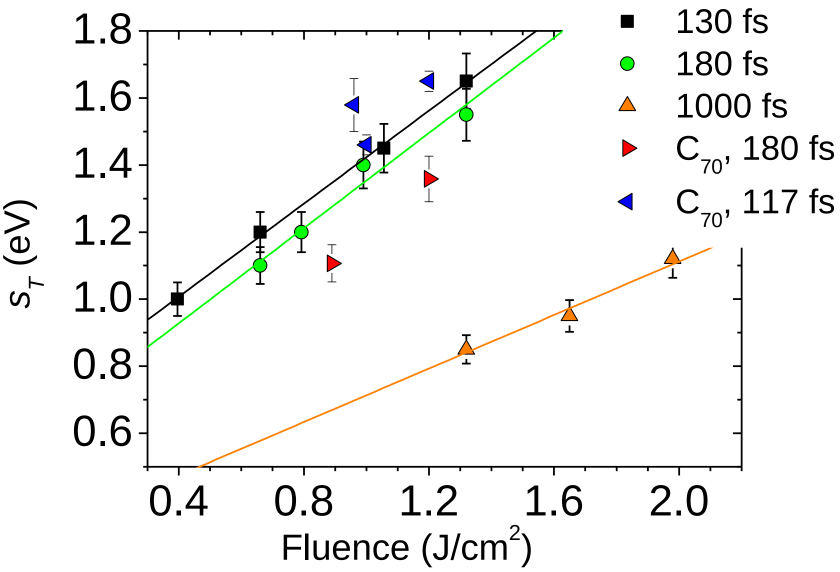

Figure 3.19: Slopes from Figure 3.17 for angular interval 50–60 degrees. Linear fits were made in *Origin*. Data for C_{70} are presented for comparison.

It is interesting to compare these results with the results obtained using 400 nm laser light. Since the photon-absorption cross section will be different for the two wavelengths it is difficult to compare apparent temperatures taken with the same laser fluence. However, the mass spectrum should give an indication of how much energy has been absorbed. The mass spectra in Figure 3.2 are similar to the ones in Figure 3.13 a,b (which are also similar to the spectra obtained using 130 fs). The fitted slopes for 800 nm (130 and 180 fs) lies between 1.0 and 1.2 eV. The two temperatures for 400 nm were about 1.1 eV. This observation supports the thermal electron emission model compared to a field ionisation mechanism since in the quasistatic model a shorter wavelength in combination with a lower intensity should further reduce the influence of field ionisation. However, it is interesting to notice that for similar apparent temperatures to what is observed with 800 nm, no asymmetry is seen in the 400 nm case (which was taken with an order of magnitude lower laser intensity).

3.3.2.3 Characterisation of the non-exponential distribution of low kinetic energy photoelectrons for high laser intensities

Thermionic PES are seen following an exponential distribution all the way to zero electron kinetic energy (chapter 2). In contrast, the angle-integrated PES show a flattening of the exponential distribution below kinetic energies of about 1–2 eV for relatively high laser intensities. In the angle-resolved data this is only seen for the 10–20 degrees angular segments but not for the 80–90 degrees. To investigate whether the flattening is due to an experimental artefact, VMI images were taken for C_{70} with laser characteristics of 120 fs, 800 nm and fluence 1.0 J/cm^2 (8 TW/cm^2). Three different oven temperatures were used (645, 680 and 715 K) in order to see if the flattening would depend on the number of molecules in the interaction region. This could, e.g., lead to space-charge effects which would give an extra kinetic energy to the electrons due to Coulomb repulsion. The oven settings were such that 1.5 and 9 times stronger signals were recorded for the two highest oven temperatures compared to the lowest one. The angle-resolved PES for two different angular segments are shown in Figure 3.20. The 10–20 degrees spectrum shows a flattening for all three oven settings which speaks against space-charge effects. Furthermore, no flattening is seen for the 80–90 degrees PES which also indicates that the flattening arises from another effect since Coulomb repulsion should give an isotropic contribution. In Figure 3.21 (a) the total signal is plotted as a function of oven temperature. The total signal can be fitted to an exponential function which is expected because the vapour pressure of a solid should depend exponentially on the temperature (which can be derived from the Clausius-Clapeyron equation). In Figure 3.21 b) a vertical cut through the raw VMI image is plotted and it can be seen that the signal decreases over an order of magnitude over a detector radius corresponding to a kinetic energy of 1.5 eV. From the experimental tests it can be concluded that the observed flattening is neither due to detector saturation nor space-charge effects.

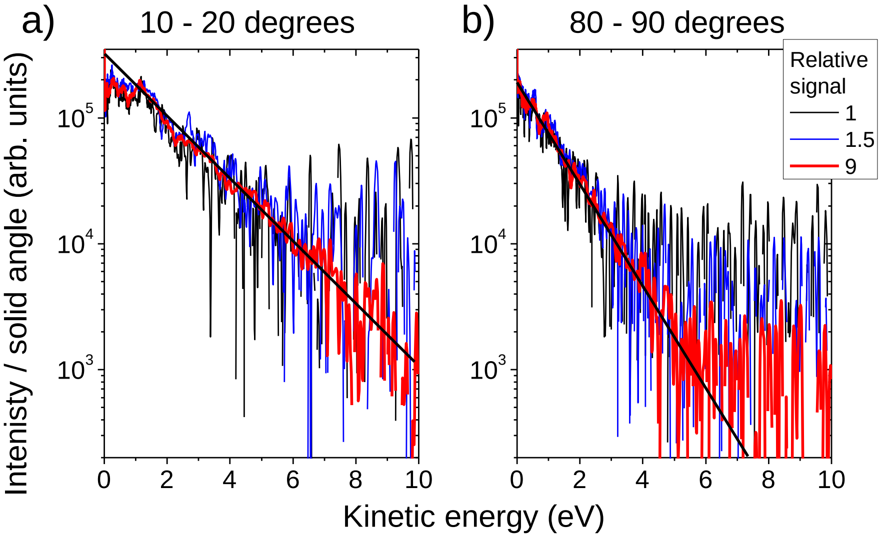

Figure 3.20: Angle-resolved PES for C_{70} taken with 120 fs, 800 nm and a fluence of 1.0 J/cm^2 (8 TW/cm^2). a) 10 – 20 degrees and b) 80 – 90 degrees. The different spectra were taken with different oven temperatures (645, 680 and 715 K) resulting in 1.5 and 9 times stronger signals for the two higher oven temperatures compared to the lowest one. Exponential functions are also shown (thick black lines) to highlight the flattening of the spectra for kinetic energies below 2 eV in a) but not in b). The spectra have been shifted vertically for display purposes.

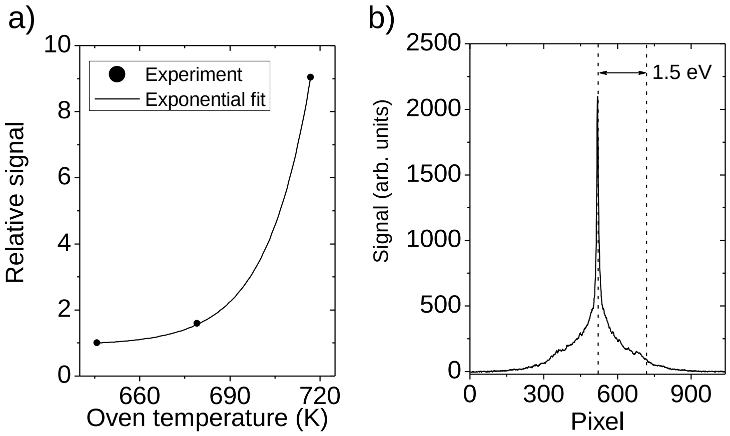

Figure 3.21: a) Recorded total signal as a function of oven temperature for the spectra shown in Figure 3.20 (normalised to the signal measured for the lowest oven setting). The oven temperatures in degrees Celsius were 370, 410 and 440 °C. An exponential fit was made in *Origin*. b) A vertical cut through the centre of the raw VMI image for the highest oven setting is shown. The dashed lines show the distance from the image centre to a calibrated kinetic energy of 1.5 eV.

3.3.2.4 Field-enhanced thermal electron emission

It is possible that the plasmon of C_{60} could contribute to the observed asymmetry discussed in section 3.3.2.2. Asymmetries in PADs after femtosecond ionisation of silver clusters were observed by Fennel *et. al.* when the ionising laser was in resonance with the plasmon frequency [90]. Connerade and Solov'yov have studied the possibility of multiphoton excitation of the plasmon in jellium clusters which could influence the PADs [91]. However, the energy needed to excite a surface plasmon of C_{60} is much higher than for sodium clusters. It therefore seems unlikely that, for the intensities used in this study, a multiphoton excitation of the plasmon (involving a coherent absorption of 15 photons) would occur. Therefore, it appears that another explanation is needed.

One can estimate when most of the thermal electrons are emitted from the rates presented in Figure 3.1. Time scales on the order of hundreds of femtoseconds up to a few picoseconds are found for a typical excitation energy taken from ref. [29]. In contrast to the thermionic case, the laser pulse will therefore be present during the thermal electron emission. This might have some implications on the preferred direction of the emitted electrons. Juraj Fedor, Jakob Stenfalk and Klavs Hansen have modelled the influence of the laser pulse by slightly modifying Equation (3.10) to calculate the rate of emission and therefore also obtaining the apparent temperature as a function emission angle. One modification is based on the reverse process where an electron is colliding with the parent ion. The detected kinetic energy ε is not the same as the energy that the electron has when it collides with the ion because the presence of the laser field introduces an additional velocity along the laser polarisation. The additional velocity v_f can be found by solving Newton's second equation of motion and is

$$v_f = \frac{eE}{m\omega}\sin(\omega t) \tag{3.11}$$

where e is the elementary charge, m is the electron rest mass, E is the electric field strength and ω is the angular frequency of the electric field. The actual collision energy with the fullerene ion will be higher due to this extra velocity. Since in detailed balance one compares the emission kinetic energy ε_{em} with the collision energy, the expression for the collision energy should equal the emission energy which then becomes

$$\varepsilon_{em} = \varepsilon + \frac{1}{2} m_e v_f^2 \sin^2(\omega t) + \sqrt{2 m_e \varepsilon} \sin(\omega t) \cos(\theta) \tag{3.12}$$

where θ is the angle between the direction of the electron and the laser polarisation. When averaged over one laser period the term containing the angular dependence will cancel to zero and this is why no asymmetry of the kinetic energy is seen in the case of multiphoton ionisation of xenon. However, when the expression for the emission energy is inserted into the Weisskopf formula the angular dependence will not cancel.

Simulations have been performed for C_{60} similar to the ones presented in ref. [29] taking into account the spatial and temporal distribution of the laser pulse and also the dissipation of excitation energy into vibrational degrees of freedom assuming a coupling constant of 250 fs. The best agreement between calculations and experiments was found for a photon absorption cross section of 0.1 Å^2 (which was the only parameter that was adjusted to fit the experimental data). This value of the photon absorption cross section was found by comparing a range of different values to experimental data for 130 fs laser pulse duration and intensity 4.8 TW/cm^2. The value that produced the best agreement with experiments was subsequently used for all other intensities and pulse durations. The obtained value of the photon absorption cross section is in agreement with the value of 0.12 Å^2 presented in ref. [29]. The results of the calculations are compared to some of the experimental data in Figure 3.22 (a)–(c). The ratio of the apparent temperature along the laser polarisation direction to the temperature perpendicular to the polarisation direction is presented in Figure 3.22 (d) as a function of laser intensity for both C_{60} and C_{70} for pulse durations from 117 fs to 3.8 ps. A comparison is also made for the ratio obtained from calculations for C_{60} assuming a 180 fs laser pulse.

Considering the simplicity of the model and that only one free fit parameter was used, the agreement between calculations and experiments is quite good. Calculations made for 400 nm and identical laser intensities as in Figure 3.2, showed no asymmetry in agreement with experiments. The experimental data consistently show a stronger angular dependence than the calculations.

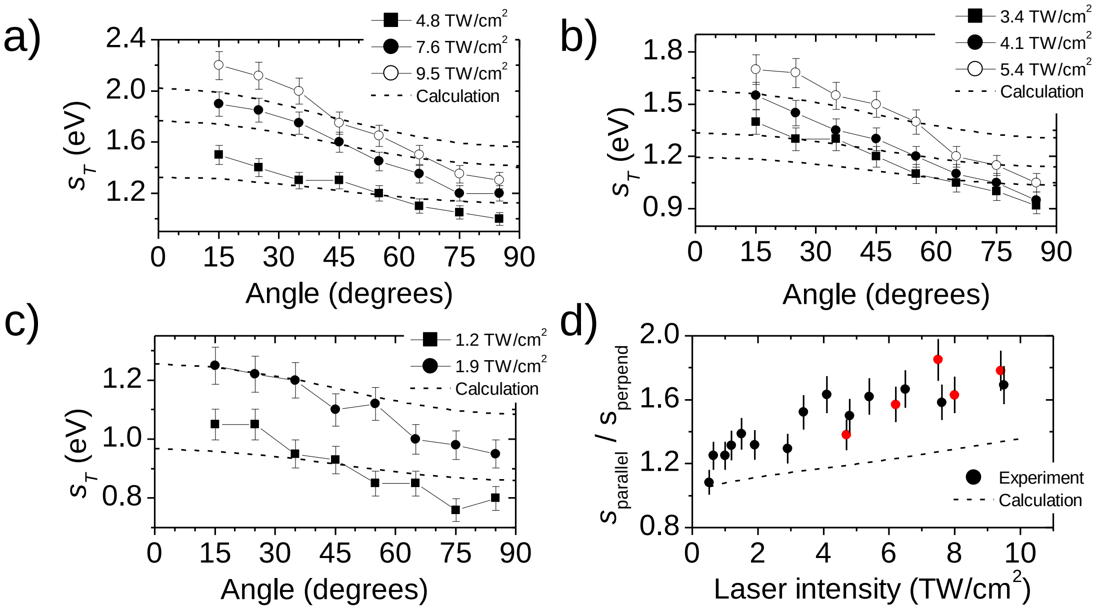

Figure 3.22: Comparison of the angular dependence of the fitted slopes (also presented in Figure 3.17) with calculations assuming a field-enhanced thermal electron emission for C_{60} and pulse duration of a) 130 fs; b) 180 fs and c) 1ps. The ratio of the slopes parallel to the laser polarisation direction and perpendicular is plotted in d) for both C_{60} and C_{70} (red dots) and for all pulse durations (130 fs to 3.8 ps). A comparison between the ratios obtained from calculations for C_{60} is also shown (assuming a 180 fs laser pulse).

As a further characterisation of the asymmetry, the total number of counts per solid angle for C_{60} (180 fs laser pulse duration) is presented in Figure 3.23 and Figure 3.24 obtained from the inverted VMI images for radii corresponding to an energy interval of 4–9 eV. The lower energy value was chosen to reduce the influence of the Rydberg peaks and the first ATI peak. The higher cut-off energy was limited to the onset of the noise level. It was found that anisotropy parameters β_2 and β_4 fitted the data very well. The data were plotted in both a normal linear scale and in a polar plot. The reason for doing this is that in the literature both types of plots are used. To easily compare the present result with literature both types of plots are therefore presented.

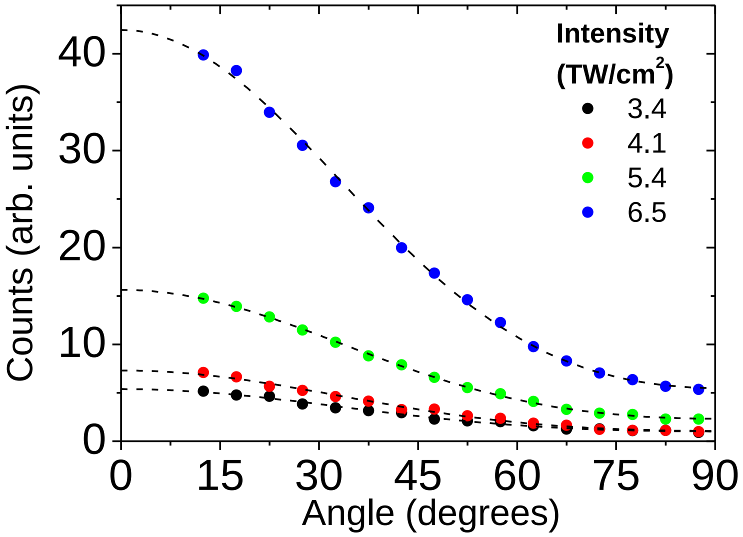

Figure 3.23: The number of counts per solid angle for C_{60} obtained from the VMI images in Figure 3.12 using 800 nm and 180 fs laser pulses. Only photoelectrons with kinetic energies of 4–9 eV were included in the analysis. Anisotropy parameters up to β_4 were fitted to the angular distributions in *Origin* (dashed lines). The value of the fitted anisotropy parameters are presented in the figure below.

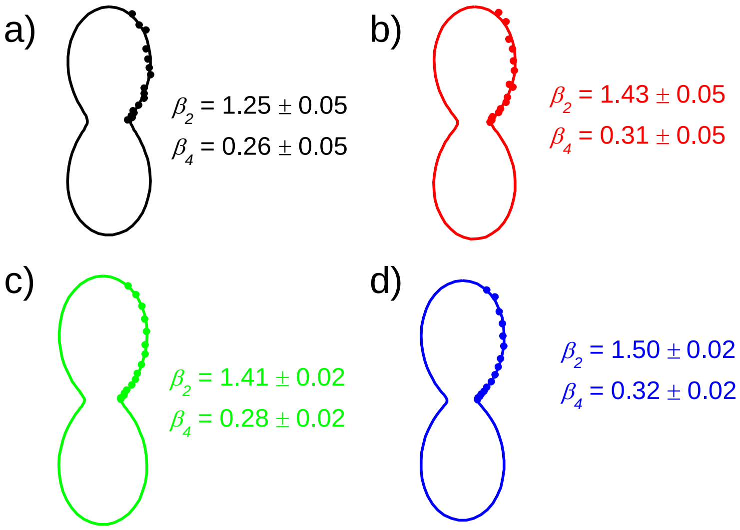

Figure 3.24: The number of counts per solid angle for C_{60} obtained from the VMI images in Figure 3.12 using 800 nm and 180 fs laser pulses (same as Figure 3.23 but in a polar plot). The intensities were a) 3.4, b) 4.1 , c) 5.4 and d) 6.5 TW/cm^2.

3.4 Application to polycyclic aromatic hydrocarbons (PAHs)

The idea of the transient thermal electron emission is based on interacting electrons in equilibrium. It is therefore interesting to investigate whether any evidence for the thermal ionisation mechanism is also seen for other molecules with an extended delocalised electronic system. Is there a minimum limit of level densities in order for the energy to be equilibrated on the experimental timescale? This requires that the electrons interact and share the absorbed energy. But if the number of electrons and therefore the level density is low it might not be possible. Polycyclic aromatic hydrocarbons were chosen in the Gothenburg lab as a test of the applicability of the model to other molecules. Measurements were made together with Mikael Kjellberg, Alexander Bulgakov, Motoshi Goto and Klavs Hansen and the results are presented in ref. [92]. The PES obtained using 780 nm, 150 fs laser pulses for coronene and benzo[GHI]perylene show structure-less Boltzmann-like spectra above the photon energy (as shown in Figure 3.25). For the smaller molecule anthracene more structure is seen in the PES (Figure 3.26). Similar measurements to the ones already presented for C_{60} and C_{70} from the Gothenburg lab were done where the pulse duration was changed. The conclusion from the study was that for the two larger molecules studied, the results indicate that transient thermal electron emission is an important ionisation mechanism for these molecules.

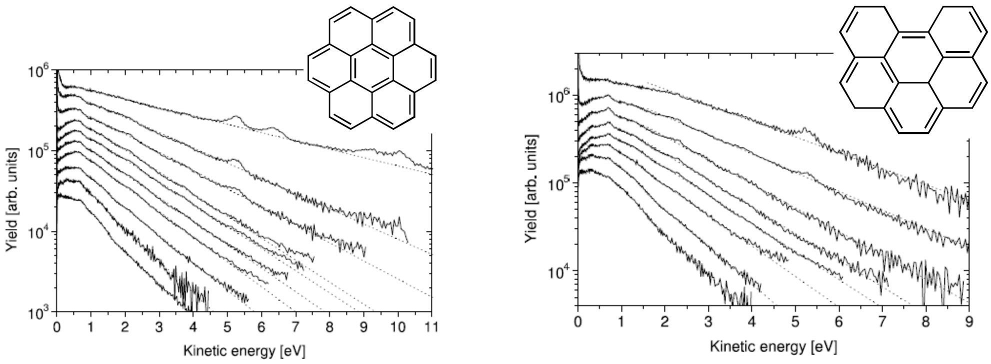

Figure 3.25: 2π angle integrated PES for different laser intensities obtained together with collaborators in the Gothenburg lab by ionising *left*) coronene (using a laser intensity of (bottom to top) 3.6, 4.9, 6.7, 8.0, 9.3, 10.9, 12, 21, 28, and 61 × 10^{12} W/cm^2) and *right*) benzo[GHI]perylene (using a laser intensity of (bottom to top) 1.8, 2.7, 4.4, 6.2, 8.0, 13, 21 and 33 × 10^{12} W/cm^2) using a Ti:Sapph 780 nm, 150 fs laser. Figure from [92].

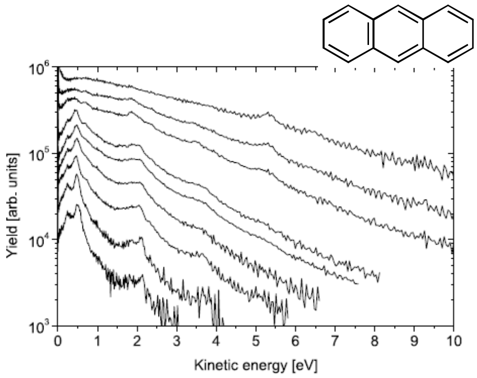

Figure 3.26: 2π angle integrated PES for laser intensities (bottom to top) 1.8, 3.1, 4.4, 8.0, 9.3, 11, 21, 27 and 61 × 10^{12} W/cm^2 obtained together with collaborators in the Gothenburg lab by ionising anthracene using a Ti:Sapph 780 nm, 150 fs laser. Figure from [92].

3.5 Detecting duration of thermal photoelectron electron emission

In time-of-flight mass spectra obtained after ns laser excitation, a tail on the main C_{60}^{+} peak is seen due to delayed, thermionic ionisation. Since charged fullerenes can be seen to be produced a long time (>μs) after the laser pulse has passed [23] it is clear that the ionisation process is not direct. This is seen in the mass spectra because a time-of-flight mass spectrometer can detect the relevant timescales. In contrast, no tail is seen on the singly charged parent ion in mass spectra taken using 100–200 fs laser pulses. It has been estimated that the rate constant for the transient electron emission model can correspond to electron emission up to a few picoseconds after the laser pulse has passed [29] which can also be seen in Figure 3.1. This short delay cannot be detected in a time-of-flight spectrometer. If one could do an experiment, to determine whether the ionisation process after excitation with 200 fs pulses is direct or delayed, it would provide convincing evidence for a thermal mechanism.

3.5.1 Detecting electrons

A field that has expanded during the last decade is ultrafast electron diffraction using femtosecond lasers. This involves producing electron pulses with femtosecond duration which allows for femtosecond resolution in diffraction experiments. Of course it is essential to measure and control the duration of the pulses. A technique presented in ref. [93] can accomplish this. If it would be possible to use this technique in combination with fullerene experiments, it would be possible to determine if photoelectrons are emitted after the femtosecond laser pulse has passed the sample. However, the electron pulses used in diffraction experiments differ from the one produced in a fullerene experiment. The wavelength of the ionising laser in the diffraction experiments is chosen so that photoelectrons are produced with almost zero initial kinetic energy. They are then accelerated by a 50 kV extraction voltage which, combined with the zero initial kinetic energy, produces electrons with essentially the same velocity. The pulse duration is then measured a few centimetres after the point of creation (for a description of the measurement method, please see ref. [93]). If however, the electron pulse possesses a wide spread in velocities, the pulse will be considerably broadened in time. In this section it is investigated whether the resulting kinetic energy distributions of photoelectrons produced in a fullerene experiment will result in a significantly broadened electron pulse to the extent that the femtosecond resolution is lost. If the electrons are ejected promptly with respect to the laser pulse, then the electron pulse duration would be the same length as the laser pulse (e.g. 120 fs). If, on the other hand, the ionisation is delayed then an electron pulse duration on the order of picoseconds could be expected. Using the technique described in ref. [93], it would be possible to distinguish between prompt and delayed ionisation given that the pulses do not stretch in time by more than a few hundred femtoseconds. In order to estimate if the aforementioned experiment is possible, an experiment has been simulated. Assume that photoelectrons are created with a certain kinetic energy distribution from a laser pulse with an infinitesimal duration. These electrons are then extracted with an electric field for a few centimetres where the duration of the electron pulse is to be measured. The equations of motion for electrons can easily be solved with a one-dimensional static electric field along one spatial coordinate. This is a simplification of what the field looks like in an actual VMI setup. However, this approximation was used in ref. [57] and for electrons with low kinetic energies compared to the extraction voltage the approximation is valid. Therefore the arrival time at the point where the electron pulse will be measured can be found. However, it is slightly more complicated to convert a distribution of kinetic energies into a distribution of arrival times because the change of variables is quite cumbersome. To circumvent the problem it is possible to find the distribution of arrival times for a given kinetic energy distribution by a Monte-Carlo simulation. A kinetic energy distribution mimicking a series of ATI peaks was chosen and is shown in Figure 3.27 (a). An isotropic PAD was chosen. The arrival time of one electron with a given velocity was derived from Newton's second law of motion, with the electric field along one dimension as mentioned previously. The Monte-Carlo code was written in Matlab. To generate a random number from an arbitrary distribution, the transformation method [9] was used in combination with the built-in random number generator in Matlab. The results from the simulation are shown in Figure 3.27 (b) where it can be seen that even for a kinetic energy spread of about 0.25 eV (FWHM of the peak at 0.5 eV in the kinetic energy distribution) and an infinitely short laser pulse duration, the electron pulse is stretched to over 5 ps. The spread in time is also due to photoelectrons emitted with different angles with respect to the extraction direction. One could however envision removing the extraction voltages and simply allowing the electrons to freely propagate just like in a time-of-flight photoelectron spectrometer. In order to compensate for the kinetic energy dispersion one could introduce a capacitor acting as an energy selector minimising the dispersion. However, even the finite size of the laser focal spot will introduce a sufficiently large distance between monoenergetic photoelectrons so that the electron pulse is stretched to ps duration. It is therefore concluded that the approaches suggested above will probably not be able to separate prompt from delayed ionisation on the femtosecond to picosecond time scale.

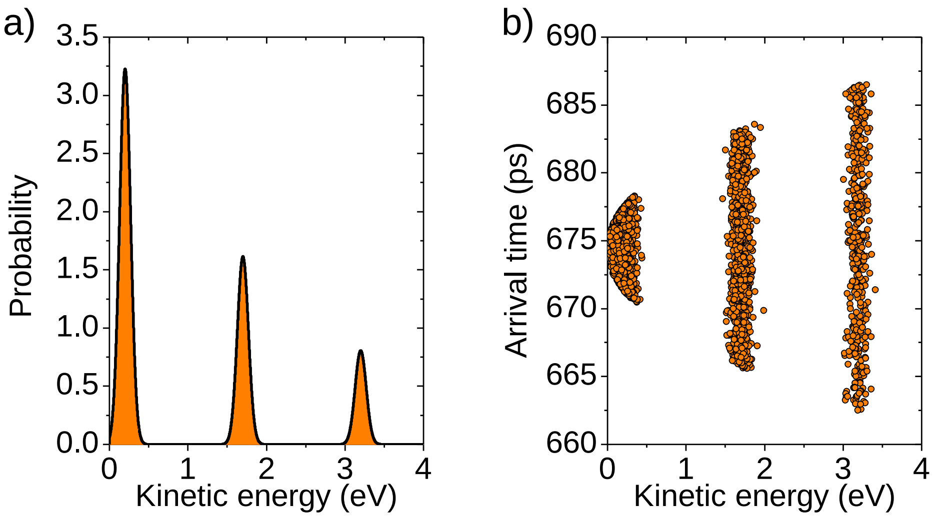

Figure 3.27: a) Kinetic energy distribution used for the Monte Carlo simulation comprising of three Gaussian peaks separated by 1.5 eV. b) Simulated arrival times after the electrons travelled a distance of 2 cm from the point of creation to detection. The arrival times are calculated from an isotropic emission of electrons with a kinetic energy distribution shown in a). A static electric field of 50 kV was used to extract the electrons towards the point of detection where the electron pulse duration would be measured.

3.5.2 Detecting ions

From the discussion above it is evident that this approach is not the best one for determining whether ionisation takes place even after the laser pulse has passed the sample. Another idea is based on a type of pump-probe experiment where the residual ion is heated by a second laser pulse. The idea is based on an experiment on the anthracene molecule using only one pulse where the wavelength is such that it is in resonance with a transition in the ion but not in the neutral molecule [94]. This results in heating of the ion through one-photon absorptions and therefore fragmentation is seen in the mass spectrum. However, by using a different wavelength that was neither in resonance with the neutral or the ion, no fragmentation was seen. There is an absorption peak for C_{60}^{+} around 1000 nm that is not present for C_{60} [95, 96]. To measure the creation of ions an 800 nm pump pulse would ionise C_{60} potentially through thermal electron emission. The ions will not move on a ps time scale and would therefore be stationary when the probe pulse comes. A probe pulse of about 1000 nm would enter the ionisation region at a later time to pump energy into the already created ions. The resulting mass spectrum would change because the additionally absorbed energy will create more fragments. If the ionisation mechanism is direct the number of ions will not change over time after the pump pulse. Therefore by changing the pump-probe delay the fragment-to-intact ratio in the mass spectrum would not change. If the ionisation mechanism is delayed, more ions would be created after the first pulse and therefore more and more fragmentation would be seen as a function of delay time.

The non-collinear optical parametric amplifier (NOPA) in the lab can produce sub-50 fs laser pulses with a variable wavelength between 850–1100 nm. The NOPA is pumped by the Legend (800 nm, 120 fs) and therefore a pump-probe experiment could be done using these two light sources.

3.6 Conclusion

Results concerning thermal electron emission from C_{60} and C_{70} have been presented using a new type of photoelectron detector allowing for PADs to be measured. The results are in agreement with previously published data. Apparent temperatures for 400 nm were in agreement with temperatures found for 800 nm when comparing fluences resulting in similar mass spectra. The PADs after 400 nm laser excitation and intensities in the range of 10^{11} W/cm^2 showed an isotropic thermal electron emission. In contrast, the PADs obtained after 800 nm laser excitation in the intensity range 10^{12}–10^{13} W/cm^2 showed a clear anisotropy along the laser polarisation which was not expected from a statistical emission process. Modelling, taking into account the presence of the strong laser field during the thermal electron emission, is consistent with experimental results indicating that for 100–200 fs excitation and intensities of 10^{12} – 10^{13} W/cm^2, field-assisted thermal electron emission takes place. Possible experiments to determine whether molecules are ionised after the laser pulse has passed the interaction region were discussed.

Chapter 4 – PADs of excited electronic states in fullerenes

4.1 Introduction

The previous chapter covered the possible thermalisation of the excitation energy in the electronic system of fullerenes after femtosecond laser excitation. A statistical redistribution of the absorbed energy implies that all states have equal probability. If the excitation energy is high enough this will result in the statistical emission of electrons. PES are consistent with this model which has been shown previously [6, 28, 29] and further support for the model was also presented in the previous chapter. However, as previously mentioned, a series of peaks are seen superimposed on the thermal background in the PES and these peaks are the subject of this chapter. It has been proposed that these peaks originate from Rydberg states that are populated in the initial part of the laser pulse and then single-photon ionised in the latter part of the pulse [7]. In order to gain more insight into the origin of the peaks, angle-resolved PES have been recorded for 400 and 800 nm laser excitation for both C_{60} and C_{70}. Before the results are presented a review of previous experimental studies on C_{60} is presented.

4.1.1 Previous experimental observations

PES obtained by Boyle *et. al.* from C_{60} ionised with various wavelengths and for different pulse durations are shown in Figure 4.1. The assignment of the peaks seen in the figure was done by modelling a single electron in the field of the positively charged ion [97]. The radial potential experienced by the electron was chosen to be a jellium-like potential with the minimum close to the carbon atoms in the fullerene as shown in Figure 4.2a. If the observed Rydberg states in C_{60} are ionised with a single photon one can calculate the binding energy E_{bind} from the photoelectron spectrum from the relation

$$E_{bind} = \mathrm{h}\upsilon - E_{kin}$$

where hν is the photon energy and E_{kin} the kinetic energy of the photoelectron. A comparison between the calculated values and the experimental peak positions is presented in Figure 4.2b. The good agreement between the relatively simple model and the experimental data is a convincing argument that the observed structure indeed arises due to population of Rydberg states. However additional peaks in PES can arise from a single initial state in the neutral species due to the population of several final states in the ion. Therefore it is possible that some of the peaks arise due to, e.g., a vibrational progression in the ion. However, previous experiments using synchrotron light [44], indicate that the geometric shape of the neutral C_{60} is very similar to the that of the ion because a steep ionisation threshold was observed and no signs of hot bands were found. Another explanation of the observed structure could be related to the high vibrational temperature of the molecules in the effusive beam from the oven. The structure in the PES could arise from multiphoton ionisation from the ground state and the structure would therefore reflect the quantised vibrational levels that are populated due to the high oven temperature.

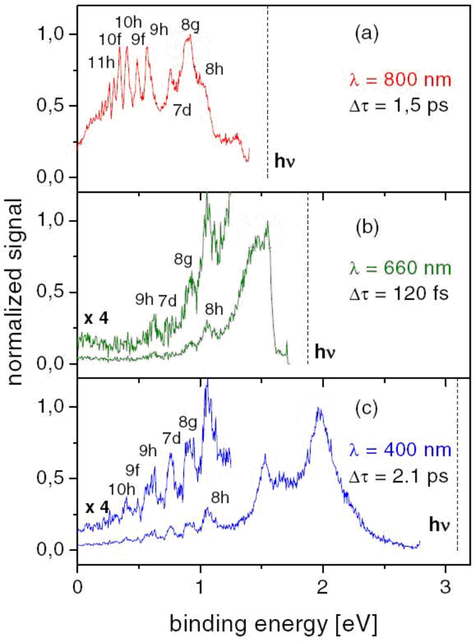

Figure 4.1: Photoelectron spectra of C_{60} ionised with different wavelengths. When subtracting the photoelectron kinetic energy from the photon energy the binding energy is obtained. The peaks seen correspond to the same binding energy independent of wavelength and have been assigned by solving the radial Schrödinger equation with a jellium-like potential [97]. The figure is adapted from ref. [98].

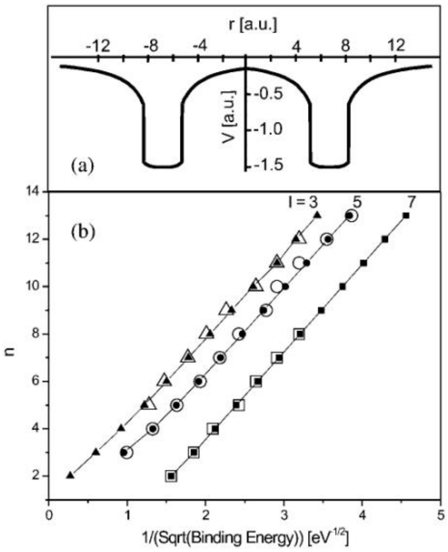

Figure 4.2: a) The radial one-particle potential used to solve the Schrödinger equation. b) Calculated Rydberg series (filled symbols) corresponding to ℓ = 3,5 and 7, are compared to experimental data (open symbols). Figure from ref. [97].

By varying the wavelength Boyle *et al.* found that the observed peaks had the same binding energy for different wavelengths [98]. Experiments have also been carried out where both fluence and duration of the exciting pulse have been varied and an example is given in Figure 4.3. As is seen in the figure the peaks do not shift position over intensities ranging from 6–40x10^{11} W/cm^2. With decreasing pulse duration the peaks become smeared out [97] and for pulse durations over 4 ps the intensity of the peaks is reduced as can be seen in Figure 4.3. The PES presented in Figure 3.11 in chapter 3 for 800 nm laser light and different pulse durations and intensities confirm that the peak positions remain constant (although the peaks are not well resolved). The influence of the chirp of the laser pulse has been tested and the results imply that when the longer wavelengths lag, the peaks are shifted towards lower kinetic energies indicating that the Rydberg states are ionised during the later part of the laser pulse [97]. Polarisation effects have also been measured indicating that the Rydberg electrons are preferably ejected along the laser polarisation direction [98] (see Figure 4.4). The angular dependent spectra (although only for a polar angle of 0–5 and 85–90 degrees) were obtained using a linear time-of-flight photoelectron spectrometer. The detection angle was varied by either aligning the laser polarisation axis parallel to the TOF spectrometer axis or perpendicular.

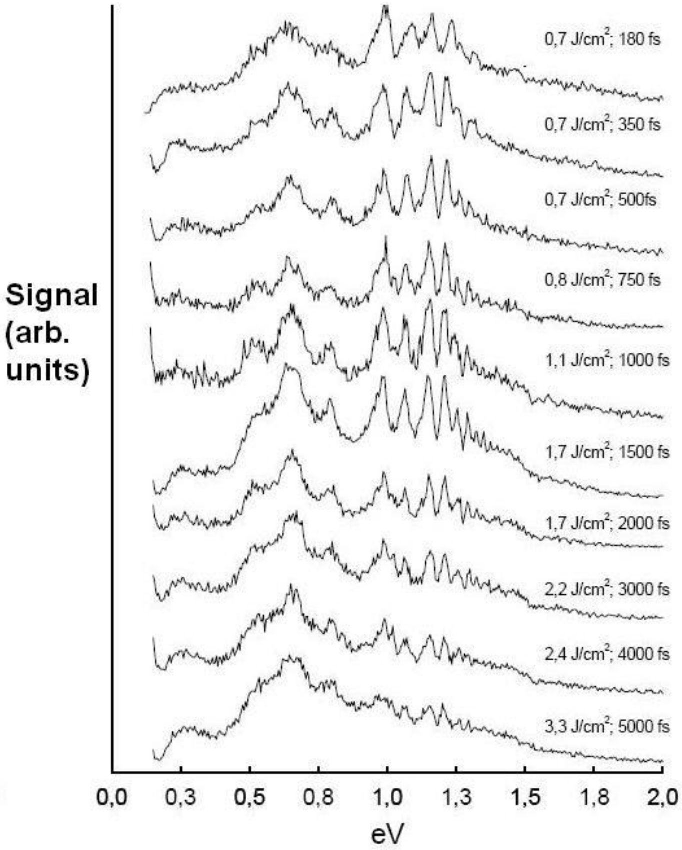

Figure 4.3: Photoelectron spectra showing the variation of pulse fluence and duration with λ=800 nm. Figure from [17].

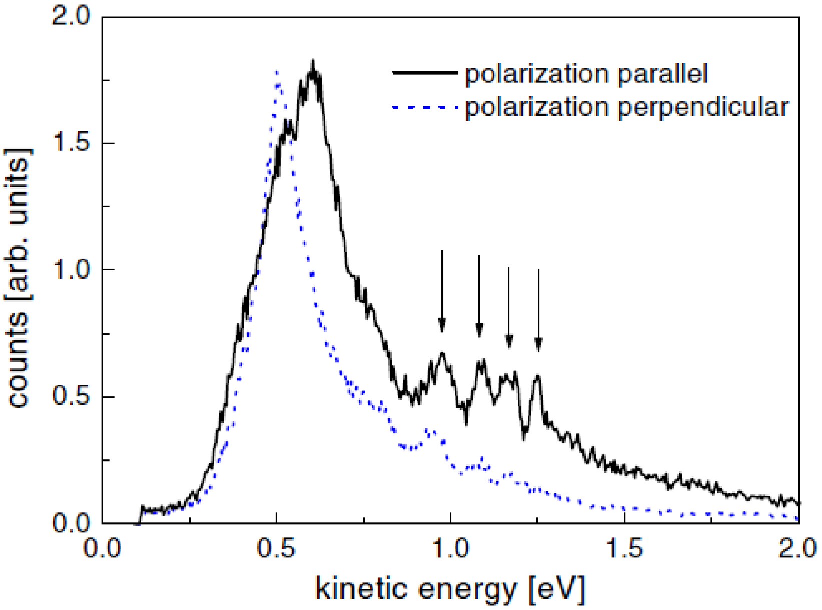

Figure 4.4: PES taken with a linear time-of-flight photoelectron spectrometer with the laser polarisation aligned either parallel to the time-of-flight axis or perpendicular. The acceptance angle of the detector was about 5 degrees. Figure from ref. [98].

Pump-probe experiments have been conducted with 400 and 800 nm pulses investigating the Rydberg states yielding a different result if the 400 nm pulse leads over the IR pulse [98, 99]. The result is presented in Figure 4.5. The authors argue that the 400 nm pulse is important for the population of an intermediate “doorway state” which is resonant with 400 nm but not with 800 nm. However, the polarisation direction of the 400 nm pump beam was perpendicular to the spectrometer axis. As was previously shown in Figure 4.4, most of the observed structure is emitted along the laser polarisation. Therefore, it is not possible from the experiment to determine whether any structure is seen in the PES when the 800 nm beam is the pump.

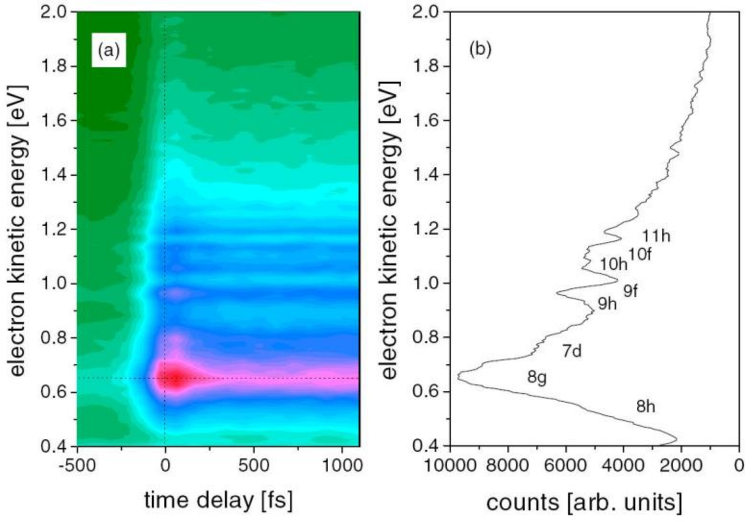

Figure 4.5: a) Two-colour pump probe experiment with a blue 400 nm pump ($1x10^{11}$ W/cm^2) and an IR 800 nm probe ($2x10^{12}$ W/cm^2). Negative time delays indicate that the probe pulse is leading the pump pulse. b) A vertical slice through the contour plot in a) along the dotted line. Figure adapted from ref. [98].

As can be seen in Figure 4.5 the signal originating from the Rydberg levels does not appear to decrease with increasing time delay between the pump and probe pulses on the timescale of the experiments. A plot with larger time delays is presented in Figure 4.6. It can be seen that lower lying states appear to have a shorter lifetime than less bound states. The “lifetime” could on the other hand be related to the population mechanism and not the actual lifetime of the Rydberg states. Since both the pump and probe beams produced a significant amount of ionisation separately (which was seen in mass spectra), it is possible that the “lifetimes” are related to the intermediate doorway state. If the doorway state is populated by the pump beam, the highly excited states could be ionised from the doorway state with the probe and therefore the dynamics of the intermediate state is measured and not that of the Rydberg levels.

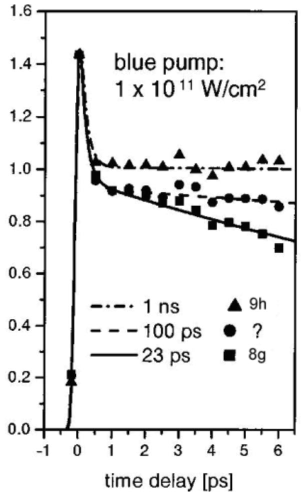

Figure 4.6: Same experiment as in Figure 4.5. The intensity dependence of three Rydberg peaks as a function of the time delay between pump and probe pulses. The Rydberg state 9h (8g) has the lowest (highest) binding energy. Fitted decay curves are also shown in the figure. Zero intensity is chosen to be the intensity at negative time delays. Adapted from ref. [99].

Highly excited states have long orbiting periods and the time scales involved may coincide with the vibrational motion of the nuclei in the molecule. In ref. [99] it was shown that the initial internal energy of the fullerene is crucial for the observation of Rydberg states. Cold C_{60} was prepared in a gas aggregation source producing fullerenes with temperatures around 80 K. A comparison with fullerenes with internal energies of 80 and 770 K is presented in Figure 4.7 where 800 nm laser pulses were used.

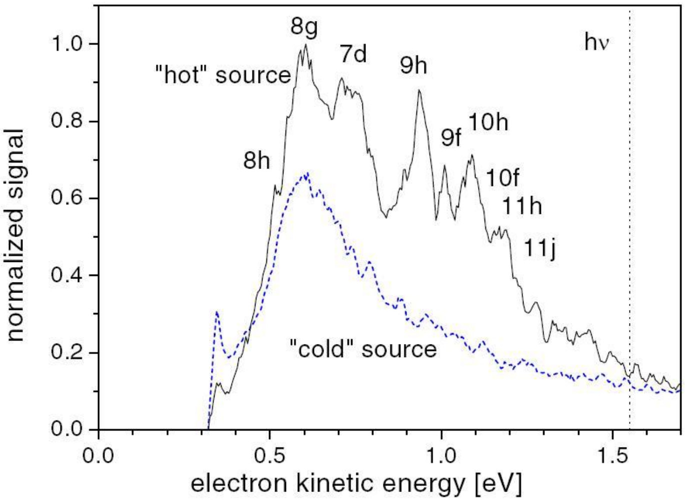

Figure 4.7: Photoelectron spectra of gas phase fullerenes with an initial internal energy of 80 K ("cold" source) and 770 K ("hot" source). The wavelength was 800 nm and the pulse duration was 100 fs. An intensity of 2.5×10^{12} W/cm^2 was used. Figure from ref. [99].

4.1.2 Possible interpretations of previous studies

The observation of what might be Rydberg states in fullerenes has been reported by Wesdorp *et. al*. They have used a method of electron recombination with singly charged C_{60} resulting in the population of Rydberg states [100]. By bombarding cations with electrons when a weak static electric field is present an electron can be found close to the ion core. If the static electric field is suddenly turned off, an electron can be captured in the field of the ion resulting in a neutral molecule in a Rydberg state. The process is illustrated in Figure 4.8. The authors claim that they can produce Rydberg states with an energy spread of 1 K. The principal quantum numbers are usually around $n=180–200$.

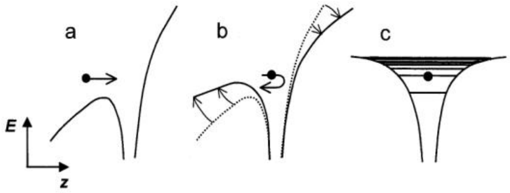

Figure 4.8: A method to produce Rydberg states as proposed by Wesdorp *et. al.* using bombardment of C_{60}^{+} with electrons [100]. a) When a static electric field is applied along the z-axis the potential of the ion is distorted. This opens the possibility to find an electron in the vicinity of the ion core. b) If the electric field is switched off while the electron is close to the nuclei this might result in c) a molecule in a Rydberg state. Figure adapted from [100].

It is possible that the population of the Rydberg states seen in experiments involving photoexcitation follows a similar mechanism presented in the electron bombardment experiments [100], where the short laser pulse would act to switch on and off the electric field and the electron recombines with the ion due to the linearly polarised laser field.

Using synchrotron radiation Yasumatsu *et al*. have proposed that “superexcited” states in C_{60} exist at 7.87, 8.12 and 9.2 eV [101]. Excitation to these states might result in the population of Rydberg states through nonradiative decay as proposed by Schick and Weber [102]. The “superexcited” states at 7.87 and 9.2 eV are resonant with 5 and 6 IR 800 nm photons. However, due to the non-linearity of multiphoton excitation, the Rydberg structures would be expected to be more sensitive to the laser intensity if excitation to the superexcited state was the mechanism for population [88].

The intensity distribution of the Rydberg structures does not seem to show strong laser intensity dependence. However, the intensity distribution does change shape as the wavelength is altered. This implies that Franck-Condon factors might be important which could be connected to the results shown with the gas aggregation source.

In experiments involving ionisation of rare gas atoms with intense ultrashort laser pulses a similar Rydberg structure is seen [77]. This has been explained with Rydberg levels being shifted into resonance by the A.C. Stark shift (see chapter 2). The probability of a multiphoton process is greatly enhanced if there is an intermediate state involved [103] which would result in the Rydberg states seen in the photoelectron spectra. Since the intensity of the laser beam is not homogenously distributed over the focal volume, different Rydberg states are tuned into resonance at different parts of the beam. The experimental observation is a spread over the Rydberg states of approximately 1–2 eV. The A.C. Stark shift can be approximated with the ponderomotive shift and the spread in Rydberg states should correspond to the shift. Rydberg states are seen in C_{60} with intensities corresponding to a ponderomotive shift of only 60 meV [98]. The shift is therefore too low to result in the broad distribution of excited states seen in the experiments. Furthermore, the 10 meV bandwidth of the laser is also too small to account for the spread. The broad distribution of excited vibrational states due to the high oven temperature used in the experiments might cause the broad energy spread of observed excited states in a direct multiphoton excitation from the ground electronic state. Another proposed mechanisms is non-adiabatic multi electron dynamics (NMED) [47]. This model is based on the excitation from the ground state to a doorway state. This doorway state is in fact a band structure of closely spaced energy levels. The energy difference between the ground state and the doorway state is typically larger than the exciting photon energy. However, the energy spacing between the levels in the doorway state should be smaller than the photon energy. In the presence of the laser field these states are mixed forming a quasi continuum (QC) and the molecule is then ionised from the QC. The authors of ref. [47] have calculated the most probable states to form a doorway state for various organic molecules. These results were then used to calculate ionisation probabilities and when the polarisability of the molecules was included, agreement between theory and experiments was reached. It might be possible to do a similar calculation for C_{60} and compare with experiments. The broad variety of available energy levels in the QC could explain the energy span of the Rydberg levels. In the model presented in ref. [47] no vibrational dependence on the population of the doorway state is included. Obviously in the case of C_{60} there is a dependence on the initial temperature of the population of the Rydberg states. In a paper by Lezius *et al*. [104] it is concluded that coupling to the QC by NMED could lead to multi electronically excited states that would not be accessible by conventional spectroscopic means. In the previous chapter, the thermalisation of the absorbed energy was discussed. The thermalised electronic system could act as a QC and Rydberg states might be reached from this.

Another suggestion for the broad range of accessible Rydberg states is that the first optically allowed state (also called the LUMO+1) can be coupled to vibrational motion [88, 98, 99]. This has been motivated by a theoretical paper by Zhang *et al*. [105] where it is proposed that the electronic and vibrational system exchange energy periodically after femtosecond laser irradiation. The period of the energy exchange is close to the period of the radial breathing mode. The HOMO is seen to be split into states with lower degeneracy and increases its energy. LUMO+1 is also split and is lowered in energy. This occurs due to electron phonon coupling. If the LUMO+1 state would not be broadened by the coupling to vibration in cold fullerenes at least a narrow band of Rydberg states corresponding to the bandwidth of the laser would be visible. However, when using the cold source no Rydberg states were seen.

The thermal background seen in the photoelectron spectra has also been seen when irradiating sodium clusters under similar laser conditions [45]. The similar photoelectron spectra seen in both fullerenes and sodium clusters further stress the statistical nature of the ionisation process. However, no Rydberg states were seen in the sodium cluster experiments. Photoelectron spectra of C_{70} (see previous chapter) show very similar peak structure to what is observed for C_{60} and La@C_{82} shows an unresolved bump which could be due to Rydberg states [106]. In the introductory chapter the superatom molecular orbitals (SAMOs) found by Feng *et. al.* were mentioned [9]. These orbitals are thought to arise for hollow-shell molecules whenever there is a lower potential inside the cage compared to outside. This results in a central potential just like for an atom and therefore atom-like molecular orbitals are seen. The authors stress that these states differ from ordinary molecular Rydberg states where the Rydberg electron is sufficiently far away from the ionic core so that it only experiences a point charge. The SAMOs on the other hand arise due to the central potential and can have electron density even inside the cage. Therefore it is necessary to have a hollow-shell molecule to see the SAMOs. This could be the reason why no structure is seen in the sodium cluster experiments[3] presented in ref. [45]. It is possible that the series of peaks observed in ultrafast laser experiments on gas-phase C_{60} originate from one-photon ionisation from populated SAMOs which for higher-lying states should converge on a Rydberg series [107]. In Figure 4.9 the energy levels of C_{60} from ref. [98] are compared to the density of states obtained by Feng *et. al* .[9]. The binding energy of the s-SAMO is about 2 eV and coincides with a peak also seen in absorption experiments [108]. Several other SAMOs coincide with previously observed absorption peaks. It is therefore feasible that these states are seen in gas-phase experiments. If the initial and final states are not well-defined it is difficult to extract any information about the initial state from measured PADs due to interference of outgoing partial electron waves (as was discussed in chapter 1). However, the s-SAMO should only comprise of an outgoing electron wave with angular

---

[3] The lack of structure can also arise because the lifetimes of the excited states are too short to be seen for the experimental conditions used to acquire the spectra by Schlipper *et. al*..

momentum corresponding to $\ell = 1$. Since the binding energy of this state is about 2 eV it should be possible to see using 400 nm laser light.

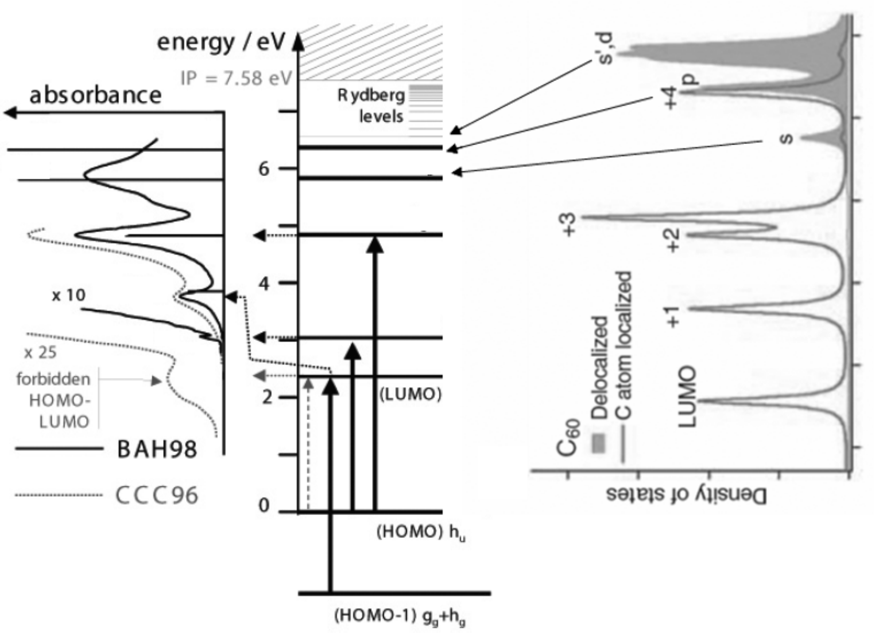

Figure 4.9: Electronic energy levels (middle) from absorption experiments (left) of C_{60} [5] are compared to the density of states for C_{60} obtained by plane-wave DFT calculations by Feng *et. al.* [9] (right). The absorption spectra were obtained in both hexane solution (BAH98 [109]) and in the gas phase (CCC96 [108]).

4.2 Results and discussion

The aim of this chapter is to present PADs obtained after 400 and 800 nm laser excitation. This will help to determine if the populated Rydberg states are single-photon ionised or arise due to coherent multiphoton ionisation from the electronic ground state or intermediate states. The PAD of the peak with corresponding binding energy of the s-SAMO will be a strong indication if the SAMOs are populated in gas-phase experiments where the vibrational temperature of the molecules is around 500 °C.

The data presented in this chapter were obtained using either 400 or 800 nm laser excitation. Both BASEX and pBASEX provide fitted anisotropy parameters for each radius of the inverted VMI image. However, most of the observed peaks were not resolved enough to extract information from the anisotropy parameters supplied by the inversion programs. Therefore Lorentzian peaks were fitted by eye to the angle-resolved PES. Lorentzian line shapes were chosen over Gaussian in ref. [7] because they produced the best fit. Therefore, Lorentzian functions were also chosen to fit the present data. The peak position was fixed within 2 % because a small drift with angle was seen in xenon experiments presented in chapter 2.

In the 400 nm case, it was shown in the previous chapter that there is an isotropic thermal electron contribution that follows an exponential distribution to zero electron kinetic energy. Therefore, the thermal component was subtracted from the data prior to the peak fitting procedure. In the 800 nm case, it was shown that electrons with low kinetic energies, followed non-exponential distributions. Therefore, a subtraction of the thermal electron contribution could lead to artefacts when analysing the angular dependence of the peak structure. Furthermore, an anisotropy in the apparent temperature was also found. In order to circumvent these problems it was necessary to use a low laser intensity. In a first attempt, this was achieved by using a relatively high laser fluence but long pulse duration (ps). The high fluence allowed for an apparent temperature to be fitted to the high-kinetic energy tail of the PES which was then subsequently subtracted. The temperature was fitted individually for each angular segment to compensate for the observed asymmetry in chapter 2. In another experiment using 120 fs laser pulses, a low fluence was used to reduce the intensity. The fluence was low enough to significantly suppress the thermal electron contribution.

4.2.1 800 nm laser excitation

An inverted VMI image obtained for C_{60} after 800 nm laser excitation with pulse duration stretched to 1 ps and intensity 1.9 TW/cm^2 (2.0 J/cm^2) is presented in Figure 4.10 together with the angle-integrated PES. The two top quadrants in the raw data were averaged and subsequently inverted. This corresponds to a polar angle interval of 0–90 degrees. The same procedure was done for the lower two quadrants corresponding to polar angle 90–180 degrees. The angle-resolved PES and a mass spectrum are presented in Figure 4.11. Apparent temperatures[4] were fitted to all angular segments and were subtracted before Lorentzian peaks were fitted to the data. Examples of the fits for the angular segments 10–20, 40–50 and 80–90 are shown in Figure 4.12. The resolution of the spectra was not good enough to distinguish all the peaks observed by Boyle *et. al.* However, the two peaks centred at 0.52 and 0.64 eV were resolved enough for an angular dependence analysis to be carried

---

[4] Apparent temperatures as a function of angle for the fully averaged raw image is also presented in chapter 3 in Figure 3.17.

out. The fitted peak areas as a function of angle are presented in Figure 4.13. The angular dependence was fitted in *Origin* using either Legendre polynomials P_0 and P_2 or P_0, P_2 and P_4 (with corresponding coefficients β_2 and β_4). It was found that the peak centred at 0.52 eV could be fitted using only the β_2 anisotropy parameter and resulted in the value $\beta_2 = -1.00 \pm 0.06$. In order to obtain a reasonable fit for the peak centred at 0.64 eV the β_4 parameter had to be included in the fit as well which gave $\beta_2 = 1.8 \pm 0.4$ and $\beta_4 = 1.0 \pm 0.4$.

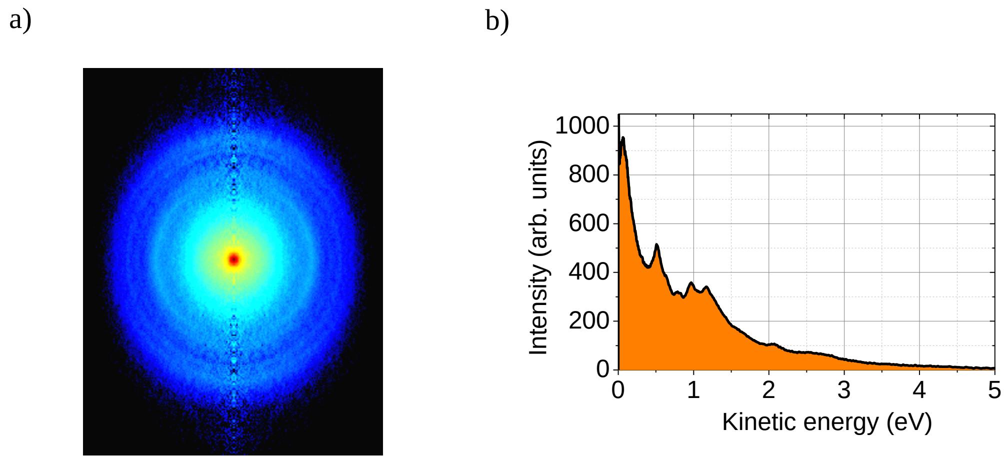

Figure 4.10: a) Inverted VMI image using BASEX for C_{60} excited with 800 nm, 1 ps laser pulses with intensity 1.9 TW/cm^2 (2.0 J/cm^2). b) Angle-integrated PES.

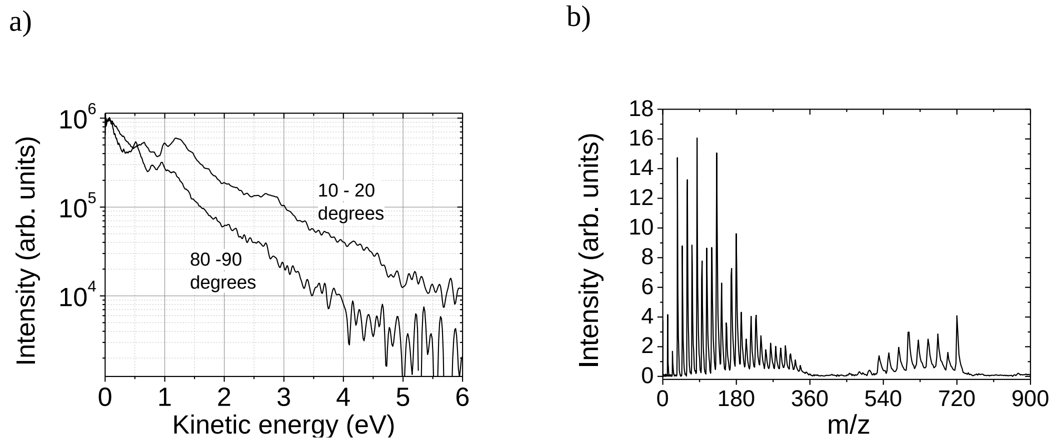

Figure 4.11: a) Angle-resolved PES for the 10 degrees angular segments for polar angle 10–20 and 80–90 degrees for the inverted VMI image in Figure 4.10 obtained after ionising C_{60} using 800 nm, 1 ps laser pulses with intensity 1.9 TW/cm^2 (2.0 J/cm^2). b) Corresponding mass spectrum.

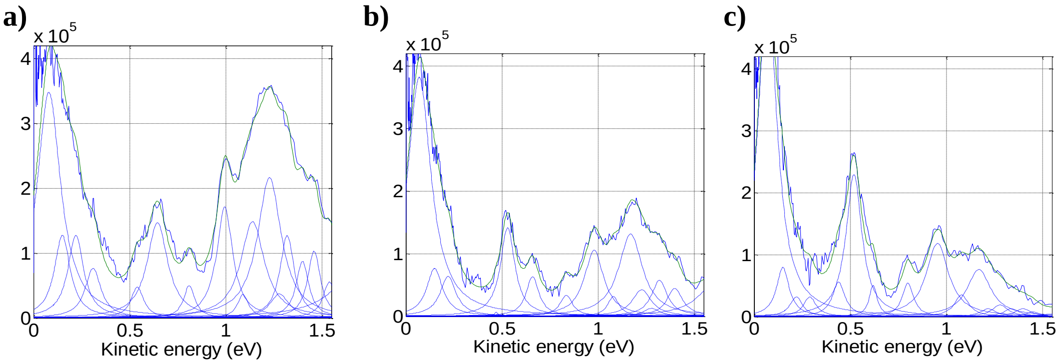

Figure 4.12: Angle-resolved PES from the data presented in Figure 4.10 (blue line) for angular segments a) 10–20 degrees; b) 40–50 degrees and c) 80–90 degrees. 800 nm, 1 ps laser pulses with intensity 1.9 TW/cm^2 (2.0 J/cm^2) were used. The fitted apparent temperature was subtracted before Lorentzian peaks (dashed lines) were fitted to the data. The green line is the sum of the Lorentzian peaks.

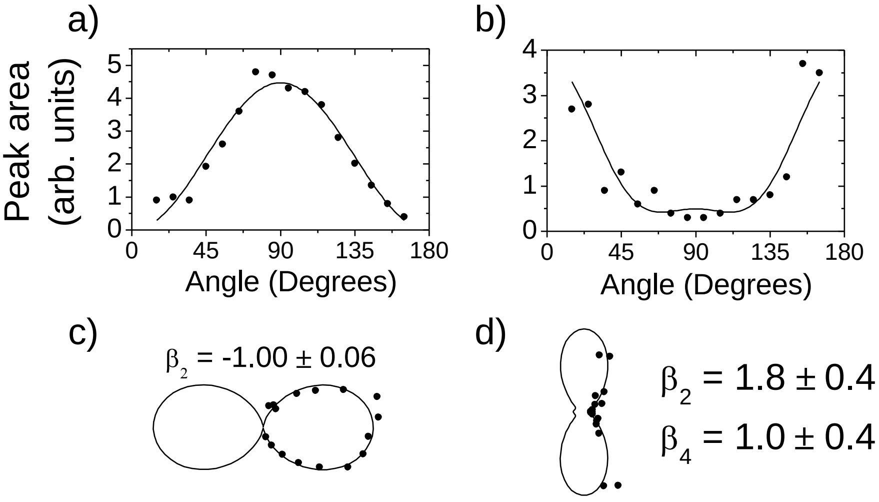

Figure 4.13: Fitted peak areas for peaks centred at a) 0.52, b) 0.64 eV from the data presented in Figure 4.10. Polar plots of the peak areas are presented for the same peak positions in c) and d). The angular dependence was fitted in *Origin* using either Legendre polynomials P_0 and P_2 or P_0, P_2 and P_4 (with corresponding coefficients β_2 and β_4). 800 nm, 1 ps laser pulses with intensity 1.9 TW/cm^2 (2.0 J/cm^2) were used.

The data were acquired using a quite high VMI extraction voltage in order to detect photoelectrons with high kinetic energies (in order to study the thermal electrons). The higher the extraction voltage, the lower the resolution of the VMI spectrometer and therefore the conditions were not optimal. From the previous work done by Boyle *et. al.* [7] it is known that the spectra become better resolved for lower laser intensities because the signal from the thermal electrons is suppressed. Therefore spectra were also acquired with the lowest power possible whilst still maintaining a reasonable signal. A pulse duration of 120 fs was used instead of 1 ps (although the bandwidth was the same). The power used resulted in mainly singly charged C_{60} in the mass spectrum. However, a small portion of doubly charged parent ions was also seen. The data were acquired using the centroiding accumulation technique to further improve the resolution. Compared to the spectra presented in chapter 3 and in Figure 4.10, the VMI extraction voltages were also lowered to improve the resolution. For the extraction conditions used, only electrons with a kinetic energy of up to about 2 eV were seen in the spectra. Most of the electrons originating from ionisation of Rydberg states are ejected along the laser polarisation direction so it was therefore desirable to use an inversion method that did not produce any noise along the polarisation axis in the VMI image. Therefore pBASEX was used. For comparison, spectra were also inverted using BASEX (which produces central-line noise) and resulting angular distributions from 10–90 degrees were fitted to a Legendre series. For all peaks it sufficed to only use Legendre Polynomials up to the fourth order to obtain a reasonable fit of the distributions. Therefore it was concluded that the number of Legendre basis functions used in the pBASEX inversion method (10) should be enough to adequately describe the data.

Although the data were accumulated for about 16 hours the signal is quite noisy. A comparison of different analysis procedures is presented in Figure 4.14. The raw image was inverted without the normal averaging over all four quadrants in the raw data. Instead, the two top quadrants were inverted and compared to an average over the bottom two quadrants. Angle-resolved spectra for 0–10 and 170–180 degrees are presented in the figure below (labelled 0–10° 2 quad. averaged and 170–180° 2 quad averaged, respectively). A spectrum obtained by averaging over all four quadrants is also shown for 0–10 degrees (labelled 4 quad. averaged). A similar spectrum obtained after using BASEX is shown for 10–20 degrees as well. The effect of fewer radial basis function used in pBASEX (126) compared to BASEX (for these data 250 was chosen but 500 basis functions can also be used) can immediately be seen because the spectrum produced by BASEX contains more noise. Although the spectra obtained from pBASEX have a lower signal to noise ratio the effect of the smoothing (by using fewer basis functions) is that peaks appear in the spectra that might not have a physical origin. For example, in the region spanning from 0.5–0.9 eV a series of peaks are seen for both spectra corresponding to 0–10 and 170–180 degrees. At first glance the peaks appear to be real since they are seen both in the southern and northern hemisphere of the electron distribution. However, when the spectrum is plotted in units of pixels the spacing between the peaks is constant and is similar to the width of the radial basis functions. The spacing in units of pixels is the same as for the structure seen at kinetic energies above 1.5 eV and because previous work has shown that the Rydberg series converges on the photon energy and the spacing between peaks becomes narrower closer to the ionisation limit, these peaks cannot have physical origin. They arise due to noise that becomes averaged over a few pixels because of the low number of radial basis functions and appears as peaks. Therefore the raw image was smoothed using the method described in chapter 2 prior to inversion. The result is also shown in the figure below (labelled 0–10 degrees, averaged and smoothed) where some of the structure is no longer seen. A comparison is also made from a measurement acquired by using the continuous acquisition method. The result was inverted using BASEX (again, 250 basis functions were chosen) and the PES for 10 – 20 degrees is also presented in the figure below (dark blue line).

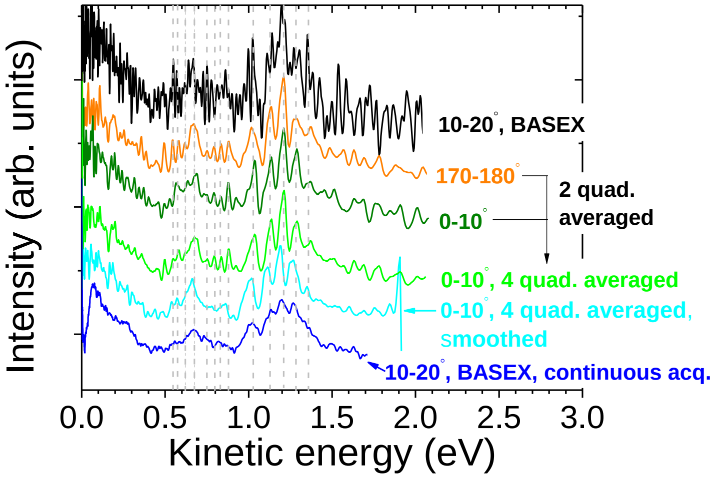

Figure 4.14: Inverted angle-resolved PES for polar angles 0–10, 10–20 and 170–180 degrees obtained after ionising C_{60} with 800 nm, 120 fs laser pulses. The spectra have been displaced vertically for display purposes.

It can be concluded that the peaks need to be better resolved in order to reduce any ambiguities regarding the inversion method (possible experiments are discussed later in this chapter). The best resolved spectra presented by Boyle *et. al.* [7] were taken with a laser bandwidth of about 10 meV. The laser bandwidth used in the present study is almost twice as large. Spectra presented by the aforementioned authors obtained with a similar laser bandwidth show that it is not possible to clearly resolve the peaks above kinetic energies of about 1.1 eV when using 800 nm. In the present study, a series of peaks with peak positions corresponding to what has previously been published are seen in all the spectra in Figure 4.14 (although poorly resolved in the one obtained using continuous acquisition). Since the peak positions are very similar to those found by Boyle *et. al.* the angular dependence for these peaks has been analysed. The analysis was carried out on the data that were smoothed before inversion. The inverted VMI image is presented in Figure 4.15. The corresponding angle-integrated PES and mass spectrum are presented in Figure 4.16.

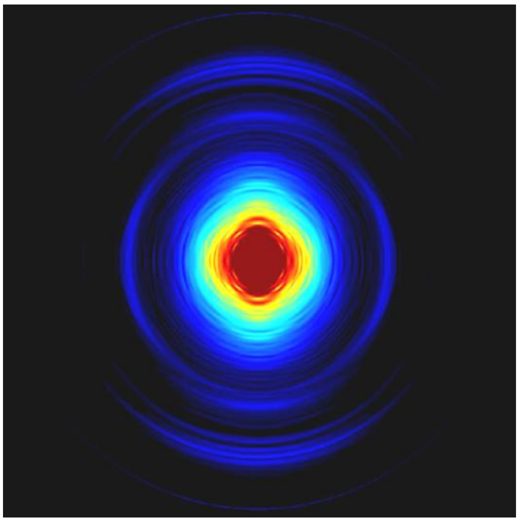

Figure 4.15: Inverted VMI image from pBASEX of C_{60} ionised with 800 nm, 120 fs laser pulses. The intensity was 3.7 ± 0.4 TW/cm^2 and the bandwidth of the laser was 9 nm (17 meV). The colour scale is saturated in the centre of the image to enhance the rings corresponding to photoelectrons of interest in the current study. The raw image after smoothing is presented in Figure 2.23 in Chapter 2.

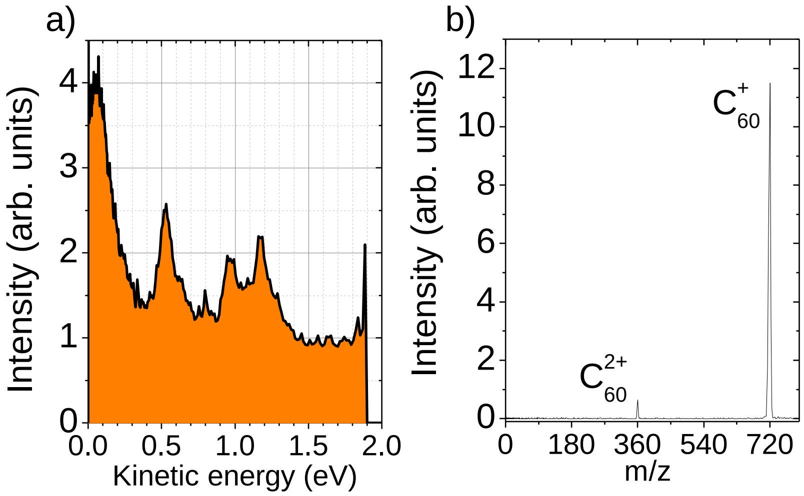

Figure 4.16: C_{60} ionised using 120 fs, 800 nm laser excitation of intensity 3.7 ± 0.4 TW/cm^2. (a) Angle-integrated PES obtained from the inverted image shown in Figure 4.15. The peak just below 2 eV is from the inversion procedure and arises when the raw image has non-zero signal at the edge of the image. (b) Mass spectrum showing that the laser intensity was just high enough to produce doubly charged C_{60}.

The angle-resolved PES for polar angle 0–90 degrees are shown in Figure 4.17 binned into 10 degrees intervals. The PES for 0–10 and 80–90 degrees can be directly compared to Figure 4.4 where PES are presented using a linear time-of-flight spectrometer with the laser polarisation direction directed parallel to the spectrometer axis (comparable to 0–10 degrees) and perpendicular (80–90 degrees). The PES corresponding to emission along the laser polarisation direction show a peak around 0.65 eV in both Figure 4.4 and Figure 4.17. Similarly a peak around 0.54 eV is seen for the perpendicular PES. At 1.0 eV there is a peak that appears to drift towards an energy of 0.95 eV with higher angle. The other peaks seen in the PES do not have this large drift and therefore it is very likely that the peak is actually comprised of two or more peaks. This is further supported by the asymmetric appearance of the peak in the 0–10 degrees PES which seems to have a shoulder at 0.95 eV. The other peaks that are clearly seen in the 0–10 degrees PES disappear in the noise for higher angles and it is difficult to separate true peaks from peaks arising due to the limited number of basis functions used in the inversion procedure.

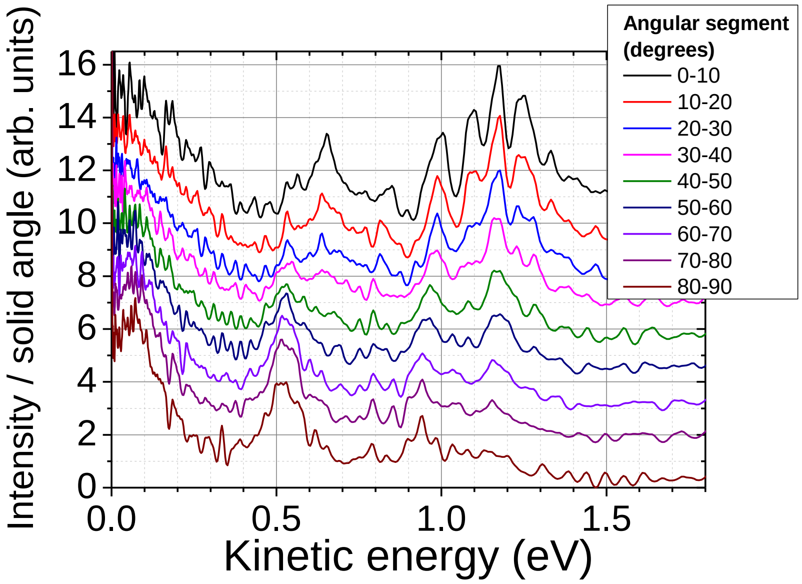

Figure 4.17: C_{60} ionised using 120 fs, 800 nm laser excitation of intensity 3.7 ± 0.4 TW/cm^2. Angle-resolved PES for the inverted VMI image shown in Figure 4.15. The spectra are shifted vertically for display purposes.

A series of Lorentzian peaks were fitted to the angle-resolved PES centred at the peak positions reported by Boyle *et. al.* [7]. Angle-resolved spectra including fits are shown for 0–10, 40–50 and 80–90 degrees in Figure 4.18 – Figure 4.20. Fitted peak areas as a function of angular segment are plotted in Figure 4.21 and Figure 4.22 for peaks centred at 0.54, 0.64, 0.95 and 1.0 eV. For two of the peaks (a and c) it was enough to only include P_2 in the fit whereas for b) and d) Legendre polynomial up to P_4 were required (excluding odd numbers).

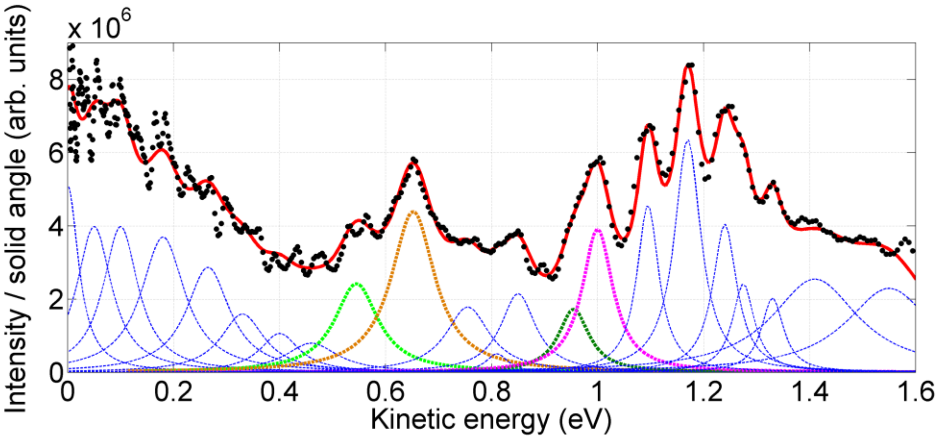

Figure 4.18: C_{60} ionised using 120 fs, 800 nm laser excitation of intensity 3.7 ± 0.4 TW/cm^2. PES for 0–10 degrees obtained from Figure 4.15. Lorentzian peaks have been fitted to the experimental data (black dots). The red line is the sum of the fitted peaks.

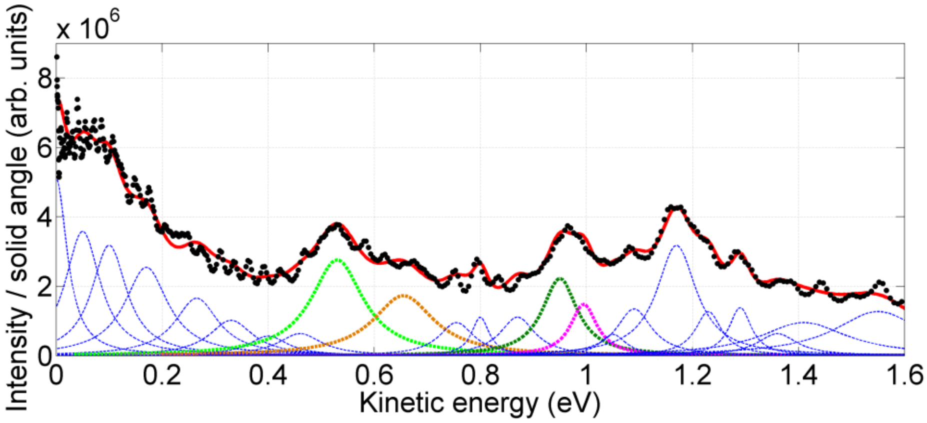

Figure 4.19: C_{60} ionised using 120 fs, 800 nm laser excitation of intensity 3.7 ± 0.4 TW/cm^2. PES for 40–50 degrees obtained from Figure 4.15. Lorentzian peaks have been fitted to the experimental data (black dots). The red line is the sum of the fitted peaks.

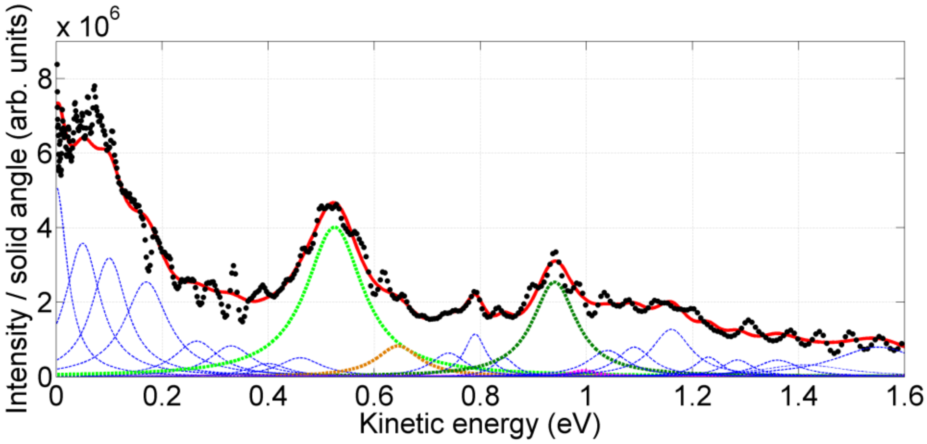

Figure 4.20: C_{60} ionised using 120 fs, 800 nm laser excitation of intensity 3.7 ± 0.4 TW/cm^2. PES for 80–90 degrees obtained from Figure 4.15. Lorentzian peaks have been fitted to the experimental data (black dots). The red line is the sum of the fitted peaks.

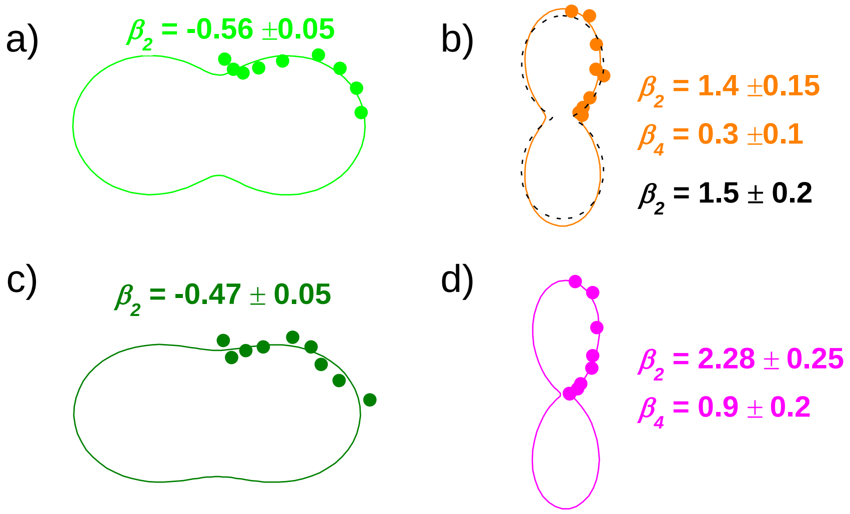

Figure 4.21: Polar plot of fitted peak areas for peaks centred at a) 0.54, b) 0.65, c) 0.95 and d) 1.0 eV. The angular dependence was fitted in *Origin* using either Legendre polynomials P_0 and P_2 or P_0, P_2 and P_4 (with corresponding coefficients β_2 and β_4). The colours correspond to the coloured Lorentzian peaks in Figure 4.18 and Figure 4.20.

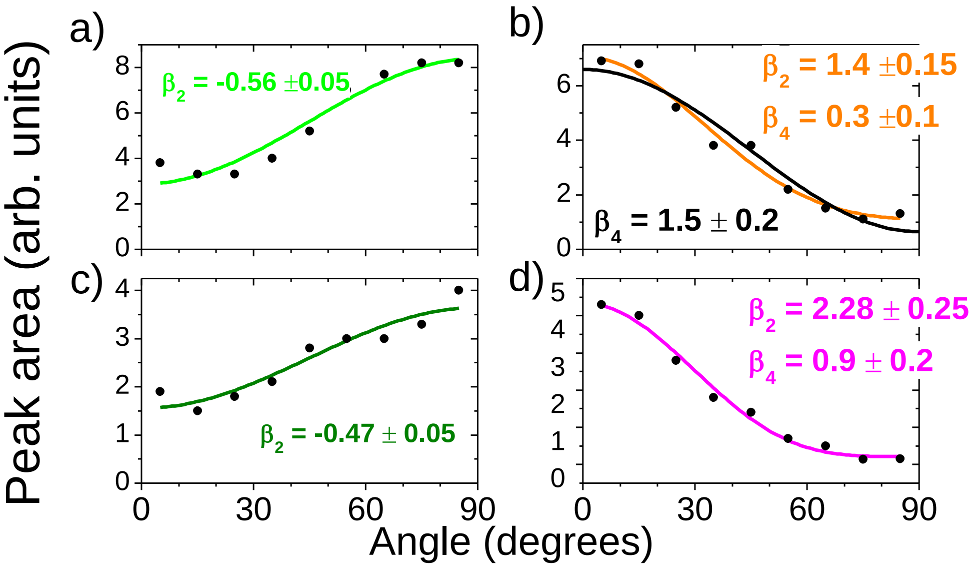

Figure 4.22: Same as Figure 4.21 but plotted in Cartesian coordinates.

The number of fitted Legendre polynomials indicates that the peaks at 0.54 and 0.95 eV result from single-photon ionised states. For the peak at 0.65 eV the best fit was obtained by including the β_4 anisotropy parameter. However, a reasonable fit was also obtained using only β_2 which would again suggest one-photon ionisation of the initial state. When only β_2 was included in the fit for the peak at 1.0 eV, a β_2 value greater than 2 was obtained and the overall fit was quite poor. A more reasonable fit was obtained when β_4 was also included. This suggests that the peak is either a result of a two-photon ionisation process or that the state has a memory of how it was populated. The binding energy of the initial state in the latter case is given by the photon energy minus the electron kinetic energy. This is also true if it is a resonant two-photon process. However, if the initial state is ionised with two photons in a non-resonant process, the binding energy is given by $2h\upsilon - E_{kin}$. A table of the peaks including the fitted β parameters are presented in the conclusion section. The peak positions are also compared to binding energies of the SAMOs.

The results presented in chapter 3 for pulse durations from 2 – 4 ps show that at the onset of thermionic emission the Rydberg structure is reduced (Figure 3.16). The fact that the Rydberg structure disappears around these pulse durations is known [7] and that thermionic emission becomes dominant at these pulse durations is also known [89]. It is possible that the Rydberg states are populated through the heated thermal electron system acting as a QC. For longer pulse durations, the energy in the valence system has time to couple to vibrations and the electronic excitation decays back to the ground electronic state. The energy difference between the ground electronic state and the Rydberg states is too large and therefore the excitation of the Rydberg states could be suppressed at the onset of thermionic emission.

4.2.2 400 nm laser excitation

In order to investigate whether the s-SAMO is populated in C_{60}, experiments using 400 nm light were carried out. First, the bandwidth-limited output from the SHBC was used (4–5 ps, 5 cm^{-1} bandwidth) but as can be seen in Figure 3.5 in chapter 3 the relatively long pulse duration resulted in mainly structure-less thermionic emission. At the highest power some structure can be seen but the signal for these peaks is too low to perform any analysis. This is in agreement with two-photon photoemission spectroscopy of excited states of thin C_{60} films on silver surfaces [110]. The peak width in these spectra indicated a lifetime around 5 – 50 fs although it might be expected that this lifetime will be longer in isolated molecules in the gas-phase. Experiments were therefore carried out with femtosecond laser pulses. The fundamental output from the Legend was frequency doubled in a BBO crystal and the pulse duration can be estimated to be the same as the fundamental (therefore it is estimated to be around 120 – 130 fs). The data were acquired using the continuous acquisition method that was described in chapter 2. The VMI image inverted using pBASEX can be seen in Figure 4.23 (the same image inverted with BASEX is shown in Figure 3.2 together with a mass spectrum in chapter 3). The laser intensity was 3×10^{11} W/cm^2.

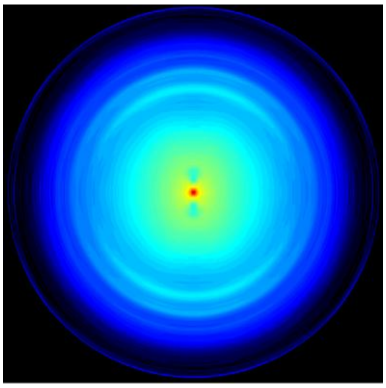

Figure 4.23: VMI image inverted using pBASEX of C_{60} ionised with 400 nm, 130 fs laser pulses. The laser intensity was $(3 \pm 1) \times 10^{11}$ W/cm^2. The corresponding mass spectrum is presented in Figure 3.2 in chapter 3.

In the previous chapter it was shown that the thermal electrons' contribution could be well-described by an exponential distribution and that the distribution was isotropic with respect to emission angle. A thermal background was therefore fitted to all angle-resolved

PES and subsequently subtracted. Examples of angle-resolved PES after subtracting the thermal electron contribution are shown for 0–10 degrees in Figure 4.24, 40–50 degrees in Figure 4.25 and 80–90 degrees in Figure 4.26. The spectrum along the laser polarisation direction is similar to the one presented by Boyle *et. al.* in ref. [7]. Lorentzian peaks were fitted by eye and are also shown in the figures (peak positions are given in the table in the conclusion section). Polar plots of the fitted peak areas are shown for peaks centred at 1.25, 1.70, 2.10 and 2.19 eV in Figure 4.27. The peak areas as a function of polar angle are shown in Figure 4.28.

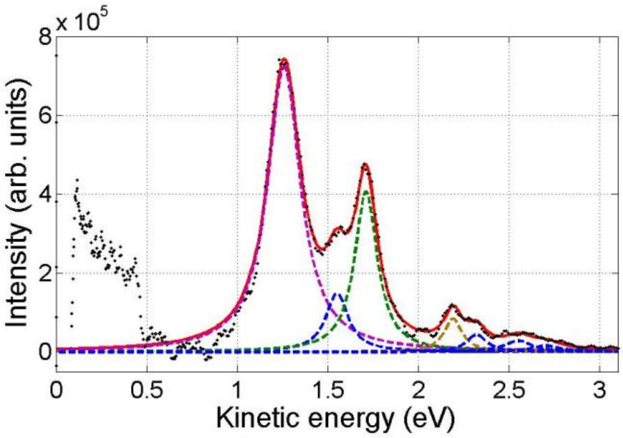

Figure 4.24: Angle-resolved PES for 0–10 degrees from the inverted image shown in Figure 4.23. A thermal electron contribution has been subtracted. The laser wavelength was 400 nm and the pulse duration 120–130 fs. The intensity was (3 ± 1) × 10^{11} W/cm^2. Black dots are experimental data and the red line is the sum of fitted Lorentzian peaks (dashed lines).

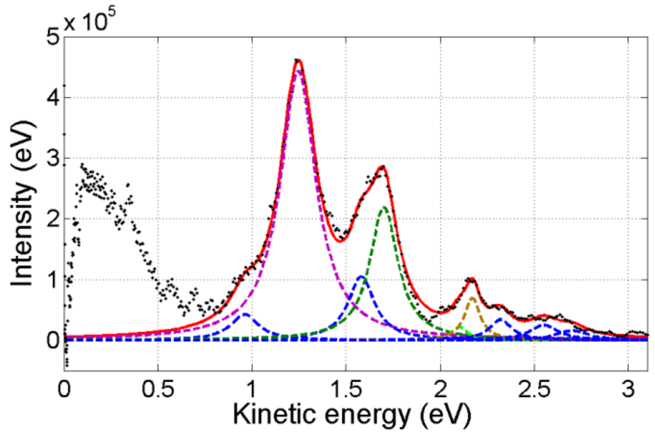

Figure 4.25: Angle-resolved PES for 40–50 degrees from the inverted image shown in Figure 4.23. A thermal electron contribution has been subtracted. The laser wavelength was 400 nm and the pulse duration 120–130 fs. The intensity was (3 ± 1) × 10^{11} W/cm^2. Black dots are experimental data and the red line is the sum of fitted Lorentzian peaks (dashed lines).

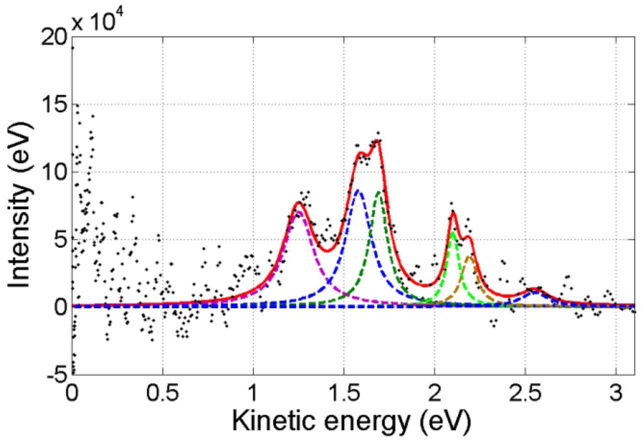

Figure 4.26: Angle-resolved PES for 80–90 degrees from the inverted image shown in Figure 4.23. A thermal electron contribution has been subtracted. The laser wavelength was 400 nm and the pulse duration 120–130 fs. The intensity was (3 ± 1) × 10^{11} W/cm^2. Black dots are experimental data and the red line is the sum of fitted Lorentzian peaks (dashed lines).

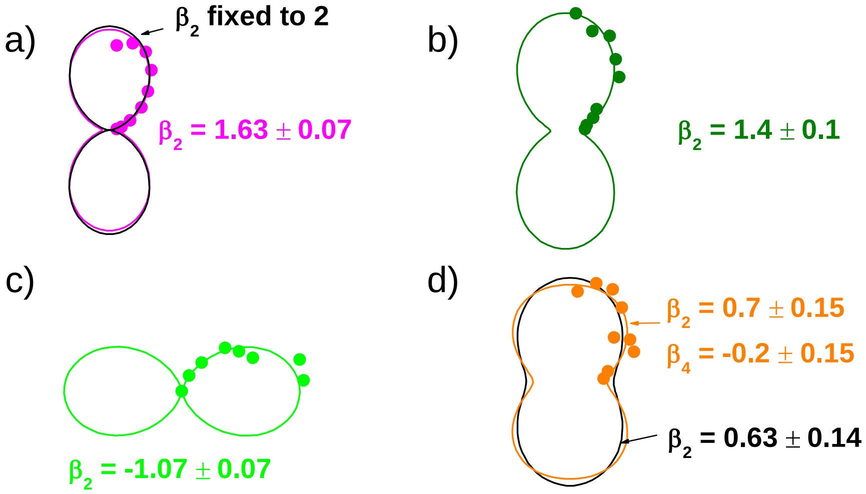

Figure 4.27: Polar plot of fitted peak areas for peaks centred at a) 1.25, b) 1.70, c) 2.10 and d) 2.19 eV. The angular dependence was fitted in *Origin* using either Legendre polynomials P_0 and P_2 or P_0, P_2 and P_4 (with corresponding coefficients β_2 and β_4). The colours correspond to the coloured Lorentzian peaks in Figure 4.24 – Figure 4.26. The black line in a) corresponds to a fit where β_2 was fixed at a value of 2.0. In d) a fit was also made using only P_0 and P_2 (black line).

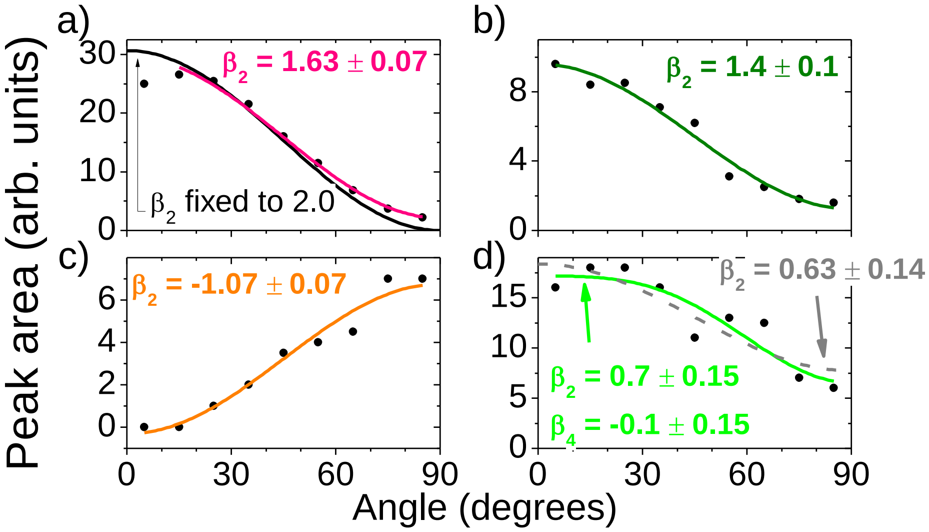

Figure 4.28: Same as Figure 4.27 but in Cartesian coordinates.

When analysing the data obtained using 400 nm and the continuous acquisition method, it has to be pointed out that the results suffer from an experimental artefact due to damage of the VMI detector. When obtaining the VMI image of xenon ionised with the same wavelength, the detector was damaged due to a very high electron signal. The same pattern as seen in Figure 2.31 in chapter 2 was also seen on images taken afterwards (seen in the centre of image Figure 4.23). In Figure 4.29 the raw angle-resolved spectrum obtained after ionisation of Xe is compared to the raw C_{60} spectrum for 0–10 degrees. The abscissa is given in units of pixels. It can be seen that the main peak at 1.25 eV coincides with a xenon peak (although in energy scale these two peaks do not coincide because the extraction voltages were different). However, already at 20–30 degrees the magnitude of the xenon peak is greatly reduced and will probably not influence the spectrum. The peak area corresponding to the 0–10 degrees angular interval was therefore excluded from the fit shown in Figure 4.27. The xenon peak at about 220 pixels corresponds to a kinetic energy of about 0.7–0.8 eV for the C_{60} measurement. It is probably the reason why the spectrum in Figure 4.24 has an intensity dip in this energy region.

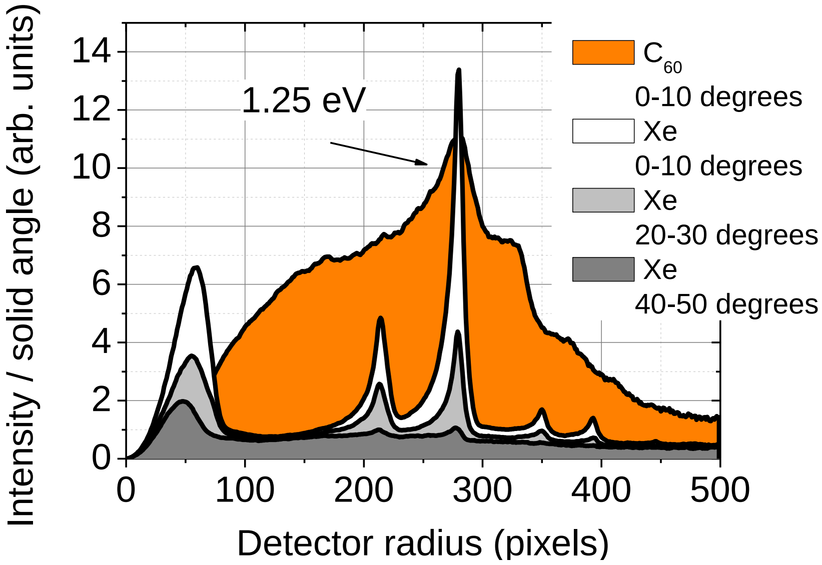

Figure 4.29: Raw velocity distributions as a function of detector radius for a measurement made with the same laser wavelength and pulse duration on Xe (raw and inverted VMI images are presented in Figure 2.31 in chapter 2). The signal for the xenon measurement was too high and caused some damage to the detector. Some of the xenon peaks coincide with the C_{60} measurements.

The binding energy of the peak at 1.25 eV is about 1.9 eV which coincides with the binding energy of the s-SAMO (about 2 eV from DFT calculations [9]). The fitted β parameter was found to be 1.63 ± 0.07 when the datum point for 0–10 was excluded from the fit (justified above). In Figure 4.27 a) a fit is also shown where the beta parameter was fixed to a value of 2 (dashed black line). The fit is reasonable and considering that it is possible that the detector damage extends to angles 10–20 degrees, it is possible that the PAD consists of a pure p-wave. If the initial state is the s-SAMO and the orbital angular momentum quantum number ℓ is a good quantum number, then the PAD should be a pure p-wave (β_2 = 2). This indicates that the peak at 1.25 eV may indeed be coming from single-photon ionisation of the s-SAMO.

Another measurement was also performed using a slightly higher laser intensity of 6×10^{11} W/cm^2. The inverted image together with a mass spectrum and the angle-resolved PES were presented in Figure 3.2 in chapter 3. In this case the only peak that was resolved enough to perform a quantitative angular analysis was the peak at 1.25 eV. The fitted peak area as a function of polar angle is presented in Figure 4.30 where the analysis was carried out by only averaging two quadrants of the raw image at the time (similar to one of the spectra presented in Figure 4.14). The raw image was inverted using BASEX and therefore the 0 – 10 degrees angular segment was not included in the analysis (due to the central-line noise produced from the inversion procedure). An anisotropy parameter of 1.5 ± 0.1 was found which is slightly lower than the value for the lower laser intensity (although within error margins).

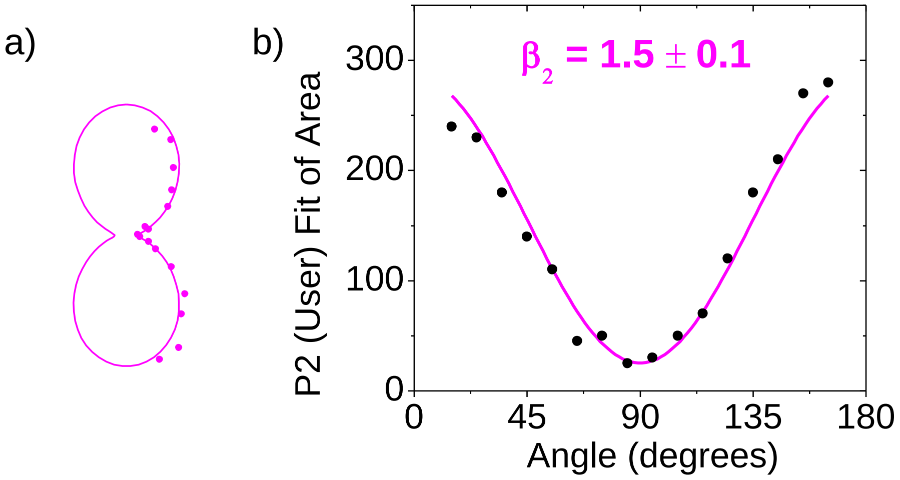

Figure 4.30: a) Polar plot of fitted peak areas for peak centred at 1.25 eV from the inverted image presented in Figure 3.2 for a laser intensity of 6×10^{11} W/cm^2 (130 fs, 400 nm). The angular dependence was fitted in *Origin* using Legendre polynomials P_0 and P_2 (with corresponding anisotropy coefficient β_2). b) Same as a) but in a linear plot.

In order to reduce the influence of the detector damage, an experiment using the centroiding technique was performed. This also allowed for the use of a lower laser intensity since this technique is more sensitive than the continuous acquisition method. The results are presented in Figure 3.3 in chapter 3. The peak structure was analysed on smoothed raw data inverted using pBASEX and a VMI image is presented in Figure 4.31. The angle-resolved PES are presented in Figure 4.31 b) and Figure 4.32. The fitted peak areas as a function of angle are presented in Figure 4.33. For the peak centred at 1.25 eV the fitted anisotropy parameter was $\beta_2 = 2.0 \pm 0.1$ in excellent agreement with what could be expected from the s-SAMO. The structure outside the 1.25 eV peak was not well resolved although a value of $\beta_2 = 1.0 \pm 0.15$ was obtained for the peak at 0.7 eV.

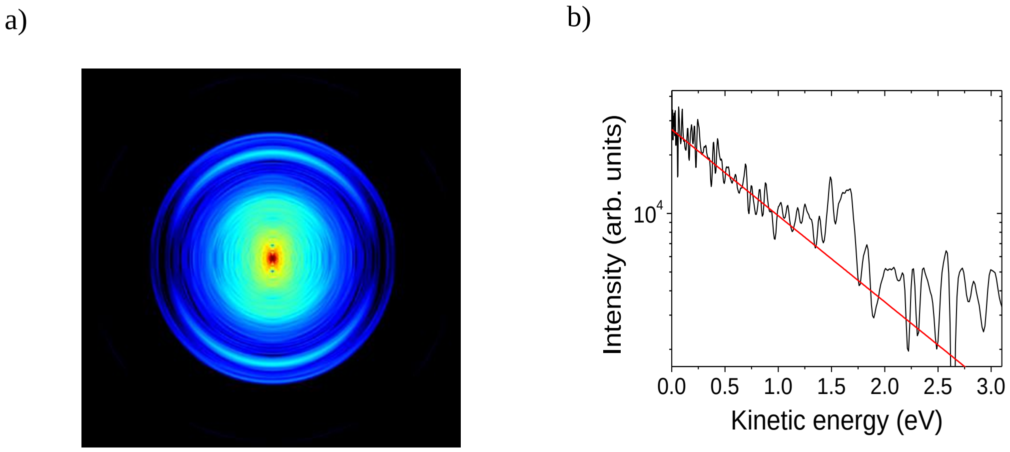

Figure 4.31: a) Inverted VMI image using pBASEX of C_{60} ionised with 400 nm, 120 fs laser pulses of intensity $1.4 \pm 0.7 \times 10^{11}$ W/cm^2 (130 fs, 400 nm). The same image inverted using BASEX is presented in Figure 3.3 in chapter 3. b) Angle-resolved PES for the 80–90 angular segment. An exponential distribution (corresponding to an apparent temperature of 0.98 eV) was fitted to the data (red line) and subsequently subtracted from all other angular segments.

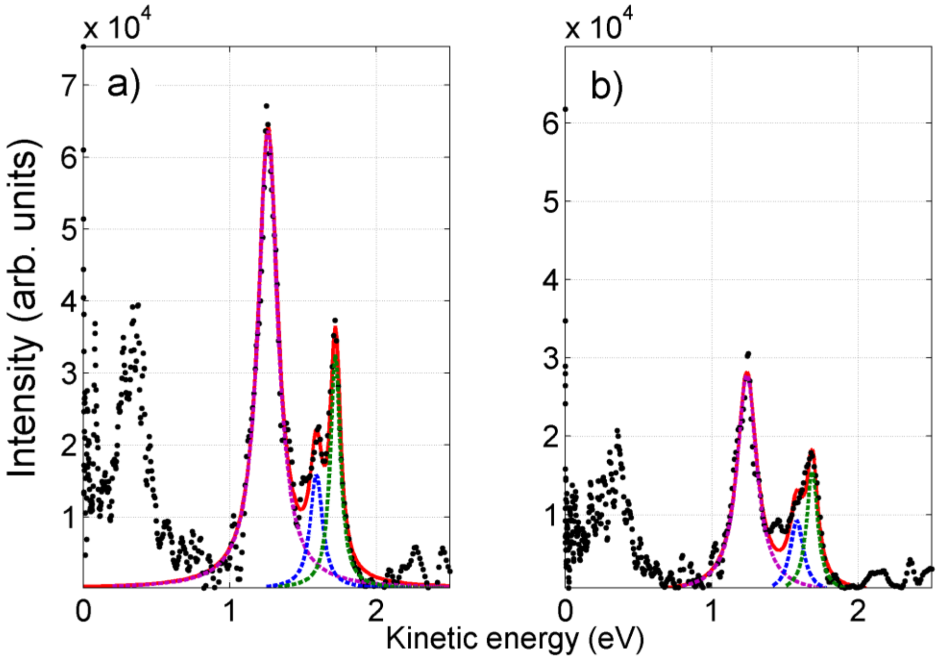

Figure 4.32: Angle-resolved PES of the inverted image in Figure 4.31 showing angular segments corresponding to polar angle of a) 0–10 degrees and b) 40–50 degrees. Spectra obtained after ionising C_{60} using 400 nm, 130 fs laser excitation of intensity $1.4 \pm 0.7 \times 10^{11}$ W/cm^2.

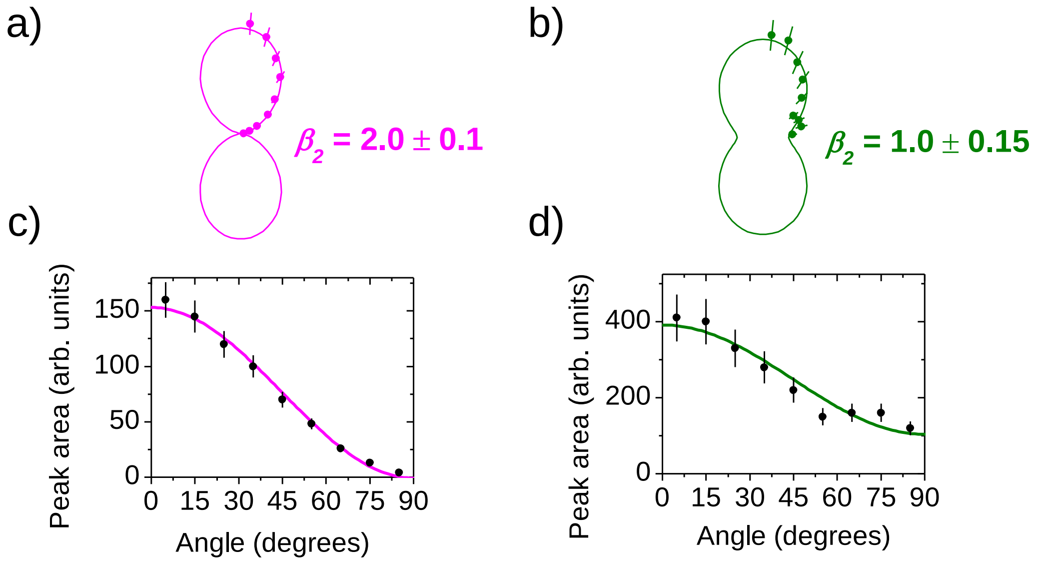

Figure 4.33: Polar plots of fitted peak areas for peaks centred at a) 1.25 eV and b) 1.7 eV. The angular dependence was fitted in *Origin* using Legendre polynomials P_0 and P_2 (with corresponding anisotropy coefficient β_2). c,d) Same as a,b) but in a linear plot.

It is possible that the s-SAMO acts as an intermediate state in a REMPI process which would result in a PAD well-characterised with only the β_2 parameter. However, the peak at 1.7 eV (corresponding to the p-SAMO) also shows a simple PAD. This speaks against a REMPI process since if this peak would be the result of a two-photon process it would have been necessary to also include the β_4 parameter in the fit. Therefore it can be concluded that the peaks corresponding to the s- and p-SAMOs are the results of a single-photon ionisation of a randomly oriented sample.

Assuming a single-photon ionisation mechanism, the two peaks at 2.10 and 2.19 eV in Figure 4.27 c, d) have the same binding energy as the two peaks in Figure 4.13 c,d) and Figure 4.21 a,b) obtained using 800 nm. The fitted anisotropy parameters are different but the angular dependences follow the same trend in all figures. The binding energies are in agreement with the s'- and d- SAMOs (see Figure 4.9 for labelling of SAMOs). A similar trend is seen in the 800 nm data for the peaks at 0.95 and 1.0 eV (Figure 4.21 c,d) although the angular dependence of the peak with the highest kinetic energy was best described using both β_2 and β_4.

The observation of a lower anisotropy parameter for what could be the s-SAMO with higher laser intensities could be an indication that multielectron dynamics are influencing the PADs. This is in agreement with the observation that the apparent temperature increases with laser power. The width of the fitted Lorentzian peaks indicates a lifetime of about 3 fs (for the lowest laser intensity) to 10 fs (for the highest laser intensity). This is in agreement with the two-photon photoemission spectroscopy results in ref. [110]. The peaks become narrower for lower pulse intensities which indicate a longer lifetime. If more electrons are excited for higher laser intensities this could mean that the electron-electron interaction time is reduced which would shorten the lifetimes. However, it is possible that other broadening effects influence the peak widths in which case the widths are not related to the natural lifetime of the states (which would be longer).

4.2.3 Excited electronic states in C_{70}

The PES of C_{70} presented in a log-lin scale in the appendix Figure H-3 is shown in a linear scale in Figure 4.34 below. Peaks can be seen at about 0.5, 0.6, 0.9 and 1.0 eV in good agreement with C_{60} within 10 %. Furthermore, the peaks at 0.6 and 1.0 eV show the largest emission along the laser polarisation. The peaks at 0.5 and 0.9 eV show maximum emission perpendicular to the laser polarisation. This angular dependence is similar to the one observed for C_{60} peaks with approximately same kinetic energy.

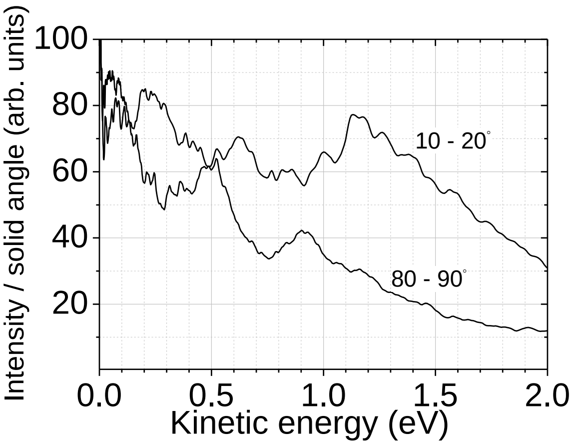

Figure 4.34: C_{70} ionised using 800 nm, 117 fs laser excitation of intensity 7.5 ± 0.8 TW/cm^2. The same PES for two angular intervals (indicated in the figure) as presented in Figure H-3 (d) in the appendix but in a linear scale. The peak positions are in agreement with what is observed for C_{60}.

Low laser intensity experiments on C_{70} using the centroiding acquisition method were also performed (inverted VMI image and mass spectrum are presented in the appendix). The wavelength was 400 nm and pulse duration 120–130 fs. The same peak positions as for C_{60} were found. As was mentioned in chapter 2, the 80–90 degrees PES showed no signs of any structure and instead a pure exponential distribution was found. The apparent temperature found for this angular segment was subtracted from all other segments and Lorentzian peaks were fitted to the peaks centred at 1.25, 1.54 and 1.7 eV. Due to the high noise level it was not possible to fit peaks with higher kinetic energies. Examples of the 0–10 and 40–50 degrees angular segments are given in Figure 4.35. Polar plots of the fitted peak areas for the peaks centred at 1.25 and 1.7 eV are shown in Figure 4.36. The fitted anisotropy parameter for the peak at 1.25 eV was β_2 = 1.9 ± 0.1 in excellent agreement with the s-SAMO and for the peak at 1.7 eV β_2 = 1.3 ± 0.1.

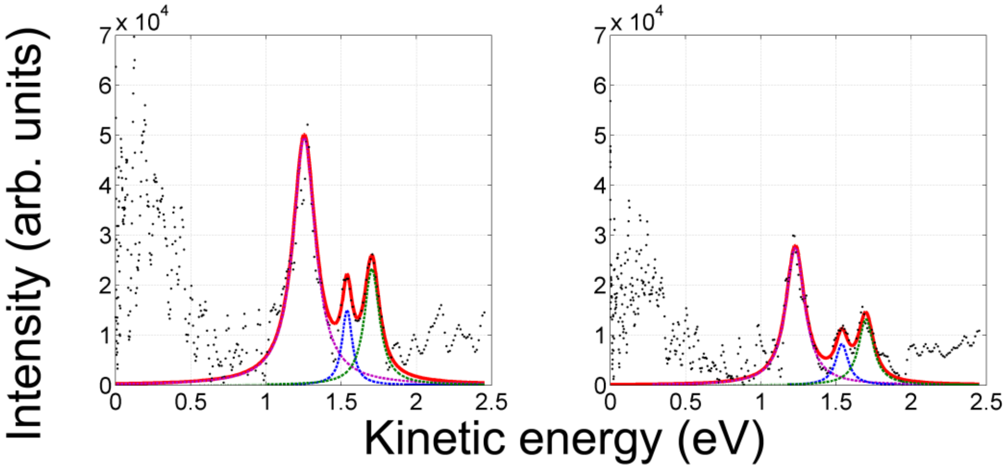

Figure 4.35: 10 degrees angle-resolved PES from the inverted image in Figure F-1 (appendix) for polar angle a) 0–10 degrees and b) 40–50 degrees. The black dots are experimental data points, dashed lines are Lorentzian peaks and full red line is the sum of the fitted peaks. Spectra obtained after ionising C_{70} using 400 nm, 130 fs laser excitation of intensity $1.3 \pm 0.6 \times 10^{11}$ W/cm^2.

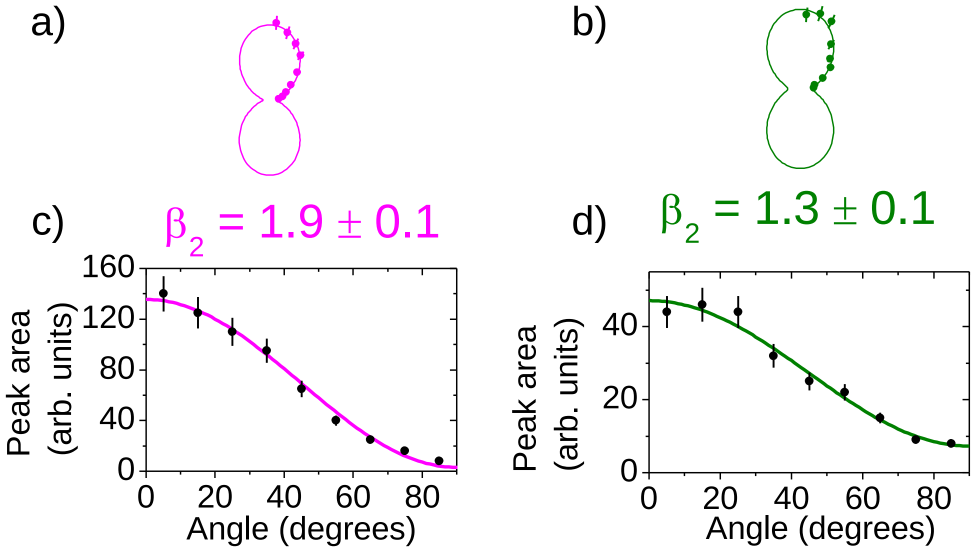

Figure 4.36: Polar plots of the fitted peak areas of the peaks centred at 1.25 and 1.7 eV from the inverted image in Figure F-1 (appendix). The angular dependence was fitted in *Origin* using Legendre polynomials P_0 and P_2 (with corresponding coefficient β_2). The colours correspond to the coloured Lorentzian peaks in Figure 4.35. The errors were estimated during the fitting procedure to be about 10 %.

4.3 Conclusions

The measured PADs are consistent with either a single- or two-photon ionisation of excited electronic states. The detected binding energies for both wavelengths used in this study are in agreement with the SAMOs as shown in Table 4 and Table 5. For the peak with binding energy corresponding to the s-SAMO, the PAD is in excellent agreement with the assignment for both C_{60} and C_{70}. For the states with higher angular momenta it would be necessary to compare experimentally determined β parameters for different excitation wavelengths with calculations as was done in e.g. refs. [53, 54]. A summary of fitted peak positions including anisotropy parameters for the two wavelengths is given in Table 4 and Table 5. Measurements on C_{70} using 800 nm laser light showed very similar peak positions and angular dependences as was measured for C_{60}. It was speculated, based on measurements using stretched pulses, that the thermalised electronic system could act as a QC to reach the Rydberg states. The present study can rule out the possibility that the observed structure is due to a coherent multiphoton ionisation process from the ground electronic state.

Table 4: Fitted peak positions corresponding anisotropy parameters for C_{60} from the angle-resolved PES obtained using both 400 nm ([a], [b], [c]) and 800 nm ([d],[e]). Errors in peak positions are estimated from the small drift in peak position as was also observed in the ionisation of xenon presented in chapter 2. Some peaks could arise due to a two-photon process and the corresponding binding energy is therefore also given (equal to $2hv - E_{kin}$). The corresponding PES can be found for [a] in Figure 4.31, [b] in Figure 4.23, [c] in Figure 3.2 a), [d] in Figure 4.15 and [e] in Figure 4.10.

SAMO	**E_{bind} (eV) DFT calc. [9]**	**E_{bind} (eV) exp.**	**$2hv$ E_{bind} (eV) exp.**	**β_2**	**β_4**
s	2.0	1.86 ± 0.02 [a]	-	2.0 ± 0.1	-
		1.86 ± 0.02 [b]	-	1.63 ± 0. 7	-
		1.86 ± 0.02 [c]	-	1.5 ± 0.1	-
p	1.5	1.40 ± 0.01[b]	-	1.4 ± 0.1	-
		1.40 ± 0.01[a]	-	1.0 ± 0.15	-
s’,d	1.0	1.00 ± 0.01[b]	-	–1.07 ± 0.07	-
		0.92 ± 0.01[b]	-	0.63 ± 0.15	-
		0.92 ± 0.01[b]	*4.00 ± 0.02*	*0.7 ± 0.15*	*–0.1 ± 0.15*
		1.01 ± 0.02 [d]	-	–0.56 ± 0.05	-
		0.90 ± 0.01 [d]	-	1.5 ± 0.2	-
		0.90 ± 0.01 [d]	*2.45 ± 0.04*	*1.4 ± 0.15*	*0.3 ± 0.1*
		1.01 ± 0.01 [e]		–1.00 ± 0.06	-
		0.92 ± 0.03 [e]	*2.5 ± 0.07*	*1.8 ± 0.4*	*1.0 ± 0.4*
?	-	0.60 ±0.01 [d]	-	–0.47 ± 0.05	-
?	-	0.55 ± 0.01 [d]	2.10 ± 0.02	2.28 ± 0.25	0.9 ± 0.2

Table 5: Same as Table 4 but for C_{70}. Corresponding spectra can be found for [a] in Figure F-1 (400 nm) and [b] in Figure 4.34 (800 nm). For the 800 nm measurements ([b]) no numerical values were assigned to the anisotropy parameters.

SAMO	**E_{bind} (eV) DFT calc. [9]**	**E_{bind} (eV) exp.**	**$2hv\ E_{bind}$ (eV) exp.**	**β_2**	**β_4**
s	2.0	1.86 ± 0.02 [a]	-	1.9 ± 0.1	-
p	1.5	1.41 ± 0.02 [a]	-	1.3 ± 0.1	-
s’,d	1.0	1.06 ± 0.01 [b]	-	Perpendicular	-
		0.93 ± 0.01 [b]	2.10 ± 0.02	Parallel	-
?	-	0.64 ± 0.02 [b]	-	Perpendicular	-
?	-	0.55 ± 0.02 [b]	2.10 ± 0.02	Parallel	-

4.4 Outlook

It would be desirable to further resolve the peaks converging on the photon energy in the 800 nm experiment. However, the bandwidth of the laser is too large. There is a possibility to pump a non-collinear optical parametric amplifier (NOPA) with the SHBC producing bandwidth-limited ps pulses over a wide range of wavelengths (about 500 – 2200 nm). However, as was demonstrated in chapter 3, the pulse duration is too long from the SHBC (and therefore also the NOPA) so that the states have time to decay before they are ionised and the main ionisation mechanism is thermionic emission. However, it could be possible to prepare the system with the 800 nm laser and then ionise the molecules using the ps NOPA in a pump-probe experiment. The narrow bandwidth of the laser would hopefully enable better resolved spectra than what have previously been reported. With the NOPA the wavelength dependence of the β parameter could also be studied which would help further in deducing the character of the initial state (if compared to calculations). By changing the probe wavelength an even better resolution should be possible. For example, if a photon energy was chosen just above the binding energy of a particular state, the photoelectrons emerging from that state would have a low kinetic energy. The resolution of the VMI detector is better for photoelectrons with low kinetic energy and the peak corresponding to the chosen state could be studied with better resolution compared to when using a shorter wavelength. This technique is called slow electron velocity-map imaging (SEVI) and was developed by Neumark and colleagues [111]. The method is based on zero-kinetic energy photoelectron spectroscopy (ZEKE) below threshold.

It would be interesting to obtain calculated binding energies for higher lying SAMOs. If these calculated energies converged on the binding energies measured by Boyle *et. al.* this could help understand where the SAMOs meet ordinary molecular Rydberg states.

Boyle suggests that a pump-probe experiment using the fourth harmonic of a titanium sapphire laser would gain more insight into the possibility of a doorway state since ionisation from this state could be done with the 4th harmonic [88]. Also a plot of the Rydberg yield as a function of laser intensity could perhaps reveal a more specific intensity dependence. However, this requires assumptions to be made about the thermal background which might influence the intensity dependence.

It was discussed in the introduction to this chapter that re-colliding electrons could be trapped in highly excited Rydberg states. If circularly polarised light is used the recollision probability would be significantly decreased and it would be interesting to see if this would have any effect on the Rydberg states. It would also be interesting to see photoelectron spectra using 1500–1800 nm radiation where re-collision is know to be an important process [33]. These experiments could be carried out in the lab in Edinburgh and VMI images using circular polarisation can be inverted using the technique presented by Wollenhaupt *et. al.* [112].

Chapter 5 – Conclusions and Outlook

In this thesis ionisation mechanisms of gas-phase fullerenes after femtosecond and picosecond laser excitation have been studied. Mass spectrometry and angle-resolved photoelectron spectroscopy techniques have been used to carry out these studies on a newly constructed experimental apparatus. Measurements on C_{60} and Xe have successfully reproduced previously published work indicating that the setup is working in a satisfactory manner.

Measured photoelectron angular distributions (PADs) for various laser intensities, wavelengths and pulse durations support a transient thermal electron emission model. When using 400 nm light, which is resonant with the first optically allowed transition in C_{60}, an isotropic thermal electron emission was found. The PADs measured after 800 nm excitation brought new insights into the emission process and it was shown that for intensities above 10^{12} W/cm^2 a field-assisted thermal electron emission could describe the experimental data.

PADs were also presented for the pronounced peak structure seen in photoelectron spectra (PES) after femtosecond and picosecond excitation. Surprisingly simple angular distributions were found ruling out the possibility that these states originate from a direct multiphoton ionisation process from the electronic ground state. The angular dependence of the majority of the peaks analysed, could be well-described using only the β_2 anisotropy parameter indicating a single-photon ionisation mechanism from a randomly oriented sample. The structure has previously been interpreted arising from Rydberg states in the neutral molecule. However, the peaks corresponding to a higher binding energy can be interpreted in terms of the newly discovered superatom molecular orbitals (SAMOs) of C_{60}. The angular dependence of the peak in the PES corresponding to the s-SAMO is in excellent agreement with this assignment for both C_{60} and C_{70}.

5.1 Outlook

In order to understand the origin of the observed peaks better it is necessary to improve the resolution of the spectra and to study their angular dependence as a function of photoelectron kinetic energy. An experiment combining femtosecond laser pulses with picosecond pulses with variable wavelength might bring further insights. Also, an experiment using uv-light could help monitor the dynamics of any intermediate state from which the states corresponding to the observed peak structure could be populated. The gas aggregation source used to produce the cold fullerene PES presented in Figure 4.7 in chapter 4 could be modified to produce an effusive molecular beam with variable temperature. This would bring more detailed information of the dependence on the initial temperature for the population of the highly excited electronic states.

The experiment discussed in chapter 3 to measure whether ions are produced after the exciting laser pulse has left the ionisation region would determine if the thermal electron emission model is correct. This experiment, together with the ones mentioned above, is underway in the Edinburgh lab.

References

1. Wollenhaupt, M., V. Engel, and T. Baumert, *FEMTOSECOND LASER PHOTOELECTRON SPECTROSCOPY ON ATOMS AND SMALL MOLECULES: Prototype Studies in Quantum Control.* Annual Review of Physical Chemistry, 2005. **56**: p. 25-56.

2. Dantus, M. and V.V. Lozovoy, *Experimental Coherent Laser Control of Physicochemical Processes.* Chemical Reviews, 2004. **104**(4): p. 1813-1860.

3. Lozovoy, V.V., et al., *Control of Molecular Fragmentation Using Shaped Femtosecond Pulses.* Journal of Physical Chemistry A, 2008. **112**(17): p. 3789-3812.

4. Campbell, E.E.B., et al., *Ionisation of fullerenes and fullerene clusters using ultrashort laser pulses.* Photochemical & Photobiological Sciences, 2006. **5**(12): p. 1183-1189.

5. Hertel, I.V., T. Laarmann, and C.P. Schulz, *Ultrafast excitation, ionization and fragmentation of* C_{60}. Adv. At., Mol. Opt. Phys., 2005. **50**: p. 219.

6. Campbell, E.E.B., et al., *From Above Threshold Ionization to Statistical Electron Emission: The Laser Pulse-Duration Dependence of* C_{60} *Photoelectron Spectra.* Physical Review Letters, 2000. **84**(10): p. 2128.

7. Boyle, M., et al., *Excitation of Rydberg Series in* C_{60}. Physical Review Letters, 2001. **87**(27): p. 273401.

8. Ball, P., *Quantum all the way.* Nature, 2008. **453**: p. 22-25.

9. Feng, M., J. Zhao, and H. Petek, *Atom like, Hollow-Core-Bound Molecular Orbitals of C60.* Science (Washington, DC, U. S.) 2008. **320**(5874): p. 359-362.

10. Blanchet, V., et al., *Discerning vibronic molecular dynamics using time-resolved photoelectron spectroscopy.* Nature, 1999. **401**(6748): p. 52-54.

11. Posthumus, J.H., *The dynamics of small molecules in intense laser fields.* Reports on Progress in Physics, 2004. **67**(5): p. 623-665.

12. Cohen-Tannoudji, C., J. Dupont-Roc, and G. Grynberg, *Atom Photon Interactions: Basic Processes and Applications* New ed. 1998: Wiley VCH.

13. Bucksbaum, P.H., et al., *Role of the ponderomotive potential in above-threshold ionization.* J. Opt. Soc. Am. B, 1987. **4**(5): p. 760.

14. Keldysh, L.V., *Ionization in the field of a strong electromagnetic wave.* Sov. Phys. JETP, 1965. **20**: p. 1307–1314.

15. Delone, N.B. and V.P. Krainov, *Atoms in Strong Light Fields*. 1985: Springer-Verlag.

16. Johnsson, P., *Attosecond Optical and Electronic Wave Packets*. 2006, Lund University: Lund, Sweden.

17. Hoffmann, K., *Femtosekunden-Laserspektroskopie an Fullerenen*, in *Fachbereich Physik*. 2000, Freie Universität Berlin: Berlin.

18. Meckel, M., et al., *Laser-Induced Electron Tunneling and Diffraction.* Science %R 10.1126/science.1157980, 2008. **320**(5882): p. 1478-1482.

19. Lewenstein, M., et al., *Theory of high-harmonic generation by low-frequency laser fields.* Physical Review A, 1994. **49**(3): p. 2117.

20. Campbell, E.E.B., et al., *Sequential ionization of C_{60} with femtosecond laser pulses.* The Journal of Chemical Physics, 2001. **114**(4): p. 1716-1719.

21. de Vries, J., et al., *Single-photon ionization of C_{60}^{-} and C_{70}^{-}fullerene with synchrotron radiation: determination of the ionization potential of C60.* Chemical Physics Letters, 1992. **188**(3-4): p. 159-162.

22. Dresselhaus, M.S., G. Dresselhaus, and P.C. Eklund, *Science of Fullerenes and Carbon Nanotubes: Their Properties and Applications* Academic Press 1996.

23. Campbell, E.E.B., G. Ulmer, and I.V. Hertel, *Delayed ionization of C_{60} and C_{70}.* Physical Review Letters, 1991. **67**(15): p. 1986.

24. Lifshitz, C., *Carbon clusters.* International Journal of Mass Spectrometry, 2000. **200**(1-3): p. 423-442.

25. Campbell, E.E.B., T. Raz, and R.D. Levine, *Internal energy dependence of the fragmentation patterns of C_{60} and C_{60}^{+}.* Chemical Physics Letters, 1996. **253**(3-4): p. 261-267.

26. Bordas, C., et al., *Time-dependent spectrum of thermionic emission from hot C60.* The European Physical Journal D - Atomic, Molecular, Optical and Plasma Physics, 2005. **34**(1): p. 151-155.

27. Lépine, F. and C. Bordas, *Time-dependent spectrum of thermionic emission from hot clusters: Model and example of C_{60}.* Physical Review A, 2004. **69**(5): p. 053201.

28. Kjellberg, M., et al., *Momentum-map-imaging photoelectron spectroscopy of fullerenes with femtosecond laser pulses.* Physical Review A, 2010. **81**(2): p. 023202.

29. Hansen, K., K. Hoffmann, and E.E.B. Campbell, *Thermal electron emission from the hot electronic subsystem of vibrationally cold C_{60}.* The Journal of Chemical Physics, 2003. **119**(5): p. 2513-2522.

30. Andersen, J.U., E. Bonderup, and K. Hansen, *Thermionic emission from clusters.* Journal of Physics B: Atomic, Molecular and Optical Physics, 2002. **35**(5): p. R1-R30.

31. Tchaplyguine, M., et al., *Ionization and fragmentation of C_{60} with sub-50 fs laser pulses.* The Journal of Chemical Physics, 2000. **112**(6): p. 2781-2789.

32. Bhardwaj, V.R., P.B. Corkum, and D.M. Rayner, *Internal Laser-Induced Dipole Force at Work in C_{60} Molecule.* Physical Review Letters, 2003. **91**(20): p. 203004.

33. Bhardwaj, V.R., P.B. Corkum, and D.M. Rayner, *Recollision during the High Laser Intensity Ionization of C60.* Physical Review Letters, 2004. **93**(4): p. 043001/1-043001/4.

34. Bauer, D., et al., *C_{60} in intense femtosecond laser pulses: Nonlinear dipole response and ionization.* Physical Review A, 2001. **64**(6): p. 063203.

35. Hertel, I.V., T. Laarmann, and C.P. Schulz, *Ultrafast excitation, ionization and fragmentation of C_{60}.* Adv. At., Mol.m Opt. Phys., 2005. **50**: p. 219.

36. Hohmann, H., et al., *Photoionization and Fragmentation Dynamics of C_{60}.* Physical Review Letters, 1994. **73**(14): p. 1919.

37. Haufler, R.E., et al., *Cold molecular beam electronic spectrum of the carbon sixty-atom and seventy-atom molecules.* Journal of Chemical Physics, 1991. **95**(3): p. 2197-9.

38. Kataura, H., et al., *Optical Absorption of Gas Phase* C_{60} *and* C_{70}. Jpn. J. Appl. Phys., 1993. **32**(Part 2, No 11B).

39. Tchaplyguine, M., et al., *Ionization and fragmentation of C[sub 60] with sub-50 fs laser pulses.* The Journal of Chemical Physics, 2000. **112**(6): p. 2781-2789.

40. Shchatsinin, I., et al., *C[sub 60] in intense short pulse laser fields down to 9 fs: Excitation on time scales below e-e and e-phonon coupling.* The Journal of Chemical Physics, 2006. **125**(19): p. 194320-15.

41. Ellert, C., et al., *Temperature Dependence of the Optical Response of Small, Open Shell Sodium Clusters.* Physical Review Letters, 1995. **75**(9): p. 1731.

42. de Heer, W.A., *The physics of simple metal clusters: experimental aspects and simple models.* Reviews of Modern Physics, 1993. **65**(3): p. 611.

43. Fennel, T., et al., *Laser-driven nonlinear cluster dynamics.* Reviews of Modern Physics, 2010. **82**(2): p. 1793.

44. Hertel, I.V., et al., *Giant plasmon excitation in free C60 and C70 molecules studied by photoionization.* Physical Review Letters, 1992. **68**(6): p. 784.

45. Schlipper, R., et al., *Thermal emission of electrons from highly excited sodium clusters.* Applied Physics A: Materials Science & Processing, 2001. **72**(3): p. 255-259.

46. DeWitt, M.J. and R.J. Levis, *Observing the Transition from a Multiphoton-Dominated to a Field-Mediated Ionization Process for Polyatomic Molecules in Intense Laser Fields.* Physical Review Letters, 1998. **81**(23): p. 5101.

47. Markevitch, A.N., et al., *Sequential nonadiabatic excitation of large molecules and ions driven by strong laser fields.* Physical Review A, 2004. **69**(1): p. 013401.

48. Reid, K.L., *PHOTOELECTRON ANGULAR DISTRIBUTIONS.* Annual Review of Physical Chemistry, 2003. **54**: p. 397-424.

49. Yang, C.N., *On the Angular Distribution in Nuclear Reactions and Coincidence Measurements.* Physical Review, 1948. **74**(7): p. 764.

50. Cooper, J. and R.N. Zare, *Angular Distribution of Photoelectrons.* The Journal of Chemical Physics, 1968. **48**(2): p. 942-943.

51. Manson, S.T. and A.F. Starace, *Photoelectron angular distributions: energy dependence for s subshells.* Reviews of Modern Physics, 1982. **54**(2): p. 389.

52. White, M.G., et al., *Resonant multiphoton ionization of NO via the A [sup 2] Sigma [sup +] state: Photoelectron spectra and angular distributions.* The Journal of Chemical Physics, 1984. **80**(2): p. 678-686.

53. Bartels, C., et al., *Probing the Angular Momentum Character of the Valence Orbitals of Free Sodium Nanoclusters.* Science, 2009. **323**(5919): p. 1323-1327.

54. Solov'yov, A.V., R.G. Polozkov, and V.K. Ivanov, *Angle-resolved photoelectron spectra of metal cluster anions within a many-body-theory approach.* Physical Review A, 2010. **81**(2): p. 021202.

55. Eppink, A.T.J.B. and D.H. Parker, *Velocity map imaging of ions and electrons using electrostatic lenses: Application in photoelectron and photofragment ion imaging of molecular oxygen.* Review of Scientific Instruments, 1997. **68**(9): p. 3477-3484.

56. Whitaker, B., ed. *Imaging in Molecular Dynamics, Technology and Applications (A User's Guide)*. 2003, Cambridge University Press: New York.

57. Bordas, C., et al., *Photoelectron imaging spectrometry: Principle and inversion method.* Review of Scientific Instruments, 1996. **67**(6): p. 2257-2268.

58. Bracewell, R.N., *The Fourier Transform and its Applications*. Third ed. 2000: McGraw-Hill.

59. Whitaker, B., ed. *Imaging in Chemical Dynamics*. 2001, American Chemical Society.

60. Piacente, V., et al., *Vapor Pressure of C60 Buckminsterfullerene.* Journal of Physical Chemistry, 1995. **99**(38): p. 14052-14057.

61. Campbell, E.E.B., *Personal communication*. 2007: Edinburgh.

62. Rulliere, C., ed. *Femtosecond Laser Pulses - Principles and Experiments*. Second ed. 2005, Springer.

63. Silfvast, W.T., *Laser Fundamentals*. Second ed. 2008, New York: Cambridge University Press.

64. Liu, J.M., *Simple technique for measurements of pulsed Gaussian-beam spot sizes.* Optics Letters, 1982. **7**(5): p. 196-198.

65. Wen, L., et al., *Megapixel ion imaging with standard video.* Review of Scientific Instruments, 2005. **76**(6): p. 063106.

66. Bor-Yu, C., et al., *Improved two-dimensional product imaging: The real-time ion-counting method.* Review of Scientific Instruments, 1998. **69**(4): p. 1665-1670.

67. Winkler, L., *smoothc.mat*. 2005, Matlab Central - http://www.mathworks.co.uk/matlabcentral/fileexchange/7951-smoothc-mat.Access date 020210.

68. Smith, L.M., D.R. Keefer, and S.I. Sudharsanan, *Abel inversion using transform techniques.* Journal of Quantitative Spectroscopy & Radiative Transfer, 1988. **39**(5): p. 367-73.

69. Winterhalter, J., et al., *Imaging of charged atomic reaction products: Inversion by a two-dimensional regularization method.* Journal of Chemical Physics, 1999. **110**(23): p. 11187-11196.

70. Vrakking, M.J.J., *An iterative procedure for the inversion of two-dimensional ion/photoelectron imaging experiments.* Review of Scientific Instruments, 2001. **72**(11): p. 4084-4089.

71. Dribinski, V., et al., *Reconstruction of Abel-transformable images: The Gaussian basis-set expansion Abel transform method.* Review of Scientific Instruments, 2002. **73**(7): p. 2634-2642.

72. Roberts, G.M., et al., *Toward real-time charged-particle image reconstruction using polar onion-peeling.* Review of Scientific Instruments, 2009. **80**(5): p. 053104.

73. Gustavo, A.G., N. Laurent, and P. Ivan, *Two-dimensional charged particle image inversion using a polar basis function expansion*. Review of Scientific Instruments, 2004. **75**(11): p. 4989-4996.

74. Schyja, V., T. Lang, and H. Helm, *Channel switching in above-threshold ionization of xenon.* Physical Review A, 1998. **57**(5): p. 3692.

75. *CRC Handbook of Chemistry and Physics*. 88 ed, ed. D. Lide. 2007-2008: CRC Press.

76. *NIST: Atomic Spectra Database Line Form*. 2010, National Institute of Standards and Technology.

77. Freeman, R.R., et al., *Above-threshold ionization with subpicosecond laser pulses.* Physical Review Letters, 1987. **59**(10): p. 1092.

78. Wiley, W.C. and I.H. McLaren, *Time-of-Flight Mass Spectrometer with Improved Resolution.* Review of Scientific Instruments, 1955. **26**(12): p. 1150-1157.

79. Shchatsinin, I., et al., *Ultrafast energy redistribution in C_{60} fullerenes: A real time study by two-color femtosecond spectroscopy.* The Journal of Chemical Physics, 2008. **129**(20): p. 204308-12.

80. Lecointre, J., et al., *Ultrafast Relaxation Dynamics Observed Through Time-Resolved Photoelectron Angular Distributions* Journal of Physical Chemistry A, 2010. **114**: p. 11216-11224.

81. Pinar, et al., *Photoelectron Imaging Spectroscopy of Small Clusters: Evidence for Non-Boltzmannian Kinetic-Energy Distribution in Thermionic Emission.* Physical Review Letters, 1998. **81**(11): p. 2225.

82. Weisskopf, V., *Statistics and nuclear reactions.* Physical Review, 1937. **52**: p. 295-303.

83. Scheier, P., et al., *Appearance and ionization energies of singly, doubly and triply charged C60 and its fragment ions produced by electron impact ionization.* International Journal of Mass Spectrometry and Ion Processes, 1994. **138**: p. 77-93.

84. Klots, C.E., *Quasiequilibrium rate constants for thermionic emission from small particles.* Chemical Physics Letters, 1991. **186**(1): p. 73-76.

85. Verlet, J.R.R., *Femtosecond spectroscopy of cluster anions: insights into condensed-phase phenomena from the gas-phase.* Chemical Society Reviews, 2008. **37**(3): p. 505-517.

86. Laarmann, T., et al., *Emission of Thermally Activated Electrons from Rare Gas Clusters Irradiated with Intense VUV Light Pulses from a Free Electron Laser.* Physical Review Letters, 2005. **95**(6): p. 063402-4.

87. Johansson, O., *Ionization of C_{60} Using Velocity Map Imaging Photoelectron Spectroscopy,* in *Department of Physics*. 2007, Gothenburg University: Gothenburg, Sweden.

88. Boyle, M., *Energy absorption and redistribution dynamics in isolated C_{60} molecules*. 2005, Max Born Institut: Berlin, Germany.

89. Campbell, E.E.B., K. Hoffmann, and I.V. Hertel, *The transition from direct to delayed ionization of C60.* European Physical Journal D: Atomic, Molecular and Optical Physics, 2001. **16**(1-3): p. 345-348.

90. Fennel, T., et al., *Plasmon-Enhanced Electron Acceleration in Intense Laser Metal-Cluster Interactions.* Physical Review Letters, 2007. **98**(14): p. 143401.

91. Connerade, J.-P. and A.V. Solov'yov, *Formalism for multiphoton plasmon excitation in jellium clusters.* Physical Review A, 2002. **66**(1): p. 013207.

92. Kjellberg, M., et al., *Femtosecond electron spectroscopy of coronene, benzo[GHI]perylene, and anthracene.* The Journal of Chemical Physics, 2010. **133**(7): p. 074308-7.

93. Hebeisen, C.T., et al., *Grating enhanced ponderomotive scattering for visualization and full characterization of femtosecond electron pulses.* Optics Express, 2008. **16**(5): p. 3334-3341.

94. Murakami, M., et al., *Ionization and fragmentation of anthracene with an intense femtosecond laser pulse at 1.4 micro-meters.* Chemical Physics Letters, 2005. **403**(4-6): p. 238-241.

95. Reed, C.A., et al., *Taming Superacids: Stabilization of the Fullerene Cations* HC_{60}^{+} *and* $C_{60}^{\cdot +}$. Science, 2000. **289**(5476): p. 101-104.

96. Gasyna, Z., L. Andrews, and P.N. Schatz, *Near-infrared absorption spectra of fullerene (C60) radical cations and anions prepared simultaneously in solid argon.* Journal of Physical Chemistry, 1992. **96**(4): p. 1525-1527.

97. Boyle, M., et al., *Excitation of Rydberg Series in C_{60}.* Physical Review Letters, 2001. **87**(27): p. 273401.

98. Boyle, M., et al., *Excitation dynamics of Rydberg states in* C_{60}. The European Physical Journal D - Atomic, Molecular, Optical and Plasma Physics, 2005. **36**(3): p. 339-351.

99. Boyle, M., et al., *Two-color pump-probe study and internal-energy dependence of Rydberg-state excitation in C_{60}.* Physical Review A, 2004. **70**(5): p. 051201.

100. Wesdorp, C., F. Robicheaux, and L.D. Noordam, *Rydberg carbon clusters prepared by pulsed field recombination.* Chemical Physics Letters, 2000. **323**(1-2): p. 192-197.

101. Yasumatsu, H., et al., *Absorption spectrum of C[sub 60] in the gas phase: Autoionization via core-excited Rydberg states.* The Journal of Chemical Physics, 1996. **104**(3): p. 899-902.

102. Schick, C.P. and P.M. Weber, *Ultrafast Dynamics in the Three-Photon, Double-Resonance Ionization of Phenol via the S2 Electronic State.* Journal of Physical Chemistry A, 2001. **105**(15): p. 3735-3740.

103. Delone, N.B. and V.P. Krainov, *Multiphoton Processes in Atoms*. 1994, Berlin Heidelberg: Springer-Verlag

104. Lezius, M., et al., *Polyatomic molecules in strong laser fields: Nonadiabatic multielectron dynamics.* The Journal of Chemical Physics, 2002. **117**(4): p. 1575-1588.

105. Zhang, G.P., X. Sun, and T.F. George, *Laser-induced ultrafast dynamics in C_{60}.* Physical Review B, 2003. **68**(16): p. 165410.

106. Lassesson, A., et al., *A femtosecond laser study of the endohedral fullerenes Li@C60 and La@C82.* European Physical Journal D: Atomic, Molecular and Optical Physics, 2005. **34**(1-3): p. 205-209.

107. Zhao, J., et al., *The Superatom States of Fullerenes and Their Hybridization into the Nearly Free Electron Bands of Fullerites.* ACS Nano, 2009. **3**(4): p. 853-864.

108. Coheur, P.F., M. Carleer, and R. Colin, *The absorption cross sections of C60 and C70 in the visible-UV region.* Journal of Physics B: Atomic, Molecular and Optical Physics, 1996. **29**(21): p. 4987-4995.

109. Bauernschmitt, R.d., et al., *Experiment versus Time Dependent Density Functional Theory Prediction of Fullerene Electronic Absorption.* Journal of the American Chemical Society, 1998. **120**(20): p. 5052-5059.

110. Zhu, X.Y., et al., *Molecular quantum well at the C_{60}/Au(111) interface.* Physical Review B, 2006. **74**(24): p. 241401.

111. Osterwalder, A., et al., *High resolution photodetachment spectroscopy of negative ions via slow photoelectron imaging.* The Journal of Chemical Physics, 2004. **121**(13): p. 6317-6322.

112. Wollenhaupt, M., et al., *Three-dimensional tomographic reconstruction of ultrashort free electron wave packets.* Applied Physics B: Lasers and Optics, 2009. **95**(4): p. 647-651.

Appendix A – Drawing of the interaction chamber

A drawing of the interaction chamber made by Richard Davies, CVT Ltd., is presented on the next page.

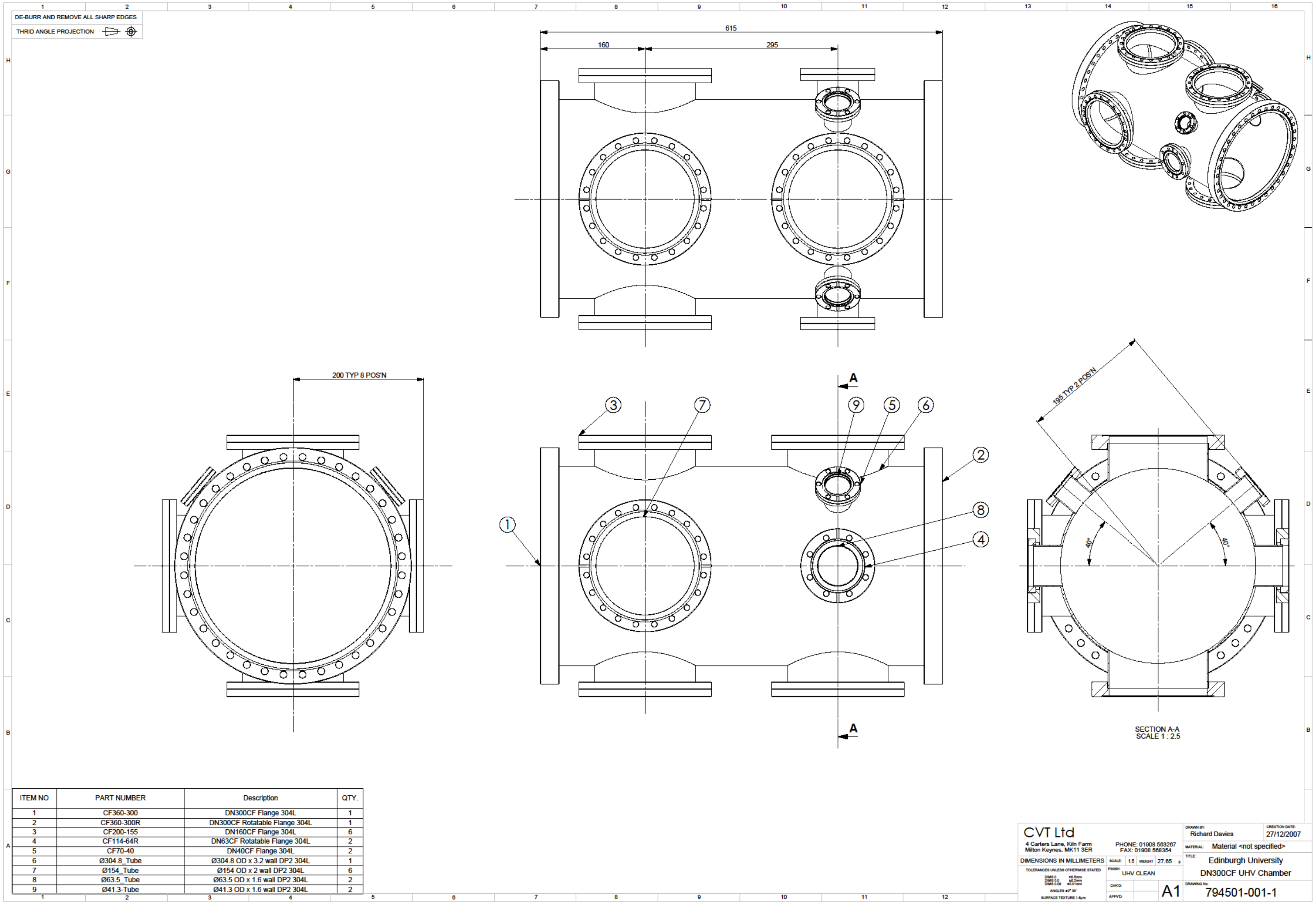

ITEM NO	PART NUMBER	Description	QTY.
1	CF360-300	DN300CF Flange 304L	1
2	CF360-300R	DN300CF Rotatable Flange 304L	1
3	CF200-155	DN160CF Flange 304L	6
4	CF114-64R	DN63CF Rotatable Flange 304L	2
5	CF70-40	DN40CF Flange 304L	2
6	Ø304.8_Tube	Ø304.8 OD x 3.2 wall DP2 304L	1
7	Ø154_Tube	Ø154 OD x 2 wall DP2 304L	6
8	Ø63.5_Tube	Ø63.5 OD x 1.6 wall DP2 304L	2
9	Ø41.3-Tube	Ø41.3 OD x 1.6 wall DP2 304L	2

CVT Ltd
4 Carters Lane, Kiln Farm
Milton Keynes, MK11 3ER
PHONE: 01908 563267
FAX: 01908 568354
DIMENSIONS IN MILLIMETERS
SCALE: 1:5
WEIGHT: 27.65 g
TOLERANCES UNLESS OTHERWISE STATED
DIMS 0 ±0.5mm
DIMS 0.0 ±0.2mm
DIMS 0.00 ±0.01mm
ANGLES ±0° 30'
SURFACE TEXTURE 1.6µm
FINISH: UHV CLEAN
CHK'D:
APPV'D:
A1
DRAWN BY: Richard Davies
CREATION DATE: 27/12/2007
MATERIAL: Material <not specified>
TITLE: Edinburgh University
DN300CF UHV Chamber
DRAWING No: 794501-001-1

Appendix B – Glass plate holder for fullerene beam characterisation

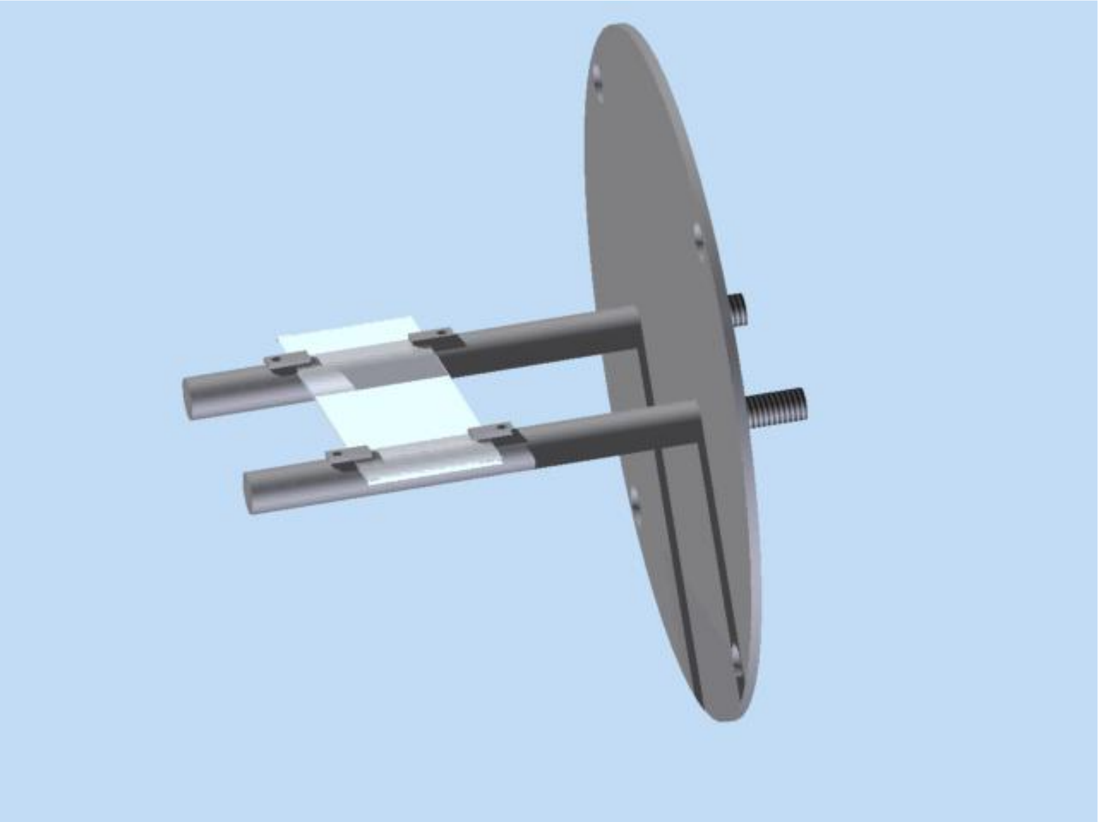

Figure B-1: Autodesk Inventor drawing showing the microscope glass plate holder used to characterise the effusive molecular beam. The setup comprises of flange onto which two rods are mounted. The glass plate is held in positions with four washers. The drawings for the three different components are shown below.

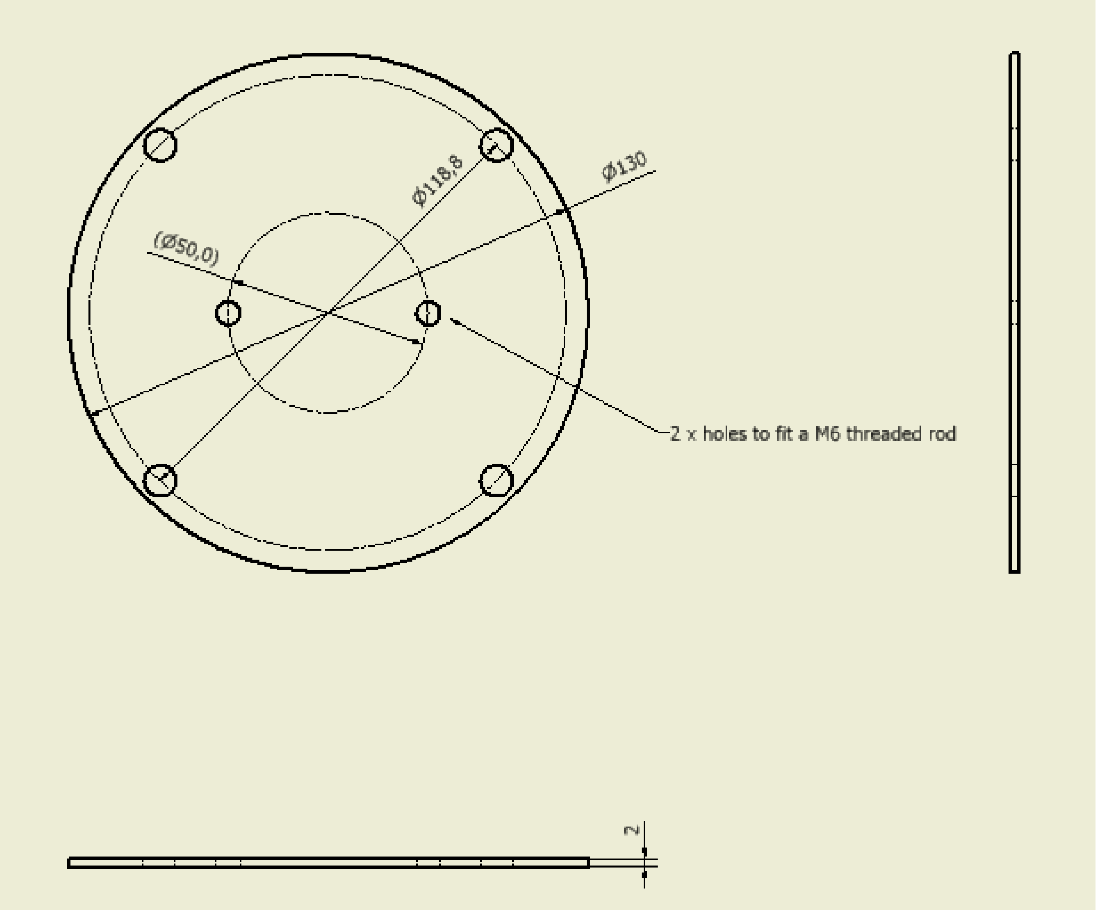

Figure B-2: Drawing of the mounting flange.

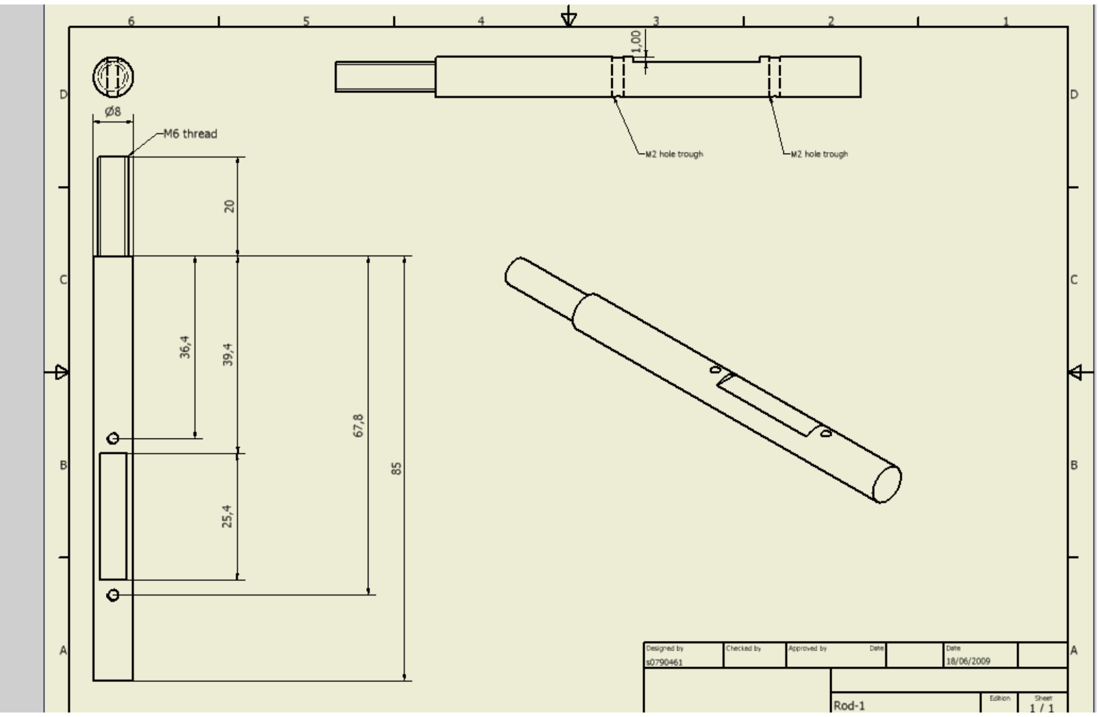

Figure B-3: Drawing of the mounting rods.

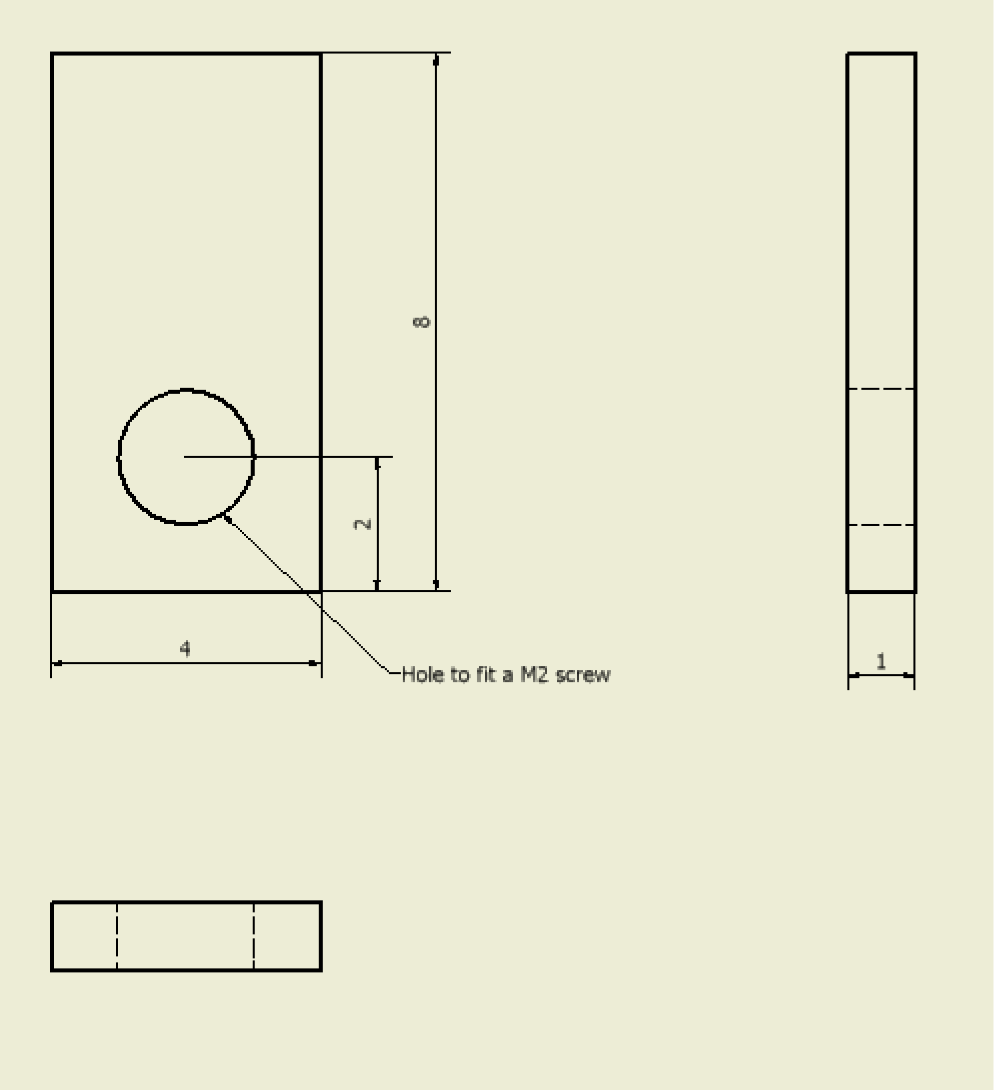

Figure B-4: Drawing of the washers used to hold the glass plate in position.

Appendix C – Ion optics drawings

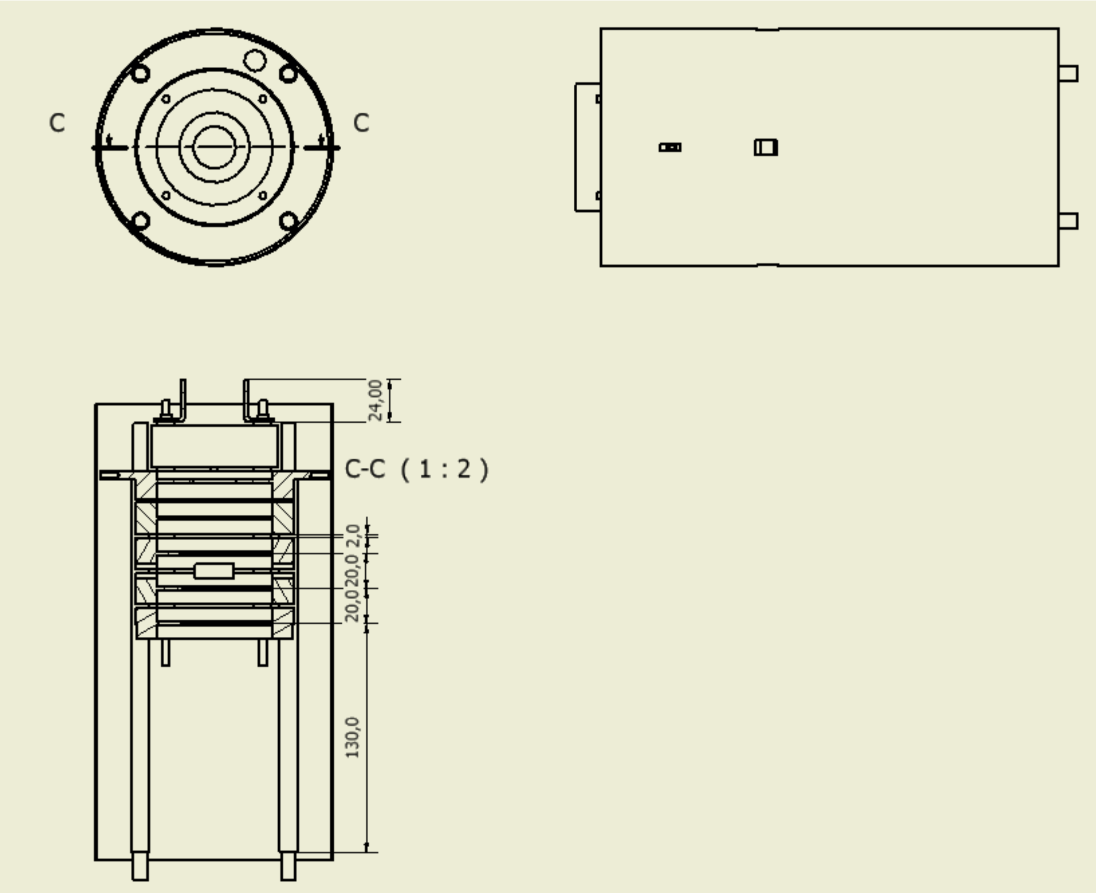

Figure C-1: Drawing of the ion optics including the mu-metal cylinder.

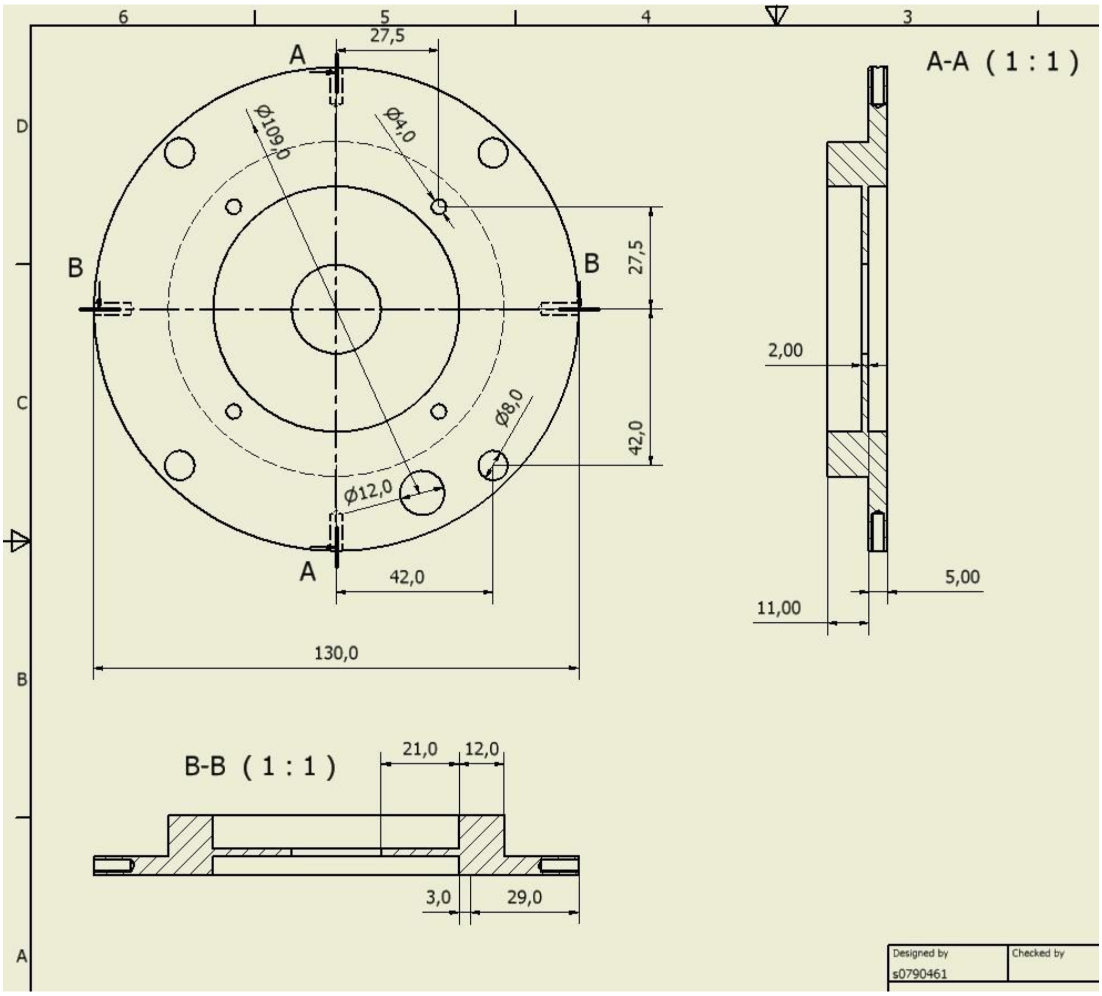

Figure C-2: Drawing of the G_2 electrode.

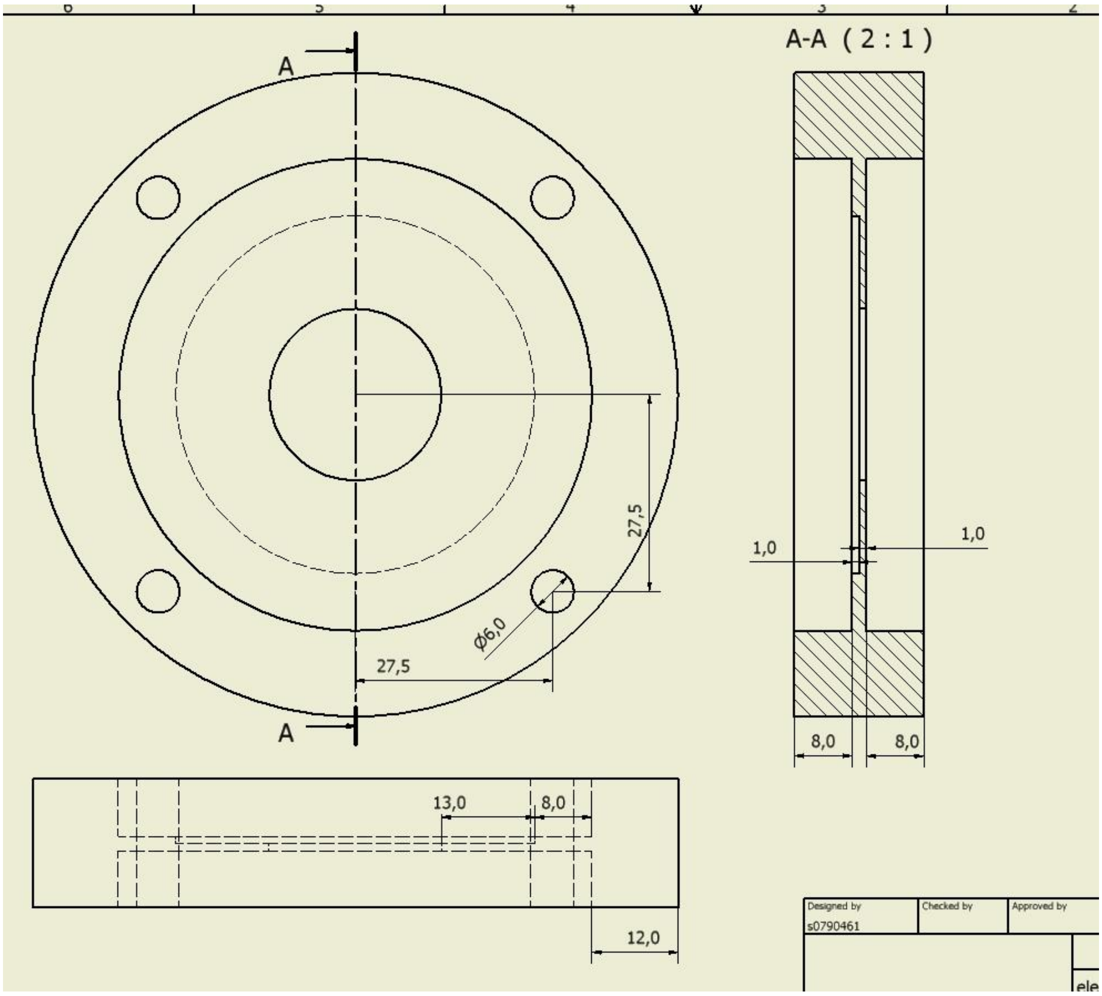

Figure C-3: Drawing of the $HV_2/2$ electrode.

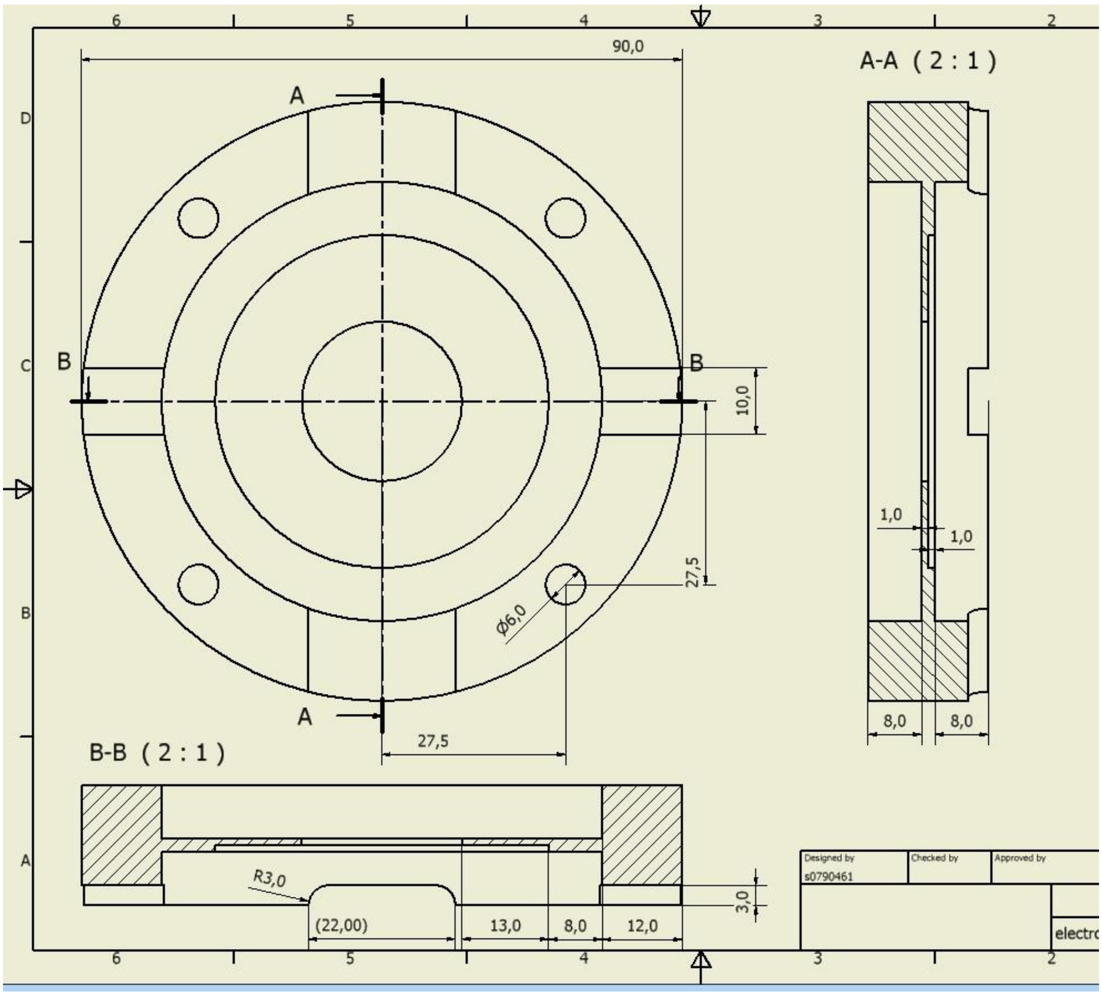

Figure C-4: Drawing of the HV_2 electrode.

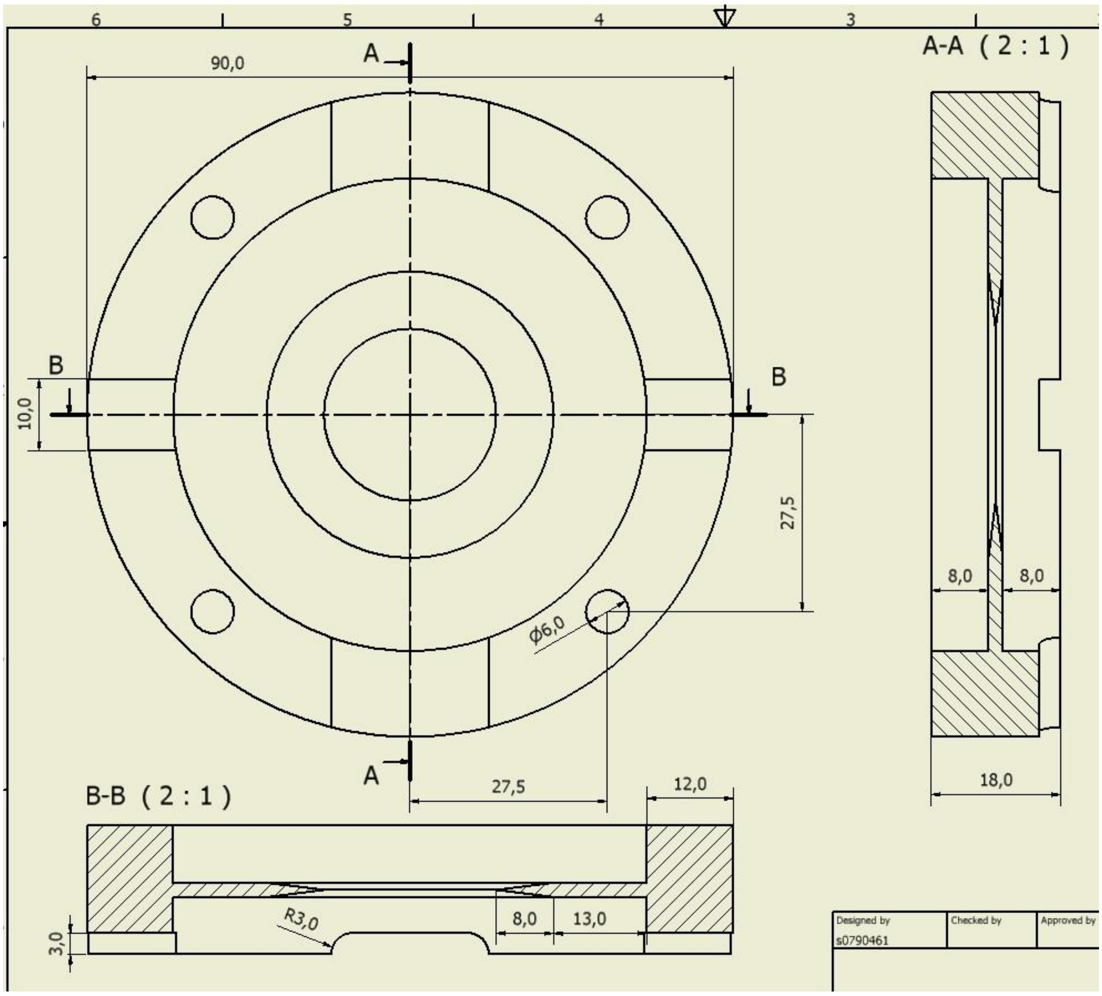

Figure C-5: Drawing of the HV_1 electrode.

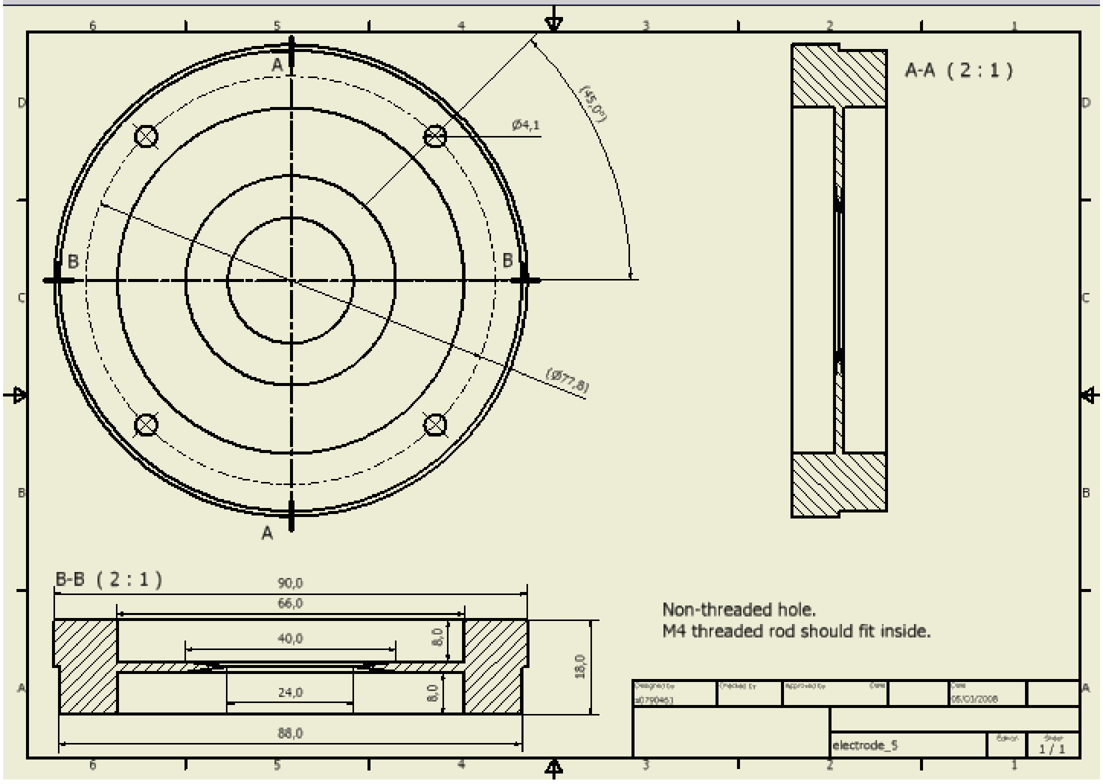

Figure C-6: Drawing of the G_1 electrode.

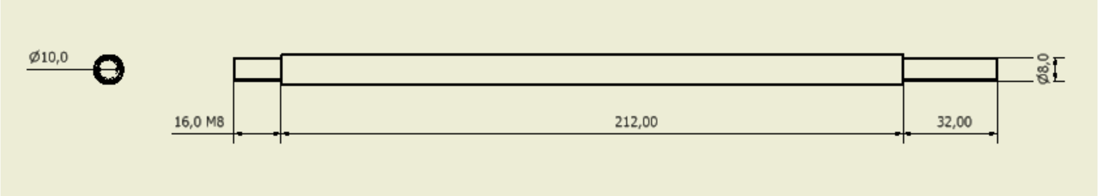

Figure C-7: Drawing of the ion optics mounting rods used to mount the ion optics in the chamber.

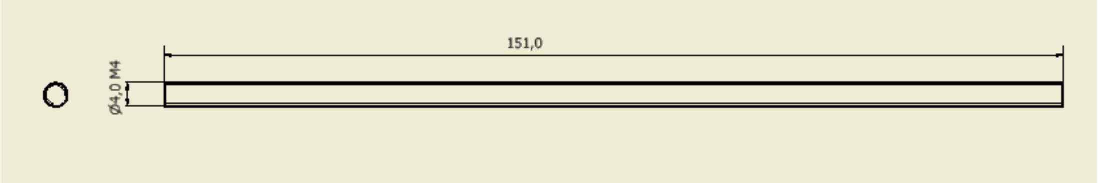

Figure C-8: Drawing of the ion optics mounting rods used to hold the electrodes together on a concentric axis.

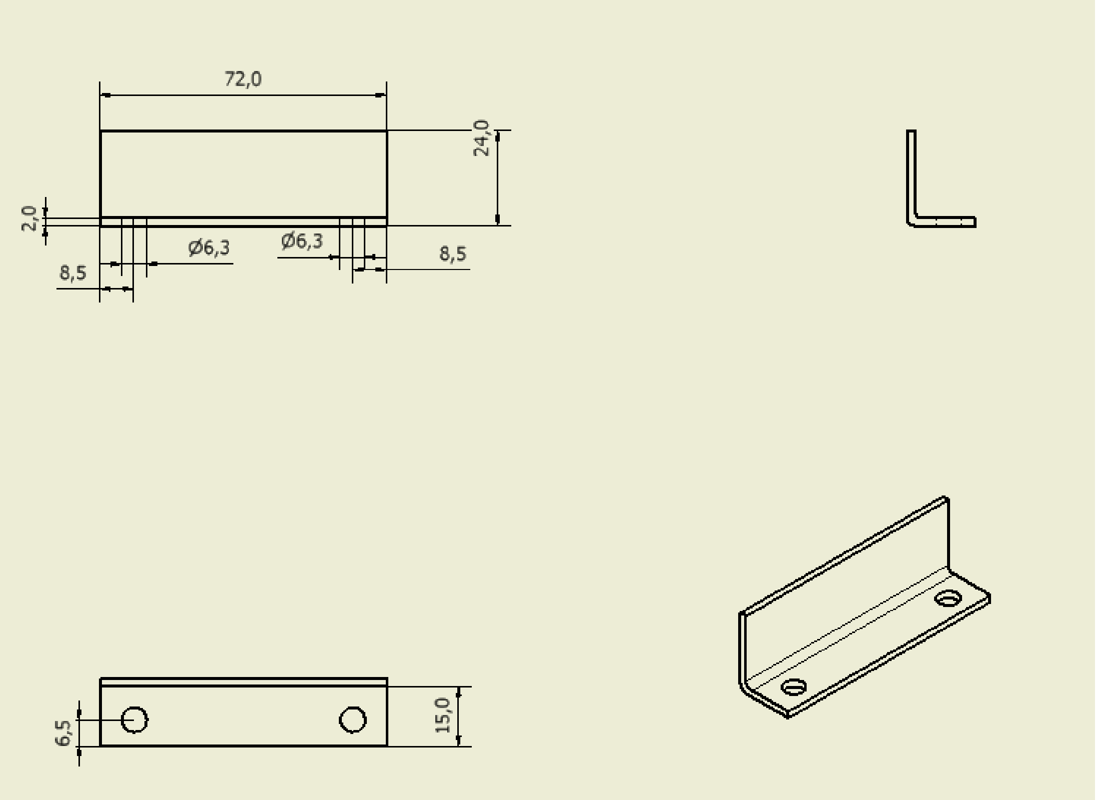

Figure C-9: Drawing of the ion deflection plates.

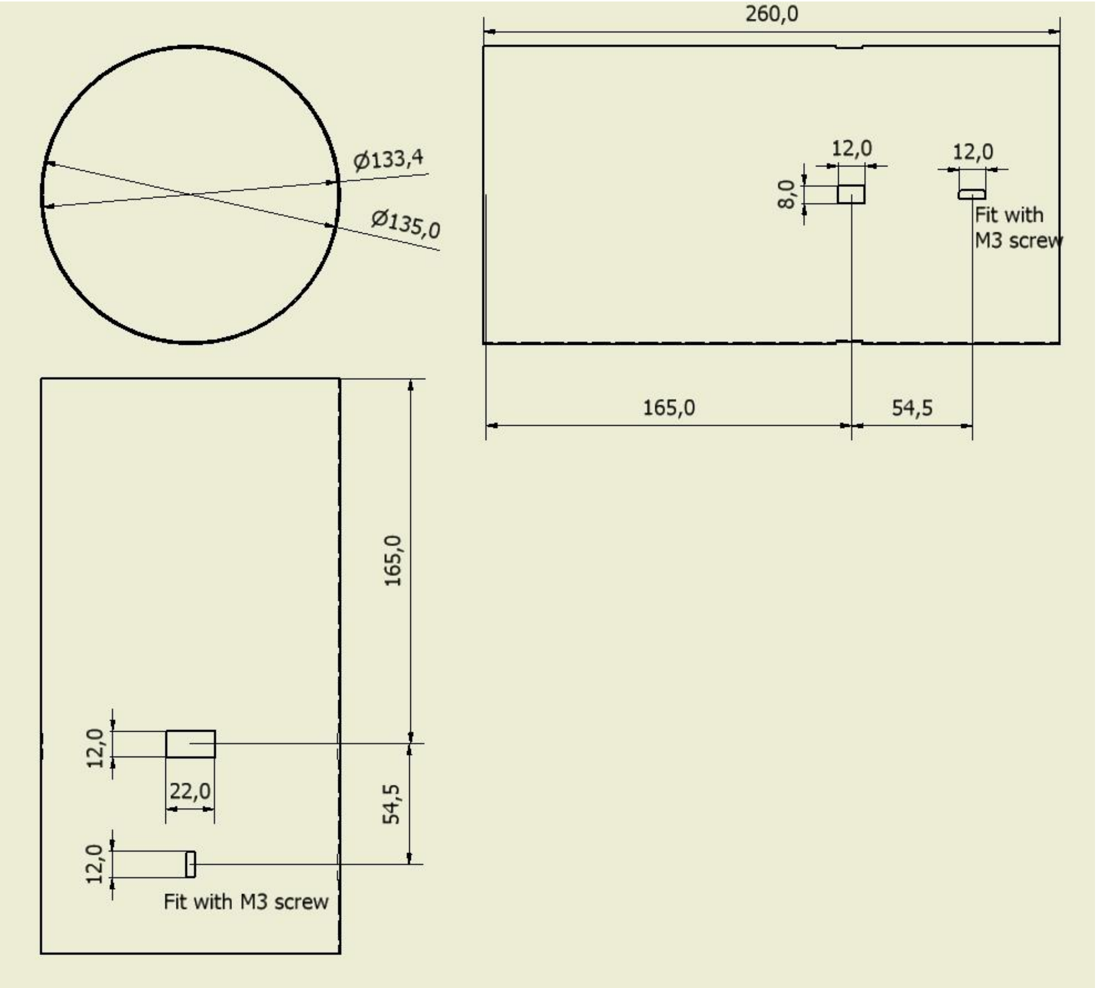

Figure C-10: Drawing of the mu-metal cylinder.

Appendix D – VMI acquisition and analysis programs

Continuous_acquisition.vi

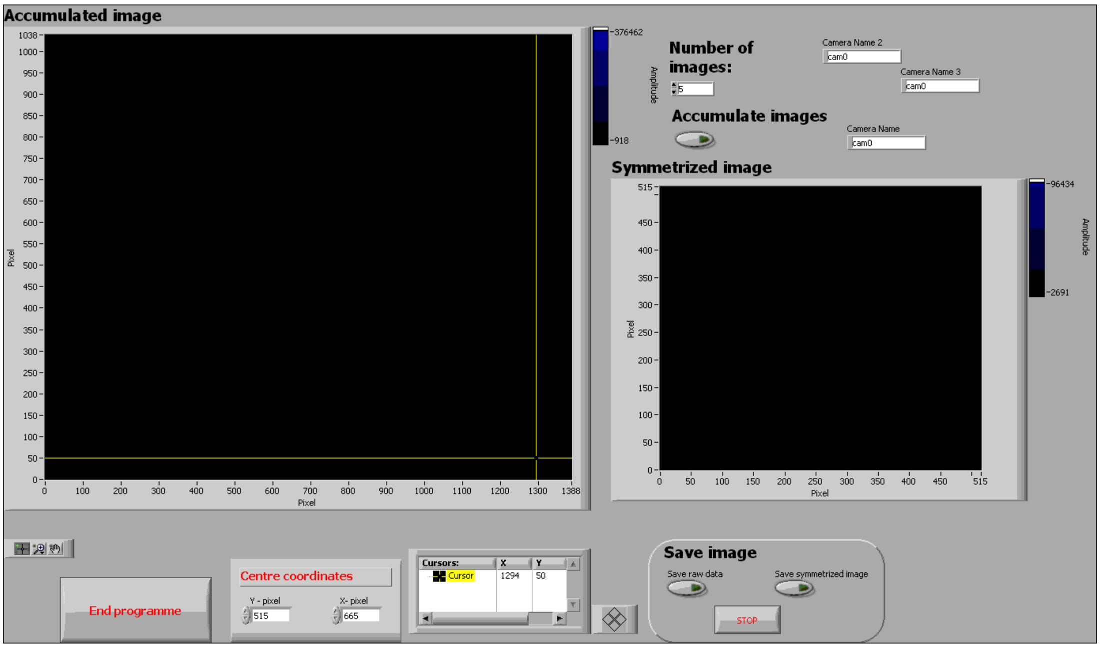

Number of images: 5

Camera Name 2: cam0

Camera Name 3: cam0

Camera Name: cam0

Y - pixel: 515

X- pixel: 665

Cursors:	X	Y
Cursor	1294	50

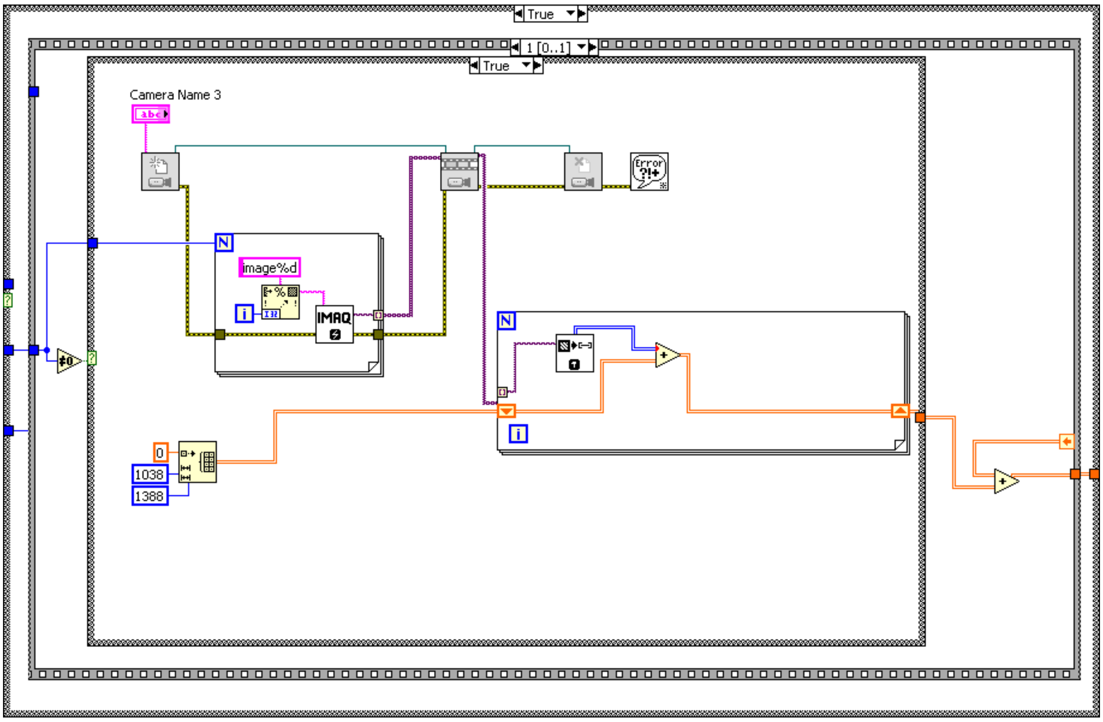

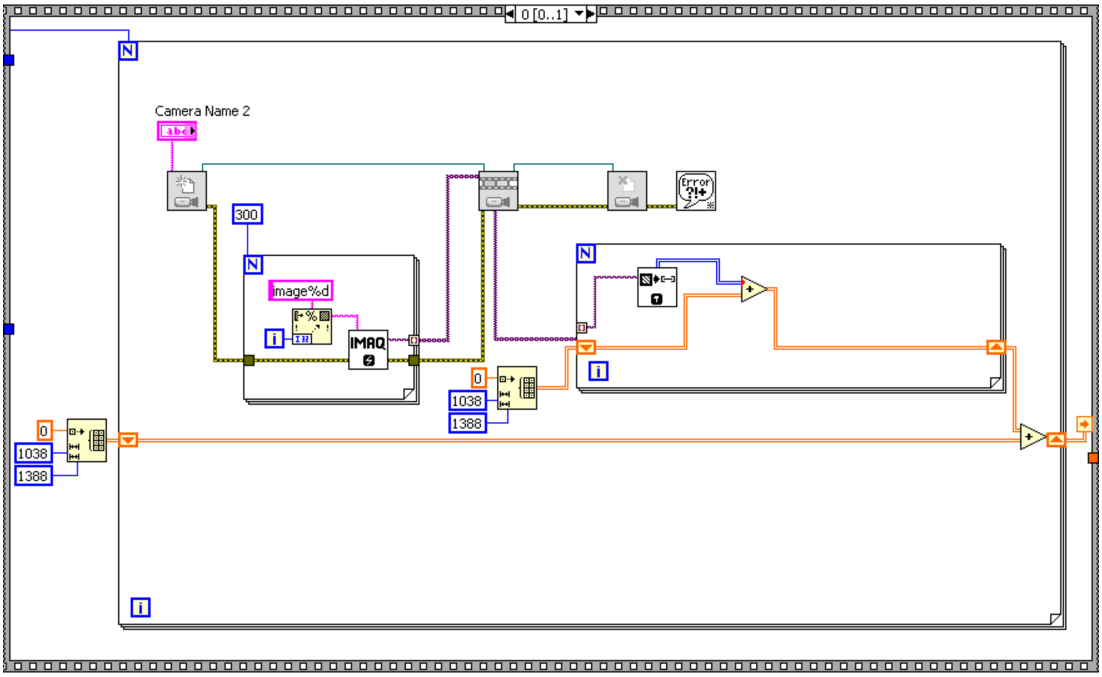
0 [0..1]
Camera Name 2
300
image%d
IMAQ
Error ?!+
0
1038
1388
0
1038
1388

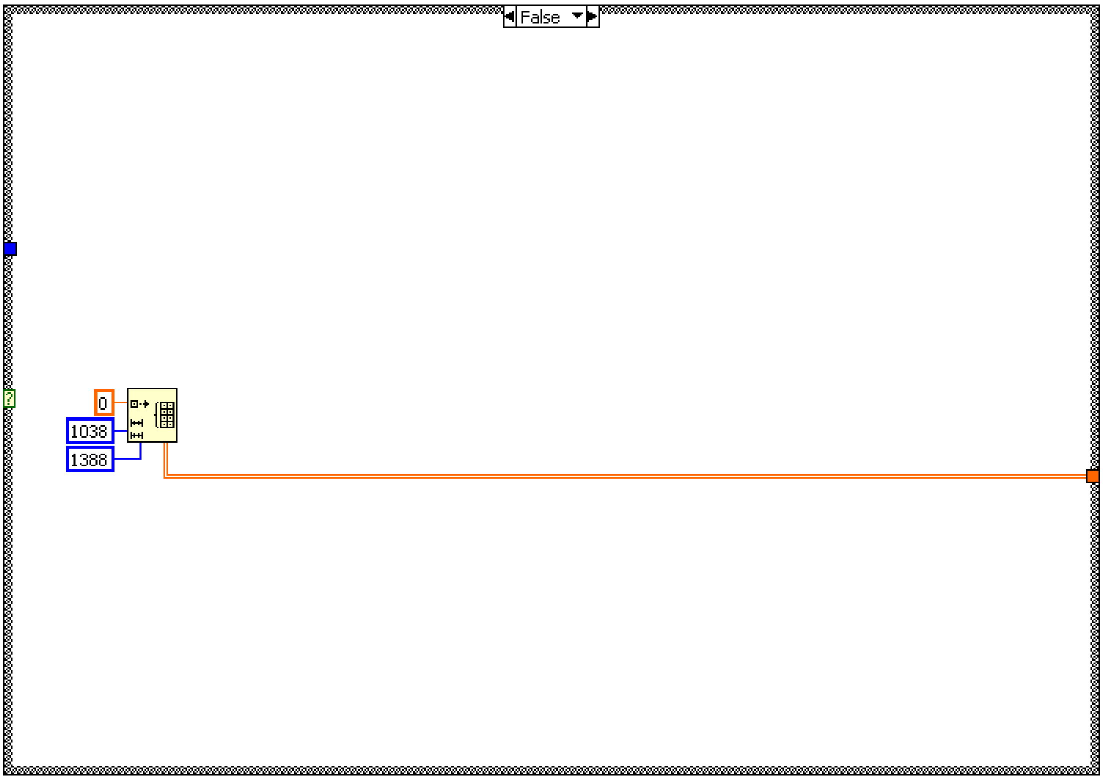
False
0
1038
1388

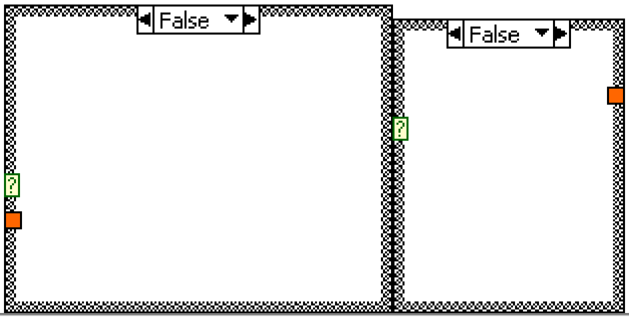

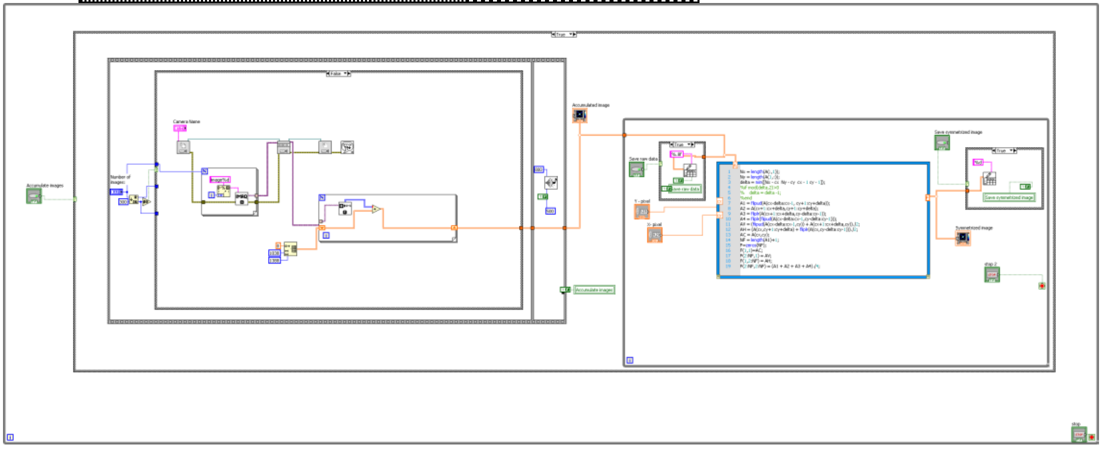

Single_count_acquisition.vi

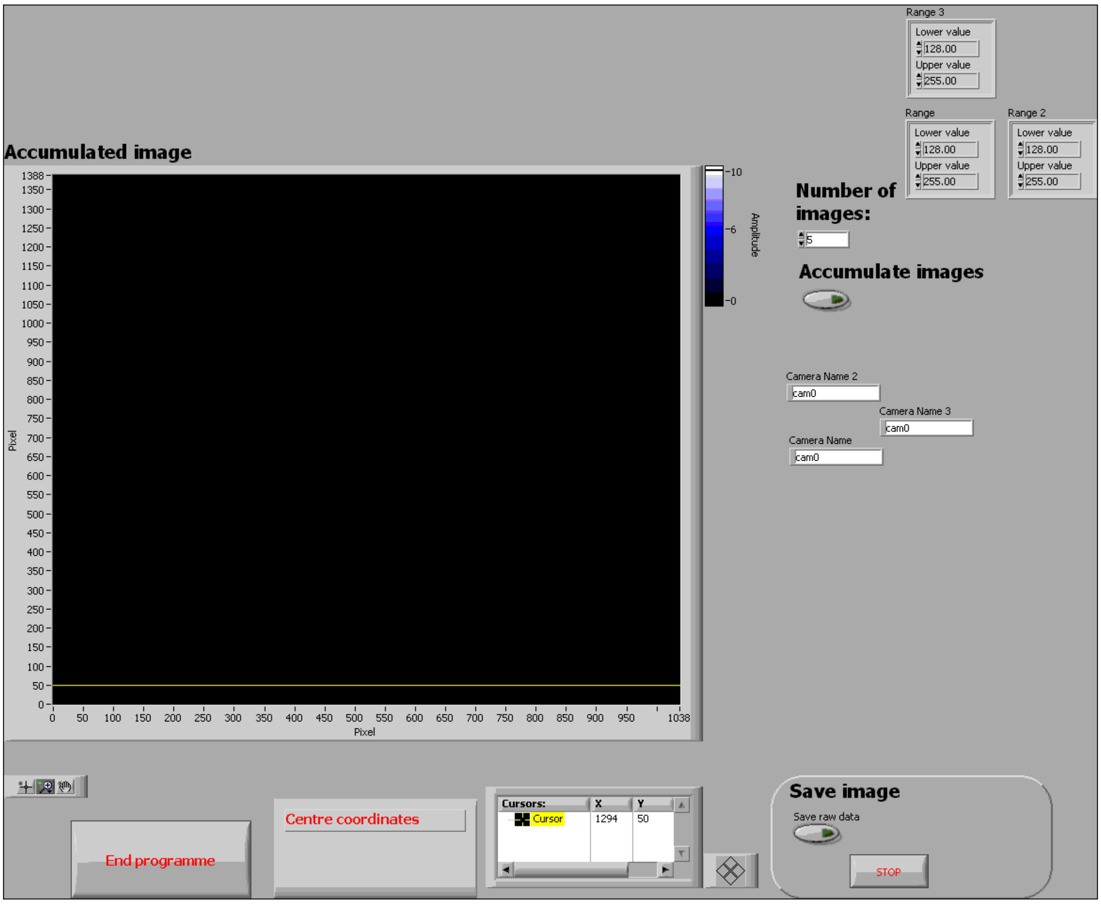

Range 3
Lower value 128.00
Upper value 255.00

Range
Lower value 128.00
Upper value 255.00

Range 2
Lower value 128.00
Upper value 255.00

Number of images: 5

Camera Name 2: cam0

Camera Name 3: cam0

Camera Name: cam0

Cursors:	X	Y
Cursor	1294	50

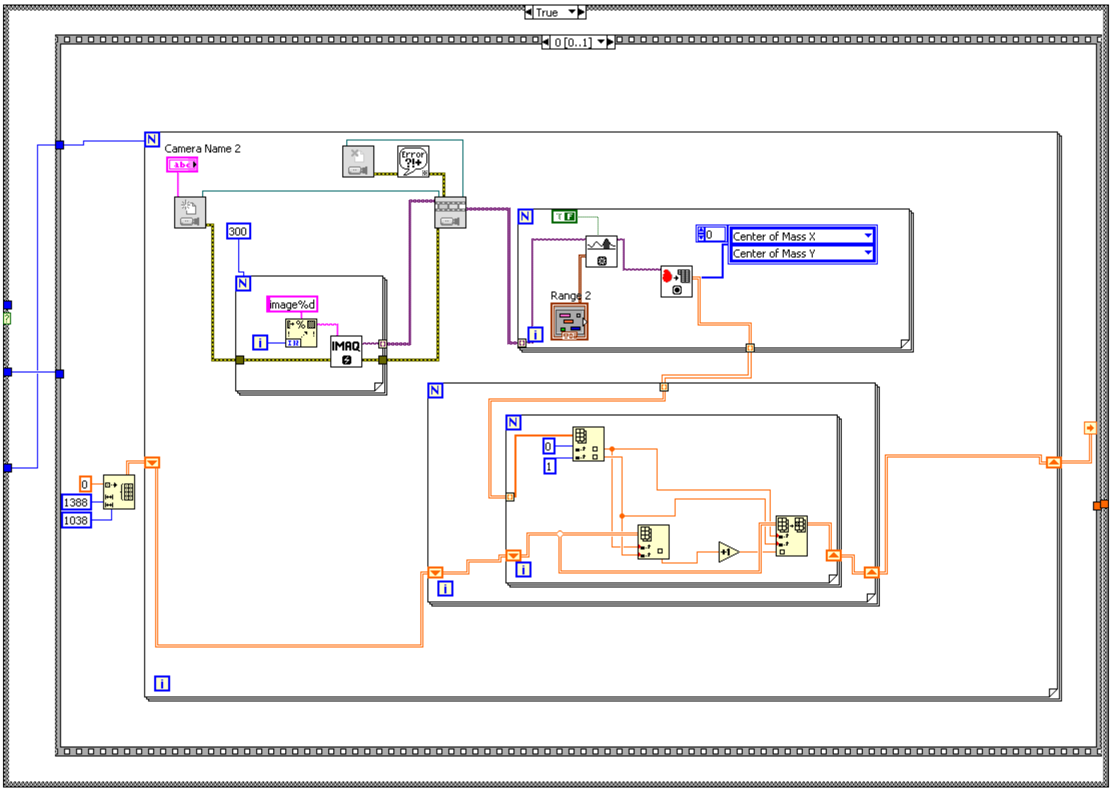

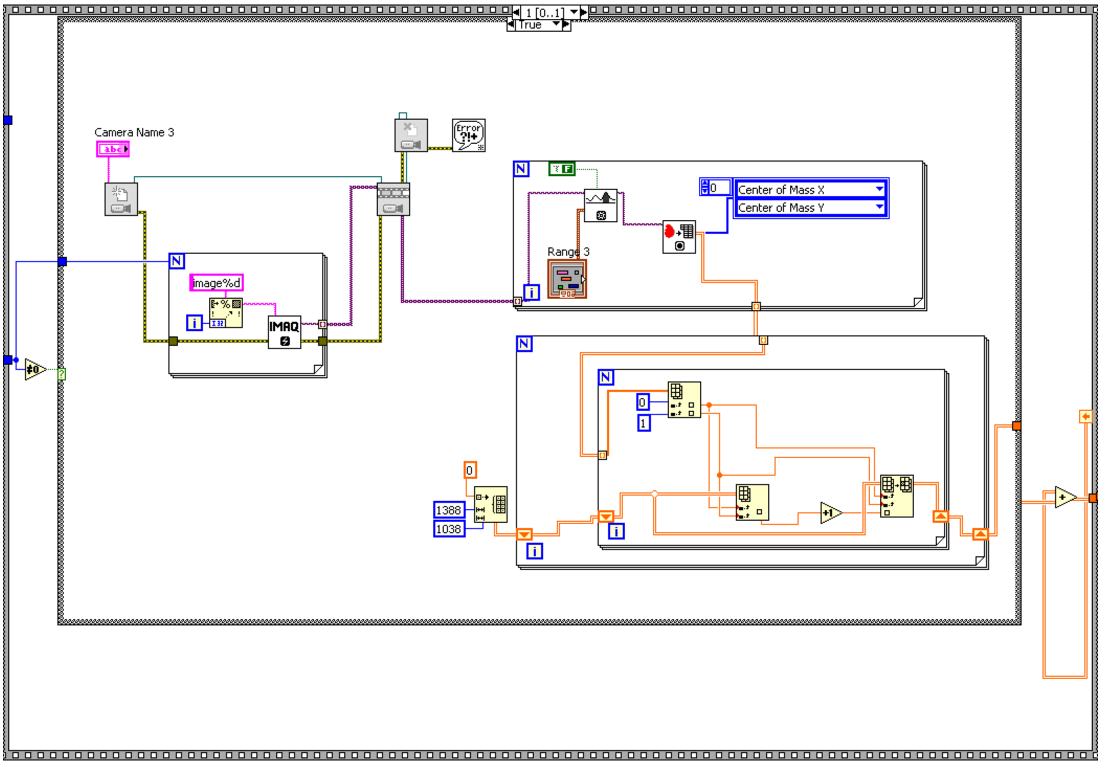
1 [0..1]
True
Camera Name 3
Error
N
image%d
i
IMAQ
Range 3
0
Center of Mass X
Center of Mass Y
0
1388
1038
0
1
+1
+
≠0

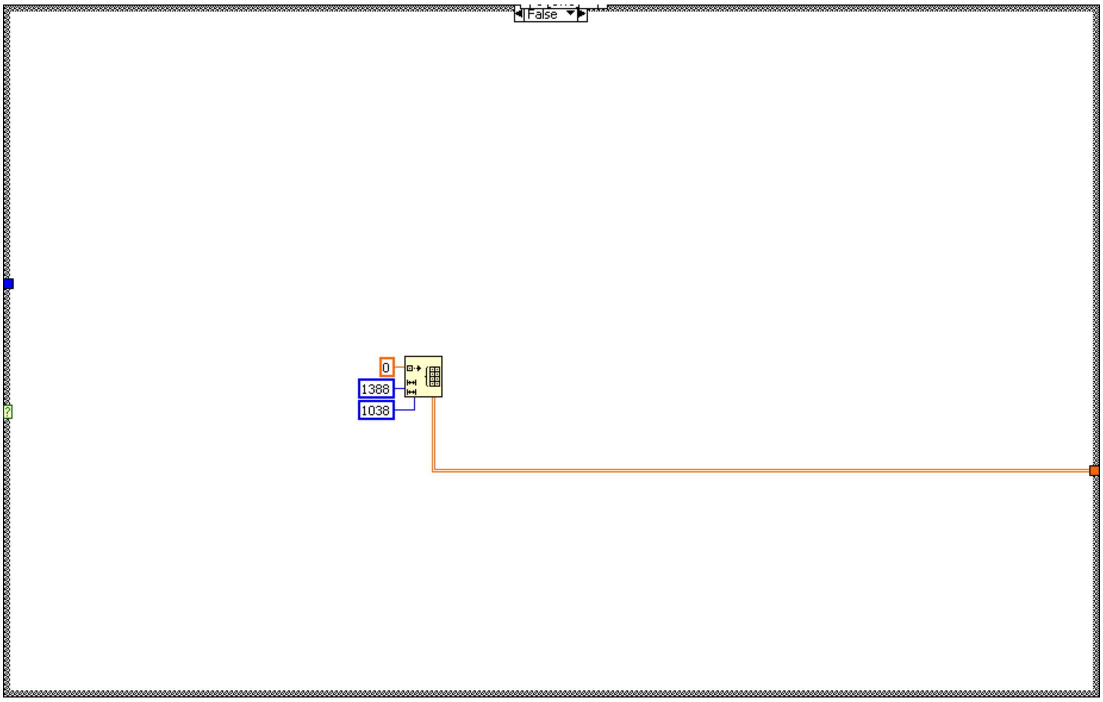
False
0
1388
1038

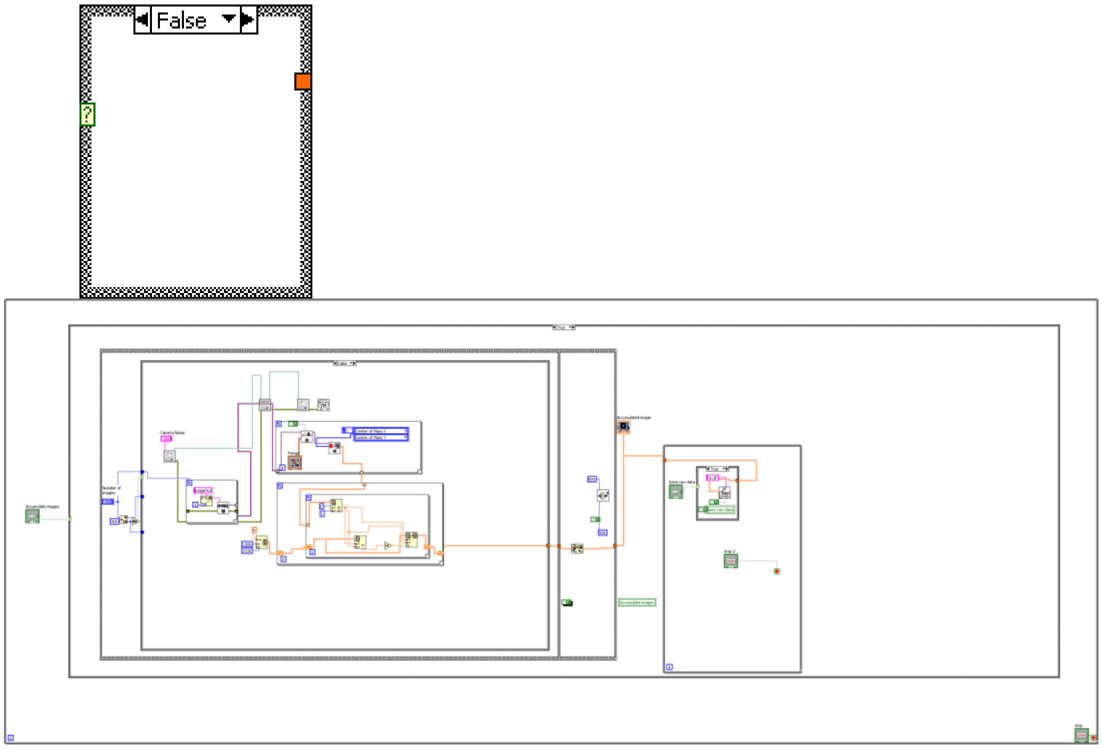

Load_cont_images.m

```
% Program to load raw images acquired using continuous_
acquisition.vi
% Written by Olof Johansson
clear all
clc

%--------------------------------------------------
% Input from user:
%--------------------------------------------------
start = 1510;% First file no. in the measurement series
stop = 1511;% Last file no.
folder = 'D:\DATA\Edinburgh\2010\06 - June\20100629\\';


%Load and subtract background
A = zeros(1038,1388);
for i=start:2:stop
    A_temp=load(strcat(folder,'El_',num2str(i),'.txt'));% Signal
```

```
    B_temp=load(strcat(folder,'El_',num2str(i+1),'.txt'));%
Background
    A = A + A_temp-B_temp;
end

%Plot final result
imagesc(real((A)));axis image;axis xy

%Save
y_or_no = input('Save data (y=yes; {Return} = no)?: ','s');
if (y_or_no == 'y')
    dlmwrite(strcat(folder,'El_',num2str(start),'_to_',...
        num2str(stop),'.txt'), A,'delimiter','\t');
end
```

Published with MATLAB® 7.8

Load_cent_images.m

```
% Program to load raw images acquired using single_count_acq.vi
% Written by Olof Johansson

clear all
clc

%--------------------------------------------------
% Input from user:
%--------------------------------------------------
start = 0751;% First file no. in the measurement series
stop = 0768; % Last file no.
folder = 'D:\DATA\Edinburgh\2009\12 - December\20091210\';


%Load and subtract background
A = zeros(1038,1388);

for i=start:1:stop
    A_temp=load(strcat(folder,'El_0',num2str(i),'.txt'));
    A =A + A_temp;
end


% Subtract contributions from dust on CCD chip
imagesc(real((A)));axis image;axis xy
% Plot image to find maximum count A_max
A_max = 780; %Supplied by user
A(1,1)=0;
%Subtract pixels and average with neighbouring  pixels
[a b] = find(A>A_max);
for i=1:length(a)
    if (a(i) == 1  || a(i) == 1038 || b(i) == 1 || b(i) == 1388)
        A(a(i),b(i)) = 0;
    else
        A(a(i),b(i)) = (A(a(i)-1,b(i)+1)+A(a(i)+1,b(i)+1)...
            +A(a(i)+1,b(i)+1)+A(a(i)+1,b(i))...
            +A(a(i)+1,b(i)-1)+A(a(i)+1,b(i)-1)...
            +A(a(i)-1,b(i)-1)+A(a(i)-1,b(i)))/8;
```

```
    end
end

%Plot final result
imagesc(real((A)));axis image;axis xy

% Save data
y_or_no = input('Save data (y=yes; {Return} = no)?: ','s');
if (y_or_no == 'y')
    dlmwrite(strcat(folder,'El_',num2str(i),'_bg_',...
        num2str(1240),'.txt'), A,'delimiter','\t');
end
```

Published with MATLAB® 7.8

Cato

```
%PLEASE READ:
%CATO (CArtesian TO polar coordinates) will carry out an 4 way
folding and
%afterwards continue with a conversion from cartesian to polar
coordinates.
%This code was translated into MATLAB from the original C-code
on
%http://www.dur.ac.uk/chemistry/lsd/groups/j.r.r.verlet/research
/clusters/pop/
%by Andreas K. Molberg (with lots of help by Olof Johansson)
%For further informations and comments to the procedure, please
check this
%website!

clear all
load Ainc_LUT.txt
load Pixels_LUT.txt


%Defining the matrix by loading the data-file
fname = 'D:\DATA\Edinburgh\2010\08 -
August\20100811\El_1587_to_1605.txt';

%Defining the coordinates for the center of the image
zzx = 595;
zzy = 518;

%Asking for reflecting
toll=input('Do you want to reflect the image? y/n:', 's');

%Loading matrix part 2
a = load (fname);
clear fname

%Size of matrix
[n,m]=size (a);

%Defining maximal permitted radius

if zzx<=(m-zzx)
```

```
    olofx=zzx;
else olofx=(m-zzx);
end

if zzy<=(n-zzy)
    olofy=zzy;
else olofy=(n-zzy);
end

if olofx<=olofy
    zz=olofx;
else zz=olofy;
end

%Preallocate a4 matrix
a4=zeros(zz);

%Preallocate polar matrix
polar=zeros(((floor(zz*pi/2))-1),zz);
polari=zeros(((floor(zz*pi/2))-1),zz);

%Defining starting point of folded matrix
a4(1, 1) = a(zzy, zzx)*4;

%Defining the rest of the matrix
for j=1:(zz-1)
    a4(1,j+1) = (a(zzy,zzx+j)+a(zzy,zzx-j))*2;
    for i=1:(zz-1)
        a4(i+1,j+1)=a(zzy+i,zzx+j)+a(zzy-i,zzx+j)+a(zzy+i,zzx-
j)+a(zzy-i,zzx-j);
        a4(i+1,1)=(a(zzy+i,zzx)+a(zzy-i,zzx))*2;
    end
end

%Take out garbage
% clear a
clear i
clear j
% clear zzx
% clear zzy
clear ans
% clear zzx
% clear zzy
clear olofx
clear olofy

%Step 2: Conversion from cartesian to polar coordinates

%Calculating Coordinates for polar pixels

%Calculating Nainc and Ainc
for rp=1:zz-2
    nainc=Pixels_LUT(rp,1);
    ainc=Ainc_LUT(rp);

    for qp=0:nainc

        %Continue with given Code
```

```
        xp=abs(rp*sin(ainc*qp))+1;
        yp=abs(rp*cos(ainc*qp))+1;

        xc=round(xp);
        yc=round(yp);

        xd=1-abs(xc-xp);
        yd=1-abs(yc-yp);

        %Determination of polar pixel intensity

        if ((xp>=xc) && (yp>=yc));
            pint=((xd*yd)*a4(yc,xc))+((xd*(1-
yd))*a4(yc+1,xc))+(((1-xd)*yd)*a4(yc,xc+1))+(((1-xd)*(1-
yd))*a4(yc,xc+1));
        else

            if ((xp>=xc) && (yp<=yc));
                pint=((xd*yd)*a4(yc,xc))+((xd*(1-yd))*a4(yc-
1,xc))+(((1-xd)*yd)*a4(yc,xc+1))+(((1-xd)*(1-yd))*a4(yc-
1,xc+1));
            else

                if ((xp<=xc) && (yp>=yc));
                    pint=((xd*yd)*a4(yc,xc))+((xd*(1-
yd))*a4(yc+1,xc))+(((1-xd)*yd)*a4(yc,xc-1))+(((1-xd)*(1-
yd))*a4(yc+1,xc-1));
                else

                    if ((xp<=xc) && (yp<=yc));
                        pint=((xd*yd)*a4(yc,xc))+((xd*(1-
yd))*a4(yc-1,xc))+(((1-xd)*yd)*a4(yc,xc-1))+(((1-xd)*(1-
yd))*a4(yc-1,xc-1));
                    end
                end
            end
        end

        %Placing polar pixel intensity in polar pixel matrix
"polar"

        polar(qp+1,rp)=polar(qp+1,rp)+pint;

    end

end

 %Reflecting of the image
if toll=='Y'

     %Defining new diagonal
    for rp=1:(zz-1)
        nainc=Pixels_LUT(rp,1);

        %Defining refleted matrix
        for qp=1:nainc+1
            if nainc+1+qp<=((floor(zz*pi/2))-1) && 1+nainc-qp>=1
                polari(nainc+1+qp,rp)=polar(1+nainc-qp,rp);
```

```
            end
        end
    end

elseif toll=='y'

    %Defining new diagonal
    for rp=1:(zz-1)
        nainc=Pixels_LUT(rp,1);

        %Defining refleted matrix
        for qp=1:nainc+1
            if nainc+1+qp<=((floor(zz*pi/2))-1) && 1+nainc-qp>=1
                polari(nainc+1+qp,rp)=polar(1+nainc-qp,rp);
            end
        end
    end
end

%Adding the two matrices to one image
polar=polar+polari;

%Plotting
figure;imagesc(polar);axis xy image

%Defining cutoff radius
rad = input('Do you want to define a cut-off radius? y/n:',
's');
if rad=='y'
    cut = input('Please define cut-off radius:');
    t = cut-1;
elseif rad=='Y'
    cut = input('Please define cut-off radius:');
    t = cut-1;
end

%Cut-off sphere
if rad=='Y'
    polar = polar(1:((floor(zz*pi/2))-1),1:t);
    zz=cut;
    figure;imagesc(polar);axis xy image
elseif rad=='y'
    polar = polar(1:((floor(zz*pi/2))-1),1:t);
    zz=cut;
    figure;imagesc(polar);axis xy image
end

%Cleaning up
clear xd
clear yd
clear xc
clear yc
clear a4
clear pint
clear xp
clear yp
clear nainc
clear ainc
```

```
clear pixels
clear rp
clear qp
clear ans
clear m
clear n
clear rad
clear cut
clear t
clear toll
clear polari
```

Carthage

```
%Note: CARTHAGE (CARTesian Transfer Helper Attaining Great
Effects) was
%translated from the original LABVIEW C-code into MATLAB by
%Andreas K. Molberg.
%It will regain the folded cartesian coordinate image from the
folded
%polar coordinate image gained with CATO.
%Thanks to Andrew Gray and Johan Ek Weis for their usefull
hints.

load Pixels_LUT.txt
load Ainc_LUT.txt

%Preallocate cartesian matrix
[m,n]=size(polar);
if m<=n
    zz=m;
else
    zz=n;
end


cart=zeros(zz-1);

polar2=zeros(((floor(zz*pi/2))-1),2*zz);

polar2(1:((floor(zz*pi/2))-1),1:zz-1)=polar(1:((floor(zz*pi/2))-
1),1:zz-1);

%Check for centre and edge Cartesian pixels to assign correct
values
for x=1:zz-2
    for y=1:zz-2

        if (x==1&&y==1)
            cart(1,1)=polar2(1,1);
            continue
        end

        if (x==1)
            cart(y,1)=polar2(1,y);
            continue
        end
```

```
        if (y==1)
            i=Pixels_LUT(x,1);
            cart(1,x)=polar2(i,x);
            continue
        end

        %Beginning of conversion for all other pixels
        Rc=(sqrt(x^2+y^2))+1;
        ac=atan(x/y);

        Rp=round(Rc);
        Qc=(ac/Ainc_LUT(Rp))+1;
        Qp=round(Qc);

        Rd=1-abs(Rp-Rc);
        QdA=1-abs(Qp-Qc);

        cint=(Rd*QdA)*polar2(Qp,Rp);

        if (Qc>Qp)
            cint=cint+((Rd*(1-QdA))*polar2(Qp+1,Rp));
        else

            if (Qc<Qp)
                cint=cint+((Rd*(1-QdA))*polar2(Qp-1,Rp));
            end
        end

        %Beginning of Move in the Radial position frame (i.e.
move to Rp
        %+/- 1?)
        if (Rc>Rp)
            Qc=(ac/Ainc_LUT(Rp+1))+1;
            Qp=round(Qc);

            QdB=1-abs(Qc-Qp);

            cint=cint+(((1-Rd)*QdB)*polar2(Qp,Rp+1));

            if (Qc>Qp)
                cint=cint+(((1-Rd)*(1-QdB))*polar2(Qp+1,Rp+1));
            else

                if (Qc<Qp)
                    cint=cint+ (((1-Rd)*(1-QdB))*polar2(Qp-
1,Rp+1));
                end
            end
        end

        if (Rc<Rp)

            Qc=(ac/Ainc_LUT(Rp-1))+1;
            Qp=round(Qc);

            QdB=1-abs(Qc-Qp);

            cint=cint+(((1-Rd)*QdB)*polar2(Qp,Rp-1));
```

```
            if (Qc>Qp)
                cint=cint+(((1-Rd)*(1-QdB))*polar2(Qp+1,Rp-1));
            else

                if (Qc<Qp)
                    cint=cint+(((1-Rd)*(1-QdB))*polar2(Qp-1,Rp-
1));
                end
            end
        end

        %Generate Cartesian pixel intensity
        cart(y,x)=cint;
    end
end

figure;imagesc(cart);axis image xy

%Stop! Cleaning time (Can't touch this)!
clear cint
clear Qc
clear Qp
clear Rd
clear QdB
%clear zz
%clear polar
clear i
clear ainc
clear pixels
clear x
clear y
clear ac
clear Rc
clear QdA
clear Rp
clear m
clear n
clear polar2
```

Published with MATLAB® 7.8

BASEX_pizza.m

```
% Program to calculate angular dependent PES from polar images
% produced by BASEX.
% Written by Olof Johansson

clear all
clc
%-------------------------------------------------
% Input from user:
%-------------------------------------------------
folder = ...
    'D:\DATA\Edinburgh\2010\08 -
August\20100804\Inverted_BASEX_broad\';
file_name = 'El_1539_to_1546_polar.dat';
```

```
sin_y_n = 0;    % Include sin(theta) in integration
                % no=0, yes=1.

%-------------------------------------------------
% Declare variables
%-------------------------------------------------
input_file = strcat(folder,file_name);
f_polar = load(input_file); %Load input file
N = length(f_polar);
deg_int = 10; %Length of angular interval
min_r = min(f_polar(:,1));
max_r = max(f_polar(:,1));
r_lut = (min_r:0.5:max_r)'; %radius look-up table
Out = zeros(length(r_lut),80/deg_int);

% Calculate velocity distribution
for ind=1:N
    angle_ind = floor(f_polar(ind,2)/deg_int-(10/deg_int-1));
    if (angle_ind > 0)
        R_index = find(r_lut == f_polar(ind,1),1);
        if (sin_y_n == 0)
            if (f_polar(ind,2) == 89);
                Out(R_index,angle_ind) =
Out(R_index,angle_ind)...
                    + 2*f_polar(ind,1)^2*f_polar(ind,3);
            else
                Out(R_index,angle_ind) =
Out(R_index,angle_ind)...
                    + f_polar(ind,1)^2*f_polar(ind,3);
            end

        elseif (sin_y_n == 1)
            if (f_polar(ind,2) == 89);
                Out(R_index,angle_ind) = ...
                    Out(R_index,angle_ind)+ ...

2*f_polar(ind,1)^2*sin(f_polar(ind,2)*2*pi/360)...
                    *f_polar(ind,3);
            else
                Out(R_index,angle_ind) =
Out(R_index,angle_ind)...
                    +
f_polar(ind,1)^2*sin(f_polar(ind,2)*2*pi/360)...
                    *f_polar(ind,3);
            end
        end
    end
end
clf

% Convert velocity distribution to PES and plot
for j=1:length(Out(1,:))
    y(:,j) = Out(:,j)./r_lut;
    plot(r_lut.^2,Out(:,j)./r_lut)
    hold on
end

% Save
```

```
y_or_no = input('Save data (y=yes; {Return} = no)?: ','s');
if (y_or_no == 'y')
    dlmwrite(strcat(folder,file_name(1:15),'_pizza_polar.txt'),
...
        [r_lut.^2 y],'delimiter','\t');
end
```

VMI_pizza_slices.m

```
%Program for converting raw and inverted VMI images to polar
coordinates
%Olof Johansson
clear all
clc

display('-------------------------------------------------------
--')
display('Polar converter')
display('-------------------------------------------------------
--')


%-------------------------------------------------
% Input from user:
%-------------------------------------------------

%Load file
folder = 'D:\DATA\Edinburgh\2010\08 - August\20100809\';
file_name = 'El_1576_to_1586_im.dat';
BASEX_YES = 0; %Is the image inverted using BASEX? Yes = 1; No =
0;
input_file = strcat(folder,file_name);
%Centre coordinates
x_c = 600;
y_c = 518;
NR = 500; %No. of radial elements
NT = 180; %No. of angular elements
ANG_BIN = 10; %No. of angular segments
NO_ANG_BIN = 90/10;

INPUT_IMAGE = load(input_file); %Load input file


%Separate northern hemisphere from southern. This is only
important
%if the image was inverted without averaging over the two
F(:,:,1)=INPUT_IMAGE(y_c:y_c+NR-1,x_c:x_c+NR-1);%0<Theta<90
F(:,:,2)=flipud(INPUT_IMAGE(y_c-NR+1:y_c,x_c:x_c+NR-
1));%90<Theta<180


%%%%%%%%%%%%%%%%%%%%%%%%%%%%%%%%%%%%%%%%%%%
% Convert to spherical coordinates using
```

```
% bicubic interpolation
%%%%%%%%%%%%%%%%%%%%%%%%%%%%%%%%%%%%%%%%%%
[X Z] = meshgrid(0:NR-1);
r = linspace(0,NR-1,NR);
t = linspace(0,90,NT);
[R T] = meshgrid(r,t);
x = sin(T*2*pi/360).*R;
z = cos(T*2*pi/360).*R;
polar = zeros(NT,NR,2);
polar_scaled = polar;
POLAR = zeros(2*NT,NR);
pizza_PES = zeros(NR,2*NO_ANG_BIN+1);
pizza_PES(:,1) = r;

for i = 1:2
polar(:,:,i) = interp2(X,Z,F(:,:,i),x,z,'*cubic'); %interpolate
polar_scaled(:,:,i) = polar(:,:,i).*R.^2;
end
polar(:,:,2)=flipud(polar(:,:,2));

for i=1:2
    POLAR((i-1)*NT+1:i*NT,:)=polar(:,:,i);
end


for i = 1:NO_ANG_BIN
    if (i == 1 && BASEX_YES == 1)
    else
    start = find(t>=(i-1)*ANG_BIN, 1, 'first' );
    stop = find(t<=i*ANG_BIN, 1, 'last' );
    pizza_PES(:,i+1) = sum(polar_scaled(start:stop,:,1));
    pizza_PES(:,2*NO_ANG_BIN+2-i) =
sum(polar_scaled(start:stop,:,2));
    end
end


%%%%%%%%%%%%%%%%%%%%%%%%%%%%%%
% Plot results
%%%%%%%%%%%%%%%%%%%%%%%%%%%%%%

figure(1)
clc
imagesc(real((POLAR)));axis image xy

figure(2)
for j=2:length(pizza_PES(1,:))
    y(:,j-1) = pizza_PES(:,j)./pizza_PES(:,1);
    plot(pizza_PES(:,1).^2,pizza_PES(:,j)./pizza_PES(:,1))
    hold on
end
hold off

%Save
y_or_no = input('Save data (y=yes; {Return} = no)?: ','s');
if (y_or_no == 'y')
    dlmwrite(strcat(folder,file_name(1:(length(file_name)-
4)),...
```

```
        '_pizza_PES.txt'), [pizza_PES(:,1).^2
y],'delimiter','\t');
end
```

Pizza_counts.m

```
%Program for calculating no of counts in a VMI pizza slice
%Olof Johansson
clear all
clc

display('-------------------------------------------------------
--')
display('Polar converter')
display('-------------------------------------------------------
--')


%-------------------------------------------------
% Input from user:
%-------------------------------------------------


%Load file
folder = 'D:\DATA\Edinburgh\2010\08 - August\20100811\';
file_name = 'El_1587_to_1605.txt';
input_file = strcat(folder,file_name);
x_c = 595;
y_c = 518;
NR = 500;
NT = 180;
ANG_BIN = 90/NT;
cutoff_radius_min = 0;
cutoff_radius_max = 510;



INPUT_IMAGE = load(input_file); %Load input file


%0<Theta<90
F(:,:,1)=INPUT_IMAGE(y_c:y_c+NR-1,x_c:x_c+NR-1);
%90<Theta<180
F(:,:,2)=flipud(INPUT_IMAGE(y_c-NR+1:y_c,x_c:x_c+NR-1));
%180<Theta<270
F(:,:,3)=fliplr(flipud(INPUT_IMAGE(y_c-NR+1:y_c,x_c-NR+1:x_c)));
%270<Theta<360
F(:,:,4)=fliplr(INPUT_IMAGE(y_c:y_c+NR-1,x_c-NR+1:x_c));

[X Z] = meshgrid(0:NR-1);
r = linspace(0,NR-1,NR);
t = linspace(0,90,NT);
[R T] = meshgrid(r,t);
x = sin(T*2*pi/360).*R;
z = cos(T*2*pi/360).*R;
polar = zeros(NT,NR,4);
polar_count_per_st = polar;
POLAR = zeros(4*NT,NR);
```

```
SLICE_COUNT = zeros(4*NT,2);
for i=1:4
SLICE_COUNT((i-1)*NT+1:i*NT,1) = (i-1)*90 +
ANG_BIN/2:ANG_BIN:i*90;
end
SLICE_COUNT_AVE = SLICE_COUNT;
r_max = find(r>=cutoff_radius_max, 1, 'first' );
r_min = find(r<=cutoff_radius_min, 1, 'last' );


%%%%%%%%%%%%%%%%%%%%%%%%%%%%%%%%%%%%%%%%%%%
% Convert to spherical coordinates using
% bicubic interpolation
%%%%%%%%%%%%%%%%%%%%%%%%%%%%%%%%%%%%%%%%%%
for i = 1:4
polar(:,:,i) = interp2(X,Z,F(:,:,i),x,z,'*cubic');
polar_scaled(:,:,i) = polar(:,:,i).*R.^2;
end
polar(:,:,2)=flipud(polar(:,:,2));
polar(:,:,4)=flipud(polar(:,:,4));
% polar_scaled(:,:,2)=flipud(polar_scaled(:,:,2));
% polar_scaled(:,:,4)=flipud(polar_scaled(:,:,4));
for i=1:4
    POLAR((i-1)*NT+1:i*NT,:)=polar(:,:,i);
end

%%%%%%%%%%%%%%%%%%%%%%%%%%%%%%%%%%%%%%%%%%%%%%%%%%%%%
% Integrate out radius dependence and binning
%%%%%%%%%%%%%%%%%%%%%%%%%%%%%%%%%%%%%%%%%%%%%%%%%%%%

SLICE_COUNT(0*NT+1:1*NT,2) = ...
    sum(polar(:,r_min:r_max,1),2);
SLICE_COUNT(1*NT+1:2*NT,2) = ...
    (sum(polar(:,r_min:r_max,2),2));
SLICE_COUNT(2*NT+1:3*NT,2) = ...
    (sum(polar(:,r_min:r_max,3),2));
SLICE_COUNT(3*NT+1:4*NT,2) = ...
    (sum(polar(:,r_min:r_max,4),2));

SLICE_COUNT_AVE(1:90/ANG_BIN,2) = ...
    sum(polar(:,r_min:r_max,1),2)/4+...
    flipud(sum(polar(:,r_min:r_max,2),2)/4)+...
    (sum(polar(:,r_min:r_max,3),2)/4)+...
    flipud(sum(polar(:,r_min:r_max,4),2)/4);



%%%%%%%%%%%%%%%%%%%%%%%%%%%%%%
% Plot results
%%%%%%%%%%%%%%%%%%%%%%%%%%%%%%

figure(1)
clc
imagesc(real((POLAR)));axis image xy

figure(2)
clc
plot(SLICE_COUNT(:,1),SLICE_COUNT(:,2),'o',...
```

```
    SLICE_COUNT_AVE(:,1),SLICE_COUNT_AVE(:,2),'s')
axis([0 360 0 1.1*max(SLICE_COUNT(:,2))])

y_or_no = input('Save data (y=yes; {Return} = no)?: ','s');
if (y_or_no == 'y')

dlmwrite(strcat(folder,file_name(1:15),'_raw_counts.txt'),...
        [strcat('r_min = ',num2str(cutoff_radius_min),{' '}),
...
        strcat('r_max =
',num2str(cutoff_radius_max))],'delimiter','');
    dlmwrite(strcat(folder,file_name(1:15),'_raw_counts.txt'),
...
        [SLICE_COUNT SLICE_COUNT_AVE(:,2)],'-append','roffset',
1,...
        'delimiter','\t');
end
```

Published with MATLAB® 7.8

Symmetry_check.m

```
% Program to divid a raw image into pizza plots and then
calculate
% the total number of counts in each pizza plot (for 360
degrees).
%The number of counts in each slice is weighted with the total
%number of pixels in that slice because that might differ.
%Olof Johansson 20091015

clear all
clc

folder = 'D:\DATA\Edinburgh\2009\03 - March\20090331\';
file_name = 'El_1_to_4_minus_5_to_8.txt';

Sub = importdata(strcat(folder,file_name));
% imagesc(real(log(Sub)));
% [xX Yy]=ginput(1)
rCenter = 496;
cCenter = 733;
% Sub(rCenter,:)=0;
% Sub(:,cCenter)=0;
% imagesc(real(log(Sub)));axis image;axis xy


Rows=450;
Columns=Rows;
% Sub(rCenter,cCenter)=0;
% imagesc(real(log(Sub)));

A1=Sub(rCenter+1:rCenter+Rows,cCenter+1:cCenter+Columns);%0<Theta
<90
A2=flipud(Sub(rCenter-Rows:rCenter-1,...
    cCenter+1:cCenter+Columns));%90<Theta<180
A3=fliplr(flipud(Sub(rCenter-Rows:rCenter-1,...
    cCenter-Columns:cCenter-1)));%180<Theta<270
```

```
A4=fliplr(Sub(rCenter+1:rCenter+Rows,...
    cCenter-Columns:cCenter-1));%270<Theta<360


r_detector=380; %radien
X=linspace(1,length(A1),length(A1));
[ax az]=meshgrid(X);
[a b]=find(sqrt(ax.^2+az.^2)>=r_detector);
for i=1:length(a);
    A1(b(i),a(i))=0;
    A2(b(i),a(i))=0;
    A3(b(i),a(i))=0;
    A4(b(i),a(i))=0;
end
A1=A1(1:r_detector+1,1:r_detector+1);
A2=A2(1:r_detector+1,1:r_detector+1);
A3=A3(1:r_detector+1,1:r_detector+1);
A4=A4(1:r_detector+1,1:r_detector+1);


r_detector_m=0; %radien
X=linspace(1,length(A1),length(A1));
[ax az]=meshgrid(X);
[a b]=find(sqrt(ax.^2+az.^2)<r_detector_m);
for i=1:length(a);
    A1(b(i),a(i))=0;
    A2(b(i),a(i))=0;
    A3(b(i),a(i))=0;
    A4(b(i),a(i))=0;
end

figure(1)
subplot(2,2,1);imagesc(real((A1)));
axis image;axis xy;title('0<\alpha<\pi/2','fontsize',20);colorbar
subplot(2,2,2);imagesc(real((A2)));
axis image;axis
xy;title('\pi/2<\alpha<\pi','fontsize',20);colorbar
subplot(2,2,3);imagesc(real((A3)));
axis image;axis
xy;title('\pi<\alpha<3\pi/2','fontsize',20);colorbar
subplot(2,2,4);imagesc(real((A4)));
axis image;axis
xy;title('3\pi/2<\alpha<2\pi','fontsize',20);colorbar


N=length(A1);
x=1:N;
[X Y]=meshgrid(x);
F=zeros(N,N);
radius=r_detector;
Steps=15; %In degrees
k=90-Steps;
NS=90/Steps;
S1=zeros(1,NS);
S2=zeros(1,NS);
S3=zeros(1,NS);
S4=zeros(1,NS);
c=1;
```

```
Theta=atan(Y./X);
for j=0:Steps:k;
    degrees1=j;
    degrees2=j+Steps;
    An1=degrees1*2*pi/360;
    An2=degrees2*2*pi/360;
    [a2 b2]=find(An1<=Theta & Theta<An2 &
sqrt(X.^2+Y.^2)<=1*radius &...
        sqrt(X.^2+Y.^2)>r_detector_m);
    for i=1:length(a2);
        S1(c)=S1(c)+A1(b2(i),a2(i));
        S2(c)=S2(c)+A2(b2(i),a2(i));
        S3(c)=S3(c)+A3(b2(i),a2(i));
        S4(c)=S4(c)+A4(b2(i),a2(i));
    end
    Number_of_pixels_per_slice(c)=length(a2);
    c=c+1;
end



S_N=length(S1);
X=1:4*S_N;
X=X*0;
x_temp=1:S_N;
x1=Steps*x_temp;
x2=Steps*x_temp+90;
x3=Steps*x_temp+180;
x4=Steps*x_temp+270;
X(1:S_N)=x1;
X(S_N+1:2*S_N)=x2;
X(2*S_N+1:3*S_N)=x3;
X(3*S_N+1:4*S_N)=x4;
%%Plot counts per pixel
S(1:S_N)=S1./Number_of_pixels_per_slice;
S(S_N+1:2*S_N)=fliplr(S2./Number_of_pixels_per_slice);
S(2*S_N+1:3*S_N)=S3./Number_of_pixels_per_slice;
S(3*S_N+1:4*S_N)=fliplr(S4./Number_of_pixels_per_slice);


S=S';
X=X';
MATRIS=[X S];
% save C60N2_14_C60N2_16.dat MATRIS -ascii -double

figure(2)
plot(X,S,'.');axis([0 max(X) 0 max(S)+0.1*max(S)])
xlabel('Radians','fontsize',24)
ylabel('Counts per number of pixels in one slice','fontsize',24)
title(strcat('Angular dependence: ',...
    num2str(Steps),'Degrees'),'fontsize',20)
%subplot(2,1,2);imagesc(real(log(Sub)));axis image;axis xy
%figure(3);imagesc(Sub);axis xy;axis image
```

Published with MATLAB® 7.8

Appendix E – Mass spectroscopy acquisition and analysis programs

Mass_spec.vi

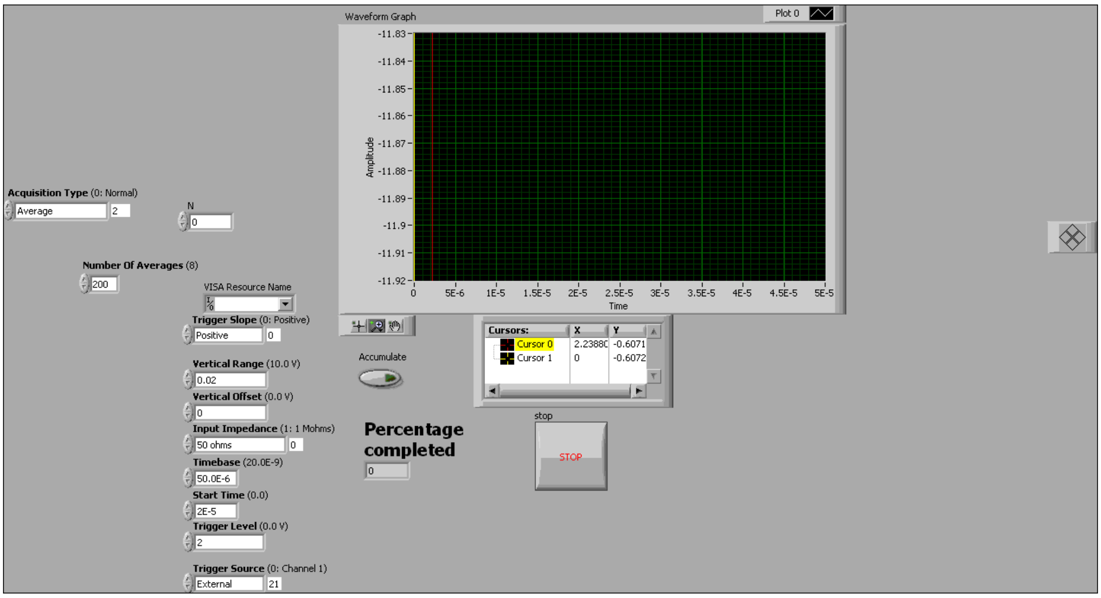

Acquisition Type (0: Normal): Average 2

N: 0

Number Of Averages (8): 200

VISA Resource Name:

Trigger Slope (0: Positive): Positive 0

Vertical Range (10.0 V): 0.02

Vertical Offset (0.0 V): 0

Input Impedance (1: 1 Mohms): 50 ohms 0

Timebase (20.0E-9): 50.0E-6

Start Time (0.0): 2E-5

Trigger Level (0.0 V): 2

Trigger Source (0: Channel 1): External 21

Cursors:	X	Y
Cursor 0	2.2388(	-0.6071
Cursor 1	0	-0.6072

Percentage completed: 0

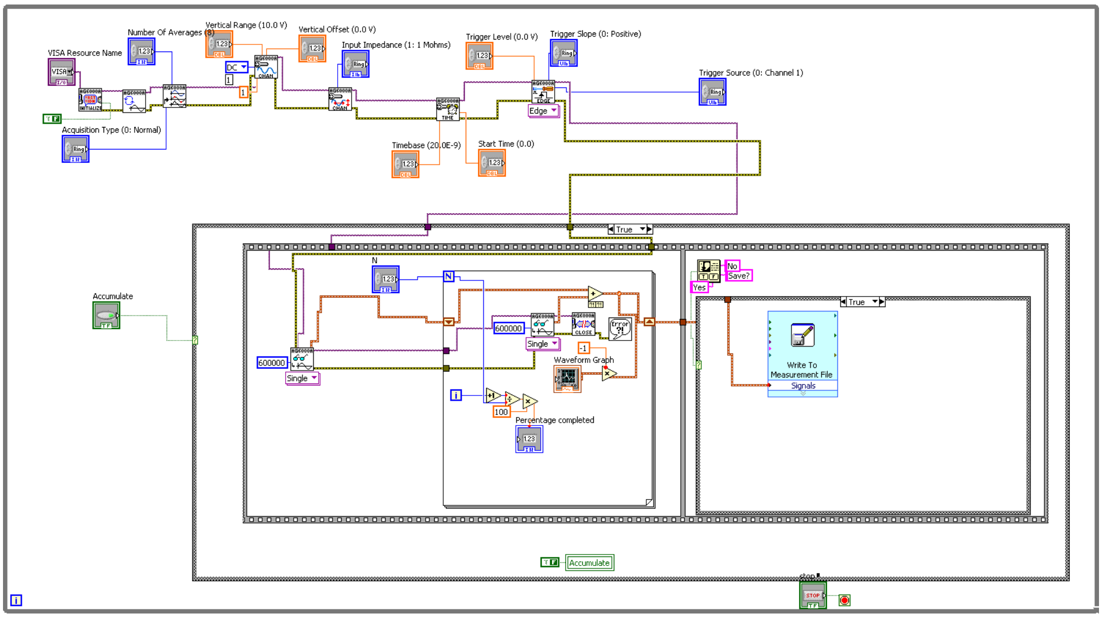

Mass_spec.m

```
%Program for loading and calibrating mass spec files obtained
%using mass_spec.vi
%Olof Johansson
clear all

%--------------------------------------------------
% Input from user:
%--------------------------------------------------

%Load file
folder = 'D:\DATA\Edinburgh\2010\05 - May\20100527\';
file_no = 438; %File no.

test = importdata(strcat(folder,'A_0',num2str(file_no),'.lvm'));
tm = test(:,1); %retrive the time axis
sig = test(:,2); %retrive the voltage signal + make positive
sig = sig/max(sig);
A(:,1) = -(test(:,2));

%Plot time-of-flight to find two peaks (tm1 and tm2) with known
%mass-to-charge ration
plot(tm,-sig)

% Give the arrival time of the two peaks and corresponding mass
tm1 = 2.94e-5;
m1 = 12*60;
tm2 = 2.08e-5;
m2 = 30*12;

%Calibrate mass spectrum
delta = tm1 - sqrt(m1)*(tm2-tm1)/(sqrt(m2)-sqrt(m1));
a = (tm2 - tm1)/(sqrt(m2)-sqrt(m1));
m2q = ((tm - delta)/a).^2;

%Plot
plot(m2q,(-sig+1))

%-------------------------
% Save data
%-------------------------
y_or_no = input('Save data (y=yes; {Return} = no)?: ','s');

if (y_or_no == 'y')

dlmwrite(strcat(folder,'A_0',num2str(file_no),'_mass2q.txt'),...
        [m2q (-sig+1)],'delimiter','\t');
end
```

Published with MATLAB® 7.8

Appendix F – C_{70}, 400 nm, 120 fs and 1.3 × 10^{11} W/cm^2.

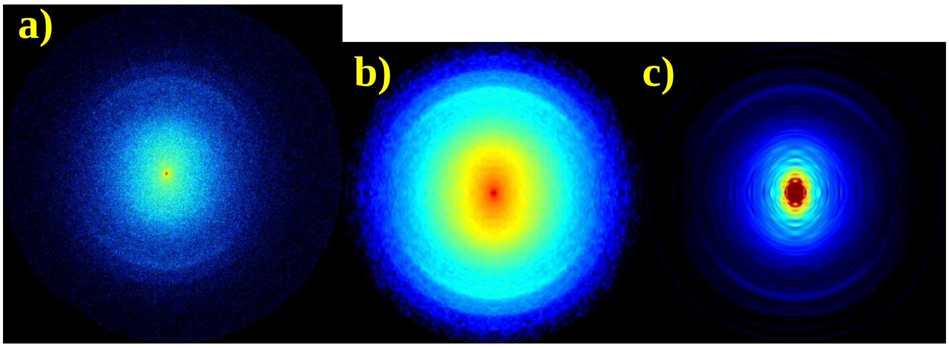

Figure F-1: a) Raw VMI image of C_{70} obtained after 400 nm, 120 fs laser excitation of intensity 1.3 ± 0.6 × 10^{11} W/cm^2. b) The raw image after smoothing. c) Inverted image using pBASEX.

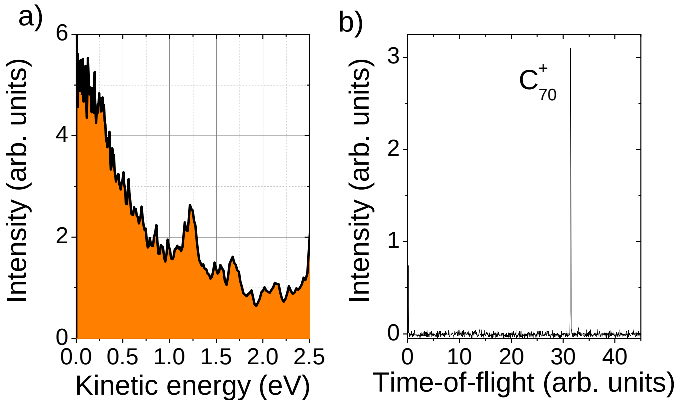

Figure F-2: C_{70} ionised using 400 nm, 120 fs laser excitation of intensity 1.3 ± 0.6 × 10^{11} W/cm^2. a) Angle-integrated PES from the inverted image presented above. b) Corresponding mass spectrum.

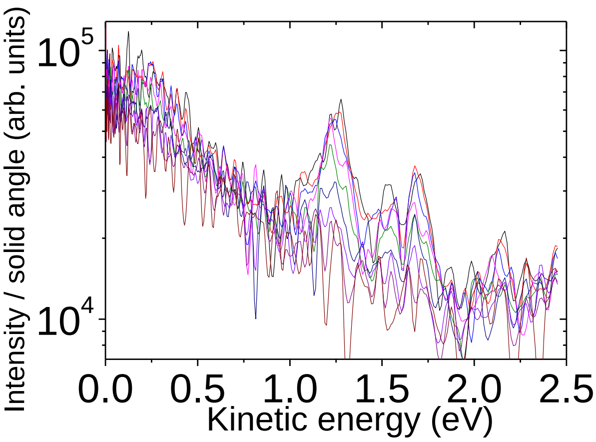

Figure F-3: Angle-resolved PES for the inverted VMI image presented above.

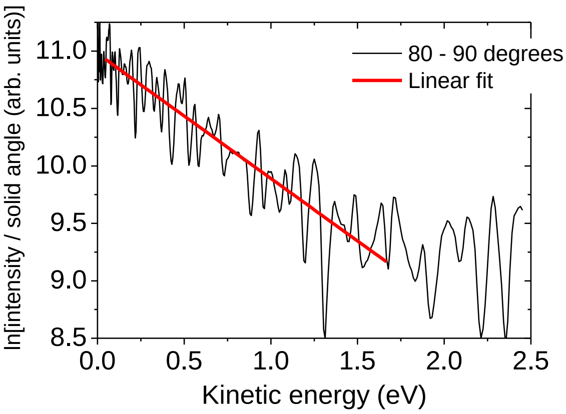

Figure F-4: Angle-resolved PES for the angular interval 80 – 90 degrees. The natural logarithm of the signal is plotted together with a linear fit made in *Origin*.

Appendix G – C_{60}, 800 nm 130 and 1000 fs

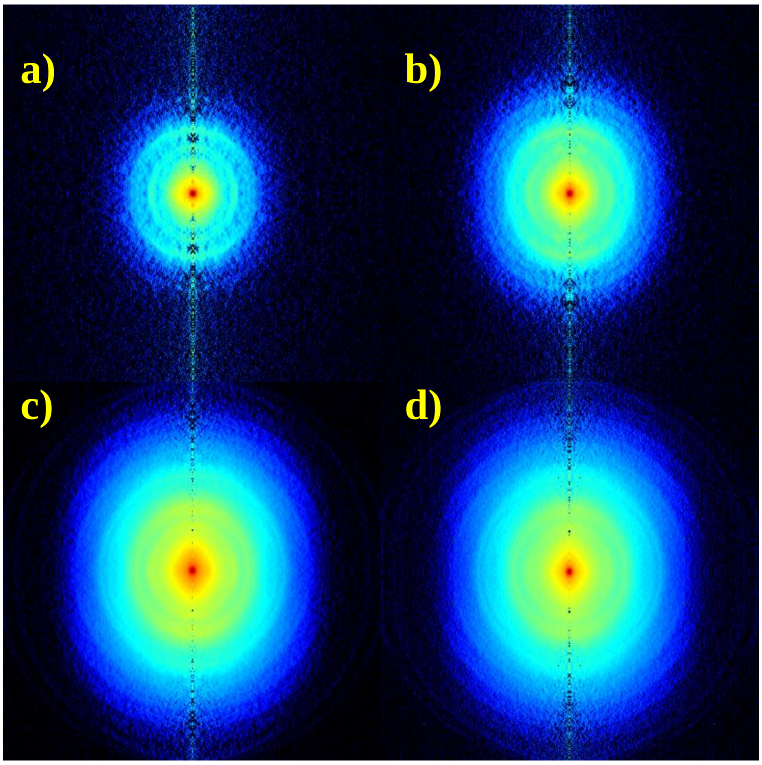

Figure G-1: Inverted C_{60} VMI images (using BASEX) for 800 nm, 130 fs laser pulse excitation. The laser fluences (intensity) were a) 0.40 ± 0.04 (2.9 ± 0.3), b) 0.66 ± 0.06 (4.8 ± 0.4), c) 1.1 ± 0.1 (7.6 ± 0.7) and d) 1.3 ± 0.1 J/cm^2 (9.5 ± 0.9 TW/cm^2).

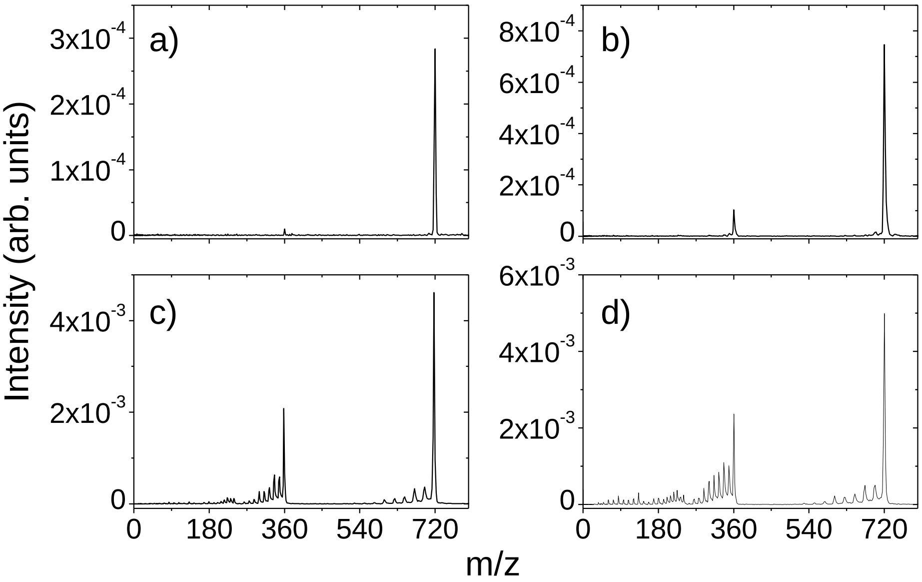

Figure G-2: C_{60} mass spectra taken with 800 nm, 130 fs laser excitation. The laser fluences (intensity) were a) 0.40 ± 0.04 (2.9 ± 0.3), b) 0.66 ± 0.06 (4.8 ± 0.4), c) 1.1 ± 0.1 (7.6 ± 0.7) and d) 1.3 ± 0.1 J/cm^2 (9.5 ± 0.9 TW/cm^2).

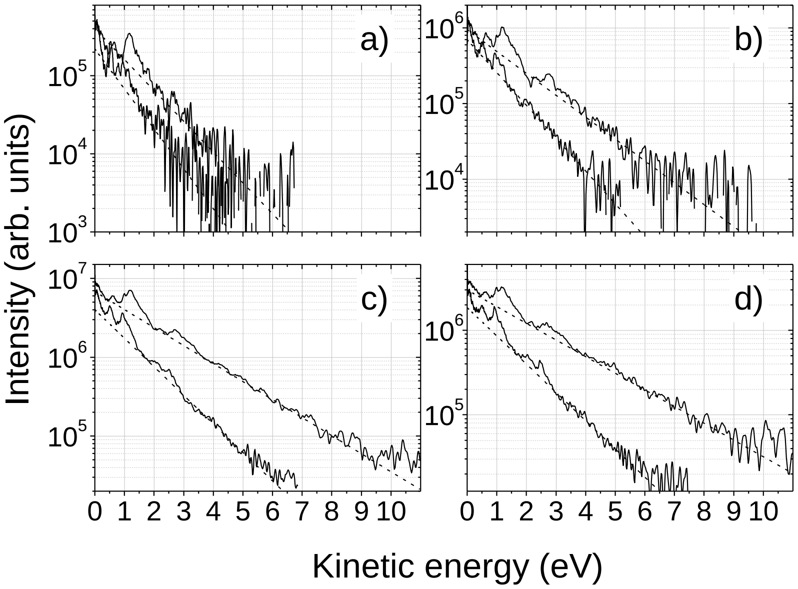

Figure G-3: C_{60} angle-resolved PES for 10-20° and 80-90° angular segments obtained from the VMI images shown in Figure G-1. Obtained after 130 fs, 800 nm laser excitation. The top curve corresponds to the 10-20° angular segment. The spectra have been cut off at the noise level. . The laser fluences (intensity) were a) 0.40 ± 0.04 (2.9 ± 0.3), b) 0.66 ± 0.06 (4.8 ± 0.4), c) 1.1 ± 0.1 (7.6 ± 0.7) and d) 1.3 ± 0.1 J/cm^2 (9.5 ± 0.9 TW/cm^2).

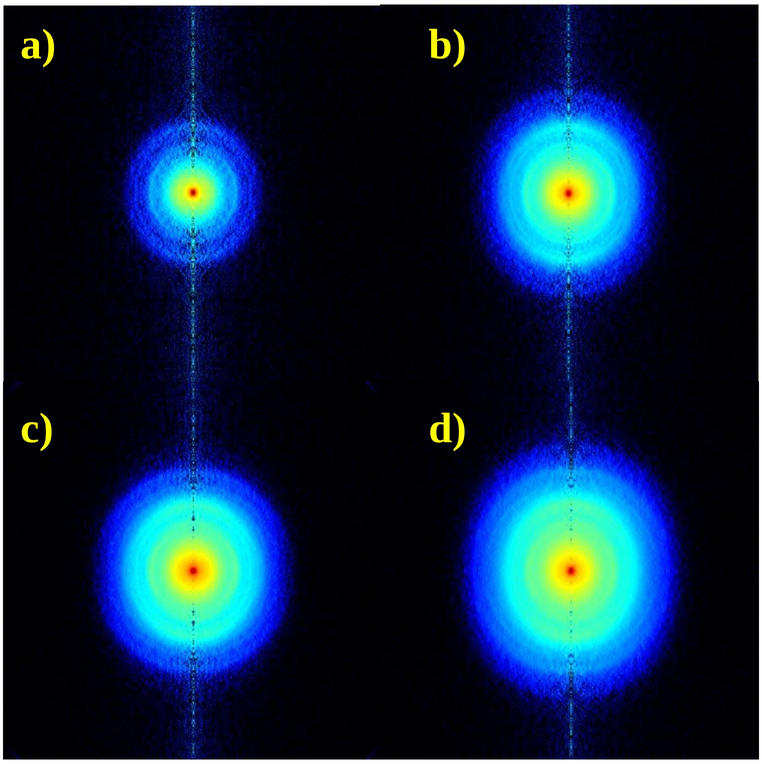

Figure G-4: Inverted C_{60} VMI images (using BASEX) for 800 nm, 1 ps laser pulse excitation. The laser fluences (intensity) were a) 0.88 ± 0.08 (0.82 ± 0.08), b) 1.3 ± 0.1 (1.2 ± 0.1), c) 1.6 ± 0.2 (1.5 ± 0.1) and d) 2.0 ± 0.2 J/cm^2 (1.9 ± 0.2 TW/cm^2).

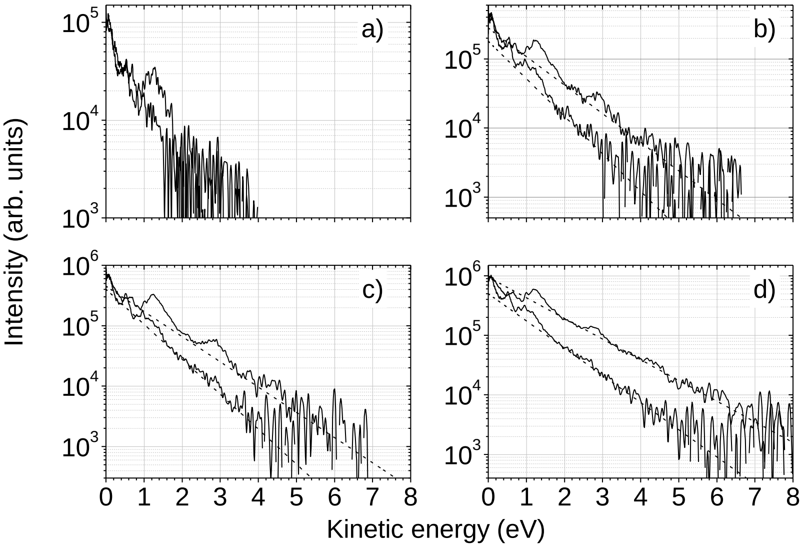

Figure G-5: C_{60} angle-resolved PES for 10–20° and 80–90° angular segments obtained from the VMI images shown in Figure G-4. The top curve corresponds to the 10-20° angular segment. The spectra have been cut off at the noise level. For the lowest power (a) it was not possible to distinguish thermal electrons from the peak structure seen below the photon energy. Therefore no fit was done for this fluence. The laser fluences (intensity) were a) 0.88 ± 0.08 (0.82 ± 0.08), b) 1.3 ± 0.1 (1.2 ± 0.1), c) 1.6 ± 0.2 (1.5 ± 0.1) and d) 2.0 ± 0.2 J/cm^2 (1.9 ± 0.2 TW/cm^2).

Appendix H – C_{70}, 800 nm, 117 and 180 fs

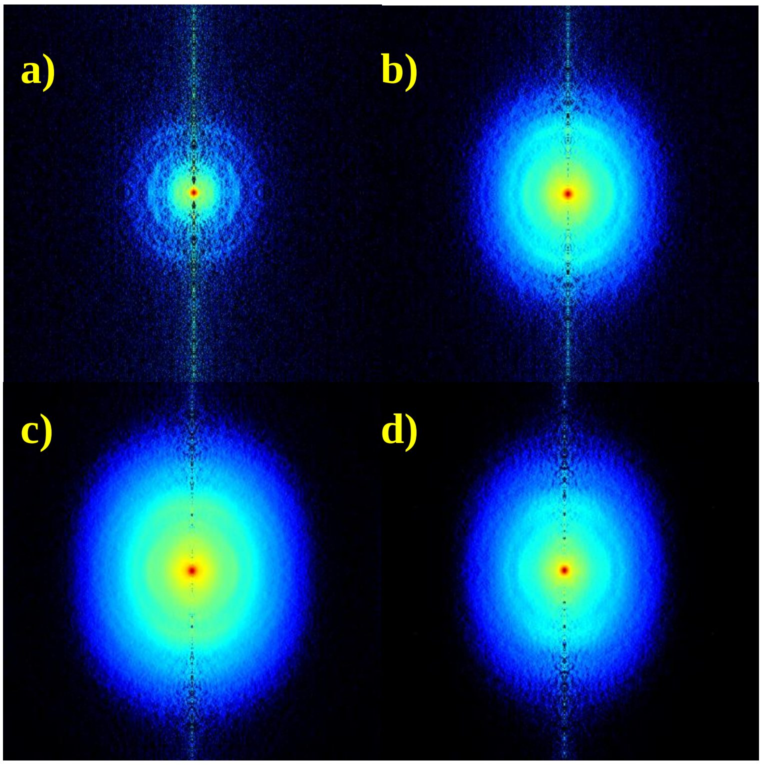

Figure H-1: Inverted C_{70} VMI images (using BASEX) for 800 nm laser pulse excitation. The laser pulse durations and fluences (intensity) were a) 180 fs, 0.60 ± 0.05 (3.0 ± 0.1), b) 180 fs, 0.9 ± 0.1 (4.5 ± 0.5), c) 180 fs, 1.2 ± 0.1 (6.1 ± 0.6) and d) 117 fs, 1.0 ± 0.1 J/cm^2 (7.5 ± 0.8 TW/cm^2).

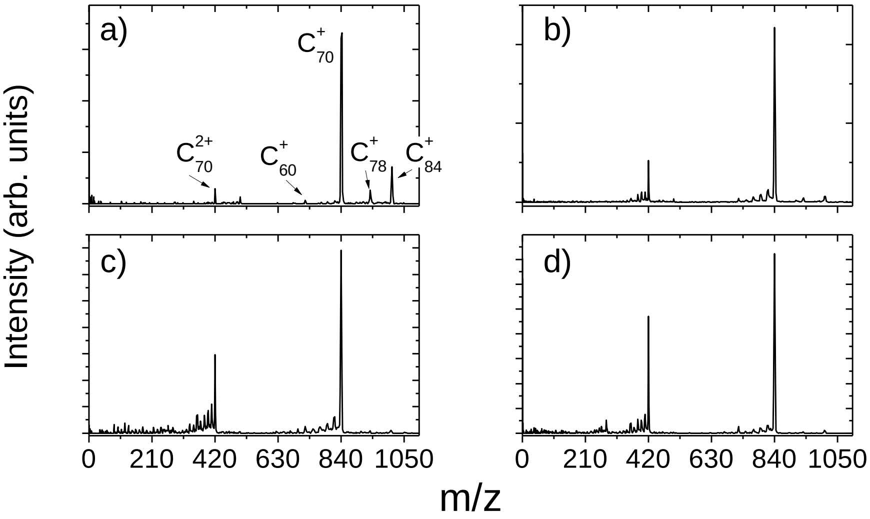

Figure H-2: C_{70} mass spectra taken with 800 nm, 130 fs laser excitation with the same fluences as in Figure H-1. The laser pulse durations and fluences (intensity) were a) 180 fs, 0.60 ± 0.05 (3.0 ± 0.1), b) 180 fs, 0.9 ± 0.1 (4.5 ± 0.5), c) 180 fs, 1.2 ± 0.1 (6.1 ± 0.6) and d) 117 fs, 1.0 ± 0.1 J/cm^2 (7.5 ± 0.8 TW/cm^2).

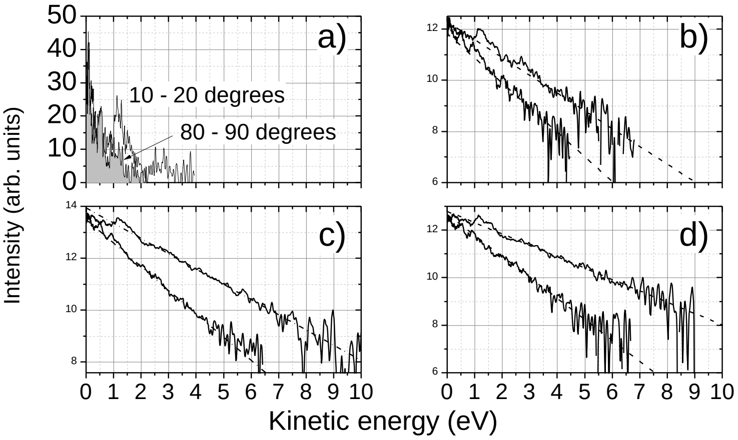

Figure H-3: C_{70} angle-resolved PES for 10-20° and 80-90° angular segments obtained from the VMI images shown in Figure H-1. The top curve corresponds to the 10-20° angular segment. The spectra have been cut off at the noise level. For the lowest power a) it was not possible to distinguish thermal electrons from the peak structure seen below the photon energy. Therefore no fit was done for this fluence. For all other spectra, the natural logarithm of the signal is plotted on the *y*-axis. The laser pulse durations and fluences (intensity) were a) 180 fs, 0.60 ± 0.05 (3.0 ± 0.1), b) 180 fs, 0.9 ± 0.1 (4.5 ± 0.5), c) 180 fs, 1.2 ± 0.1 (6.1 ± 0.6) and d) 117 fs, 1.0 ± 0.1 J/cm^2 (7.5 ± 0.8 TW/cm^2).